



HUEI-TING CHIEN

**Spatial Homogeneity and Environmental Degradation Affected by
Hole-Transport Layers in Organic Solar Cells**

DOCTORAL THESIS

For obtaining the academic degree of
Doktor der technischen Wissenschaften

Doctoral Programme of Technical Sciences
Technical Physics

Graz University of Technology

Supervisor:

Ao.Univ.-Prof. Mag. Dr.rer.nat. Robert Schennach

Institute of Solid State Physics

Co-Supervisor:

Dipl.-Phys. Dr.rer.nat. Bettina Friedel

Institute of Solid State Physics

Graz, February 2018

AFFIDAVIT

I declare that I have authored this thesis independently, that I have not used other than the declared sources/resources, and that I have explicitly indicated all material which has been quoted either literally or by content from the sources used. The text document uploaded to TUGRAZonline is identical to the present doctoral thesis.

01.03.2018

HUEI-TING, CHIEN

Date

Signature

Abstract

Organic photovoltaic cells (OPV) have received considerable attention as a potential source of renewable energy for their advantages such as easy fabrication, lightweight, low manufacturing cost, and mechanical flexibility. The improvement of device efficiency due to the incorporation of a hole-transport layer (HTL) in bulk-heterojunction (BHJ) solar cells (SCs) has been extensively reported. However, the most widely-used HTL material, poly(3,4-ethylenedioxythiophene):poly(styrenesulfonate) (PEDOT:PSS) is frequently suspected to be the dominating source for the device's instability under environmental conditions for its hygroscopic and acidic nature. Moreover, its colloidal nature is suspected to be responsible for spatial inhomogeneity and irreproducibility. Transition metal oxide (TMO) semiconductors are considered attractive alternative materials for the replacement of PEDOT:PSS. In this study, two different solution-processed molybdenum trioxide (MoO_3), obtained from two liquid precursors, a quasi-continuous MoO_3 with alcohol-based precursor solution and a colloidal MoO_3 with water-based precursor solution were demonstrated and incorporated as the HTL in OPV for the comparison of PEDOT:PSS HTL and a bare Indium tin oxide (ITO) electrode. The study was accomplished by combining and comparing different spatial imaging techniques, surface and bulk chemistry, device physics, photophysics, and so on to clarify the effects of HTL affecting the device's homogeneity and stability under different environmental conditions, dry air in the dark, illumination in the air and humid air in the dark. Initially, different material properties of HTLs and the bare ITO electrodes were characterized and the impacts of different HTLs upon implementation into OPVs were compared. Furthermore, degradation mechanisms of SCs influence by HTL were discussed by exposing different HTLs to various environments prior to device finalization under inert conditions. This allowed the investigation of any effects within the HTL and reactions at the interface between ITO electrode and active layer. Finally, the induced degradation of OPVs under different environmental conditions, uncoupled from the influence of any HTL was studied. This enabled observation of degradation mechanisms without the influence of HTL materials. It has been discovered that independent of colloidal or continuous form, MoO_3 presents a better candidate for solution-processed HTL materials, leading to higher homogeneity and performance of OPV. Among different environments, humid air has been proved to be the major environmental source, which strongly and fast deteriorates device performance regardless of with and/or without the influence of HTLs. The contact loss between anode/HTL or HTL/active layer interface induced by the partial film delamination was found on the device with moisture-absorbed nanoparticle HTLs, especially hygroscopic PEDOT:PSS, due to the swelling/shrinkage of the layer. When a device without HTL was exposed to the humid air environment, a detrimental contact loss was observed owing to the formation of the insulating barrier at the interface between cathode and active layer as water penetrated into the device through pinholes of the Al cathode. In conclusion, this thesis provides the knowledge on the influence of interlayers, interfaces and environmental effect in the SC from the device's inhomogeneity. This will help to improve stability and develop high performance OPV.

Zusammenfassung

Organische Photovoltaik (OPV) hat erhebliche Aufmerksamkeit als mögliche Quelle erneuerbarer Energie angezogen, weil ihre Vorteile, wie einfache Herstellung, geringes Gewicht, geringe Kosten für Herstellung und mechanische Flexibilität überzeugend klingen. Die Verbesserung der Effizienz durch die Einführung eines Hole Transport Layer (HTL) in Bulk-Heterojunction solarzellen wurde ausführlich berichtet. Allerdings ist das am weitesten verbreitete HTL Material, Poly(3,4-ethylenedioxythiophene):Poly(stirenesulfonate) (PEDOT:PSS) vermutlich häufig die dominierende Quelle für Instabilität der Solarzelle unter Umgebungsbedingungen, weil PEDOT:PSS hygroskopisch und sauer ist. Darüber hinaus wird vermutet, dass die kolloidale Natur verantwortlich für die räumlichen Inhomogenitäten und schlechte Reproduzierbarkeit der Zellen ist. Übergangsmetalloxid Halbleiter sind als attraktive alternative Materialien für den Ersatz von PEDOT:PSS in den Fokus gekommen. In dieser Arbeit werden zwei verschiedene flüssig-verarbeitete Molybdäntrioxide (MoO_3), die aus zwei flüssigen Vorläufern, einer quasi-kontinuierlichen MoO_3 Schicht aus einer Alkohol-basierten Precursorlösung und eines kolloidalen MoO_3 aus Wasser-basierter Precursorlösung demonstriert. Die MoO_3 Schichten wurden als HTL in OPV eingebaut für den Vergleich mit PEDOT:PSS und reinen Indium-Zinnoxid (ITO) Elektroden. Für die Studie wurden unterschiedliche räumliche Bildgebungsverfahren, Oberflächen- und Bulk Chemie, Physik, Photophysik usw. durchgeführt, um die Auswirkungen der HTL auf die Homogenität und Stabilität der Solarzellen unter verschiedenen Umgebungsbedingungen, trockene Luft im Dunkeln, Beleuchtung an Luft und feuchte Luft im dunkeln zu klären. Anfangs wurden verschiedene Materialeigenschaften der HTL und der reinen ITO-Elektroden charakterisiert und die Auswirkungen verschiedener HTL auf die Implementierung in OPVs verglichen. Zusätzlich wurden die Abbaumechanismen der Solarzellen, die durch HTL beeinflusst wurden, diskutiert, indem verschiedene HTL unterschiedlichen Umgebungen ausgesetzt wurden, bevor die Zelle unter inerten Bedingungen fertiggestellt wurde. Dies ermöglichte die Untersuchung der Effekte innerhalb der HTL und Reaktionen an der Grenzfläche zwischen der ITO-Elektrode und der aktiven Schicht. Schließlich wurde der Abbau der OPV unter verschiedenen Umweltbedingungen ohne den Einfluss der HTL untersucht. Dies ermöglichte die Beobachtung der Degradationsmechanismen ohne den Einfluss von HTL-Materialien. Es wurde gefunden, dass MoO_3 unabhängig von der kolloidalen oder kontinuierlichen Form ein besserer Kandidat für die flüssigverarbeitete HTL ist als PEDOT:PSS, was sich in hoher Homogenität und Leistungsfähigkeit der OPV zeigte. Unter den verschiedenen untersuchten Umgebungen hat sich feuchte Luft als die Hauptumweltquelle gezeigt, die stark und schnell die Leistung der Zelle, unabhängig ob mit und/oder ohne den Einfluss der HTLs, abbaut. Der Kontaktverlust zwischen der Anoden/HTL- oder HTL/aktiven Schicht-Grenzfläche, der durch die Delaminierung des partiellen Films induziert wurde, wurde auf den Zellen mit feuchtigkeitsabsorbierten Nanopartikel-HTL, besonders hygroskopischem PEDOT:PSS, aufgrund der Schwellung / Schrumpfung der Schicht gefunden. Wenn eine Zelle ohne HTL der feuchten Luft ausgesetzt wurde, beobachtet man einen Kontaktverlust aufgrund der Bildung einer isolierenden Barriere an der Grenzfläche zwischen Kathode und aktiver Schicht aus Wasser. Letzteres ist durch die Nadellöcher der Al Kathode in die Zelle eingedrungen. Zusammengefasst liefert diese Arbeit das neues Wissen über den Einfluss der Zwischenschichten, Grenzflächen und Umwelteinflüsse auf die Solarzelle. Dies wird dazu beitragen, die Stabilität zu verbessern und OPV mit hoher Leistung zu entwickeln.

Table of Content

| | |
|--|------|
| Abstract..... | II |
| Zusammenfassung..... | III |
| List of Figures..... | V |
| List of Tables..... | VII |
| List of Abbreviations..... | VIII |
| List of original articles..... | X |
| Chapter 1: Introduction..... | 1 |
| 1.1 World energy crisis..... | 1 |
| 1.2 Advantages of solar energy | 2 |
| 1.3 Types of solar cells | 3 |
| 1.3.1 First-Generation solar cells..... | 3 |
| 1.3.2 Second-Generation solar cells | 4 |
| 1.3.3 Third-Generation solar cells | 4 |
| 1.4 Aim of the thesis | 5 |
| 1.5 References | 6 |
| Chapter 2: Fundamental Device Physics of OPV..... | 8 |
| 2.1 Materials of organic electronics | 8 |
| 2.2 Development of OPV | 9 |
| 2.2.1 Single layer OPV | 9 |
| 2.2.2 Bilayer-heterojunction OPV | 9 |
| 2.2.3 Bulk-heterojunction (BHJ) OPV | 10 |
| 2.2.4 Comparison of conventional and inverted OPV | 10 |
| 2.3 Operating principles of OPV | 11 |
| 2.4 Characterization of OPV | 12 |
| 2.4.1 J-V curve parameters | 12 |
| 2.4.2 Equivalent circuit mode | 15 |
| 2.5 Materials for high efficient bulk-heterojunction (BHJ) OPV | 17 |
| 2.5.1 Active layer | 17 |
| 2.5.2 Electrode Materials | 18 |
| 2.5.3 Interfacial buffer Layers | 19 |
| 2.6 Degradation mechanisms of OPV | 20 |
| 2.6.1 Moisture and oxygen diffusion into OPV | 21 |
| 2.6.2 Light induced active layer degradation | 21 |
| 2.6.3 HTL PEDOT:PSS and electrodes related device instability | 22 |
| 2.6.4 Thermal instability | 23 |
| 2.6.5 Other device deterioration related factors | 24 |
| 2.7 Imaging techniques for studying inhomogeneity and stability of OPV | 24 |
| 2.8 References | 25 |
| Chapter 3: Experimental and Characterization..... | 34 |
| 3.1 Materials and chemicals | 34 |
| 3.2 Preparation of MoO ₃ HTLs | 34 |

| | | |
|---|---|-----|
| 3.2.1 | Fundamentals of sol-gel process | 34 |
| 3.2.2 | Experimental methods for MoO ₃ HTL preparation | 36 |
| 3.3 | Solar cells fabrication | 36 |
| 3.4 | Characterization techniques | 37 |
| 3.4.1 | Atomic force microscopy (AFM) | 37 |
| 3.4.2 | Kelvin probe force microscopy (KPFM) | 39 |
| 3.4.3 | X-ray photoelectron spectroscopy (XPS) | 41 |
| 3.4.4 | Ambient pressure photoemission spectroscopy system (APS) | 42 |
| 3.4.5 | Spectroscopic ellipsometry (SE) | 44 |
| 3.4.6 | Profilometry | 45 |
| 3.4.7 | X-ray powder diffraction (XRD) | 46 |
| 3.4.8 | Raman spectrometers and microscopes | 47 |
| 3.4.9 | Ultraviolet-visible (UV-Vis) spectroscopy | 49 |
| 3.4.10 | Fluorescence | 51 |
| 3.4.11 | Illuminated and dark current density–voltage (J–V) characteristics | 53 |
| 3.4.12 | Dark injection space-charge-limited current (DI-SCLC) | 54 |
| 3.4.13 | External quantum efficiency (EQE) | 56 |
| 3.4.14 | Light-Beam Induced current (LBIC) Microscopy | 57 |
| 3.4.15 | Transient photocurrent (TPC) measurement | 57 |
| 3.5 | References | 59 |
| Chapter 4: | Results and Publications | 64 |
| 4.2 | 4.1 Effects of hole-transport layer homogeneity in organic solar cells – A multi-length scale study | 65 |
| 4.2 | Influence of environmentally affected hole transport layers on spatial homogeneity and charge transport dynamics of organic solar cells | 75 |
| 4.3 | Short-term environmental effects and their influence on spatial homogeneity of organic solar cell functionality | 104 |
| Chapter 5: | Conclusions..... | 119 |
| Acknowledgements | | 121 |
| Publications and Conference contributions | | 122 |

List of Figures

| | | |
|------------|--|---|
| Figure 1.1 | World energy consumption from 1990 to 2040 projection period by energy source from U.S. Energy Information Administration.: | 1 |
| Figure 1.2 | The renewable generation in (a) OECD Europe and (b) India from 2010 to 2040 projection period by energy source from U.S. Energy Information Administration. | 2 |
| Figure 1.3 | The atmospheric path lengths in units of Air Mass according to the zenith angle. | 2 |
| Figure 1.4 | Solar spectral irradiances according to AM0, AM1.5 global and AM1.5 direct spectrum. | 3 |
| Figure 2.1 | Hybridization of (a) 2s and 2p bonds to form sp ² hybrid bonds (b) two sp ² orbitals to create sigma bond and π bond. | 8 |
| Figure 2.2 | Band diagram of molecular orbital from the double bond of discrete energy level to | |

| | |
|---|----|
| energy band with increasing double bands. | 9 |
| Figure 2.3 Typical OPV architecture of the different active layer structures (a) single layer (b) double layer (c) bulk heterojunction layer. | 9 |
| Figure 2.4 Schematic device architectures of a conventional and an inverted BHJ OPV. | 11 |
| Figure 2.5 Illustration of fundamental physical processes of a BHJ OPV. (i) Photo-induced exciton, (ii) exciton diffusion, (iii) exciton dissociation, (iv) charge separation, (v) charge transport, (vi) charge extraction at electrodes. | 11 |
| Figure 2.6 Typical J-V characteristics of a solar cell in the dark and illuminated conditions in (a) linear and (b) semilogarithmic plot. | 13 |
| Figure 2.7 Schematic energy diagram of open circuit voltage in BHJ OPV. | 14 |
| Figure 2.8 The equivalent circuit of (a) an ideal solar cell and (b) a solar cell with series resistance (R_s) and shunt resistance (R_{sh}). | 16 |
| Figure 2.9 Obtaining values for R_s and R_{sh} from the photocurrent-voltage curve. | 17 |
| Figure 2.10 Molecular structures of (a) MDMO-PPV and (b) P3HT. | 17 |
| Figure 2.11 Structure of (a) C_{60} and fullerene derivatives of (b) $PC_{60}BM$ and (c) $PC_{70}BM$ | 18 |
| Figure 2.12 Schematic energy diagram of different materials in the BHJ OPV. | 19 |
| Figure 2.13 Schematic illustration of degradation paths occurring in a BHJ OPV. | 21 |
| Figure 2.14 Schematic energy diagram of how the presence of trap states limits mobility in PCBM domains. | 22 |
| Figure 3.1 A schematic diagram showing the sol–gel process and its various products. | 35 |
| Figure 3.2 Device architecture of the standard studied solar cell | 37 |
| Figure 3.3 Schematic of typical AFM setup | 38 |
| Figure 3.4 Different modes of AFM and their corresponding force-distance curve. | 39 |
| Figure 3.5 Energy band diagram illustrating working principle of Kelvin probe technique | 40 |
| Figure 3.6 A general KPFM operating system | 41 |
| Figure 3.7 The principle of the photoemission spectroscopy technique and its corresponding band structure. | 42 |
| Figure 3.8 Schematic showing the setup of ambient photoemission spectroscopy. | 43 |
| Figure 3.9 Schematic energy band diagram of ambient pressure photoemission system | 43 |
| Figure 3.10 Schematic of a spectroscopic ellipsometer | 44 |
| Figure 3.11 Schematic set up of a stylus profilometer | 46 |
| Figure 3.12 Schematic diagram of Bragg diffraction. | 46 |
| Figure 3.13 Schematic diagram of a diffractometer using the Bragg-Brentano geometry. | 47 |
| Figure 3.14 Schematic diagram of a Raman analyzer and its basic principle | 48 |
| Figure 3.15 Energy transitions for Rayleigh and Raman Scattering of Raman Spectroscopy | 48 |
| Figure 3.16 Schematic diagram of Raman spectroscopy. | 48 |
| Figure 3.17 Schematic energy diagram based on Franck–Condon principle | 49 |
| Figure 3.18 Schematic absorption and fluorescence spectra refer to different electronic transitions | 50 |
| Figure 3.19 Schematic diagram of a simple absorption spectrometer | 50 |
| Figure 3.20 Method for bandgap approximation by the absorption spectrum | 51 |
| Figure 3.21 The Jablonski diagram displays the energy states of a molecule | 52 |
| Figure 3.22 Schematic diagram of absorption and emission spectra of Rhodamine 6G | 52 |
| Figure 3.23 Typical J-V curve (a) with a linear and (b) with semi-log scale plot for an organic solar cell. | |

| | |
|---|----|
| | 54 |
| Figure 3.24 Space charge–limited current as a function of bias for organic semiconductor in (a) ideal mode without traps (b) real mode with traps in the devices..... | 55 |
| Figure 3.25 Schematic of an EQE set up..... | 56 |
| Figure 3.26 Schematic of a light-beam induced current measurement setup..... | 57 |
| Figure 3.27 Simplified experimental setup of a photo-induced transient photocurrent..... | 58 |
| Figure 3.28 Schematic diagram of normalized transient photocurrent response | 58 |

List of Tables

| | |
|---|----|
| Table 3.1: Solar simulator classification according to IEC 60904-9 Ed. 2.0..... | 53 |
|---|----|

List of abbreviations

| | | | |
|---|---|--|--|
| AFM | Atomic force microscopy | He | Helium |
| Ag | Silver | HJ | Heterojunction |
| Al | Aluminum | HOMO | Highest occupied molecular orbital |
| Al ₂ O ₃ | Aluminum oxide | HTL | Hole-transport layer |
| AM | Air mass | In | Indium |
| APS | Ambient pressure photoemission spectroscopy | In ₂ O ₃ | Indium oxide |
| Au | Gold | IQE | Internal quantum efficiency |
| Ba | Barium | J _{sc} | Short-circuit current |
| BHJ | Bulk-heterojunction | ITO | Indium tin oxide |
| C | Carbon | J-V | Current-voltage |
| C ₆₀ | Buckminsterfullerene | k | Extinction coefficient |
| Ca | Calcium | KPFM | Kelvin probe force microscopy |
| CdS | Cadmium sulfide | K α | Emission line resulting from electron transition from innermost L (n=2) shell to the K (n=1) shell |
| CdTe | Cadmium telluride | LBIC | Light-beam induced current |
| CH ₃ NH ₃ PbBr ₃ | Methylammonium lead bromine | LED | Light-emitting diode |
| CH ₃ NH ₃ PbI ₃ | Methylammonium lead iodide | LiF | Lithium fluoride |
| CIGS | Copper indium gallium diselenide | LUMO | Lowest unoccupied molecular orbital |
| CIS | Copper indium diselenide | MDMO-PPV | Dimethyloctyloxyd-1,4-phenyl enevinylene |
| CO ₂ | Carbon dioxide | Mg | Magnesium |
| CPD | Contact potential difference | MoO ₂ (acac) ₂ | Bis(acetylacetonato)dioxomolybdenum(VI) |
| CT | Charge-transfer | MoO ₃ | Molybdenum trioxide |
| Cu | Copper | N | Nitrogen |
| CZTS | Copper zinc tin sulfide | n | Refractive index |
| D ₂ | Deuterium | (NH ₄) ₂ MoO ₄ | Ammonium molybdate |
| D-A | Donor-acceptor | Ni | Nickel |
| DI-SCLC | Dark injection space-charge-limited current | NiO | Nickel oxide |
| DSSC | Dye-sensitized solar cell | O ₂ | Molecular oxygen |
| DUV | Deep ultra-violet | OECD | Organization for Economic Cooperation and Development |
| EL | Electroluminescence | OLED | Organic light emitting diode |
| EQE | External quantum efficiency | OPV | Organic photovoltaic cell |
| ETL | Electron-transport layer | P3HT | Poly-3-hexylthiophene |
| EUV | Extreme ultraviolet | | |
| Fe | Iron | | |
| FF | Fill factor | | |
| H ₂ O ₂ | Hydroperoxide | | |
| HCl | Hydrochloric acid | | |

| | | | |
|---------------------|---|-------------------------------|--|
| Pb | Lead | SnO ₂ | Tin dioxide |
| PC ₆₀ BM | [6,6]-phenyl-C ₆₁ -butyric acid methyl ester | STC | Standard test condition |
| PC ₇₀ BM | [6,6]-Phenyl C ₇₁ butyric acid methyl ester | TFL | Trap-filled-limit |
| PCE | Power conversion efficiency | Tg | Glass transition temperature |
| PECVD | Plasma-enhanced chemical vapor deposition | Ti | Titanium |
| PEDOT:PSS | Poly(3,4-ethylenedioxythiophene):poly(styrenesulfonate) | TiO ₂ | Titanium dioxide |
| PL | Photoluminescence | TMO | Transition metal oxide |
| PPV | Polyphenylenevinylenes | TPC | Transient photocurrent |
| Pt | Platinum | UV | Ultraviolet |
| QE | Quantum efficiency | UPS | Ultraviolet photoelectron spectroscopy |
| R _s | Series resistance | UV-Vis | Ultraviolet-visible |
| R _{sh} | Shunt resistance | V ₂ O ₅ | Vanadium pentoxide |
| RuO ₂ | Ruthenium oxide | V _{oc} | Open-circuit voltage |
| SC | Solar cell | WO ₃ | Tungsten trioxide |
| SE | Spectroscopic ellipsometry | XPS | X-ray photoelectron spectroscopy |
| Si | Silicon | XRD | X-ray powder diffraction |
| Sn | Tin | Zn | Zinc |
| | | ZnO | Zinc oxide |
| | | ZrO ₂ | Zirconium dioxide |

List of original articles

The thesis is based on the following articles.

Huei-Ting Chien, Florian Pilat, Thomas Griesser, Harald Fitzek, Peter Poelt, Bettina Friedel. Influence of Environmentally Affected Hole Transport Layers on Spatial Homogeneity and Charge Transport Dynamics of Organic Solar Cells. (accepted in *ACS Appl. Mater. Interfaces*)

Huei-Ting Chien, Peter W. Zach, Bettina Friedel. Short-Term Environmental Effects and Their Influence on Spatial Homogeneity of Organic Solar Cell Functionality. *ACS Appl. Mater. Interfaces* **2017**, *9*, 27754

Huei-Ting Chien, Markus Pölzl, Georg Koller, Susanna Challinger, Callum Fairbairn, Iain Baikie, Markus Kratzer, Christian Teichert, Bettina Friedel. Effects of Hole-Transport Layer Homogeneity in Organic Solar Cells—A Multi-Length Scale Study. *Surfaces and Interfaces*, **2017**, *6*, 72

Introduction

1.1 World energy crisis

In 2015, the total world energy consumption was approximately 17 terawatts, which is estimated to reach more than 22 terawatts by 2040 with a projected 28 % increase [1]. Currently, the energy consumption relies mainly on fossil fuels (coal, oil, and gas), which induce serious environmental issues, such as CO₂ emissions, greenhouse effects, global warming, and so on. With the awareness of this crisis, alternative, clean, and renewable energy sources are being widely-developed for the replacement of fossil fuels. Nowadays, renewable energies (hydroelectricity, wind, solar, geothermal, biofuels etc.) are reported to be the world's fastest-growing energy sources, increasing an average 2.3% per year between 2015 and 2040. Figure 1.1 shows the world energy consumption by energy source from 1990 to the estimation in 2040, indicating not only the significantly emerging usage of renewable energy but also constantly increasing use of all fuels except for coal. Although renewable energy has become one of the world's fastest growing forms of energy, fossil fuels continue to meet much of the world's energy demand [1]. Reliance on this limited resource is a short-term solution.

Figure 1.2 shows the renewable generation in the Organization for Economic Cooperation and Development (OECD) Europe and an emerging country, India. Among all the renewable energies, hydropower dominates the sector, being the oldest and most widely-used technology of power generation. The growth in renewable energy in the last decade has been driven by wind and solar sectors. Especially in recent years, the solar cell (SC) has become one of the most promising clean energy sources, which meets the global energy and environmental challenges.

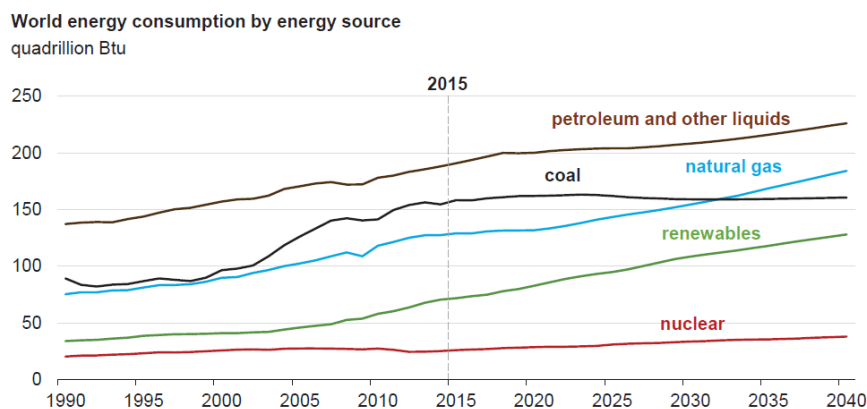


Figure 1.1 World energy consumption from 1990 to 2040 projection period by energy source from U.S. Energy Information Administration [1].

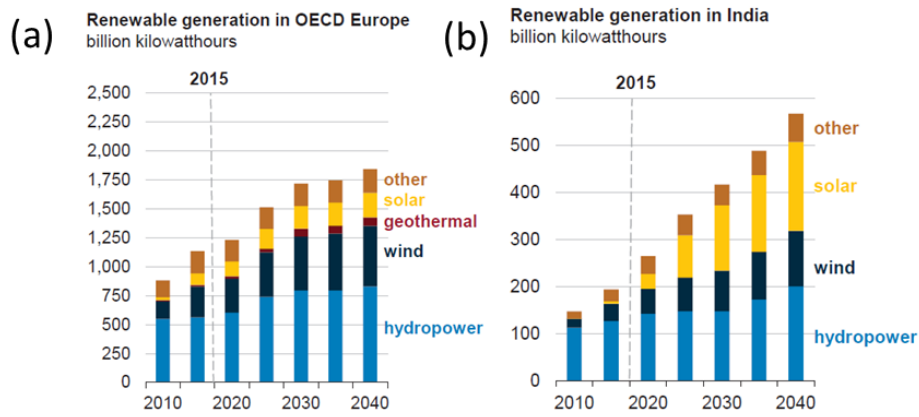


Figure 1.2 The renewable generation in (a) OECD Europe and (b) India from 2010 to 2040 projection period by energy source from U.S. Energy Information Administration [1].

1.2 Advantages of solar energy

Solar energy is an excellent choice for an environmentally-friendly reliable energy source, with the surface of Earth irradiating approximately 100 petajoules (10¹⁵ W) of energy every second [2], over 5000 times the current energy consumption in the world. In another word, solar radiation received by the earth's surface in 90 minutes is enough to feed the global energy requirement for an entire year [3]. This abundance of solar radiation energy can be converted directly into electricity through photovoltaic panels via the photoelectric effect. This offered a remarkable potential of solar energy in the renewable technology during past decades. The intensity of sunlight that hits earth's surface is related to the path it has taken through the atmosphere and its solid angle. Air mass (AM) is determined in order to describe the relative solar position and is defined in the equation (1.1) [4],

$$AM = \frac{P}{P_0} \approx \frac{1}{\cos \theta_z} \quad (1.1)$$

where P is the path length of solar radiation through the atmosphere, P₀ is the zenith path length normal to the Earth's surface at sea level and θ_z is the zenith angle. Figure 1.3 shows different atmospheric path lengths in units of AM, corresponding to the zenith angle. The spectrum outside of the atmosphere, which traverses through no air mass, is defined as "AM0", meaning "zero atmospheres". When sun radiation at zenith (or overhead position) traverses directly through the atmosphere to reach the ground, the radiation is known as "AM1". "AM1.5" corresponds to a solar zenith angle at 48.2°.

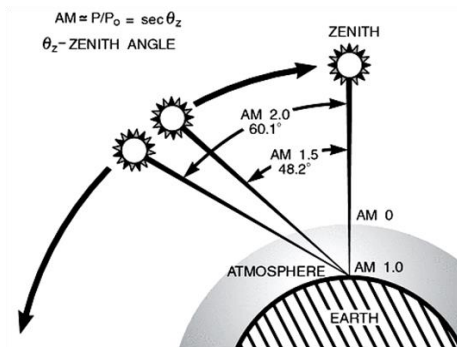


Figure 1.3 The atmospheric path lengths in units of Air Mass according to the zenith angle [4].

Figure 1.4 shows the solar spectral irradiances according to AM0, AM1.5 global and AM1.5 direct spectrum, respectively. The standard spectrum of AM0 has an integrated power of 1366.1 W/m^2 . The AM1.5 global spectrum is designed for flat plate modules with an integrated power of 1000 W/m^2 (100 mW/cm^2). The AM1.5 direct spectrum is determined for solar concentrators with an integrated power density of 900 W/m^2 [5]. For comparison purposes based on analysis of solar irradiance data from all over the world, all standardized testing of photovoltaic devices is carried out under AM1.5 G spectra at 1000 Wm^{-2} . This standard condition was selected according to a reasonable average for the 48 states of the United States of America (U.S.A.) over a period of one year. The tilt angle is approximately the average latitude for the contiguous U.S.A [6].

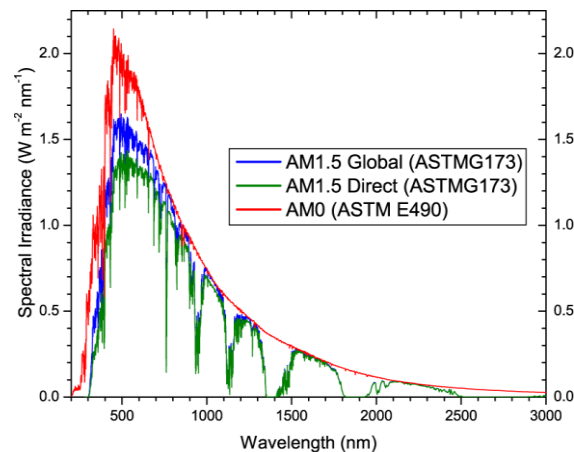


Figure 1.4 Solar spectral irradiances according to AM0, AM1.5 global and AM1.5 direct spectrum [5].

1.3 Types of solar cells

SC technologies are traditionally divided into three generations.

1.3.1. First-Generation solar cells

First-generation SCs are mainly based on crystalline silicon wafers, including monocrystalline and multicrystalline silicon (Si) SCs [7]. A typical conventional Si device is fabricated from crystalline Si, which is doped to form a p–n junction. The power conversion efficiency (PCE) of the single crystal silicon SC has been over 26% in recent years [8]. The high efficiency of these devices is due to the low bandgap of silicon ($\sim 1.1 \text{ eV}$) [9], contributing to the efficient absorption of the solar spectrum in the 400-800nm region and its excellent charge generation properties. This type of SCs dominates the current commercial market of photovoltaic technologies for its high efficiency and stability [10]. However, the difficulties of growing large crystals of pure mono-crystalline Si and the manufacturing process, resulting in a considerable material loss, energy and cost during production, has led to the development of multi-crystalline Si cells. Multi-crystalline wafers are cheaper and easier for device assembling, but they generally result in cells and modules with conversion efficiencies that are 2 to 4% lower than those obtained with mono-crystalline wafers, whose efficiency is still up to 20% [8]. For this generation of SCs, the economic cost could be cheaper due to the development of multi-crystalline Si devices, but the substantial amount of energy cost remains a big challenge [11].

1.3.2. Second-Generation solar cells

The second generation SCs are also named as thin-film SCs, including amorphous silicon and three non-Si materials, Copper indium diselenide (CIS), copper indium gallium diselenide (CIGS), and cadmium telluride (CdTe). Amorphous Si SCs were the first type of thin-film SC. Different from the traditional Si SCs using rigid silicon wafer, amorphous Si SCs utilize a backing substrate, such as stainless steel, aluminum, glass or even plastic with deposition of a very thin Si layer, allowing the manufacturing possibility for flexible devices. The deposition of amorphous silicon layers is generally operated by plasma-enhanced chemical vapor deposition (PECVD), which can reach large area deposition up to 1 m² or more [11]. However, this technology suffers from low efficiencies (4-8% for commercial modules) and long deposition times (~1 hour) due to slow deposition rates (~1 Å/s). CIS, CIGS, and CdTe SCs have received wide attention owing to their direct-gap property and high optical absorption coefficients, enabling absorption of the full visible light range within 1 μm. Since CIS, CIGS, and CdTe are p-type semiconductor materials, their devices are mostly coupled with a very thin n-type cadmium sulfide (CdS) layer for a heterojunction (HJ) structure SC [11]. One of the biggest advantages of second-generation SCs is that only a few micrometers thickness of semiconductor materials are required for high-efficiency device performance. The production cost is greatly reduced owing to less material consumption and lower cost manufacturing processes compared to the first-generation devices. However, the drawbacks of high energy cost from the high vacuum processes and temperature treatments and the use of environmentally unfriendly materials, such as CdS in this type of devices, have facilitated the development of the third-generation SCs in recent decades.

1.3.3. Third-Generation solar cells

Third-generation solar cells are the emerging photovoltaic technologies based on the materials of organic molecules, inorganic nanoparticles or hybrids, including dye-sensitized SC (DSSC) [12], perovskite SC [13], OPV [14-15], copper zinc tin sulfide SC (CZTS) [16], quantum dot SC [17], etc. Most developed third generation SCs are the DSSC, perovskite SCs and OPV, due to the low cost, solution processable and flexible manufacturing possibilities and tunable electronic properties [12-15].

DSSC is composed of a porous layer of n-type TiO₂ electrode, covered with a light-absorbing dye molecule, which is usually a metal organic complex, a metal cathode (e.g. Pt) and an electrolyte containing a redox mediator [12]. Charge transport is driven by the electron diffusion through TiO₂ and ionic diffusion in the electrolyte solution [18]. This concept allows efficient separation of generation and transportation of charge carriers, resulting in a minimized recombination. So far, the highest efficiency of DSSC is around 12% [8]. One of the major concerns in the DSSC design is the use of liquid electrolyte due to its instability at varying temperatures and leakage/evaporation from the solvent materials. Sealing remains a major challenge in this type of SCs. Therefore, replacement of the liquid electrolyte with a solid material has become a main ongoing field of research. Additionally, DSSCs have been studied in solid state form by utilizing a p-type semiconductor material in the device to substitute the liquid electrolyte. However, the efficiency of this type of devices is generally lower than original structure and with

poor stability [19].

Perovskite SC was first demonstrated by the replacement of dye material with organic-inorganic lead-halide perovskite compounds, $\text{CH}_3\text{NH}_3\text{PbI}_3$ and $\text{CH}_3\text{NH}_3\text{PbBr}_3$ as visible-light sensitizers in the DSSC [13]. These perovskite materials can be synthesized from abundant sources (Pb, C, N, and halogen), and have unique optical, excitonic and electronic properties. The SC efficiencies of this type of devices have increased initially from 3.8% in 2009 [13] to 22.1% in early 2016 [8], making it the fastest emerging potential solar technology to date. However, the device's instability caused by Ultraviolet (UV)-photodegradation of TiO_2 [20] and fast decomposition of perovskite materials under humid conditions [21] and the usage of toxic perovskite sensitizer, such as $\text{CH}_3\text{NH}_3\text{PbI}_3$ and $\text{CH}_3\text{NH}_3\text{PbBr}_3$ remain the major obstacles for commercialization of this type of SC.

OPV is based on small organic molecules or conjugated polymers (CPs) for light absorption and charge transport to generate electricity via the photovoltaic effect. This type of device offers several advantages. It is lightweight, non-toxic, low cost, mechanically flexible and has a low-temperature manufacturing process, and disposable processability, high chemical versatility and large-scale production ability [14-15]. Compare to all aforementioned SCs, OPV is one of the most environmentally friendly technologies with the highest environmental compatibility. One of the main disadvantages associated with organic SC is the lower efficiency around 12-13% [22,23] compared to traditional inorganic devices (between 20-25% [8]) owing to their narrow absorption bands, small exciton diffusion lengths, low carrier mobilities, high exciton binding energy (around 0.2-0.5 eV), low intrinsic carrier concentration and so on. Although the performance and stability of the third-generation SCs are still limited compared to first and second-generation SCs, they have great potential for commercialization. This thesis focuses on topics relating to organic SCs, in particular, on bulk-heterojunction (BHJ) OPV.

1.4 Aim of the thesis

One of the biggest advantages of OPV is the solution processability that can be prepared easily by mixing various components in an appropriate solvent and coating them onto different substrates, which make it the higher possibility for flexible, large-scale, high-speed roll to roll manufacturing processes [24-25]. Moreover, the efficiency of SC is tunable by numerous factors such as the combination and mixing ratio of different donor and acceptor materials, dissolving solvent, processing conditions, post-deposition treatments, and so on [26-27]. However, the solution processed technique and the multiple-layer process may lead to poor device homogeneities, reproducibility and environmental instability, which can occur at various steps of device preparation and appear in all layers. Understanding, controlling or blocking the effects of these fluctuations will help to achieve high performance and stable devices.

The aim of this study is to use the imaging technique to investigate the predominant factors of OPV on the generation of local microscopic inhomogeneities and their impact on local device physics and charge transport variations with and/or without the influence of different solution-processed colloidal hole-transport layers (HTLs) and environmental factors. First, different HTLs were synthesized and their chemical, physical properties and morphology were

investigated. Moreover, the device physics and spatial homogeneity SCs with different HTL materials were compared. Finally, the environmental degradation mechanisms of the devices were studied with and without the influence of HTLs.

The structure of the thesis is shown as follows:

Chapter 2: This chapter gives a broad overview of the background theory and working principle of OPV. Furthermore, different organic SC configurations, utilized material properties, and device degradation mechanisms are discussed in this chapter.

Chapter 3: The materials and configurations of the studied devices and experimental techniques utilized in the fabrication and characterization of OPV are covered in this chapter.

Chapter 4: Results and discussions are presented as three major topics:

- (i) Effects of hole-transport layer homogeneity in organic SCs – A multi-length scale study.
- (ii) Influence of environmentally affected hole-transport layers on spatial homogeneity and charge transport dynamics of organic SCs.
- (iii) Short-term environmental effects and their influence on the spatial homogeneity of organic SC functionality.

Chapter 5: The conclusions of this thesis are given in this chapter.

1.5 References

- [1] Administration, U.S.E.I., International Energy Outlook 2017. (accessed 19/02/2018). URI: <https://www.eia.gov/outlooks/ieo/>.
- [2] Cho, A. Energy's Tricky Tradeoffs. *Science (New York, N.Y.)* **2010**, *329*, 786–787.
- [3] International Energy Agency, Solar Energy Perspectives. URI: https://www.iea.org/publications/freepublications/publication/Solar_Energy_Perspectives2011.pdf. (accessed 19/02/2018).
- [4] Würfel, P.; Würfel, U. *Physics of Solar Cells: From Basic Principles to Advanced Concepts*; Wiley-VCH: Weinheim, 2009
- [5] Standard Solar Spectra. (accessed 19/02/2018). URI: <http://www.pveducation.org/pvcdrom/appendices/standard-solar-spectra>.
- [6] Gueymard, C. A.; Myers, D.; Emery, K. Proposed Reference Irradiance Spectra for Solar Energy Systems Testing. *Solar Energy* **2002**, *73*, 443–467.
- [7] Green, M. A. The Path to 25% Silicon Solar Cell Efficiency: History of Silicon Cell Evolution. *Prog. Photovolt: Res. Appl.* **2009**, *17*, 183–189.
- [8] National Renewable Energy Laboratory (NREL), Best Research-Cell Efficiencies. (accessed 19/02/2018). URI: <https://www.nrel.gov/pv/assets/images/efficiency-chart.png>.
- [9] Tiedje, T.; Yablonovitch, E.; Cody, G. D.; Brooks, B. G. Limiting Efficiency of Silicon Solar Cells. *IEEE Trans. Electron Devices* **1984**, *31*, 711–716.
- [10] *Seventh E.C. High Efficiency Silicon Solar Cells*. In *Photovoltaic Solar Energy Conference*; Goetzberger, A.; Palz, W.; Willeke, G., Eds.; Springer Netherlands: Dordrecht, 1987; pp 681-687
- [11] Shah, A. Photovoltaic Technology: The Case for Thin-Film Solar Cells. *Science (New York, N.Y.)* **1999**, *285*, 692–698.
- [12] O'Regan, B.; Grätzel, M. A Low-Cost, High-Efficiency Solar Cell Based on Dye-Sensitized Colloidal TiO₂ Films. *Nature* **1991**, *353*, 737–740.

- [13] Kojima, A.; Teshima, K.; Shirai, Y.; Miyasaka, T. Organometal Halide Perovskites as Visible-Light Sensitizers for Photovoltaic Cells. *Journal of the American Chemical Society* **2009**, *131*, 6050–6051.
- [14] Yu, G.; Gao, J.; Hummelen, J. C.; Wudl, F.; Heeger, A. J. Polymer Photovoltaic Cells: Enhanced Efficiencies via a Network of Internal Donor-Acceptor Heterojunctions. *Science (New York, N.Y.)* **1995**, *270*, 1789–1791.
- [15] Halls, J. J. M.; Walsh, C. A.; Greenham, N. C.; Marseglia, E. A.; Friend, R. H.; Moratti, S. C.; Holmes, A. B. Efficient Photodiodes from Interpenetrating Polymer Networks. *Nature* **1995**, *376*, 498–500.
- [16] Rao, S.; Morankar, A.; Verma, H.; Goswami, P. Emerging Photovoltaics: Organic, Copper Zinc Tin Sulphide, and Perovskite-Based Solar Cells. *Journal of Applied Chemistry* **2016**, *2016*, 1–12.
- [17] Chong, L.-W.; Chien, H.-T.; Lee, Y.-L. Assembly of CdSe onto Mesoporous TiO₂ Films Induced by a Self-Assembled Monolayer for Quantum Dot-Sensitized Solar Cell Applications. *Journal of Power Sources* **2010**, *195*, 5109–5113.
- [18] Sarker, S.; Ahammad, A. J. S.; Seo, H. W.; Kim, D. M. Electrochemical Impedance Spectra of Dye-Sensitized Solar Cells: Fundamentals and Spreadsheet Calculation. *International Journal of Photoenergy* **2014**, *2014*, 1–17.
- [19] Meng, Q.-B.; Takahashi, K.; Zhang, X.-T.; Sutanto, I.; Rao, T. N.; Sato, O.; Fujishima, A.; Watanabe, H.; Nakamori, T.; Uragami, M. Fabrication of an Efficient Solid-State Dye-Sensitized Solar Cell. *Langmuir* **2003**, *19*, 3572–3574.
- [20] Leijtens, T.; Eperon, G. E.; Pathak, S.; Abate, A.; Lee, M. M.; Snaith, H. J. Overcoming Ultraviolet Light Instability of Sensitized TiO₂ with Meso-Superstructured Organometal Tri-halide Perovskite Solar Cells. *Nature communications* **2013**, *4*, 2885.
- [21] Noh, J. H.; Im, S. H.; Heo, J. H.; Mandal, T. N.; Seok, S. I. Chemical Management for Colorful, Efficient, and Stable Inorganic-Organic Hybrid Nanostructured Solar Cells. *Nano letters* **2013**, *13*, 1764–1769.
- [22] Zhao, W.; Li, S.; Yao, H.; Zhang, S.; Zhang, Y.; Yang, B.; Hou, J. Molecular Optimization Enables over 13% Efficiency in Organic Solar Cells. *Journal of the American Chemical Society* **2017**, *139*, 7148–7151.
- [23] Li, M.; Gao, K.; Wan, X.; Zhang, Q.; Kan, B.; Xia, R.; Liu, F.; Yang, X.; Feng, H.; Ni, W.; Wang, Y.; Peng, J.; Zhang, H.; Liang, Z.; Yip, H.-L.; Peng, X.; Cao, Y.; Chen, Y. Solution-Processed Organic Tandem Solar Cells with Power Conversion Efficiencies >12%. *Nature Photon* **2017**, *11*, 85–90.
- [24] Shaheen, S. E.; Radspinner, R.; Peyghambarian, N.; Jabbour, G. E. Fabrication of Bulk Heterojunction Plastic Solar Cells by Screen Printing. *Appl. Phys. Lett.* **2001**, *79*, 2996–2998.
- [25] Krebs, F. C.; Tromholt, T.; Jørgensen, M. Upscaling of Polymer Solar Cell Fabrication Using Full Roll-to-Roll Processing. *Nanoscale* **2010**, *2*, 873–886.
- [26] van Bavel, S. S.; Bärenklau, M.; With, G. de; Hoppe, H.; Loos, J. P3HT/PCBM Bulk Heterojunction Solar Cells: Impact of Blend Composition and 3D Morphology on Device Performance. *Adv. Funct. Mater.* **2010**, *20*, 1458–1463.
- [27] Brabec, C. J.; Heeney, M.; McCulloch, I.; Nelson, J. Influence of Blend Microstructure on Bulk Heterojunction Organic Photovoltaic Performance. *Chemical Society reviews* **2011**, *40*, 1185–1199.

Fundamental Device Physics of OPV

2.1 Materials of organic electronics

Organic electronics are mainly based on conjugated polymers (CPs) or small molecules organic semiconductors. Especially, CPs have received great attention for its application on electronic devices since the report of conjugated polyacetylene and widely utilized as the photoactive materials in OPV in recent years [1]. CPs present a carbon-based backbone along the molecule with alternating single and double bonds. The carbon atoms are sp^2 hybridized with one remaining p-orbital combined from the mixing of a 2s orbital and two of 2p orbitals, as shown in Figure 2.1 (a) [2]. As two sp^2 hybridized carbon atoms are bonding together, a sigma bond (σ) (single bond) is formed when two sp^2 orbitals combine and a delocalized π -bond (double bond) is formed when the two remaining unhybridized $2p_z$ orbitals overlap, as seen in Figure 2.1 (b) [2]. This is called conjugation.

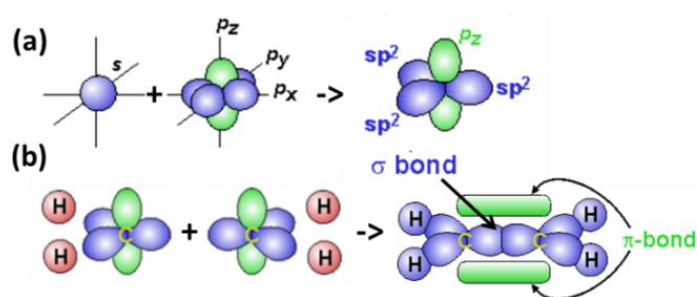


Figure 2.1 Hybridization of (a) 2s and 2p bonds to form sp^2 hybrid bonds (b) two sp^2 orbitals to create sigma bond and π bond [2].

As the π orbitals are delocalized, they overlap across the undisturbed backbone forming a band-like structure, similar to valence band and conduction band in a solid. Thereby the binding π orbital forms the highest occupied molecular orbital (HOMO) and the anti-binding π^* orbital forms the lowest unoccupied molecular orbital (LUMO). With extension of the conjugation length across the backbone or even intermolecular (in ordered structures), the delocalized π orbitals form the HOMO level of the polymer, and the higher energy π^* orbitals form the LUMO level, as shown in Figure 2.2. Thereby the delocalized π -electrons enable charge transport within the molecule of a CP, leading to optical and electronic properties and the conductivity of the materials [3]. The bandgap energy (E_g) of the organic semiconductor is defined as the difference between the HOMO and the LUMO. The bandgap energy of CPs mostly lies in the range of 1-3 eV [4], which is relevant to the absorption range in the visible wavelength region, making the organic semiconductors highly attractive materials for optoelectronic applications. By varying the components of the CP chains, the electronic properties of organic materials are tunable, giving them great potential for the application on electronic devices [5-6].

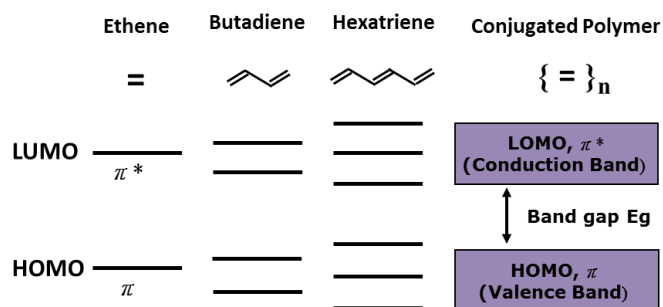


Figure 2.2 Band diagram of molecular orbital from the double bond of discrete energy level to energy band with increasing double bands.

2.2 Development of OPV

2.2.1. Single layer OPV

The first reported OPV was based on a monolayer of a conductive photoactive material, poly(acetylene), sandwiched between two electrodes of different work functions, one with high work function ITO coated glass, and the other with a low work function metal layer, for example, aluminum, magnesium, or calcium [7]. The work function difference between the two electrodes helps to split exciton pairs, pulling electrons to the cathode and holes to the anode [8]. These cells exhibit low quantum efficiencies (<1%) and low power conversion efficiencies (PCEs) (<0.1%) mainly due to the unfavorable dissociation of the created excitons for its high binding energy approximately 0.5-1 eV [9] (only around 100 meV for crystalline Si [10]), insufficient electric field to split excitons and recombination of electrons and holes before reaching to electrodes [11-12]. This single layer structure is the simplest architecture of OPV, illustrated in Figure 2.3 (a).

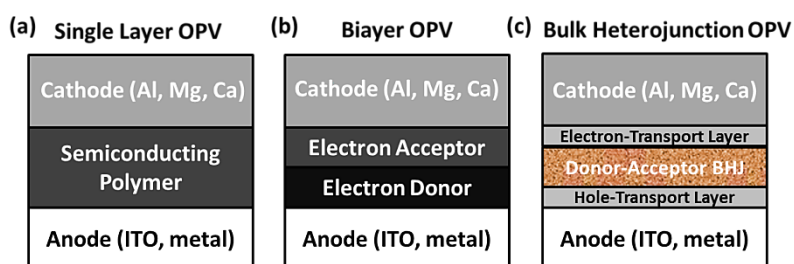


Figure 2.3 Typical OPV architecture of the different active layer structures (a) single layer (b) double layer (c) bulk heterojunction layer.

2.2.2. Bilayer heterojunction OPV

Tang et al. in 1986 demonstrated the first bilayer heterojunction (HJ) OPV [13], as shown in Figure 2.3 (b). This type of device uses two different materials as photoactive materials, known as donor and acceptor for charge separation. The material with higher electron affinity and ionization potential is the electron acceptor, and another material is the electron donor [14]. The electrostatic force generated by the energy offset between two layers improves exciton

dissociation compared to single layer SCs. Although bilayer devices have obtained better performance than single layer SCs, the achieved performances are only around 1 % [13]. A significant drawback of bilayer devices is the short exciton diffusion length of organic materials, typically 10 nm. The exciton diffusion length indicates the average distance that exciton can travel before it recombines. Thereby only excitons generated close to the interface could be separated into free charge carriers. The recombination occurs when the photogenerated excitons are unable to reach the donor-acceptor interface. Maximum absorption of the incident light is normally achieved when the thickness of the conductive layer is above 100 nm. If the donor or acceptor layer is too thick, the excitons dissociated at the donor and acceptor interface is far from the HJ, leading to the recombination of electrons and holes before they reach to the electrodes. On the contrary, if the donor and acceptor layers are limited in 10 nm, weak absorption will induce poor photocurrent of the SCs. Therefore, the low overall charge carrier generation of bilayer OPV is mainly attributed to the limited interface region between donor and acceptor [15].

2.2.3. Bulk-heterojunction (BHJ) OPV

In order to overcome the limitation of the bilayer HJ OPV due to the short exciton diffusion length and low exciton dissociation efficiency, a new device architecture known as BHJ was developed in 1995 by Friend [16] and Heeger [17]. The BHJ structure is depicted in Figure 2.3 (c). In this type of device, the stacked active layers of the bilayer structure are replaced by a blend of electron donor and acceptor materials. As a result of the intimate mixing of two materials, the interfaces in the active layer have increased enormously for exciton dissociation and charge transfer. The phase separation within the polymer blend is approximately 10–20 nm. Thereby the effective length scale of the active layer blend is similar to the exciton diffusion length, leading to the effective charge extraction and improving device performances [16-17]. Nearly unity internal quantum efficiency has been achieved for BHJ OPV since almost all photogenerated excitons are dissociated and then the carriers are effectively transported toward the respective electrodes [18]. Therefore, a thicker active layer can be applied in the BHJ devices compared to the bilayer ones. In a word, the structure of BHJ OPV fulfills the requirements of sufficient light absorption, suitable exciton diffusion length, and efficient charge transport [17]. Different from standard bilayer HJ SCs with only active layer and electrodes, the hole-transport layer (HTL) and the electron-transport layer (ETL) are inserted in BHJ OPV, as shown in Figure 2.3 (c). These thin layers are utilized to modify the work function of the electrodes, reducing leakage current losses from ohmic contacts as donor and acceptor materials direct in contact with electrodes and improving the charge transport efficiency of holes and electrons to the electrodes [19-20].

2.2.4. Comparison of conventional and inverted OPV

After OPVs have achieved the efficiency higher than 10%, the improvement of device stability has become the important task. In recent years, longer device lifetime and higher stability of OPV has been reported for the inverted configuration [21-22]. Figure 2.4 shows the architecture of conventional and inverted BHJ OPV. In the inverted structure, the high work

function metals or metal oxides (e.g. ITO) are utilized as the cathode for electron collection and the low work function metals (e.g. Ag) as the anode for hole collection. In this configuration, the device stability has been improved by replacing the oxygen sensitive Al metal with less air sensitive metals such as Ag or Au [23]. Not only in the conventional BHJ OPV, PEDOT:PSS is also commonly used as the HTL in inverted SCs [24-25], deposited on top of the active layer. In the inverted structure, the ITO corrosion from the ITO and acidic-PEDOT:PSS interface can be avoided [26]. The TMOs are widely studied as HTL and ETL for high performance and stability devices [23,25-26]. Recently, the inverted device architecture has been suggested as the best candidate to meet all these requirements including high efficiency, stability, low cost and high-speed production into one system [27].

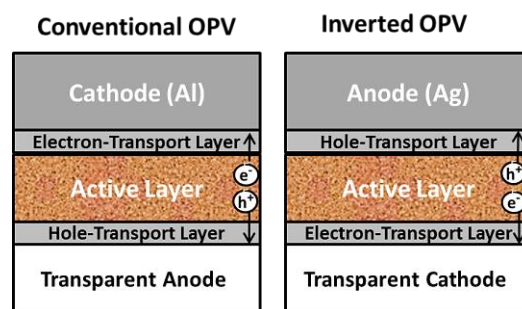


Figure 2.4 Schematic device architectures of a conventional and an inverted BHJ OPV.

2.3 Operating principles of OPV

There are several steps of charge generation, transfer, and transport process during the operation of OPV. Figure 2.5 presents a schematic energy diagram of fundamental physical processes from light absorption to charge extraction of a donor-acceptor (D-A) BHJ system in an OPV [9].

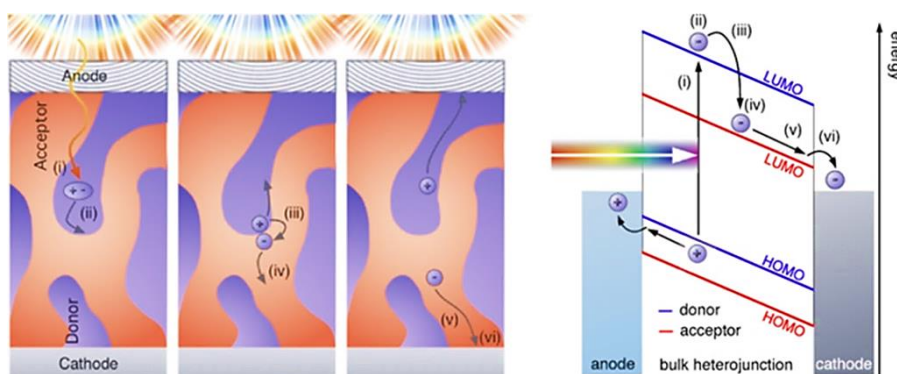


Figure 2.5 Illustration of fundamental physical processes of a BHJ OPV. (i) Photo-induced exciton, (ii) exciton diffusion, (iii) exciton dissociation, (iv) charge separation, (v) charge transport, (vi) charge extraction at electrodes [9].

(i) Photo-induced exciton

First, excitons are created in the donor material as incident photons are absorbed in the active layer. Exciton is a combined electron-hole pair which is bound by the Coulomb force. The main limit for the photon absorption is the band gap of the polymer active layer. The absorption of an incoming photon with energy larger than the bandgap is able to excite an electron from the donor's HOMO level to its LUMO level, leading to the formation of an exciton.

(ii) Exciton diffusion

In this step, the neutral excitons have to diffuse to the D-A interface within its lifetime in order to generate free charge carriers efficiently due to small diffusion length of excitons, in the order of 10 nm [15]. The recombination will occur when the excitons are unable to reach the D-A interface.

(iii) Exciton dissociation

As the energy offset of ionization potentials (HOMO level energy) and electron affinities (LUMO level energy) between materials at the D-A interface are higher than the exciton Coulomb binding energy, photogenerated excitons are dissociated at the D-A interface. In that process, the charge pair on the donor side will dissociate by transferring the electron to the LUMO level of the acceptor and retaining the positive charge on the LUMO of donor. Thereby charge transfer leads to the formation of a Coulomb bound polaron pair across the D-A interface [28].

(iv) Charge separation (Charge-pair dissociation)

The internal electric field in the device obtained from the work function difference of the electrodes triggers the separation of Coulomb bound polaron pairs at the D-A interface to free electron and hole charge carriers [9]. The separation of hole and electron is called charge separated state. Bound charge-transfer (CT) states at the D-A interface are only separated into free charge carriers, if the work function offset of the electrodes exceeds the binding energy of the bound charges. At the CT state, the polaron pairs may also recombine and decay to the ground state, leading to the current loss [28].

(v) Charge transport

Owing to the internal electric field, free charge carriers are transported by a mixture of band like transport and hopping transport through respective materials, electrons in the acceptor material and holes in the donor material, towards the electrodes, respectively. At this state, the transport efficiency of the charge carriers to the electrodes is affected by the mobilities of active layer materials and non-geminate recombination [9,28].

(vi) Charge extraction at electrodes

In this step, the electrons are collected by the cathode and the holes are collected at the anode.

2.4 Characterization of OPV

2.4.1. J-V curve parameters

The performance and electrical behavior of SCs are commonly characterized by their current-voltage (J-V) characteristics. Apply different voltages (e.g. between -1.0 and 1.0 V) to the devices under illumination, typically AM 1.5 G, with the intensity of 100 mW/cm² at room temperature of 25 °C and in the dark, and then record their electrical responses. By analyzing the J-V curves, the most important SC parameters such as open-circuit voltage (V_{OC}), short-circuit current (J_{SC}), fill factor (FF), and power conversion efficiency (PCE) can be obtained. Figure.2.6 depicts the typical J-V characteristics of a SC in the dark and illuminated conditions in (a) linear and (b) semi-logarithmic plot [9].

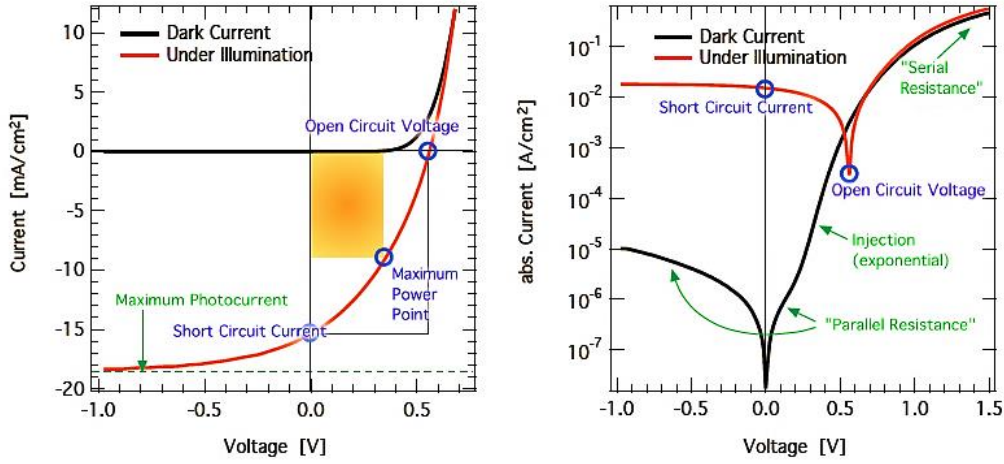


Figure.2.6 Typical J-V characteristics of a solar cell in the dark and illuminated conditions in (a) linear and (b) semi-logarithmic plot [9].

Short-circuit current density (J_{SC})

J_{SC} is the current density when $V = 0$ V, defined as the generated current of the SC under illumination in the absence of an externally applied potential. It is the maximum photocurrent density that can be extracted from the device at short-circuit conditions. In the ideal case, J_{SC} of the SC can be described by Equation 2.1 [29-30],

$$J_{SC} = eGL \quad (2.1)$$

where e is the elementary charge, G is absorbed photon flux density/ L and L the device thickness.

Moreover, J_{SC} is directly dependent on the external quantum efficiency (EQE), defined as the incident photon-to-current conversion efficiency at the specific wavelength. The value of J_{SC} is determined by Equation 2.2 [31],

$$J_{SC} = \int_{AM\ 1.5} e \cdot N_{Ph}(\lambda) \cdot \eta_{EQE}(\lambda) d(\lambda) \quad (2.2)$$

where e is the elementary charge, $N_{Ph}(\lambda)$ the photon flux density at the wavelength λ , and $\eta_{EQE}(\lambda)$ the external quantum efficiency at the wavelength λ , which is defined by Equation 2.3 [32],

$$\eta_{EQE} = \eta_A \cdot \eta_{ED} \cdot \eta_{CT} \cdot \eta_{CC} \quad (2.3)$$

where η_A is the light absorption efficiency, η_{ED} the exciton diffusion efficiency, η_{CT} the charge transfer efficiency, and η_{CC} the carrier collection efficiency.

To achieve a high J_{SC} of the SC, an active layer material with high charge carrier mobility, small

bandgap for a broad solar spectrum, maximize exciton dissociation, charge transfer and charge separation efficiency and minimize charge recombination are essential for consideration.

Open circuit voltage (V_{OC})

V_{OC} is the applied voltage when $J = 0 \text{ mA/cm}^2$, which is defined as the voltage where no current flows in the circuit. In a typical metal-insulator-metal (MIM) device, V_{OC} is determined by the offset between work functions of the two metal electrodes [33]. The maximal achievable V_{OC} of BHJ OPV is determined by the energy difference between the HOMO of the donor material and the LUMO of the acceptor material [34], as shown in Figure 2.7 [35].

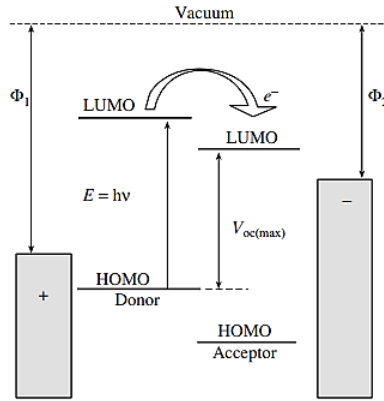


Figure 2.7 Schematic energy diagram of open circuit voltage in BHJ OPV [35].

The value of V_{OC} is also a function of other parameters, such as the temperature, referred from Equation 2.5 [36],

$$V_{OC} = \frac{kT}{e} \ln\left(\frac{J_{SC}}{J_0} + 1\right) \quad (2.5)$$

where k is the Boltzmann's constant, e the elementary charge, T the absolute temperature, and J_0 the dark saturation current.

It has been also reported that V_{OC} is significantly affected by the morphology of the active layer [37], effective area and recombination at the donor and acceptor interface [38-40], and by modifying work functions of the electrodes or interfacial effect by inserting a buffer layer or forming a barrier layer between active layer and electrodes [41].

Fill Factor (FF)

FF is a parameter to describe the degree of squareness, rectangularity or the quality of the J-V curve. The value of FF is defined as the ratio of the maximum power generated by the device (yellow rectangle in Figure 2.6) to the product of the V_{OC} and J_{SC} (white rectangle in Figure 2.6) and determined by Equation 2.6,

$$FF = \frac{J_{MPP} V_{MPP}}{J_{SC} V_{OC}} \quad (2.6)$$

where J_{MPP} and V_{MPP} are the current density and voltage at maximum power density (P_{max}).

The FF presents a competing result between charge carrier recombination and transport [42]. Most FF values of the OPV are between 0.2-0.7 owing to various losses during charge dissociation,

charge carrier transport, and the recombination processes in the device. Additionally, the FF is directly influenced by the serial resistance (R_s) and shunt resistance (R_{sh}) of the device, which will be discussed in the following section.

Power conversion efficiency (PCE)

PCE is defined as the percentage between the device maximum power output (P_{OUT}) and the incident irradiance light power per unit area (P_{IN}). The PCE of a SC is determined by Equation 2.7 [9],

$$PCE = \frac{P_{OUT}}{P_{IN}} = \frac{V_{oc}J_{sc}FF}{P_{IN}} \quad (2.7)$$

Quantum efficiency (QE)

QE is determined by the number of charge carriers collected at the electrodes to the number of incident photons on the area of the SC at the specific wavelength. In SC there are two types of QE: External Quantum Efficiency (EQE) and Internal Quantum Efficiency (IQE). EQE is determined by the ratio of the number of charge carriers collected by the SC to the incident number of photons at the given wavelength, as shown in Equation 2.8:

$$\eta_{EQE} = \frac{\text{Number of extracted electrons}}{\text{Number of incident photons}} \quad (2.8)$$

IQE is defined as the ratio between the number of charge carriers collected by the SC to the number of photons absorbed by the active layer at a given wavelength, can be calculated as Equation 2.9:

$$\eta_{IQE} = \frac{\text{Number of extracted electrons}}{\text{Number of absorbed photons}} \quad (2.9)$$

IQE only considers photons, which are absorbed in the active layer and does not take into account the photons that transmit through and reflect from the SC or absorbed by other layers. In view of the fact that the absorbed light is usually less than the incident light owing to some loss of light from reflections or transmissions, IQE is normally higher than EQE. The difference between IQE and EQE is essential for observing loss pathways between optical absorption properties of the device and photo-conversion properties of the active layer materials [43].

2.4.2. Equivalent circuit mode

When the SC is measured under dark conditions, the electrical characteristics behave like an ideal diode. The dark current density (J_D) is a function of the applied voltage of the device and described by the Shockley equation, as shown in Equation 2.10 [44]:

$$J_D(V) = J_0 \left(\exp\left(\frac{eV}{k_B T}\right) - 1 \right) \quad (2.10)$$

where J_0 is the dark saturation current, V the applied bias, e the elementary charge, k_B the Boltzmann constant, T the temperature in Kelvin, kT the thermal energy, and kT/e the thermal voltage V_T (25.69 mV at 25°C).

In the ideal case, when the SC is illuminated, the J-V characteristic is performed with an offset

from the original Equation 2.10 by the photogenerated current density, J_{ph} , given by Equation 2.11 [44]:

$$J(V) = J_D - J_{ph} = J_0 \left(\exp \left(\frac{eV}{k_B T} - 1 \right) \right) - J_{ph} \quad (2.11)$$

This diode behavior can be described by a simple equivalent circuit, illustrated in Figure 2.8 (a), in which a diode and a current source are connected in parallel [45].

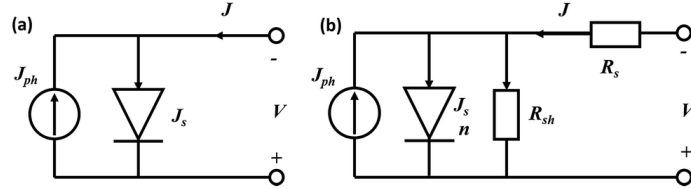


Figure 2.8 The equivalent circuit of (a) an ideal solar cell and (b) a solar cell with series resistance (R_s) and shunt resistance (R_{sh}) [45].

Different from the ideal diode behavior, additional resistances and recombination losses commonly exist in the real SC, therefore, the electrical model derived from the ideal Shockley equation has to be described including shunt resistance (R_{sh}) and a serial resistance (R_s). R_s , which is in series with the ideal diode, describes contact, interface and bulk resistances such as injection barriers and charge carrier mobility of SCs. R_{sh} , which is in parallel with the ideal diode, covers the influence of local shunts and shorts between the two electrodes such as low resistance leakage pathway through the semiconductor and direct contact between electrodes [9]. The influence of R_s and the R_{sh} on the J-V characteristic of the SC can be studied using the equivalent circuit presented in Figure 2.8 (b) [45] and described by the Equation 2.12 [46],

$$J(V) = J_0 \left\{ \exp \left[\frac{e(V-A)R_s}{nk_B T} - 1 \right] \right\} + \frac{V-A)R_s}{AR_{sh}} - J_{ph} \quad (2.12)$$

where A is the active area of the device and n the diode ideality factor.

Figure.2.6 (b) demonstrates where R_s and R_{sh} can influence the shape of a J-V curve. R_s accounts for the shape in the zero photocurrent regions and R_{sh} in the zero voltage regions. Thereby the R_s and R_{sh} can be approximated from the slopes of the J-V curve at V_{OC} and J_{SC} , respectively. R_s is estimated by the inverse of the slope near the V_{OC} and R_{sh} near the J_{SC} , as shown in Figure 2.9. The R_s and R_{sh} in the device can significantly influence the FF value of the SC. In the literature, it has been reported that the higher serial resistance, R_s is relevant to the increased resistivity of all materials of the OPV stack, the resistivity of the metallization, the contact resistance between the various materials, especially at the active layer and electrode interface or degradation of the bulk material. The decreased R_{sh} is corresponding to higher leakage current through the whole device or imperfect production process with the presence of shunts and shorts [47]. The reduction of the active layer and electrode interface and the degradation of blend materials can lead to the drop of V_{OC} and J_{SC} . The changes of electrode work function and the existence of shorts will induce lower V_{OC} . The increased resistivity can influence the charge transport and extraction efficiency, leading to lower J_{SC} of the device. In chapter 4.2 and 4.3 of the thesis, the R_s and R_{sh} are utilized to clarify device degradation mechanisms.

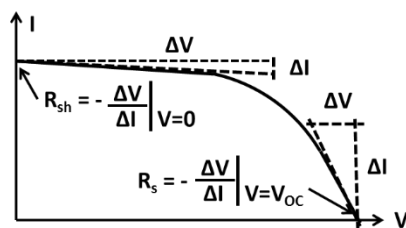


Figure 2.9 Obtaining values for R_s and R_{sh} from the photocurrent-voltage curve.

2.5 Materials for high efficient bulk-heterojunction (BHJ) OPV

2.5.1. Active layer

Donor materials

The first polymer donor was based on polyphenylenevinylene (PPV) derivatives such as dimethyloctyloxyd-1,4-phenylenevinylene (MDMO-PPV) [16-17] (see Figure 2.10 (a)). PPV derivatives were widely used as electron donor material until the development of poly-3-hexylthiophene (P3HT) (see Figure 2.10 (b)). The low charge transport mobility and the relatively large bandgap (around 2.3 eV) of PPV type polymers, which limit the absorption wavelengths below 550 nm, leading to limited device efficiency around 3% [48]. P3HT has an optical bandgap of 1.9 eV [49], which is able to absorb photons at higher wavelengths than the PPV derivatives, the excellent charge carrier mobility and the highly ordered packing structure, promoting the device efficiency to around 5% [50]. Nowadays, P3H has become a standard material and been widely used in OPV studies. To further enhance SC efficiency, polymers with smaller bandgaps (typically below 1.5 eV) have been developed to extended light absorption into the infrared region [51].

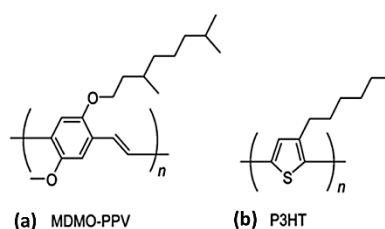


Figure 2.10 Molecular structures of (a) MDMO-PPV and (b) P3HT.

Acceptor materials - Fullerenes

A major breakthrough in OPV was made in 1992, Sariciftrci N.S., et al. proposed the first fullerene acceptor, buckminsterfullerene (C_{60}), which has a high electron affinity and high electron mobility, allowing for charge separation of the bound excitons in the active layer [52]. Figure 2.11 (a) shows the structure of C_{60} . When C_{60} is paired with a donor material, photo-induced charge transfer from the donor material onto C_{60} can reach a picosecond timescale. However, the poor solubility of C_{60} restricted its application as only bilayer structures

were achieved, limiting the device efficiency due to the short diffusion length of the generated excitons [54]. Consequently, the synthesis of soluble fullerene derivatives such as [6,6]-phenyl-C₆₁-butyric acid methyl ester (PC₆₀BM) (see Figure 2.11(b)), and with its application in BHJ structure led to a successful combination with various donor materials that have been widely utilized as electron acceptor materials nowadays [16-17].

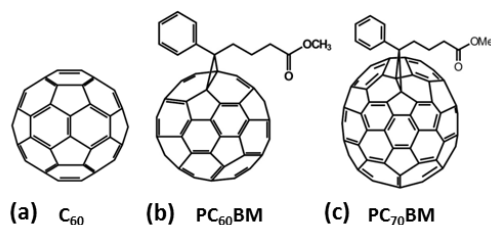


Figure 2.11 Structure of (a) C₆₀ and fullerene derivatives of (b) PC₆₀BM and (c) PC₇₀BM [53].

The LUMO energy level of PC₆₀BM, approximately -4.3 eV, makes it an excellent energy match to meet the requirement of LUMO offset greater than 0.3 eV with many polymer donor materials for the efficient exciton dissociation [18]. The photocurrent of the device was further improved by replacing PC₆₀BM with [6,6]-phenyl C₇₀-butyric acid methyl ester (PC₇₀BM) (see Figure 2.11 (c)) as acceptor due to the enhanced absorption in the visible range, increased absorption coefficient and more favorable interpenetration properties [55-56]. However, the fixed LUMO values of these two fullerene derivatives acceptor materials (PC₆₀BM and PC₇₀BM) limit the V_{OC} and the efficiency of their devices. Therefore, the devices with non-fullerene acceptors so-called all-polymer SCs, where both donor and acceptor materials are CPs, have been developed and reached power conversion efficiencies around 11 % [57-58]. All in all, the favorable LUMO level, high electron mobility, and proper miscibility when being blended with donor materials are crucial parameters for being considered as an ideal candidate of acceptor material in BHJ OPV [59].

2.5.2. Electrode Materials

Anode

The most commonly used anode electrode material is ITO, which is typically a mixture of In₂O₃ (90%) and SnO₂ (10%) [60]. ITO has a large bandgap of 3.8 eV and high transparency (80%) in the visible range, allowing the limitation of the absorption wavelengths to shorter than 350 nm [61]. The material has high electric conductivity with low sheet resistances between 5-15 Ωsq⁻¹ in the thickness region around 60-100 nm [62]. In general, the smoothness of the anode is critical for fabrication of high efficient OPV since the rough ITO surface may come into direct contact with the cathode or induce electrical inhomogeneity of the device. A suitable work function matched to the HOMO of the donor is essential for an ideal anode material. However, the work function of ITO is usually reported at around 4.7 eV [63], which is not well aligned with the HOMO level of most commonly used donor polymers, for example, around 5.2 eV for P3HT [64]. Therefore, the buffer layer like HTL is introduced to improve the roughness of ITO electrode and compensate for

the energetic mismatch between the anode and the active layer interface.

Cathode

Efficient photogenerated electron collection of SC requires a cathode with a work function well matched to the LUMO level of the acceptor material. For instance, low work function materials, such as Al (4.2 eV), Ca (2.9 eV), and Ag (4.3 eV) are commonly utilized as the cathode materials for the electron collection in OPV [65].

2.5.3. Interfacial buffer Layers

The interfacial layer such as HTL and ETL are widely used to improve the surface contact and energy level alignment between the active layer materials and the electrodes in the OPV [20]. Figure 2.12 shows the schematic energy diagram of different materials in the BHJ OPV.

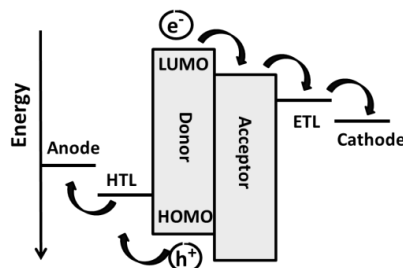


Figure 2.12 Schematic energy diagram of different materials in the BHJ OPV.

HTL promotes hole extraction at the anode and ETL improves electron extraction at the cathode, preventing unfavorable interfacial charge recombination at the electrodes. Polymer (e.g. PEDOT:PSS) and metal oxide (e.g. NiO, MoO₃, V₂O₅, WO₃, etc.) based HTLs have been widely used in solution processed BHJ OPV. Low work function metal (e.g. Ca, Ba) and inorganic salts (e.g. LiF) have been commonly applied as ETL to improve device performance [20,41].

Hole-transport layers (HTLs)

PEDOT:PSS is a CP from a mixture of two polymers, polyethylene dioxythiophene (PEDOT) and poly(styrenesulfonate) (PSS). It is one of the most commonly used HTL materials in OPVs, connecting between the ITO anode and the active layer due to its solution processability, high electrical conductivity, high charge carrier mobility, good optical transparency in the visible spectral range, mechanical flexibility, and environmental stability [66-68]. Pristine PEDOT is insoluble in most common solvents and unstable in its neutral state [69]. The poor solubility of aqueous dispersion PEDOT was resolved by using a water-soluble polyelectrolyte, PSS, as a charge-balancing dopant during polymerization, giving a PEDOT:PSS aqueous composite consisting of a colloidal suspension [70]. As PEDOT:PSS is applied as HTL in the SC, the work function of the anode electrode is increased due to its high work function, around 5.1 eV [68]. This improves the energy level mismatch between the anode and the donor material in the active layer, prompting a better hole extraction at the interface and preventing electron leakage. Furthermore, PEDOT:PSS HTL also improves the surface roughness of the ITO substrate, resulting

in a lower electric resistance of the electrode, increasing the adhesion and reducing the residual stress of the ITO film [71]. However, due to the acidic (usually a pH value between 1.5-2.5) and hygroscopic nature of PEDOT:PSS, it is known to generate instability and shorter lifetimes of devices especially after exposure to humidity [72]. A post-deposition thermal treatment plays an important role in removing the moisture in the film during the fabrication process. However, the long-term stability of these SCs is still a big challenge.

It has been demonstrated that high work-function transition metal oxides (TMOs) might be suitable alternatives for PEDOT:PSS. TMOs were first utilized in organic electronics by Tokito et al. in the late 1990's, where thin layers of MoO_3 , V_2O_5 , and RuO_2 were used as interlayers between the anode and organic material in organic light emitting diodes (OLEDs), leading to a significant increase in hole injection in the devices [73]. Nowadays, TMOs are widely applied as either HTLs or ETLs in the OPV due to its wide range of work functions, covering values from the extreme low end of 3.5 eV for ZrO_2 to the extreme high end of 7.0 eV for V_2O_5 [74]. High work function metal oxides are often utilized as HTL for the anodes, such as MoO_3 [75], WO_3 [76], NiO [77], and V_2O_5 [78]. The low work function TMOs are used as ETL for the cathode, including TiO_2 [79], ZnO [80], and ZrO_2 [81]. In most cases, TMO layers are prepared via thermal evaporation, molecular beam epitaxy, electron beam evaporation, pulsed laser deposition or sputtering [82-84]. These approaches possess several advantages, including well-controlled film thickness, high purity, and desired physical properties for metal oxide film preparation [85]. However, those techniques require considerably high vacuum and temperature conditions. For the aim of low cost, large-scale, high-throughput production and flexible ability of OPV, the all-solution processed approach is favorable for device fabrication. Therefore, solution-processed TMOs have attracted significant attention in recent years. The solution-processed methods have been widely applied on the preparation of V_2O_5 [86] and MoO_3 nanoparticle films [87-88]. A slight drawback of V_2O_5 is the relatively low band gap of around 2.3 eV. A thicker layer (>10 nm) of V_2O_5 may cause substantial absorption losses in the spectral region [88]. MoO_3 has a larger band gap around 3 eV [89], which leads to a good transparency of the film. Combining with its high work function, around 5.5 eV [89], making MoO_3 an ideal HTL material for high efficient OPV.

Electron transport layers

Except for low work function TMOs, LiF, Ca, and Ba are also widely used as ETL materials in OPVs. For instance, an extremely thin layer (0.5-2 nm) of lithium fluoride (LiF), was applied between the active layer and cathode as ETL layer to improve device performance [41,90-91], especially on the V_{OC} , owing to the decreased effective work function of the Al electrode. In addition, a LiF film can protect the organic layer from the hot Al atoms during thermal deposition, inhibiting oxygen diffusion into the organic layers and improving the stability of devices [41]. Ca and Ba (around 20 nm) have also been reported to significantly increase device performance as ETL material [91].

2.6 Degradation mechanisms of OPV

Understanding the degradation mechanisms of SCs and how they affect operating

lifetimes are crucial steps to develop high-efficiency devices. Literature has identified several pathways that deteriorate device performance, including chemical, physical, and mechanical issues that influence single active layer, interfaces, contacts, and so on [92-94]. Figure 2.13 shows common degradation mechanisms occurring in OPV [92]. The following sections will present the major pathways that generate device instability and short lifetime.

2.6.1. Moisture and oxygen diffusion into OPV

Moisture and oxygen are considered to be the major degradation sources of OPV [95-97]. The presence of oxygen or water molecules in the organic SC is either from the direct diffusion through the sides of the device, wet PEDOT:PSS film, or absorption by the Al cathode with diffusion through the microscopic pinholes or grain boundaries at the surface towards all interfacial layers of the device (see Figure 2.13). Organic active layer materials and metal electrodes such as Al are directly sensitive to water and oxygen, thus the penetration of these molecules into the device can result in the photodegradation of polymers and formation of oxide composites near the metal electrodes. With PEDOT:PSS, humidity triggers corrosion of other layers, which induces an ion diffusion effect and degradation at the ITO electrode, leading to an indirect origin that causes device failure [92,96].

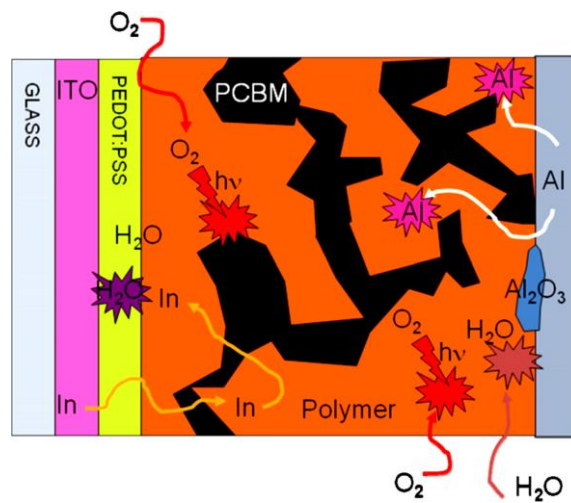


Figure 2.13 Schematic illustration of degradation paths occurring in a BHJ OPV [92].

2.6.2. Light-induced active layer degradation

Illumination induces photochemical reactions on many organic components in the active layer of OPV, named photolysis. This chemical reaction is accelerated in the presence of oxygen and/or water, known as photooxidation [98-99]. It has been reported that illumination stimulates the deterioration of organic SCs due to the photooxidation effect of CPs [100]. For instance, P3HT as well as P3HT:PCBM blend as active layer materials are proposed intrinsically and photochemically stable under an inert atmosphere in the absence of oxygen [100-101]. However, the photooxidation of a CP induces oxidation of the polymer side chains and backbone, leading to

the disappearance of alkyl groups and thiophene rings [102-103]. This process causes the break of the conjugation along the backbone and reduces the conjugation length of the polymer, inducing light absorption loss, which is known as the photo-bleaching process [101,104]. Literature has also reported that as the polymer exposes to oxygen molecules upon illumination, a charge transfer complex, P3HT:O₂-complex, is formed in the active layers [92,101]. This polymer-oxygen complex reduces the concentration of neutral P3HT in the active layer, leading to a dramatically decreased light absorption intensity with less photogenerated charge carriers that induce lower photocurrent of the device [97,104]. Moreover, it has been suggested that the photooxidation of organic compounds creates oxidation products in the active layer that act as charge traps, inducing recombination in the active layer. This results in a reduction of V_{OC}, FF, and, J_{SC} of device performances [98]. Literature has also proposed that the formation of H₂O₂ at the benzylic position from a side chain oxidation is responsible for the polymer degradation [105-106]. Furthermore, it has been demonstrated that the conductivity of the P3HT:PCBM blend under light exposure in the air decreases faster than the pure P3HT polymer [100,107], indicating that the PCBM acceptor upon oxygen absorption and light illumination is also an origin for the SC degradation. M.O. Resse et al. proposed that when PCBM fullerene cages reacted with oxygen in the air, the lower LUMO level oxidized PCBM (O_n(PCBM)) created deeper trap states within PCBM domains after photooxidation. Figure 2.14 shows how the presence of trap states limits mobility in PCBM domains. These trap states result in an increased energetic disorder in the system, leading to a reduced electron mobility of PCBM, and consequently influence the photocurrent of the SC [100].

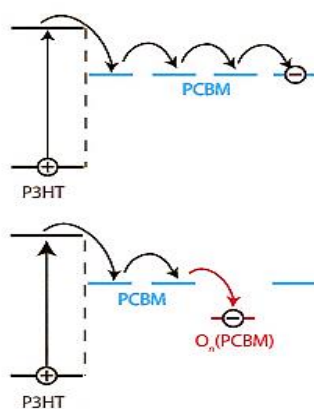


Figure 2.14 Schematic energy diagram of how the presence of trap states limits mobility in PCBM domains [100].

2.6.3. HTL PEDOT:PSS and electrodes related device instability

Most of the degradation effects mentioned in this section are independent of illumination.

HTL PEDOT:PSS

It has been discussed in the previous section, that PEDOT:PSS is widely used as a HTL to enhance OPV performance. However, PEDOT:PSS is also one of the major sources, which causes device instability due to its hygroscopic and acidic nature. As PEDOT:PSS absorbs atmospheric moisture, an injection barrier in the device is created, leading to a decreased photocurrent of the

SC [108]. The acidic PEDOT:PSS after absorption of moisture may react with the underlying ITO surface, resulting in dewetting and delamination of the interface that will cause disastrous device failure. It has also been reported that the chemical bonds of the PEDOT:PSS are decomposed upon UV-light illumination in the presence of oxygen, inducing a decreased HTL conductivity [109], but this effect is often neglected.

Anode

The most used anode material, ITO, is also reported as an origin that induces instability of SC due to corrosion of the ITO film. The ITO corrosion occurs when devices are exposed to humidity [110-111]. For instance, when the hygroscopic and acidic PEDOT:PSS absorbs the moisture, it triggers etching of ITO at the interface between the two materials, with the diffusion of In ions and Sn ions through the PEDOT:PSS film to the active layer or across the device [110-111]. In and Sn ions have been found at saturation concentrations of 2.7% throughout the entire PEDOT:PSS layer, from where they diffuse further into the active layer creating quenching centers for excitons.

Cathode

Metal electrodes such as Ca or Al are commonly used in the OPV for their low work function and high conductivity. However, those metal electrodes, especially Al, have high reactivity with oxygen. As a device is exposed to ambient atmosphere, oxygen or water molecules diffuse through metal pinholes or grain boundaries into the active layer, leading to the formation of a metal oxide insulating barrier layer such as Al_2O_3 at the cathode and active layer interface, reducing charge extraction efficiency and therefore deteriorating device performance [94,112,113]. Furthermore, it has been reported that active layer materials have also chemical reactions with cathode materials. Take Al for example, as Al penetrates into the active layer, the interaction between the polymer and Al forms aluminum–carbon bonds (Al–C bonds) at the Al and organic interface, inevitably breaking the π -conjugated system of the organic layer [114-115]. It has also been shown that Al reacts with fullerene molecules, such as C_{60} , forming Al- C_{60} bonds, which lead to reduced charge transport and device performance [94].

2.6.4. Thermal instability

Thermal treatments of the active layers are commonly applied to improve the phase segregation between the donor and acceptor materials to achieve an optimal morphology for better exciton dissociation and charge transport efficiency of the BHJ OPV [116-118]. In fact, the thermal treatment can either improve or deteriorate the device performance according to different experimental conditions. For example, a thermal annealing above glass transition temperature (T_g) of P3HT, PCBM or polymer films allows the free-flowing chains in the polymer to untangle into lower energy conformation and increase the degree of inter-chain interactions [119-120]. This improves the crystallinity and chain packing of the materials, leading to a better charge conduction of the active layer and promoting a higher photocurrent in the device [117,120]. However, extremely high temperatures induce conformational changes within P3HT, which decreases its conjugation length, and thereby increases the bandgap of the material. This

may drastically reduce the conductivity of the active layer and decrease device performance [119]. Moreover, many studies have been reported that thermal annealing induces the formation of crystalline PCBM-clusters that reduces the interfacial area between donor and acceptor, resulting in lower photocurrent and serious deterioration of the device [121]. Furthermore, the thermal treatment can trigger the diffusion of different materials within the SC which induce chemical reactions within different layers and deteriorate device performance. For instance, hot Al atoms generated during the thermal evaporation process diffuse into the active layer, leading to a chemical reaction at the metal and organic interface and inducing electrical failures of the device such as shunts [122].

2.6.5. Other device deterioration related factors

Encapsulation

Encapsulation of the SC greatly improves device lifetime by protecting the cell from the diffusion of oxygen, moisture, and UV radiation. Ideal encapsulation can seal the device completely. However, in most SCs oxygen and water penetrate or diffuse through the encapsulation material or from the sides of the device [92,98], especially roll-to-roll processes for flexible encapsulation. Therefore, the lifetime of the flexible OPV was still much shorter in comparison with the glass substrate devices [123]. The choices of the encapsulating materials, substrates and techniques play important roles on extending lifetimes of SCs. On the contrary, the wrong selection of the materials and techniques may even reduce the lifetime, trigger the instability or induce deterioration of the devices. (e.g. choice of encapsulating resin or UV-curing.)

Delamination

Delamination, electrode failure, packaging failure and low adhesion between layers can highly affect the stability of OPVs [124-125]. Among that, delamination can be triggered in various ways and present at any interfaces in the SC. For example, the thermo-mechanical stresses such as repeated bending of flexible devices [124] or the presence of moisture in the device induce delamination, leading to significantly reduced charge transport and extraction efficiency of the SC [126].

2.7 Imaging techniques for studying inhomogeneity and stability of OPV

It has been shown that large-area semiconductor thin-film inorganic devices present significant inhomogeneous V_{OC} and J_{SC} in the lateral directions due to macroscopic imperfections such as defects in the glass substrate, structural inhomogeneity or contaminants in the film. The observed inhomogeneities cover different length scales from millimeters to centimeters, especially on the large (1 cm) scale. These nonuniformities considerably affect the device physics and stability of the inorganic thin-film diodes [127]. The solution-processed OPV provides great large-scale processability. However, large-area, thin-film semiconductor devices often exhibit strong fluctuations in electronic properties on a mesoscale level (nanometer to micrometer dimensions) that originates from subtle local microscopic fluctuations in material structures such

as domain size, chemical composition, contact properties, film thickness, and the presence of impurities or grain boundaries [127]. For the OPV, the devices' fluctuation could be caused by the photoactive layer alone, the use of charge selective interlayer, their material and preparation details, or the choice of deposition of the electrode. These lead to significant batch-to-batch and device-to-device variation in the SC. Since J-V characteristics alone cannot explain the exact origins of failure of these devices, lateral and local imaging methods are applied in order to obtain a more profound information of the local nonuniformities of devices [128]. Moreover, spatial scanning techniques have also been successfully utilized to monitor degradation of optoelectronic devices [128-129]. Spatially resolved characterization delivers information about the topography, composition, electrical and optical properties, using a combination of imaging and spectroscopic methods, such as conductive atomic force microscopy (AFM) [130], near-field scanning optical microscopy [131], lock-in thermography [132], photo- and electroluminescence (PL, EL) imaging [133], light-beam induced current (LBIC) [134], and so on. In the literature, it has been found that the spatial photocurrent mapping of OPV appears as identical feature in AFM topography image of active layer at different length scale imaging [130]. Literature has shown that cross-sectional transmission electron microscopy and dispersive X-ray spectroscopy are able to identify the cathode material oxidation [112]. The PL imaging can be used to investigate the loss of π -conjugated system in the active layer due to the photooxidation. By combining the EL and PL imaging techniques, the interface and active layer degradation of the device can be distinguished [133]. The dark and illuminated lock-in thermography images have been utilized to observe local shunts of SC upon degradation [132]. LBIC and EL imaging techniques can be applied to observe the spatial photocurrent of the device, in particular, LBIC, has been widely used to evaluate spatially resolved electrical characterization of the SC and localize fabrication defects and degradation of the devices [129,134]. This technique allows characterizing individually each cell to understand the predominating factors of device failure by an inhomogeneous effect. Furthermore, local J-V characteristics at different sites of the device can be used to identify the origin of the defects inducing the local photocurrent inhomogeneity. In short, the understanding of the origins of inhomogeneities of SCs will help to improve the device performance and stability. The different length scale characterization from nano- to micro- or even centimeters can assist to explain how a microscopic inhomogeneity of individual films influence macroscopically large areas of devices [127].

2.8 References

- [1] Skotheim, T. A.; Reynolds, J. R., Eds. *Handbook of conducting polymers*; CRC: Boca Raton, Fla., London, 2007.
- [2] W. R. Salzman, Department of Chemistry University of Arizona, Bonding in Alkenes - sp^2 Hybrid Orbitals. (accessed 19/02/2018). URI: <http://pages.uoregon.edu/ch111/L30.htm>.
- [3] Salaneck, W. R.; Friend, R. H.; Brédas, J. L. Electronic Structure of Conjugated Polymers: Consequences of Electron–Lattice Coupling. *Physics Reports* **1999**, *319*, 231–251.
- [4] Cardona, M.; Fulde, P.; Klitzing, K. von; Queisser, H.-J.; Lotsch, H. K. V.; Lotsch, H. K. V.; Kiess, H. G. *Conjugated Conducting Polymers*; Kiess, H. G., Ed.; Springer Berlin Heidelberg: Berlin, Heidelberg, 1992.

- [5] Woo, C. H.; Beaujuge, P. M.; Holcombe, T. W.; Lee, O. P.; Fréchet, J. M. J. Incorporation of Furan into Low Band-Gap Polymers for Efficient Solar Cells. *Journal of the American Chemical Society* **2010**, *132*, 15547–15549.
- [6] Kim, B.; Yeom, H. R.; Yun, M. H.; Kim, J. Y.; Yang, C. A Selenophene Analogue of PCDTBT: Selective Fine-Tuning of LUMO to Lower of the Bandgap for Efficient Polymer Solar Cells. *Macromolecules* **2012**, *45*, 8658–8664.
- [7] Weinberger, B. R.; Akhtar, M.; Gau, S. C. Polyacetylene Photovoltaic Devices. *Synthetic Metals* **1982**, *4*, 187–197.
- [8] Nelson, J. Organic Photovoltaic Films. *Current Opinion in Solid State and Materials Science* **2002**, *6*, 87–95.
- [9] Deibel, C.; Dyakonov, V. Polymer–Fullerene Bulk Heterojunction Solar Cells. *Rep. Prog. Phys.* **2010**, *73*, 96401.
- [10] Nelson, J. Polymer: Fullerene Bulk Heterojunction Solar Cells. *Materials Today* **2011**, *14*, 462–470.
- [11] Spanggaard, H.; Krebs, F. C. A Brief History of the Development of Organic and Polymeric Photovoltaics. *Solar Energy Materials and Solar Cells* **2004**, *83*, 125–146.
- [12] Chamberlain, G. A. Organic Solar Cells: A review. *Solar Cells* **1983**, *8*, 47–83.
- [13] Tang, C. W. Two-Layer Organic Photovoltaic Cell. *Appl. Phys. Lett.* **1986**, *48*, 183–185.
- [14] Wang, X.; Wang, Z. M., Eds. *High-Efficiency Solar Cells*; Springer International Publishing: Cham, 2014.
- [15] Krebs, F. C., Ed. *Polymeric Solar Cells: Materials, Design, Manufacture*; DEStech Publications: Lancaster, Pa., 2010.
- [16] Halls, J. J. M.; Walsh, C. A.; Greenham, N. C.; Marseglia, E. A.; Friend, R. H.; Moratti, S. C.; Holmes, A. B. Efficient Photodiodes from Interpenetrating Polymer Networks. *Nature* **1995**, *376*, 498–500.
- [17] Yu, G.; Gao, J.; Hummelen, J. C.; Wudl, F.; Heeger, A. J. Polymer Photovoltaic Cells: Enhanced Efficiencies via a Network of Internal Donor-Acceptor Heterojunctions. *Science* **1995**, *270*, 1789–1791.
- [18] Park, S. H.; Roy, A.; Beaupré, S.; Cho, S.; Coates, N.; Moon, J. S.; Moses, D.; Leclerc, M.; Lee, K.; Heeger, A. J. Bulk Heterojunction Solar Cells with Internal Quantum Efficiency Approaching 100%. *Nature Photon* **2009**, *3*, 297–302.
- [19] Ma, H.; Yip, H.-L.; Huang, F.; Jen, A. K.-Y. Interface Engineering for Organic Electronics. *Adv. Funct. Mater.* **2010**, *20*, 1371–1388.
- [20] Steim, R.; Kogler, F. R.; Brabec, C. J. Interface Materials for Organic Solar Cells. *J. Mater. Chem.* **2010**, *20*, 2499.
- [21] Han, D.; Yoo, S. The Stability of Normal vs. Inverted Organic Solar Cells under Highly Damp Conditions: Comparison with the Same Interfacial Layers. *Solar Energy Materials and Solar Cells* **2014**, *128*, 41–47.
- [22] Chen, L.-M.; Hong, Z.; Li, G.; Yang, Y. Recent Progress in Polymer Solar Cells: Manipulation of Polymer:Fullerene Morphology and the Formation of Efficient Inverted Polymer Solar Cells. *Adv. Mater.* **2009**, *21*, 1434–1449.
- [23] Kyaw, A. K. K.; Sun, X. W.; Jiang, C. Y.; Lo, G. Q.; Zhao, D. W.; Kwong, D. L. An Inverted Organic Solar Cell Employing a Sol-Gel Derived ZnO Electron Selective Layer and Thermal Evaporated

- MoO₃ Hole Selective Layer. *Appl. Phys. Lett.* **2008**, *93*, 221107.
- [24] Steim, R.; Choulis, S. A.; Schilinsky, P.; Brabec, C. J. Interface Modification for Highly Efficient Organic Photovoltaics. *Appl. Phys. Lett.* **2008**, *92*, 93303.
- [25] Hau, S. K.; Yip, H.-L.; Baek, N. S.; Zou, J.; O'Malley, K.; Jen, A. K.-Y. Air-Stable Inverted Flexible Polymer Solar Cells Using Zinc Oxide Nanoparticles as an Electron Selective Layer. *Appl. Phys. Lett.* **2008**, *92*, 253301.
- [26] Zhao, D. W.; Tan, S. T.; Ke, L.; Liu, P.; Kyaw, A.; Sun, X. W.; Lo, G. Q.; Kwong, D. L. Optimization of an Inverted Organic Solar Cell. *Solar Energy Materials and Solar Cells* **2010**, *94*, 985–991.
- [27] Zhang, F.; Xu, X.; Tang, W.; Zhang, J.; Zhuo, Z.; Wang, J.; Wang, J.; Xu, Z.; Wang, Y. Recent Development of the Inverted Configuration Organic Solar Cells. *Solar Energy Materials and Solar Cells* **2011**, *95*, 1785–1799.
- [28] Parisi, J.; Dyakonov, V.; Pientka, M.; Riedel, I.; Deibel, C.; Brabec, C. J.; Sariciftci, N. S.; Hummelen, J. C. Charge Transfer and Transport in Polymer-Fullerene Solar Cells. *Zeitschrift für Naturforschung A* **2002**, *57*, 995–1000.
- [29] Schilinsky, P.; Waldauf, C.; Hauch, J.; Brabec, C. J. Simulation of Light Intensity Dependent Current Characteristics of Polymer Solar Cells. *Journal of Applied Physics* **2004**, *95*, 2816–2819.
- [30] Kumar, P.; Jain, S. C.; Kumar, V.; Chand, S.; Tandon, R. P. A Model for the Current–Voltage Characteristics of Organic Bulk Heterojunction Solar Cells. *J. Phys. D: Appl. Phys.* **2009**, *42*, 55102.
- [31] Kippelen, B.; Brédas, J.-L. Organic photovoltaics. *Energy Environ. Sci.* **2009**, *2*, 251.
- [32] Forrest, S. R. The Limits to Organic Photovoltaic Cell Efficiency. *MRS Bull.* **2005**, *30*, 28–32.
- [33] Parker, I. D. Carrier Tunneling and Device Characteristics in Polymer Light-Emitting Diodes. *Journal of Applied Physics* **1994**, *75*, 1656–1666.
- [34] Brabec, C. J.; Cravino, A.; Meissner, D.; Sariciftci, N. S.; Fromherz, T.; Rispen, M. T.; Sanchez, L.; Hummelen, J. C. Origin of the Open Circuit Voltage of Plastic Solar Cells. *Adv. Funct. Mater.* **2001**, *11*, 374–380.
- [35] Troshin, P. A.; Lyubovskaya, R. N.; Razumov, V. F. Organic Solar Cells: Structure, Materials, Critical Characteristics, and Outlook. *Nanotechnol Russia* **2008**, *3*, 242–271.
- [36] Vandewal, K.; Tvingstedt, K.; Gadisa, A.; Inganäs, O.; Manca, J. V. On the Origin of the Open-Circuit Voltage of Polymer-Fullerene Solar Cells. *Nature materials* **2009**, *8*, 904–909.
- [37] Liu, Z.; Liu, Q.; Huang, Y.; Ma, Y.; Yin, S.; Zhang, X.; Sun, W.; Chen, Y. Organic Photovoltaic Devices Based on a Novel Acceptor Material: Graphene. *Adv. Mater.* **2008**, *20*, 3924–3930.
- [38] Rand, B. P.; Burk, D. P.; Forrest, S. R. Offset Energies at Organic Semiconductor Heterojunctions and their Influence on the Open-Circuit Voltage of Thin-Film Solar Cells. *Phys. Rev. B* **2007**, *75*, 1793.
- [39] Potscavage, W. J.; Yoo, S.; Kippelen, B. Origin of the Open-Circuit Voltage in Multilayer Heterojunction Organic Solar Cells. *Appl. Phys. Lett.* **2008**, *93*, 193308.
- [40] Vandewal, K.; Widmer, J.; Heumueller, T.; Brabec, C. J.; McGehee, M. D.; Leo, K.; Riede, M.; Salleo, A. Increased Open-Circuit Voltage of Organic Solar Cells by Reduced Donor-Acceptor Interface Area. *Advanced materials (Deerfield Beach, Fla.)* **2014**, *26*, 3839–3843.
- [41] Brabec, C. J.; Shaheen, S. E.; Winder, C.; Sariciftci, N. S.; Denk, P. Effect of LiF/Metal Electrodes on the Performance of Plastic Solar Cells. *Appl. Phys. Lett.* **2002**, *80*, 1288–1290.
- [42] Günes, S.; Neugebauer, H.; Sariciftci, N. S. Conjugated Polymer-Based Organic Solar Cells. *Chemical reviews* **2007**, *107*, 1324–1338.

- [43] Suren Gevorgyan, Incident Photon-to-Current Efficiency (IPCE). (accessed 20/02/2018). URI: <http://plasticphotovoltaics.org/lc/characterization/lc-advanced-c/lc-ipce.html>
- [44] Shockley, W. The Theory of p-n Junctions in Semiconductors and p-n Junction Transistors. *Bell System Technical Journal* **1949**, *28*, 435–489.
- [45] Jao, M.-H.; Liao, H.-C.; Su, W.-F. Achieving a High Fill Factor for Organic Solar Cells. *J. Mater. Chem. A* **2016**, *4*, 5784–5801.
- [46] Kumar, P.; Jain, S. C.; Kumar, V.; Chand, S.; Tandon, R. P. A Model for the J-V Characteristics of P3HT: PCBM Solar Cells. *Journal of Applied Physics* **2009**, *105*, 104507.
- [47] Madogni, V. I.; Kounouhéwa, B.; Akpo, A.; Agbomahéna, M.; Hounkpatin, S. A.; Awanou, C. N. Comparison of Degradation Mechanisms in Organic Photovoltaic Devices upon Exposure to a Temperate and a Subequatorial Climate. *Chemical Physics Letters* **2015**, *640*, 201–214.
- [48] Shaheen, S. E.; Brabec, C. J.; Sariciftci, N. S.; Padinger, F.; Fromherz, T.; Hummelen, J. C. 2.5% Efficient Organic Plastic Solar Cells. *Appl. Phys. Lett.* **2001**, *78*, 841–843.
- [49] Kim, Y.; Cook, S.; Tuladhar, S. M.; Choulis, S. A.; Nelson, J.; Durrant, J. R.; Bradley, D. D. C.; Giles, M.; McCulloch, I.; Ha, C.-S.; Ree, M. A Strong Regioregularity Effect in Self-Organizing Conjugated Polymer Films and High-Efficiency Polythiophene: Fullerene Solar Cells. *Nature materials* **2006**, *5*, 197–203.
- [50] Dang, M. T.; Hirsch, L.; Wantz, G. P3HT: PCBM, Best Seller in Polymer Photovoltaic Research. *Adv. Mater.* **2011**, *23*, 3597–3602.
- [51] BUNDGAARD, E.; KREBS, F. Low band Gap Polymers for Organic Photovoltaics. *Solar Energy Materials and Solar Cells* **2007**, *91*, 954–985.
- [52] Sariciftci, N. S.; Smilowitz, L.; Heeger, A. J.; Wudl, F. Photoinduced Electron Transfer from a Conducting Polymer to Buckminsterfullerene. *Science* **1992**, *258*, 1474–1476.
- [53] Solenne BV, Product of Fullerene Derivatives. (accessed 20/02/2018). URI: <http://solennebv.com/>.
- [54] Sariciftci, N. S.; Braun, D.; Zhang, C.; Srdanov, V. I.; Heeger, A. J.; Stucky, G.; Wudl, F. Semiconducting Polymer-Buckminsterfullerene Heterojunctions: Diodes, Photodiodes, and Photovoltaic Cells. *Appl. Phys. Lett.* **1993**, *62*, 585–587.
- [55] He, Y.; Li, Y. Fullerene Derivative Acceptors for High Performance Polymer Solar Cells. *Physical chemistry chemical physics : PCCP* **2011**, *13*, 1970–1983.
- [56] Arbogast, J. W.; Foote, C. S. Photophysical Properties of C₇₀. *J. Am. Chem. Soc.* **1991**, *113*, 8886–8889.
- [57] Zhao, W.; Qian, D.; Zhang, S.; Li, S.; Inganäs, O.; Gao, F.; Hou, J. Fullerene-Free Polymer Solar Cells with over 11% Efficiency and Excellent Thermal Stability. *Advanced materials* **2016**, *28*, 4734–4739.
- [58] Bin, H.; Gao, L.; Zhang, Z.-G.; Yang, Y.; Zhang, Y.; Zhang, C.; Chen, S.; Xue, L.; Yang, C.; Xiao, M.; Li, Y. 11.4% Efficiency non-Fullerene Polymer Solar Cells with Trialkylsilyl Substituted 2D-Conjugated Polymer as Donor. *Nature communications* **2016**, *7*, 13651.
- [59] Li, M.; Liu, Y.; Ni, W.; Liu, F.; Feng, H.; Zhang, Y.; Liu, T.; Zhang, H.; Wan, X.; Kan, B.; Zhang, Q.; Russell, T. P.; Chen, Y. A Simple Small Molecule as an Acceptor for Fullerene-Free Organic Solar Cells with Efficiency near 8%. *J. Mater. Chem. A* **2016**, *4*, 10409–10413.
- [60] Robert Ploessl, Indium Tin Oxide (In₂O₃):(SnO₂), (accessed 20/02/2018). URI: <http://www.indium.com/inorganic-compounds/indium-compounds/indium-tin-oxide/>.

- [61] Guo, E.-J.; Guo, H.; Lu, H.; Jin, K.; He, M.; Yang, G. Structure and Characteristics of Ultrathin Indium Tin Oxide Films. *Appl. Phys. Lett.* **2011**, *98*, 11905.
- [62] Sigma-Aldrich, Indium tin oxide coated glass slide, (accessed 20/02/2018). URI:<http://www.sigmaaldrich.com/catalog/product/aldrich/636916?lang=de®ion=AT>.
- [63] Tao, C.; Ruan, S.; Zhang, X.; Xie, G.; Shen, L.; Kong, X.; Dong, W.; Liu, C.; Chen, W. Performance Improvement of Inverted Polymer Solar Cells with Different Top Electrodes by Introducing a MoO₃ Buffer Layer. *Appl. Phys. Lett.* **2008**, *93*, 193307.
- [64] Liu, K.; Qu, S.; Zhang, X.; Tan, F.; Wang, Z. Improved Photovoltaic Performance of Silicon Nanowire/Organic Hybrid Solar Cells by Incorporating Silver Nanoparticles. *Nanoscale research letters* **2013**, *8*, 88.
- [65] Sze, S. M.; Lee, M. K. *Semiconductor Devices, Physics and Technology*; Sze, S. M., Ed.; Wiley: Hoboken New Jersey, 2012.
- [66] Groenendaal, L.; Jonas, F.; Freitag, D.; Pielartzik, H.; Reynolds, J. R. Poly(3,4-ethylenedioxythiophene) and Its Derivatives: Past, Present, and Future. *Adv. Mater.* **2000**, *12*, 481–494.
- [67] Kirchmeyer, S.; Reuter, K. Scientific Importance, Properties and Growing Applications of Poly(3,4-ethylenedioxythiophene). *J. Mater. Chem.* **2005**, *15*, 2077.
- [68] Nardes, A. M.; Kemerink, M.; Kok, M. M. de; Vinken, E.; Maturova, K.; Janssen, R. Conductivity, Work Function, and Environmental Stability of PEDOT: PSS Thin Films Treated with Sorbitol. *Organic Electronics* **2008**, *9*, 727–734.
- [69] Jönsson, S.; Birgersson, J.; Crispin, X.; Greczynski, G.; Osikowicz, W.; van der Denier Gon, A.; Salaneck, W.; Fahlman, M. The Effects of Solvents on the Morphology and Sheet Resistance in Poly(3,4-ethylenedioxythiophene)–Polystyrenesulfonic Acid (PEDOT–PSS) Films. *Synthetic Metals* **2003**, *139*, 1–10.
- [70] Huang, J.; Miller, P. F.; Mello, J. C. de; Mello, A. J. de; Bradley, D. Influence of Thermal Treatment on the Conductivity and Morphology of PEDOT/PSS Films. *Synthetic Metals* **2003**, *139*, 569–572.
- [71] Li, T.-C.; Chang, R.-C. Improving the Performance of ITO thin Films by Coating PEDOT: PSS. *Int. J. of Precis. Eng. and Manuf.-Green Tech.* **2014**, *1*, 329–334.
- [72] Jong, M. P. de; van IJzendoorn, L. J.; Voigt, M. J. A. de. Stability of the Interface between Indium-Tin-Oxide and Poly(3,4-ethylenedioxythiophene)/Poly(styrenesulfonate) in Polymer Light-Emitting Diodes. *Appl. Phys. Lett.* **2000**, *77*, 2255–2257.
- [73] Tokito, S.; Noda, K.; Taga, Y. Metal Oxides as a Hole-Injecting Layer for an Organic Electroluminescent Device. *J. Phys. D: Appl. Phys.* **1996**, *29*, 2750–2753.
- [74] Greiner, M. T.; Chai, L.; Helander, M. G.; Tang, W.-M.; Lu, Z.-H. Transition Metal Oxide Work Functions: The Influence of Cation Oxidation State and Oxygen Vacancies. *Adv. Funct. Mater.* **2012**, *22*, 4557–4568.
- [75] Meyer, J.; Khalandovsky, R.; Görrn, P.; Kahn, A. MoO₃ Films Spin-Coated from a Nanoparticle Suspension for Efficient Hole-Injection in Organic Electronics. *Advanced materials* **2011**, *23*, 70–73.
- [76] Tao, C.; Ruan, S.; Xie, G.; Kong, X.; Shen, L.; Meng, F.; Liu, C.; Zhang, X.; Dong, W.; Chen, W. Role of Tungsten Oxide in Inverted Polymer Solar Cells. *Appl. Phys. Lett.* **2009**, *94*, 43311.

- [77] Steirer, K. X.; Chesin, J. P.; Widjonarko, N. E.; Berry, J. J.; Miedaner, A.; Ginley, D. S.; Olson, D. C. Solution Deposited NiO Thin-Films as Hole Transport Layers in Organic Photovoltaics. *Organic Electronics* **2010**, *11*, 1414–1418.
- [78] Zilberberg, K.; Trost, S.; Schmidt, H.; Riedl, T. Solution Processed Vanadium Pentoxide as Charge Extraction Layer for Organic Solar Cells. *Adv. Energy Mater.* **2011**, *1*, 377–381.
- [79] Lin, Z.; Jiang, C.; Zhu, C.; Zhang, J. Development of Inverted Organic Solar Cells with TiO₂ Interface Layer by Using Low-Temperature Atomic Layer Deposition. *ACS applied materials & interfaces* **2013**, *5*, 713–718.
- [80] Noh, Y.-J.; Na, S.-I.; Kim, S.-S. Inverted Polymer Solar Cells Including ZnO Electron Transport Layer Fabricated by Facile Spray Pyrolysis. *Solar Energy Materials and Solar Cells* **2013**, *117*, 139–144.
- [81] Tan, Z.; Li, S.; Wang, F.; Qian, D.; Lin, J.; Hou, J.; Li, Y. High Performance Polymer Solar Cells with as-Prepared Zirconium Acetylacetonate Film as Cathode Buffer Layer. *Scientific reports* **2014**, *4*, 4691.
- [82] Meyer, J.; Winkler, T.; Hamwi, S.; Schmale, S.; Johannes, H.-H.; Weimann, T.; Hinze, P.; Kowalsky, W.; Riedl, T. Transparent Inverted Organic Light-Emitting Diodes with a Tungsten Oxide Buffer Layer. *Adv. Mater.* **2008**, *20*, 3839–3843.
- [83] Meyer, J.; Hamwi, S.; Bülow, T.; Johannes, H.-H.; Riedl, T.; Kowalsky, W. Highly Efficient Simplified Organic Light Emitting Diodes. *Appl. Phys. Lett.* **2007**, *91*, 113506.
- [84] Pawar, S. M.; Pawar, B. S.; Kim, J. H.; Joo, O.-S.; Lokhande, C. D. Recent Status of Chemical Bath Deposited Metal Chalcogenide and Metal Oxide Thin Films. *Current Applied Physics* **2011**, *11*, 117–161.
- [85] Wu, L.; Yu, Y.; Han, X.; Zhang, Y.; Zhang, Y.; Li, Y.; Zhi, J. An Electroless-Plating-Like Solution Deposition Approach for Large-Area Flexible Thin Films of Transition Metal Oxide Nanocrystals. *J. Mater. Chem. C* **2014**, *2*, 2266–2271.
- [86] Huang, J.-S.; Chou, C.-Y.; Liu, M.-Y.; Tsai, K.-H.; Lin, W.-H.; Lin, C.-F. Solution-Processed Vanadium Oxide as an Anode Interlayer for Inverted Polymer Solar Cells Hybridized with ZnO Nanorods. *Organic Electronics* **2009**, *10*, 1060–1065.
- [87] Liu, F.; Shao, S.; Guo, X.; Zhao, Y.; Xie, Z. Efficient Polymer Photovoltaic Cells Using Solution-Processed MoO₃ as Anode Buffer Layer. *Solar Energy Materials and Solar Cells* **2010**, *94*, 842–845.
- [88] Zilberberg, K.; Gharbi, H.; Behrendt, A.; Trost, S.; Riedl, T. Low-Temperature, Solution-Processed MoO_x for Efficient and Stable Organic Solar Cells. *ACS applied materials & interfaces* **2012**, *4*, 1164–1168.
- [89] Meyer, J.; Shu, A.; Kröger, M.; Kahn, A. Effect of Contamination on the Electronic Structure and Hole-Injection Properties of MoO₃/Organic Semiconductor Interfaces. *Appl. Phys. Lett.* **2010**, *96*, 133308.
- [90] Hung, L. S.; Tang, C. W.; Mason, M. G. Enhanced Electron Injection in Organic Electroluminescence Devices Using an Al/LiF Electrode. *Appl. Phys. Lett.* **1997**, *70*, 152–154.
- [91] Reese, M. O.; White, M. S.; Rumbles, G.; Ginley, D. S.; Shaheen, S. E. Optimal Negative Electrodes for Poly(3-hexylthiophene): [6,6]-phenyl C₆₁-Butyric Acid Methyl Ester Bulk Heterojunction Photovoltaic Devices. *Appl. Phys. Lett.* **2008**, *92*, 53307.

- [92] Jørgensen, M.; Norrman, K.; Krebs, F. C. Stability/Degradation of Polymer Solar Cells. *Solar Energy Materials and Solar Cells* **2008**, *92*, 686–714.
- [93] Norrman, K.; Larsen, N. B.; Krebs, F. C. Lifetimes of Organic Photovoltaics: Combining Chemical and Physical Characterisation Techniques to Study Degradation Mechanisms. *Solar Energy Materials and Solar Cells* **2006**, *90*, 2793–2814.
- [94] Reese, M. O.; Morfa, A. J.; White, M. S.; Kopidakis, N.; Shaheen, S. E.; Rumbles, G.; Ginley, D. S. Pathways for the Degradation of Organic Photovoltaic P3HT: PCBM Based Devices. *Solar Energy Materials and Solar Cells* **2008**, *92*, 746–752.
- [95] Hermenau, M.; Riede, M.; Leo, K.; Gevorgyan, S. A.; Krebs, F. C.; Norrman, K. Water and Oxygen Induced Degradation of Small Molecule Organic Solar Cells. *Solar Energy Materials and Solar Cells* **2011**, *95*, 1268–1277.
- [96] Krebs, F. C. Degradation and Stability of Polymer and Organic Solar Cells. *Solar Energy Materials and Solar Cells* **2008**, *92*, 685.
- [97] Guerrero, A.; Boix, P. P.; Marchesi, L. F.; Ripolles-Sanchis, T.; Pereira, E. C.; Garcia-Belmonte, G. Oxygen Doping-Induced Photogeneration Loss in P3HT: PCBM Solar Cells. *Solar Energy Materials and Solar Cells* **2012**, *100*, 185–191.
- [98] Grossiord, N.; Kroon, J. M.; Andriessen, R.; Blom, P. W. Degradation Mechanisms in Organic Photovoltaic Devices. *Organic Electronics* **2012**, *13*, 432–456.
- [99] Rivaton, A.; Tournebize, A.; Gaume, J.; Bussi re, P.-O.; Gardette, J.-L.; Therias, S. Photostability of Organic Materials Used in Polymer Solar Cells. *Polym. Int.* **2014**, *63*, 1335–1345.
- [100] Reese, M. O.; Nardes, A. M.; Rupert, B. L.; Larsen, R. E.; Olson, D. C.; Lloyd, M. T.; Shaheen, S. E.; Ginley, D. S.; Rumbles, G.; Kopidakis, N. Photoinduced Degradation of Polymer and Polymer-Fullerene Active Layers: Experiment and Theory. *Adv. Funct. Mater.* **2010**, *20*, 3476–3483.
- [101] Manceau, M.; Chambon, S.; Rivaton, A.; Gardette, J.-L.; Guillerez, S.; Lema tre, N. Effects of Long-Term UV-Visible Light Irradiation in the Absence of Oxygen on P3HT and P3HT: PCBM Blend. *Solar Energy Materials and Solar Cells* **2010**, *94*, 1572–1577.
- [102] Manceau, M.; Rivaton, A.; Gardette, J.-L. Involvement of Singlet Oxygen in the Solid-State Photochemistry of P3HT. *Macromol. Rapid Commun.* **2008**, *29*, 1823–1827.
- [103] Hintz, H.; Egelhaaf, H.-J.; Peisert, H.; Chass , T. Photo-Oxidation and Ozonization of Poly(3-hexylthiophene) Thin Films as Studied by UV/VIS and Photoelectron Spectroscopy. *Polymer Degradation and Stability* **2010**, *95*, 818–825.
- [104] Rivaton, A.; Chambon, S.; Manceau, M.; Gardette, J.-L.; Lema tre, N.; Guillerez, S. Light-induced Degradation of the Active Layer of Polymer-Based Solar Cells. *Polymer Degradation and Stability* **2010**, *95*, 278–284.
- [105] Manceau, M.; Rivaton, A.; Gardette, J.-L.; Guillerez, S.; Lema tre, N. The Mechanism of Photo- and Thermooxidation of Poly(3-hexylthiophene) (P3HT) Reconsidered. *Polymer Degradation and Stability* **2009**, *94*, 898–907.
- [106] Motaung, D. E.; Malgas, G. F.; Arendse, C. J. Insights into the Stability and Thermal Degradation of P3HT: C₆₀ Blended Films for Solar Cell Applications. *J Mater Sci* **2011**, *46*, 4942–4952.

- [107] Song, Q. L.; Li, F. Y.; Yang, H.; Wu, H. R.; Wang, X. Z.; Zhou, W.; Zhao, J. M.; Ding, X. M.; Huang, C. H.; Hou, X. Y. Small-Molecule Organic Solar Cells with Improved Stability. *Chemical Physics Letters* **2005**, *416*, 42–46.
- [108] Kawano, K.; Pacios, R.; Poplavskyy, D.; Nelson, J.; Bradley, D. D.; Durrant, J. R. Degradation of Organic Solar Cells due to Air Exposure. *Solar Energy Materials and Solar Cells* **2006**, *90*, 3520–3530.
- [109] Nagata, T.; Oh, S.; Chikyow, T.; Wakayama, Y. Effect of UV–Ozone Treatment on Electrical Properties of PEDOT: PSS Film. *Organic Electronics* **2011**, *12*, 279–284.
- [110] Elshobaki, M.; Andereg, J.; Chaudhary, S. Efficient Polymer Solar Cells Fabricated on Poly(3,4-ethylenedioxythiophene):Poly(styrenesulfonate)-Etched Old Indium Tin Oxide Substrates. *ACS applied materials & interfaces* **2014**, *6*, 12196–12202.
- [111] Sharma, A.; Andersson, G.; Lewis, D. A. Role of humidity on indium and tin migration in organic photovoltaic devices. *Physical chemistry chemical physics : PCCP* **2011**, *13*, 4381–4387.
- [112] Voroshazi, E.; Verreet, B.; Buri, A.; Müller, R.; Di Nuzzo, D.; Heremans, P. Influence of Cathode Oxidation via the Hole Extraction Layer in Polymer: Fullerene Solar Cells. *Organic Electronics* **2011**, *12*, 736–744.
- [113] Wang, M.; Xie, F.; Du, J.; Tang, Q.; Zheng, S.; Miao, Q.; Chen, J.; Zhao, N.; Xu, J. B. Degradation Mechanism of Organic Solar Cells with Aluminum Cathode. *Solar Energy Materials and Solar Cells* **2011**, *95*, 3303–3310.
- [114] Lögdlund, M.; Brédas, J. L. Theoretical Studies of the Interaction between Aluminum and Poly(p -phenylenevinylene) and Derivatives. *The Journal of Chemical Physics* **1994**, *101*, 4357–4364.
- [115] Antoniadis, H.; Hsieh, B. R.; Abkowitz, M. A.; Jenekhe, S. A.; Stolka, M. Photovoltaic and Photoconductive Properties of Aluminum/Poly(p-phenylene vinylene) Interfaces. *Synthetic Metals* **1994**, *62*, 265–271.
- [116] Chambon, S.; Derue, L.; Lahaye, M.; Pavageau, B.; Hirsch, L.; Wantz, G. MoO₃ Thickness, Thermal Annealing and Solvent Annealing Effects on Inverted and Direct Polymer Photovoltaic Solar Cells. *Materials* **2012**, *5*, 2521–2536.
- [117] Bertho, S.; Janssen, G.; Cleij, T. J.; Conings, B.; Moons, W.; Gadisa, A.; D'Haen, J.; Goovaerts, E.; Lutsen, L.; Manca, J.; Vanderzande D. Effect of Temperature on the Morphological and Photovoltaic Stability of Bulk Heterojunction Polymer: Fullerene Solar Cells. *Solar Energy Materials and Solar Cells* **2008**, *92*, 753–760.
- [118] Chu, C.-W.; Yang, H.; Hou, W.-J.; Huang, J.; Li, G.; Yang, Y. Control of the Nanoscale Crystallinity and Phase Separation in Polymer Solar Cells. *Appl. Phys. Lett.* **2008**, *92*, 103306.
- [119] Chiguvare, Z.; Parisi, J.; Dyakonov, V. Influence of Thermal Annealing on the Electrical Properties of Poly(3-hexylthiophene)-Based Thin Film Diodes. *Zeitschrift für Naturforschung A* **2007**, *62*, DOI: 10.1515/zna-2007-10-1109.
- [120] Bertho, S.; Haeldermans, I.; Swinnen, A.; Moons, W.; Martens, T.; Lutsen, L.; Vanderzande, D.; Manca, J.; Senes, A.; Bonfiglio, A. Influence of Thermal Ageing on the Stability of Polymer Bulk Heterojunction Solar Cells. *Solar Energy Materials and Solar Cells* **2007**, *91*, 385–389.
- [121] Swinnen, A.; Haeldermans, I.; vande Ven, M.; D'Haen, J.; Vanhoyland, G.; Aresu, S.; D'Olieslaeger, M.; Manca, J. Tuning the Dimensions of C₆₀-Based Needlelike Crystals in Blended Thin Films. *Adv. Funct. Mater.* **2006**, *16*, 760–765.

- [122] Hirose, Y.; Kahn, A.; Aristov, V.; Soukiassian, P. Chemistry, Diffusion, and Electronic Properties of a Metal/Organic Semiconductor Contact: In/Perylenetetra-carboxylic Dianhydride. *Appl. Phys. Lett.* **1996**, *68*, 217–219.
- [123] Krebs, F. C.; Alstrup, J.; Spanggaard, H.; Larsen, K.; Kold, E. Production of Large-Area Polymer Solar Cells by Industrial Silk Screen Printing, Lifetime Considerations and Lamination with Polyethyleneterephthalate. *Solar Energy Materials and Solar Cells* **2004**, *83*, 293–300.
- [124] Dupont, S. R.; Oliver, M.; Krebs, F. C.; Dauskardt, R. H. Interlayer Adhesion in Roll-to-Roll Processed Flexible Inverted Polymer Solar Cells. *Solar Energy Materials and Solar Cells* **2012**, *97*, 171–175.
- [125] Brand, V.; Bruner, C.; Dauskardt, R. H. Cohesion and Device Reliability in Organic Bulk Heterojunction Photovoltaic Cells. *Solar Energy Materials and Solar Cells* **2012**, *99*, 182–189.
- [126] Glen, T. S.; Scarratt, N. W.; Yi, H.; Iraqi, A.; Wang, T.; Kingsley, J.; Buckley, A. R.; Lidzey, D. G.; Donald, A. M. Dependence on Material Choice of Degradation of Organic Solar Cells Following Exposure to Humid Air. *Journal of polymer science. Part B, Polymer physics* **2016**, *54*, 216–224.
- [127] Karpov, V. G.; Compaan, A. D.; Shvydka, D. Random Diode Arrays and Mesoscale Physics of Large-Area Semiconductor Devices. *Phys. Rev. B* **2004**, *69*, 258.
- [128] Rösch, R.; Tanenbaum, D. M.; Jørgensen, M.; Seeland, M.; Bärenklau, M.; Hermenau, M.; Voroshazi, E.; Lloyd, M. T.; Galagan, Y.; Zimmermann, B.; Würfel, U.; Hösel, M.; Dam, H. F.; Gevorgyan, S. A.; Kudret, S.; Maes, W.; Lutsen, L.; Vanderzande, D.; Andriessen, R.; Teran-Escobar, G.; Lira-Cantu, M.; Rivaton, A.; Uzunoğlu, G. Y.; Germack, D.; Andreasen, B.; Madsen, M. V.; Norrman, K.; Hoppe, H.; Krebs, F. C. Investigation of the Degradation Mechanisms of a Variety of Organic Photovoltaic Devices by Combination of Imaging Techniques—the ISOS-3 Inter-Laboratory Collaboration. *Energy Environ. Sci.* **2012**, *5*, 6521.
- [129] Krebs, F. C., Ed. *Stability and Degradation of Organic and Polymer Solar Cells*; Wiley: Chichester, 2012.
- [130] Coffey, D. C.; Reid, O. G.; Rodovsky, D. B.; Bartholomew, G. P.; Ginger, D. S. Mapping Local Photocurrents in Polymer/Fullerene Solar Cells with Photoconductive Atomic Force Microscopy. *Nano letters* **2007**, *7*, 738–744.
- [131] McNeill, C. R.; Frohne, H.; Holdsworth, J. L.; Furst, J. E.; King, B. V.; Dastoor, P. C. Direct Photocurrent Mapping of Organic Solar Cells Using a Near-Field Scanning Optical Microscope. *Nano letters* **2004**, *4*, 219–223.
- [132] Rösch, R.; Krebs, F. C.; Tanenbaum, D. M.; Hoppe, H. Quality Control of Roll-to-Roll Processed Polymer Solar Modules by Complementary Imaging Methods. *Solar Energy Materials and Solar Cells* **2012**, *97*, 176–180.
- [133] Seeland, M.; Rösch, R.; Hoppe, H. Luminescence Imaging of Polymer Solar Cells: Visualization of Progressing Degradation. *Journal of Applied Physics* **2011**, *109*, 64513.
- [134] Krebs, F. C.; Søndergaard, R.; Jørgensen, M. Printed Metal Back Electrodes for R2R Fabricated Polymer Solar Cells Studied Using the LBIC Technique. *Solar Energy Materials and Solar Cells* **2011**, *95*, 1348–1353.

Chapter 3

Experimental and Characterization

3.1 Materials and chemicals

Anode:

ITO (Indium-doped tin oxide(SnO_2 : In), 20 Ω /square, Ossila.)

Hole transport layer:

PEDOT:PSS: Poly(3,4-ethylenedioxythiophene):poly(4-styrenesulfonate), Heraeus Deutschland GmbH & Co. KG (Clevios P Jet (OLED))

MoO₃-1: Bis(acetylacetonato)dioxomolybdenum(VI) ($\text{MoO}_2(\text{acac})_2$), Sigma-Aldrich; Isopropanol, VWR International LLC.

MoO₃-2: Ammonium molybdate ($(\text{NH}_4)_2\text{MoO}_4$) ($\geq 99.98\%$), Sigma Aldrich; Hydrochloric acid HCl ($\geq 37\%$), Sigma-Aldrich

Active layer:

Donor: Poly(3-hexylthiophene) (P3HT), Rieke Metals Inc. (MW 50,000–70,000 g mol^{-1} , regioregularity 91–94%).

Acceptor: [6,6]-Phenyl-C₆₁-butyric acid methyl ester (PC₆₀BM), Nano-C Inc. (99.5% purity).

Solvent: Anhydrous chlorobenzene, Sigma-Aldrich.

Electron transport layer:

LiF (Lithium fluoride)

Cathode:

Al (Aluminum)

3.2 Preparation of MoO₃ HTLs

3.2.1. Fundamentals of sol-gel process

In this study, MoO₃ HTLs were prepared by the sol-gel process. The sol-gel transition can be used to prepare materials with a variety of shapes, such as porous structures, microspheres, monoliths, thin fibers, dense powders and thin films [1]. The sol-gel method is widely developed for the fabrication of metal oxide films due to its simple technique with low cost, and solution processability at the room temperature [2-3].

A sol is a stable dispersion of colloidal particles ($\sim 0.1-1 \mu\text{m}$) or polymers in a liquid solvent, where only the Brownian motions suspend the particles. A gel is a state where both liquid and solid are dispersed in each other, which presents a porous, three dimensional continuous solid network containing a continuous liquid phase, named wet gel. Sol-gel processes involve a state change from monomers into a colloidal dispersion solution (sol) that acts as the precursor, typical metal alkoxides, to an integrated network (gel) of either discrete particles or network polymers [1,4]. This transformation process could be finished through agglomeration, poly-condensation reactions, subsequent chemical cross-linking, electrostatic destabilization, evaporation or some combination thereof [4]. Figure 3.1 shows a schematic diagram of the sol-gel process and its various products. The process can be summarized in the following key steps [1,4-6]:

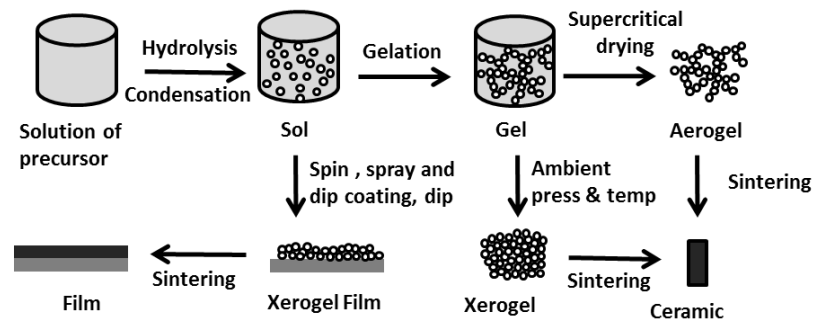


Figure 3.1 A schematic diagram showing the sol-gel process and its various products.

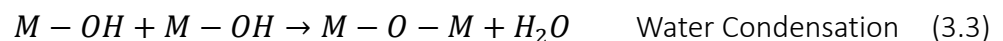
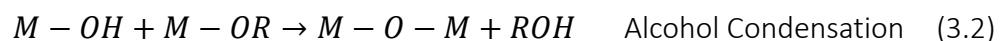
(1) Formation of a sol

Synthesis of the “sol” is usually from hydrolysis and partial condensation of alkoxide precursors [6]. Hydrolysis is a reaction in which a metal alkoxide ($M-OR$) reacts with water to form a metal hydroxide ($M-OH$) [7], as seen in Equation 3.1 [5]:



(2) Gelation (sol-gel transformation)

Condensation is a reaction which occurs when two metal hydroxides ($M-OH$) combine to form a metal oxide species ($M-O-M$) [7], as shown below in Equation 3.2 and 3.3 [5]:



The particles in the sol are polymerized through the removal of the stabilizing components to produce a gel in a state of a continuous network [5]. The structure of gelation is related to glass-forming processes that may be changed significantly with time, depending on the temperature, solvent, or pH conditions.

(3) Ageing (syneresis)

In the process step of aging or syneresis, the condensation within the gel network continues, the stiffness of the gel increases and the thin film shrinks due to the removal of the solvent [5].

(4) Drying

The conventional drying process is induced by increasing temperature or decreasing pressure for evaporation of the liquid in the wet gel. Drying of the gel can either form a dense “xerogel” via the collapse of the porous network or an “aerogel” through supercritical drying [6]. The structure of xerogel and aerogel are shown in Figure 3.1. Xerogels are formed by evaporation

of the pore liquid from the initial wet gels under ambient conditions or with the heat treatment that gives rise to capillary forces and leads to shrinkage of the gel network. Aerogel structures are established by a supercritical drying for removal of solvent, yielding a product more similar to the size and shape of the original gel. Aerogels may have low solid volume fractions near 1% with very high porous volumes [8].

The preparation of metal oxide thin films by the sol-gel method can be processed as shown below (see Figure 3.1). First, the desired colloidal particles are dispersed in a liquid to form a sol. Then, deposit the sol solution on the substrates by spraying, dipping or spinning to produce the thin film coatings. Gelation is formed by rapid evaporation of the solvent. The final thermal treatments pyrolyze the remaining organic or inorganic components and form an amorphous or crystalline coating [5].

3.2.2. Experimental methods for MoO₃ HTL preparation

MoO₃-1

The MoO₃-1 precursor solution was prepared according to the procedure reported by K. Zilberberg et al. [9]. MoO₂(acac)₂ was dissolved in isopropanol to form a 0.5% (w/v) solution. This MoO₃ precursor formulation was spin-coated onto ITO substrates at 3000 rpm for 40 s, followed by hydrolysis reaction at room temperature in ambient air for 1 hour and post-annealed at 160 °C for 20 min, and then formed a continuous MoO₃ layer [10].

MoO₃-2

The MoO₃-2 precursor formulation was prepared by hydration method in aqueous solution as reported by Dong et al. [11] and Liu et al. [12]. (NH₄)₂MoO₄ was dissolved in distilled water to form a 0.005 mol/L solution. Then 2 mol/L aqueous HCl was added drop-wise under stirring until the pH value of the solution was between 1 and 1.5. The prepared formulation deposited onto ITO substrates by spin-coating at 3000 rpm for 40s. The obtained film was annealed at 160 °C for 20 min in air, and then the MoO₃ nanoparticle film was formed [10].

3.3 Solar cells fabrication

Figure 3.2 shows the device architecture of standard studied SCs with P3HT: PCBM active layer and different HTLs materials, continuous MoO₃ (MoO₃-1), nanoparticle MoO₃ (MoO₃-2), and PEDOT:PSS, or without HTL (=ITO). First, ITO substrates were cleaned by sonication in acetone and isopropanol for 10 min, respectively. O₂-plasma etching (100 W for 15 min) was applied to the substrates briefly before use to achieve the desired low work function [13] of the ITO and improve the hydrophilicity of the surface [14] to obtain better wetting and adhesion for the deposition of the uniform following layers. After plasma-etching the HTL was spin-coated onto the ITO substrates at 4000 rpm for PEDOT:PSS and 3000 rpm for MoO₃ (both MoO₃-1 and MoO₃-2) for 40 s, respectively, from its aqueous solution filtered by 0.22 μm Polyvinylidene difluoride (PVDF) membrane filters (Sigma Aldrich). The MoO₃-1 and MoO₃-2 films were kept in air for 1 h for hydrolysis at room temperature and then annealed at 160 °C for 20 min. The PEDOT:PSS anode buffer layers were annealed at 160 °C for 20 min under Ar flow to remove moisture in the film.

The film thickness of PEDOT:PSS is around 40 nm, and MoO₃ layers are around 10 nm measured by spectroscopic ellipsometry [10,15]. For the preparation of studied devices with different environments exposed HTLs, the as-prepared HTLs were exposed to dry air with <20% relative humidity or humid air with >80% relative humidity without illumination, or to dry air under white light illumination (tungsten halogen) at 10% equivalent of AM1.5G. The exposure duration was 18 hours at 25°C [15]. The active layer was spin-coated in an Ar atmosphere from a solution of P3HT and PCBM (1:1 weight ratio, each 18 mg/mL) in 70 °C chlorobenzene at 2500 rpm for 60 s, followed by annealing at 120 °C for 10 min for better crystallinity and higher mobility of the active layer to enhance its charge transport properties [16]. The obtained film thickness of the active layer was around 150 nm measured by profilometry. The cathode and ETL were deposited by a thermal evaporation as a bilayer of LiF/Al in the glovebox. Approximately 2 nm thick LiF was evaporated at a rate of 0.2 Å/s and with a start pressure of 1×10⁻⁵ mbar and followed by 100 nm of Al with an evaporation rate between 0.5-2 Å/s [10]. For the preparation of studied devices without HTL exposing to different environments on the entire SCs, the nonencapsulated devices without HTL were exposed to static Ar, aforementioned dry air, or humid air without any illumination, and to dry air under white light illumination. The duration of exposure differed from 0 to 240 min at 25°C [17].

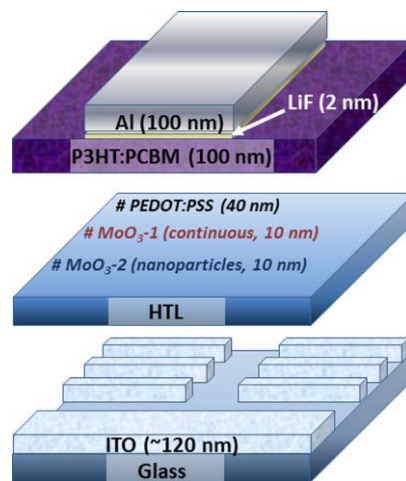


Figure 3.2 Device architecture of the standard studied solar cell [10].

3.4 Characterization techniques

3.4.1. Atomic force microscopy (AFM)

AFM, one of the scanning probe microscopes (SPM), is widely utilized as a tool to investigate the physical topography, surface forces as well as material properties of the specimen such as height, magnetism, stiffness, surface chemistry etc. on the nanoscale. The resolution of AFM is comparable to electronic microscopes, but the major difference is that AFM can be applied to detect electrically non-conductive materials [18-19]. Figure 3.3 shows a typical AFM setup.

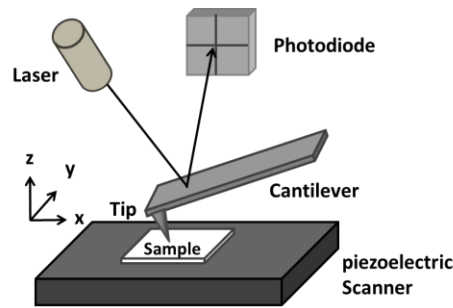


Figure 3.3 Schematic of typical AFM setup.

AFM is based on raster scanning a cantilevered tip in the x-y plane over the surface of a specimen, by attaching the sample or the cantilevered tip itself to a scanner [20]. As the tip moves toward the sample surface, forces between the tip and the surface induce the deflection of the cantilever. The deflections of cantilever towards or away from the sample surface are measured by the reflection of a laser beam. The position of the laser spot from the reflected laser beam is recorded by a four-quadrant photo-detector. The measurement of an AFM is achieved by using a piezoelectric controlled X, Y stage to move the sample relative to the probe and record the value from vertical Z dimension. By scanning in a specific range on the sample surface and utilizing a feedback loop to control the height of the tip above the sample surface to keep a constant laser position, the relative height of the surface can be determined [18]. For imaging sample topography, the surface can be scanned in different modes, as shown in Figure 3.4 [21,22] and described below:

Contact mode:

In this mode, the tip physically contacts with the surface of the specimen with strong repulsive force on the tip. The feedback loop system adjusts the height of the cantilever to keep the deflection constant as the tip moves over the sample [22]. Thereby the deflection of the tip is directly related to the height of the sample. Contact mode imaging gives high resolution but is significantly influenced by frictional and adhesive forces, and can easily damage the surface of samples. This mode is suitable for dried or fixed samples and also when dissection or displacement of a particle is desired [23].

Non-contact mode:

Non-contact mode works by sensing Van der Waals attractive forces between surface and probe tip. The cantilever is oscillated at the resonance frequency in low amplitude close to the surface without touching the sample and the amplitude of the oscillation is kept constant. The change in amplitude and frequency of the oscillation is used to determine the height of the surface. Non-contact imaging generally provides lower resolution than either contact mode or tapping mode due to the weak attractive force. This technique is also easily influenced by a fluid contaminant layer on the surface since the contaminant layer is generally thicker than the range of the Van der Waals force gradient that would induce interference with the oscillation [24]. Thereby, this mode is usually utilized when the sample surface is susceptible to the tip contact.

Tapping mode:

Tapping or intermittent contact mode, where the tip is oscillated with a high amplitude to tap the surface. In this mode the tip only intermittently contacts with the surface instead of direct contact like contact mode. It is a mode designed between the contact and non-contact mode to achieve high resolution images without inducing destructive forces and damage on the samples. This technique resolves the problems associated with friction, adhesion, electrostatic forces between the tip and the specimen, avoid harming the sample by intermittently contacting the sample surface and prevents the tip from being trapped and interfered through the contaminant layer by oscillating with adequate amplitude. Tapping mode is commonly applied to image non-fixed samples or samples in liquid media, such as soft and fragile samples [24-25].

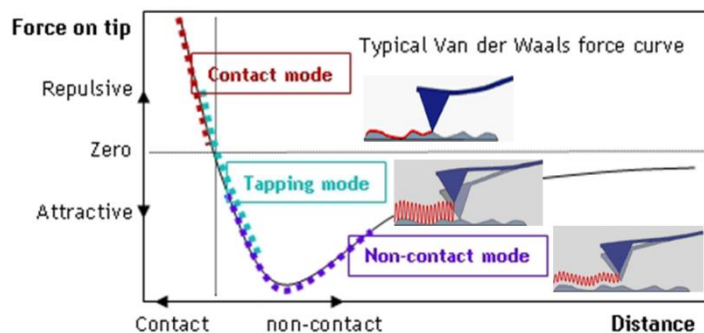


Figure 3.4 Different modes of AFM and their corresponding force-distance curve [21-22].

In this study, material structure and film morphologies were analysed by AFM using two systems: For $1\ \mu\text{m} \times 1\ \mu\text{m}$ a Nanosurf, EasyScan2, and for $3\ \mu\text{m} \times 3\ \mu\text{m}$ a MFP 3D AFM System from Asylum Research. The images with the EasyScan2 were taken in tapping mode using a Tap190 cantilever (Budgetsensors, Bulgaria) with a nominal frequency of 190 kHz. The MFP 3D AFM was operated in intermittent contact mode using SSS NCHR AFM probes from APPNano with a typical tip radius below 2 nm. The AFM topography and particle size distribution data were visualized and analysed using the Gwyddion 2.40 software [10].

3.4.2. Kelvin probe force microscopy (KPFM)

KPFM, also known as surface potential microscopy, was proposed by Nonnenmacher in 1991 [26]. It is a technique based on noncontact AFM that allows the investigation of topographic images in combination with spatial surface potential images and electrical properties at the nanometer-scale [26-27]. KPFM was originally developed to measure work function differences or contact potential difference (CPD) variations between a conducting AFM tip and a metallic sample, but nowadays the technique has been extended further to semiconductors [28-29], and insulators [30]. The cantilever in the AFM is used as the reference electrode to form a capacitor with the surface. Figure 3.5 shows the energy band diagram illustrating the working principle of the Kelvin probe technique.

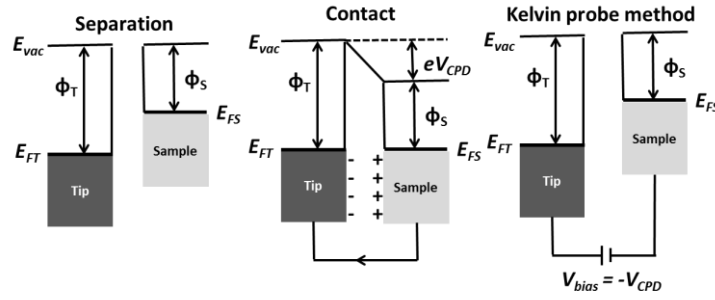


Figure 3.5 Energy band diagram illustrating working principle of Kelvin probe technique.

The work functions of the tip and the sample are ϕ_T and ϕ_S , respectively. When tip and sample are brought into contact, a net electric current would flow from the one with lower work function to the one with higher work function until the Fermi energies are aligned. The established potential between the work functions of tip and sample surfaces is called the CPD (V_{CPD}). Then, an external bias (V_{bias}) is applied between the tip and the sample to compensate electrostatic force between tip and surface (F_{el}) and align their vacuum level (E_{VAC}). As the electrostatic force reaches zero and two vacuum levels are aligned in the same level, the external potential (V_{bias}) is equal to the CPD (V_{CPD}), which is equivalent to the CPD between the tip and sample ($\phi_{tip} - \phi_{sample}$) [31-32]. The relationship between F_{el} , V_{bias} , V_{CPD} , ϕ_{tip} , and ϕ_{sample} can be briefly described in Equation 3.4:

$$F_{el} = 0 \iff V_{bias} = V_{CPD} = \frac{\phi_{tip} - \phi_{sample}}{-e} \quad (3.4)$$

where e is the elementary charge .

A general KPFM operating system is shown in Figure 3.6. A voltage, which consists of an AC voltage $V_{AC} \sin(\omega t)$ at the frequency ω with a DC offset bias V_{DC} , is applied between tip and sample to generate an electrostatic force between the tip and the sample, as shown in Figure 3.6 and Equation 3.5 [31-32]:

$$V_{tip} = (V_{DC} - V_{CPD}) + V_{AC} \sin(\omega t) \quad (3.5)$$

where V_{tip} is the applied tip voltage between tip and surface, V_{AC} a sinusoidal voltage modulation at the excitation frequency (ω), and V_{DC} a backing voltage controlled by the bias feedback loop. The electrostatic force between two surfaces is described by Equation 3.6:

$$F_{el} = \frac{1}{2} \frac{dC}{dz} V_{tip}^2 \quad (3.6)$$

where C is the capacitance, and z the direction normal to the sample surface. The deflection of the cantilever by an electrostatic force is detected by a photodetector and a lock-in amplifier is used to detect the cantilever oscillation at ω . The signal is then transferred to a feedback controller. By adjusting the dc offset bias V_{DC} until the electrostatic forces between the tip and the sample become zero and thus the response at the frequency ω also becomes zero. The intended potential, CPD, is obtained [31-32].

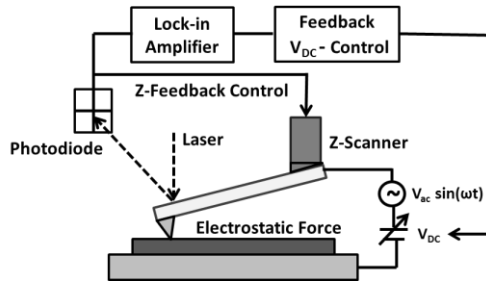


Figure 3.6 A general KPFM operation system.

In this thesis, KPFM was utilized to observe surface potential homogeneity of HTLs. Local CPD maps of $3 \mu\text{m} \times 3 \mu\text{m}$ areas were measured by KPFM using the MFP3D system with Pt coated ACCESS EFM probes from APPNano. The CPD data were analyzed by the Gwyddion 2.40 software. Surface CPD distribution maps of SC pixels ($4 \text{ mm} \times 1.5 \text{ mm}$) area were investigated by the SKP5050 Scanning Kelvin probe (KP Technology Ltd.) [10].

3.4.3. X-ray photoelectron spectroscopy (XPS)

Photoemission spectroscopy (PES), also named as photoelectron spectroscopy, is a technique that measures electronic structure and kinetic energy of photon excited electrons emitted from a sample surface through the external photoelectric effect to detect the binding energies of electrons in the material [33]. The photoelectric effect is a phenomenon describing electron emission from a substance after light absorption. PES can be utilized to probe the energy levels of electrons, the properties of chemical bonding and electron motion of the material. The PES technique is classified into different types depending on the provided ionization energy, a X-ray photon (XPS), an ultraviolet photon (UPS), or an EUV photon [33]. The major difference of XPS and UPS technique is that XPS uses higher energy mono-energetic Al $K\alpha$ or Mg $K\alpha$ as X rays source with an energy of 1486.6 eV or 1253.6 eV, respectively and UPS utilizes a much lower energy source, He(I) or He(II) lamps with energies of 21.2 eV or 40.8 eV, respectively [34].

The principle of the PES technique and its corresponding band structure are shown in Figure 3.7. When the photon energy ($h\nu$) is greater than the electron binding energy (E_B) of the sample, a photoelectron is emitted from the atom and transported to the surface with a kinetic energy (E_k) [33]. During the process, all of the photon energies are absorbed, one part is used to free the electron from the atom, and the rest goes into the electron's kinetic energy as a free particle. An electron energy analyzer is utilized to measure the energy of the emitted photoelectrons. By fixing the incident photon energy ($h\nu$) and observing the velocity or kinetic energy (E_k) of excited photoelectrons, the density of states at a fixed binding energy (E_B) of electrons in the sample can be obtained [34-35], as shown in Equation 3.7:

$$E_B = h\nu - E_K - \phi \quad (3.7)$$

where ϕ is the work function induced by the analyzer and can be compensated artificially. For the analysis, owing to $h\nu$ and ϕ are the known values, E_B can be determined as E_k is experimentally observed.

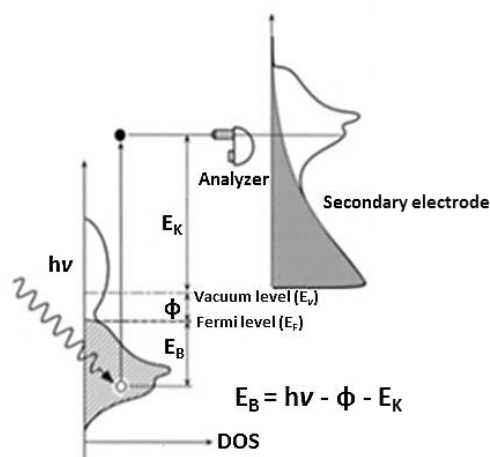


Figure 3.7 The principle of the photoemission spectroscopy technique and its corresponding band structure [35].

XPS is also known as electron spectroscopy for chemical analysis (ESCA). This technique is widely used for the surface analysis to identify the elements and the chemical state of the material, relative composition of the constituents, and the valence band structure from the observed binding energy and intensity of a photoelectron peak [36]. The light source of monochromatic X-rays such as Al $K\alpha$ is produced by bombarding an Al target with high energy electrons. These higher energy incident photons hit the sample surface in a high vacuum environment, allowing the ejection of core-level electrons from the sample atoms. The electrons are emitted from their initial state with a kinetic energy dependent on the incident X-ray and binding energy of the atomic orbital. Owing to the small mean free path γ (order of 1 nm) of the emitted electrons and considerable energy loss, only photoelectrons out of the first 10 nm may leave the surface and be observed as photoelectrons [37]. The photoelectron peaks are corresponding to a particular core level of an element. By observing shifts in the binding energy of a specific orbital for an atom, the chemical structures of the material can be identified [37].

In this study, XPS measurements were performed on a commercial spectrometer (HR-XPS, SPECS Surface Nano Analysis GmbH), using monochromatic Mg $K\alpha$ radiation ($h\nu= 1253.6$ eV) [10].

3.4.4. Ambient pressure photoemission spectroscopy system (APS)

APS is a photoemission technique from the company KP Technology Ltd. The technique uses a Kelvin probe to detect electrons and atmospheric ions ejected from metallic surfaces (Au, Ag, Cu, Fe, Ni, Ti, Zn, Al) upon illumination by a deep ultra-violet (DUV) light source in air [38]. This APS system has a broad excitation range of 3.4-7.0 eV, which enable it to investigate the absolute work function of metals and the ionization potential of semiconductors [39]. This technique works by the combination of the Kelvin method and the photoelectric effect to detect absolute work function values of materials in air atmosphere [38]. Figure 3.8 shows the schematic diagram of the APS system. A chamber consists of a DUV lamp (D_2), motorized spectrometer and DUV optical filter arrangement to generate a tuneable 3.0-7.0 eV beam. A second tuneable visible source lamp and spectrometer are applied for surface photovoltage measurements. B Chamber is equipped

with a vertically mounted Kelvin probe, which is utilized to detect both photoemission and CPD measurement modes. V_b is the tip bias potential [38].

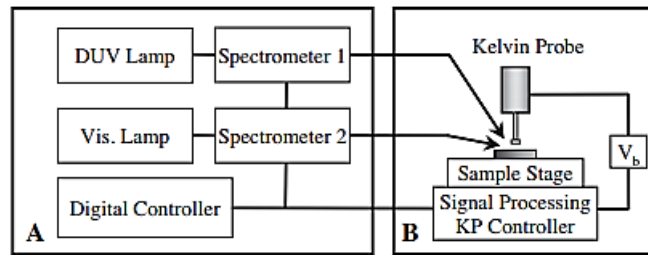


Figure 3.8 Schematic showing the setup of ambient photoemission spectroscopy [38].

In this APS system, the photoelectron emission and ion-current detection process consist of a four-step process, as shown in Figure 3.9 [38].

1. Exposure of DUV photons: DUV photons are absorbed in the sample surface. After exiting the material, photoejected electrons are affected by the image force (IF) between the positively charged Kelvin probe and the negatively charged sample. The IF extends to approximately 30 nm from the sample surface, further away from this range the electrons are scattered by atmospheric molecules and external electric fields.
2. Photoejected electrons form an electron cloud about 1–3 μm from the sample surface ($Z=0$) [42]. In this region atmospheric ions such as N_2^- and O_2^- are created.
3. Ions drift toward the positively biased (+10 V) Kelvin probe tip in the electric field.
4. The obtained ion current is recorded as a function of incident photon energy (E_{ph}) [38]. No current appears when the photon energy is below the work function threshold energy (ϕ), and the current increases with $(E_{\text{ph}} - \phi)^N$ with $N=1/2$ for metal and $N=1/3$ for semiconductor as it gets above the threshold energy [40-41].

In this thesis, the absolute work functions of different HTL materials were obtained by Ambient Pressure Photoemission Spectroscopy System (APS) (APS02, KP Technology Ltd.) [10].

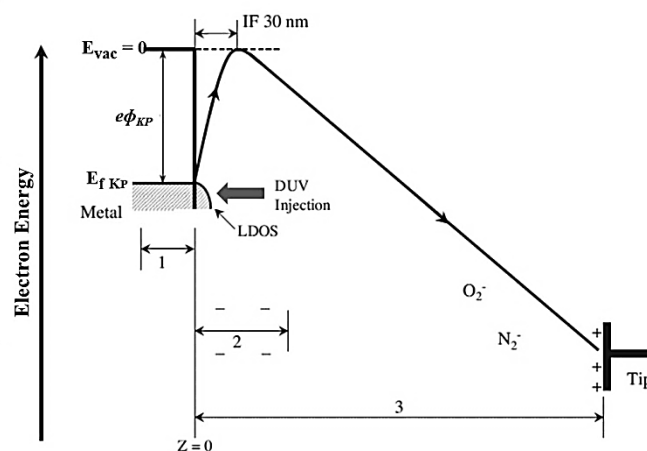


Figure 3.9 Schematic energy band diagram of ambient pressure photoemission system. LDOS represents the local density of states and IF the image force [38].

3.4.5. Spectroscopic ellipsometry (SE)

SE is a non-destructive optical metrology technique widely used for analysis of thin films properties of a material, including refractive index (n), extinction coefficient (k) and thickness by characterization of light reflection or transmission from the sample [42]. SE technique works by measuring the changes in intensity and phase polarization of light upon reflection or transmission from the surface of a thin film material. A typical ellipsometer equipped with various optical elements includes a source of collimated unpolarized light, a polarizer, an analyzer, and a photodetector. The polarizer and analyzer are employed to extract linearly polarized light from unpolarized light [43]. A schematic of an ellipsometer is demonstrated in Figure 3.10.

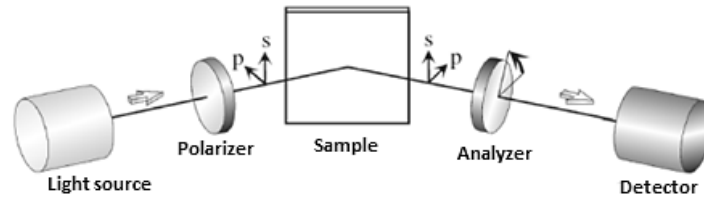


Figure 3.10 Schematic of a spectroscopic ellipsometer [43].

Light is generated from a discharge lamp which consists of multiple wavelengths in the ultraviolet-visible (UV-Vis) to the near IR region. After light passes through a monochromator, it becomes a single wavelength light. This light is then passed through a polarizer to be rotated to the polarized light with specified polarizations (s- and p-polarizations). P- and s-polarized light waves are irradiated onto a sample at the Brewster angle [43]. Brewster's angle is a specific angle of incident light that produces a 90° angle between the reflected and the refracted ray [44]. Upon light reflection on a sample, p- and s-polarizations perform different changes in amplitude and phase due to the difference of electric dipole radiation [43]. Then the polarized light is transmitted through the film and reflected off from the substrate. Finally, the reflected light passes through the analyzer, and the intensity of the light is then measured by a detector. Thereby the optical constants and the film thickness of the sample can be determined.

For the ellipsometry analysis, an incidence angle is chosen for the maximum sensitivity of the measurement. By varying the incidence angle and the wavelength of light, the two ellipsometric angles (ψ , Δ), which represent the phase difference (Δ) and the amplitude ratio of polarization (ψ) between the incident and reflected light of p- and s-polarizations can be measured (see Equation 3.8 and 3.9) [45]. The two ellipsometric angles (ψ , Δ) are relevant to the ratio of the amplitude reflection coefficients for p- and s-polarizations, R_s and R_p , respectively. Equation 3.10 shows the relationship between two ellipsometry parameters (ψ , Δ), the reflectance ratio (ρ), and the reflection coefficients, R_p and R_s at the interface [45].

$$\tan \Psi = \frac{R_p}{R_s} \quad (3.8)$$

$$\Delta = \delta_p - \delta_s \quad (3.9)$$

$$\rho = \frac{R_p}{R_s} = \tan(\psi) e^{i\Delta} \quad (3.10)$$

The complex refractive index (N), where $N = n + ik$, where n is the refractive index and k is the absorption index, can be determined by the Fresnel equations [46], as shown in Equation 3.11 and 3.12:

$$R_s = \frac{(N_1 \cos \theta_i - N_2 \cos \theta_t)}{(N_1 \cos \theta_i + N_2 \cos \theta_t)} \quad (3.11)$$

$$R_p = \frac{(N_2 \cos \theta_i - N_1 \cos \theta_t)}{(N_1 \cos \theta_t + N_2 \cos \theta_i)} \quad (3.12)$$

where N_1 and N_2 are the complex refractive index of the incident and transmitting material, respectively, and θ_i and θ_t the incidence and transmission angle. θ_t can be calculated from the incidence angle θ_i by Snell's law, as shown in Equation 3.13 [43,46]:

$$N_1 \sin \theta_i = N_2 \sin \theta_t \quad (3.13)$$

In general, SE is not able to directly determine the thickness or optical properties of a material by the experimentally obtained results. The data analysis of SE requires an optical model that approximates the layer structure of the sample and defines its optical constants and layer thicknesses. A Si layer is widely used as an underlying substrate and a thermal oxide layer, native SiO_2 as a top layer. A Cauchy model can be applied to determine the optical coefficients and thickness of the sample [47]. The Cauchy refractive index model with the assumption of no absorption is shown in Equation 3.14. By adjusting the model parameters (A , B , C , and layer thickness) to minimize the fitting error, the refractive index and film thickness of the specimen can be obtained.

$$n(\lambda) = A + \frac{B}{\lambda^2} + \frac{C}{\lambda^4} \quad (3.14)$$

where A , B , C are calculated fitting coefficients and λ is the wavelength.

In this study, the thickness of the MoO_3 and PEDOT:PSS films was determined by variable angle SE (M-2000 V, J.A. Woolam). The measurements were performed at three different angles (65° , 70° , and 75°) in the wavelength range of 200–1000 nm under the three-layer optical model, the Si substrate, the native SiO_2 layer (1.7 nm), and the film bulk layer were determined by the Cauchy function [10].

3.4.6. Profilometry

Profilometry is a technique utilized to determine the thickness and surface topographical features of the sample. There are two types of profiler, stylus and optical. Stylus is a contact mechanical profilometer which physically moves a probe along the sample surface to detect the surface features [48]. Figure 3.11 shows a schematic set up of a stylus profilometer. A diamond stylus moves vertically (Z) in contact with a sample and then moves laterally (X, Y) across the sample with specified constant contact force between tip and surface [49]. A feedback loop is utilized to maintain the arm with a specific amount of torque on it and keep the constant force between the sample and the probe [48]. The deflection of the stylus tip is detected by a displacement sensor, and then the surface variations as a function of position can be determined. The stylus profilometer can detect specimens with vertical features between 10 nm to 1 mm. The

resolution is controlled by the scan speed and data signal sampling rate [49]. However, this technique is sensitive and destructive to soft surfaces, and the probe can be contaminated by the specimen due to the direct contact between the tip and the sample surface. Optical profilometry is a non-contact technique, using the light source to replace a physical probe [48]. It improves the possibility to detect the surface in 3D dimension and prevents the damage of the sample.

In this thesis, the stylus profilometer, Dektak II Profilometer was applied to observe the thickness of polymer active layers.

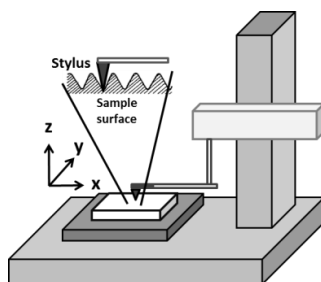


Figure 3.11 Schematic set up of a stylus profilometer.

3.4.7. X- ray powder diffraction (XRD)

XRD is a non-destructive analytical technique, utilized to determine the crystalline phases, crystal structure, and atomic spacing, chemical composition and physical properties of crystalline compounds for powders or thin film samples [50]. XRD works by hitting a focused monochromatic X-ray beam to the sample at varying incident angles. X-ray is filtered by foils or crystal monochromators to produce a monochromatic X-ray radiation which is collimated to a single direction before hitting the crystal sample. Copper is the most commonly used target material for the single crystal diffraction, with $\text{CuK}\alpha$ radiation = 1.5418\AA [51]. After the X-ray beam bombarding a sample at selected incident angles, diffraction occurs when the light is scattered by a periodic array with long-range order. At the specific wavelength and angle of the incident beam, the geometry of the X-ray system satisfies the Bragg law, as shown in Equation 3.15 [52], leading to constructive interference and intense peaks of reflected radiation. The diffraction is known as Bragg diffraction, as shown in Figure 3.12 [52] and the observed intense peaks are the Bragg peaks.

$$n\lambda = 2d\sin\theta \quad (3.15)$$

where d is the spacing between diffracting planes, θ the incident angle, n an integer, and λ the wavelength of the beam.

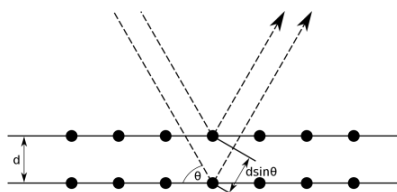


Figure 3.12 Schematic diagram of Bragg diffraction [52].

Figure 3.13 shows a schematic diagram of a diffractometer using the Bragg-Brentano geometry [53]. The diffraction vector (s) is normal to the sample surface and bisects the angle between the incident and scattered beam. The detector and the sample are both rotated so that the detector can collect the diffracted X-rays at 2ω as the incident X-ray beam hits the sample surface at the angle ω . This geometry gives a great combination of peak shape, intensity, and angular resolution for a wide variety of materials [53].

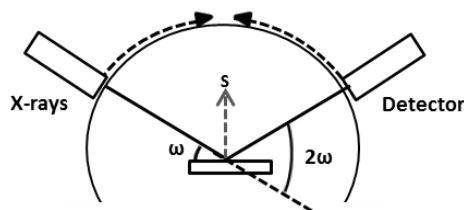


Figure 3.13 Schematic diagram of a diffractometer using the Bragg-Brentano geometry [53].

XRD works only on materials where the atoms are arranged in a periodic array in the crystal for the diffraction of light. X-Ray diffracts differently and produces different diffraction patterns with various crystal structures of the samples. By comparing the peak shapes and the intensities of the sample collected during XRD analysis with the standard reference patterns, the crystalline form of the specimens can be identified. In contrast, the amorphous materials such as glass do not have a periodic array with the long-range order so that they do not produce a diffraction patterns.

In this thesis, XRD was used to determine the identity of synthesized MoO_3 HTL materials. The XRD profiles were obtained on a Siemens D 501 diffractometer in Bragg–Brentano geometry using $\text{CuK}\alpha$ radiation ($\lambda = 1.54178 \text{ \AA}$) and a graphite monochromator at the secondary side. Data were fitted using EVA X-ray diffraction analysis software [10].

3.4.8. Raman spectrometers and microscopes

Raman spectroscopy is a nondestructive technique utilized for quantitation and chemical and structural identification of materials based on their molecular vibrations [54]. The vibrational modes of a molecule are relevant to the atomic mass of the atoms, the orientation of the atoms and bonds, the bond order and hydrogen bonding [55]. Each mode is triggered by a certain frequency, mostly in the infrared region of the spectrum. Raman spectroscopy relies on the inelastic scattering of monochromatic light upon interaction with a sample. Figure 3.14 illustrates a schematic diagram of a Raman analyzer and its basic principle. As a monochromatic light hits the sample, it scatters in all directions after the interaction with the molecules in the sample. Most of the scattered radiation has the same frequency (ν_0) as the incident light source, which is known as Rayleigh or elastic scattering. Only a small fraction of the scattered light (ca. 10^{-6} times the incident light intensity) has the frequency (ν_M) different from the frequency of the incident light, which is inelastic or Raman scattering. Raman scattered light is shifted to a higher or lower energy than the incident photon by the energies of molecular vibrations.

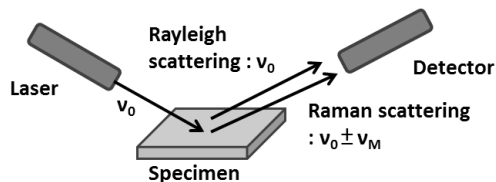


Figure 3.14 Schematic diagram of a Raman analyzer and its basic principle.

The higher or lower frequency of scattered light than incident light leads to Anti-Stokes or Stokes Raman scattering, respectively, as shown in Figure 3.15 Rayleigh scattering releases the same photon energy as incident light. Stokes scattering occurs when the molecule is excited from the ground state (E_0) by the incident photon and results in a molecule at a higher energy state ($E_0+h\nu_M$). Some incident photon energy is absorbed by the sample molecule to excite the molecule to a higher energy state, and the rest energy is emitted as a photon with reduced energy, which is known as Raman photon [55]. The energy of the Raman photon is equal to the difference between the incident light and the energy absorbed by the molecule. Anti-Stokes scattering occurs when a molecule in a vibrational state ($E_0+h\nu_M$) obtains the energy from the incident photon, decaying to a lower energy level, ground state (E_0), with the corresponding emission [55]. Hence, Anti-Stokes scattering is often used to detect fluorescing samples [56].

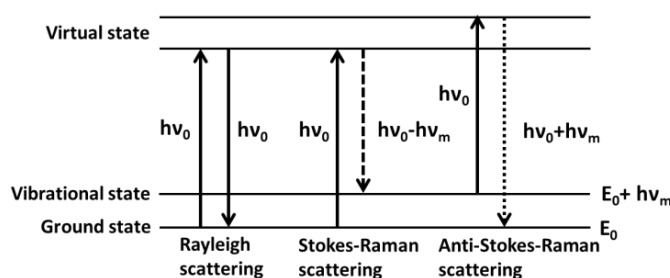


Figure 3.15 Energy transitions for Rayleigh and Raman Scattering of Raman Spectroscopy.

Figure 3.16 shows the schematic setup of Raman spectroscopy. A monochromatic laser beam shines on the sample, originating a scattered light after the incident light interacts with the molecules. The scattered light is filtered to remove the incident laser wavelength, and then the remaining light is focused on a dispersive spectroscopy to separate the different energies of light before it is collected by the detector.

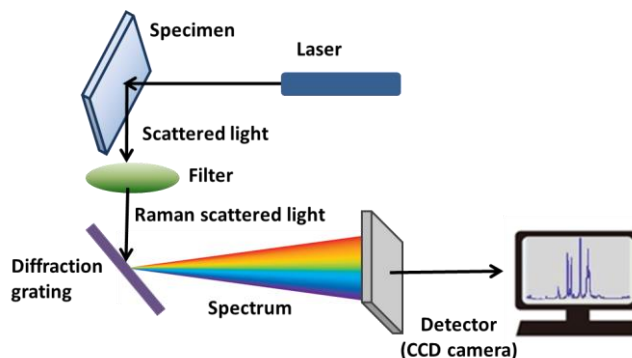


Figure 3.16 Schematic diagram of Raman spectroscopy.

The Raman microscope couples a standard optical microscopy with a Raman spectrometer [57]. Since traditional Raman spectroscopy allows only one spectrum measurement in one scan, the development of the Raman microscope has extended the ability of this technique to the spatial measurement of chemical compositions and structures over the whole specimen area or a 3D sample.

In this thesis, Raman measurements were performed with a Horiba Jobin Yvon LabRam 800 HR spectrometer equipped with a 1024 x 256 CCD (Peltier-cooled) and an Olympus BX41 microscope. All scans were performed using a laser wavelength of 532 nm (50 mW), an x50 Olympus LMPlanFLN (N.A. 0.5) objective and a 300 l/mm grating (spectral resolution of 3 cm^{-1}). Spatial Raman spectroscopy characteristics for point-to-point analysis were investigated along 100 μm scanning area with 2 μm step size for PEDOT:PSS, and with 4 μm for MoO₃-1 and MoO₃-2 [15].

3.4.9. Ultraviolet-visible (UV-Vis) spectroscopy

UV-vis spectroscopy is a technique based on the measurement of the absorption or transmission spectra of specimens in the wavelength range of UV-Vis spectral region to determine optical properties of the material. UV and visible radiation can interact with molecules, causing electronic transitions to promote the electrons from the ground energy state (E_0) to an excited energy state (E_1), as shown in Figure 3.17 [58].

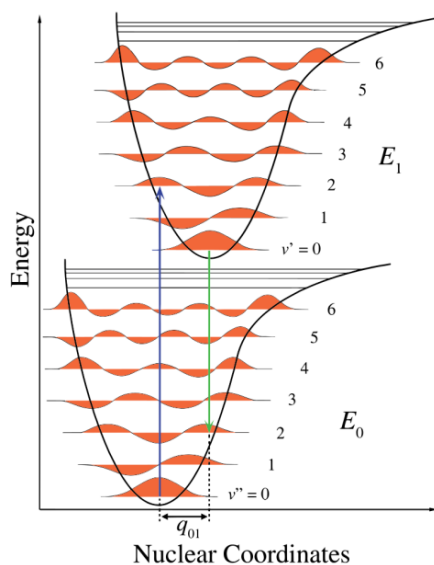


Figure 3.17 Schematic energy diagram based on Franck-Condon principle [58].

By measuring the spectrum of an unknown material, the molecule can be identified from the characteristic electronic transitions. In ordered molecule structures further transitions occur by vibronic coupling of the rings's C-C stretching and show in the absorption spectrum as a substructure in the absorption with characteristic distance, as shown in Figure 3.18 [58]. When the incident light is absorbed in the sample, the excess energy higher than the bandgap of the material leads to excitation to a higher vibrational energy level. The material with higher crystallinity shows stronger vibrational transitions for the measure of the structure of materials.

The increased crystallinity of a matter leads to a red-shift of the absorption spectrum due to the decreased band gap of the material. Thereby the peaks in the spectrum can depict the crystalline property of a matter.

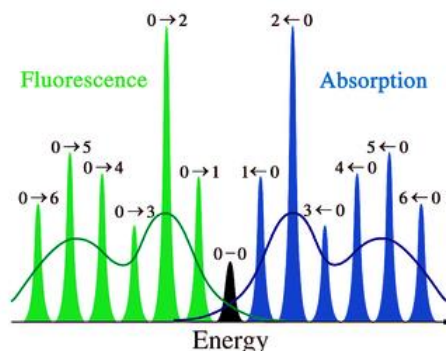


Figure 3.18 Schematic absorption and fluorescence spectra refer to different electronic transitions [58].

UV-Vis Spectroscopes are equipped with two light sources, usually a hydrogen lamp for the UV region and a tungsten lamp for the visible region, a holder for the sample, a diffraction grating monochromator, and a detector. Figure 3.19 shows a schematic diagram of a simple absorption spectrometer. The technique works by shining a monochromatic light on the sample and recording the transmitted light by a detector. The absorption for the given wavelength can be calculated from the value of the transmitted light.

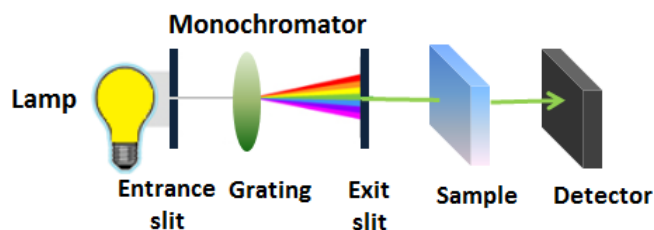


Figure 3.19 Schematic diagram of a simple absorption spectrometer.

Under the assumption of neglected reflection, the transmittance (T) of the sample is calculated by using the relationship in Equation 3.13.

$$T(\lambda) = \frac{I(\lambda)}{I_0(\lambda)} \quad (3.13)$$

where $T(\lambda)$ is the fraction of light transmitted at wavelength λ , $I_0(\lambda)$ the intensity of the incident light transmitted through the blank, and $I(\lambda)$ the intensity of the light transmitted through the sample.

The absorbance (A) of the sample can be calculated from the transmission, as shown in Equation 3.14:

$$A(\lambda) = -\log_{10} \left(\frac{I(\lambda)}{I_0(\lambda)} \right) = -\log_{10}(T(\lambda)) \quad (3.14)$$

The absorbance of a solution is commonly utilized to determine the concentration of an absorber

in the solution according to Beer-Lambert law [59], as seen in Equation 3.15:

$$A = -\log_{10} \left(\frac{I(\lambda)}{I_0(\lambda)} \right) = \epsilon l c \quad (3.15)$$

where ϵ is the molar absorptivity ($\text{L mol}^{-1}\text{cm}^{-1}$), l the sample path length (cm), c the concentration of the solution of the absorbing species (mol/L).

Since the absorption process can measure the energy difference between the ground state and the excited state of the atom or molecule as electromagnetic radiation is absorbed, the optical bandgap of the absorbing semiconductor can be roughly estimated from its absorption spectra. The most common and easy method to approximate the bandgap is the estimation by the onset wavelength of the absorption spectrum from the low energy side, as shown in Figure 3.20. By intersecting the two slopes in the spectrum, the onset wavelength is obtained. The energy value of the bandgap can be calculated from this onset wavelength (λ) by the Planck relation, as shown in Equation 3.16 or 3.17:

$$E(J) = \frac{hc}{\lambda(m)} \quad (3.16)$$

$$E(eV) = \frac{1239.84187 \text{ eV nm}}{\lambda(m)} \quad (3.17)$$

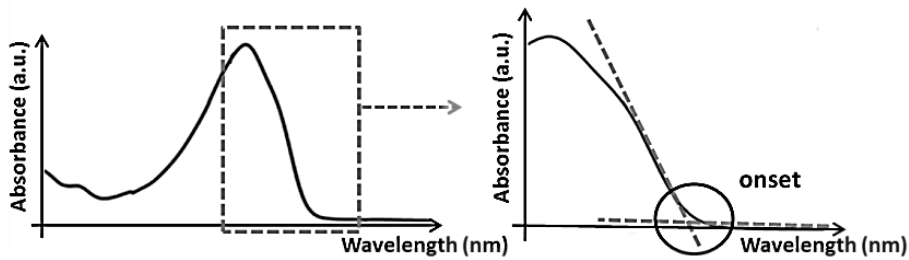


Figure 3.20 Method for bandgap approximation by the absorption spectrum.

In this work, the absorption and transmission spectra were recorded with the UV-VIS UV1800 spectrophotometer by Shimadzu. UV-Vis optical absorbance spectra of the P3HT:PCBM active layers were recorded between 300 and 800 nm, using a Shimadzu UV-1800 UV-Vis spectrophotometer [17].

3.4.10. Fluorescence

Fluorescence is a type of photoluminescence (PL), which describes the emission of light from a material after the absorption of electromagnetic radiation. Fluorescence occurs when an electron of a molecule returns to its electronic ground state from an excited state and loses its excess energy by emission of a photon [60]. It is complementary to the absorption spectroscopy since the fluorescence records the transitions from the excited state to the ground state but the absorption detects the transitions from the ground state to the excited state [56]. Figure 3.21 shows the Jablonski diagram displaying the energy states of a molecule relevant to the photon absorption and fluorescence emission.

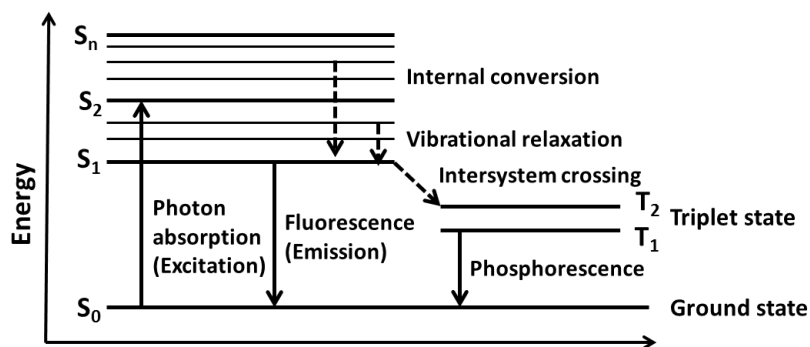


Figure 3.21 The Jablonski diagram displays the energy states of a molecule.

The Fluorescence process consists of the photon absorption by the fluorophore, the creation of an excited electronic singlet state (S_n'), partial energy dissipation due to the internal conversion or vibrational relaxation, and fluorescence emission from a relaxed singlet excited state (S_1) to the ground state (S_0) [61]. Between excitation and emission, not all the molecules excited by absorption return to the ground state via fluorescence emission due to some energy losses during the relaxation processes. Non-radiative relaxation may occur, leading to the dissipation of excitation energy as heat or fluorescence quenching through the interaction with another molecule, such as O_2 [62]. Excited molecules can also relax through conversion to a triplet state, which may consequently relax to the ground state by phosphorescence [62]. Owing to the energy dissipation within the lifetime of the excited state, the emitted light has a lower energy and longer wavelength than the absorbed radiation, which is known as the Stokes shift. Thereby the emission spectrum usually produces a red-shifted spectrum compared to the excitation spectrum, as shown in Figure 3.22 [63].

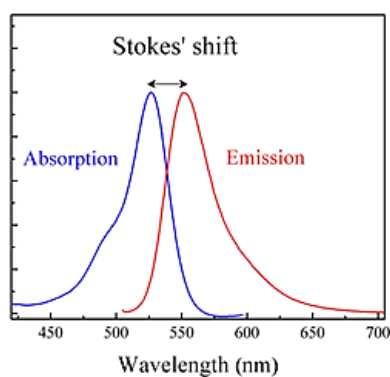


Figure 3.22 Schematic diagram of absorption and emission spectra of Rhodamine 6G [63].

The fluorescence quantum yield is utilized to determine the fluorescence efficiency. The quantum yield (Φ) is defined as the ratio of the number of fluorescence emitted photons by the sample (n_E) to the number of absorbed photons (n_A), as shown in Equation 3.18 [60]:

$$\Phi = \frac{n_E}{n_A} \quad (3.18)$$

In this study, Fluorescence is used to observe the effectiveness of the excited charge separation at the interface between donor and acceptor, leading to changes in the Fluorescence

spectrum of the active layer after exposing the OPV to different environmental conditions. Fluorescence spectra were acquired on a Fluorolog3 spectrofluorometer (Horiba Jobin Yvon) equipped with a near-infrared-sensitive photomultiplier R2658 from Hamamatsu (300–1050 nm). The excitation wavelength was 530 nm. The absolute luminescence quantum yields were determined using an integrating sphere from Horiba [17].

3.4.11. Illuminated and dark current density–voltage (J–V) characteristics

The most fundamental technique for evaluation of SC performance is the J-V characteristic of the device. The light J-V analysis process includes shining light on the device, sweeping the external voltage, often in the range -1 to +1V by a source meter across the electrodes and recording the photogenerated current. From the obtained light J-V curve, the SC parameters such as V_{oc} , J_{sc} , FF, PCE, R_{sh} , R_s can be calculated. For a reliable J-V characteristic, the measurement is required to be performed under standard test conditions (STCs). The standardized test allows the comparison of devices manufactured at different facilities. The STCs for SC testing are AM1.5 with the intensity of 100 mW/cm^2 and a cell temperature of $25 \text{ }^\circ\text{C}$ for the terrestrial cells and AM0 for space cells. A stable light source closely matching sunlight conditions is essential for the SC characterization. An ideal illumination source is determined according to its spectral performance, uniformity of irradiance and temporal stability [64]. There are three classes relevant to different elements required for an ideal solar simulator, where 'A' is the top rating an 'C' is the lowest rating, as shown in table 3.1.

| Class | Spectral Match | Irradiance inhomogeneity | Temporal Instability | |
|-------|----------------|--------------------------|----------------------|--------------|
| | | | Long Term | Short Term |
| A | 0.75 – 1.25% | $\leq 2 \%$ | $\leq 0.5 \%$ | $\leq 2 \%$ |
| B | 0.6 – 1.4 % | $\leq 5 \%$ | $\leq 2 \%$ | $\leq 5 \%$ |
| C | 0.4 – 2.0 % | $\leq 10 \%$ | $\leq 10 \%$ | $\leq 10 \%$ |

Table 3.1: Solar simulator classification according to IEC 60904-9 Ed. 2.0.

For instance, a simulator with the designation ABB would have a spectral match $< 1.25\%$, an inhomogeneity of 2-5%, and a stability $< 2\%$ in the long term and $< 5\%$ in the short term test.

Dark J-V characteristics provide valuable information of diode properties. Dark current under forward bias can estimate the origins of the current and different recombination mechanisms [65]. The linear plot of the dark J-V curve does not provide much information. However as it is plotted in the semi-log, the curve provides the crucial information about different current transport mechanisms within the device. Figure 3.23 show the typical J-V curve with a linear and semi-log scale plot of a SC [66]. The entire forward bias J-V plot can be distinguished into three voltage regimes. At the low voltages region (Regime I), the shunt region, the J-V characteristics are primarily determined by the shunt resistance (R_{sh}), which accounts for leakage or shunt currents. The intermediate voltage region (Regime II) is an exponential region, where current is proportional to $\exp(eV/nk_B T)$ corresponding to Equation 2.10. This region is significantly

influenced by the diode ideal factor, n (usually between 1 and 2), which is relevant to the presence of recombination currents within the device. At high voltage region (Regime III), where the current is saturated from its exponential, is mainly affected by the series resistance (R_s) [67-68].

In the thesis, this method was widely used to check the device performance of SCs. The illuminated J-V characteristics of the SCs were measured in an Ar-filled glovebox using a computer-controlled Keithley 2636 A source meter under AM1.5 G illumination (100 mW/cm^2) from a solar simulator (Model 10,500, ABET Technologies, rated ABB) [10,15,17].

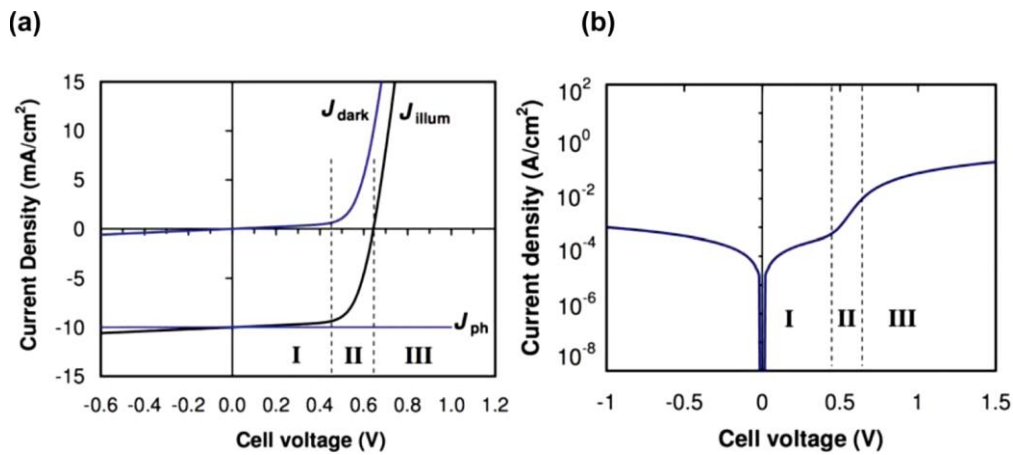


Figure 3.23 Typical J-V curve (a) with a linear and (b) with semi-log scale plot for an organic solar cell. [66].

3.4.12. Dark injection space-charge-limited current (DI-SCLC)

DI-SCLC is the simplest method used to determine charge carrier mobility of semiconductors in electronic devices [69-70]. The DI-SCLC describes the behavior from the relationship between applied voltages and collected currents in the device. To determine the hole-mobility in the active layer of OPV with the DI-SCLC method, the active layer is usually sandwiched between cathode and anode with high work functions, to avoid injection of electrons. By analysis of the obtained dark J-V curve, the hole mobility in the active layer of the device can be calculated. Moreover, this DI-SCLC can also be used on devices with standard electrodes, under the assumption that the much higher barrier for injection of electrons into the acceptor LUMO from the cathode compared to the injection of holes into the donor HOMO from the anode, thereby these devices will be hole-dominated under forward bias [71]. This technique gives a reliable estimation of the mobility of the major charge carrier within the active layer. Therefore, the fitted mobility can be used as a measure for the hole mobility in the active layer [71]. Figure 3.24 shows the J-V characteristics of a CP diode in (a) ideal mode without traps, (b) real mode with traps in the device [69-70]. The J-V characteristic of an ideal diode mode shows only two regions, one is the ohmic region and the other is the space charge region. At lower voltages, or ohmic regime, the number of injected charge carriers is smaller than the number of resident charge carriers, and the device performs an ohmic behavior. The current is mainly driven by the charge carriers primarily present in the polymer so that the current is proportional to the

applied voltage, as shown in Equation 3.19:

$$J = ne\mu E = ne\mu \frac{V}{L} \quad (3.19)$$

where J is current density, n the thermal generated carrier concentration, e the elementary charge of the electron, μ the mobility of a charged particle, E the applied electric field, V the applied voltage and L the film thickness.

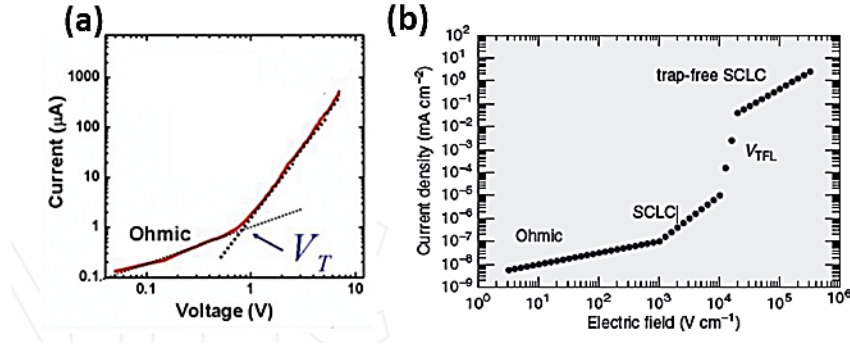


Figure 3.24 Space charge–limited current as a function of bias for an organic semiconductor in (a) ideal mode without traps (b) real mode with traps in the devices [69-70].

As the applied voltage increases to a specific voltage or threshold voltage (V_T), the injected charge carriers are equivalent to the resident charge carriers. From the V_T , the obtained current deviates differently from its original linear path. SCLC occurs when the concentration of the injected charge carriers is larger than the equilibrium charge carriers concentration in a semiconductor so that the current is mainly affected by the applied bias. The pure SCLC without any traps was first given by the Mott Gurney law, as shown in Equation 3.20 [72]:

$$J = \frac{9}{8} \epsilon \epsilon_0 \frac{V^2}{L^3} \quad (3.20)$$

where μ is the free carrier mobility, ϵ the dielectric constant of the material, ϵ_0 the dielectric constant in vacuum, V the applied voltage and L the distance between the electrodes.

However, the SCLC is strongly dependent on the charge traps. The SCLC incorporated with the Poole-Frenkel equation is further modified by Murgatroyd to address the lowering of trap the barrier height, given in Equation 3.21 [73]:

$$J = \frac{9}{8} \epsilon \mu_0 e^{0.891\gamma} \sqrt{\frac{V_{int}}{L}} \frac{V_{int}^2}{L^3} \quad (3.21)$$

where μ_0 is the zero-field mobility, γ is the field activation parameter, ϵ is the permittivity, V_{int} is the internal voltage, and L is the film thickness. In the SCLC region, the current quadratically changes with the applied voltage ($J \propto V^2$). The current is only relevant to the mobility of the polymer without the influence of generated charge carriers. Hence, the mobility can be estimated from this simple J-V curve. Figure 3.25(b) shows the SCLC of OPV with the traps. An intermediate region is observed between the trap-SCLC region and trapped free space charge region, known as trap-filled-limit (TFL) region. The charge transport of the polymer within this region is controlled by the trapping and de-trapping of carriers at both energetic and positional distribution [69]. The

nearly vertical rising current in TFL region is corresponding to the filling of traps by the injected carriers from the applied bias. As the applied voltage is higher than the average energy associated with traps density, then the polymer behaves trap-free SCLC [69]. The density of defects or trap states can be approximated by the onset of trap-free limit voltage V_{TFL} .

In this study, charge mobility of the devices was extracted by modeling the dark current under forward bias using the space-charge-limited expression for the current density [17].

3.4.13. External quantum efficiency (EQE)

Quantum Efficiency (QE) or spectral response gives information about current generation, recombination and collection in the SC. Spectral response is defined as the ratio of the current output from the SC to the power input of light on the device. The QE is determined by the number of charge carriers generated by the SC to the number of incident photons on the device. In general, QE and spectral response are two similar techniques but in different units. The QE of the device can be calculated from its spectral response. This relation between spectral response $S(\lambda)$ and $QE(\lambda)$ is shown in Equation 3.22 [74]:

$$S(\lambda) = \frac{e\lambda}{hc} QE(\lambda) \quad (3.22)$$

where e is the elementary charge, h the Planck's constant, and c the speed of light, $S(\lambda)$ in units of AW^{-1} and the $QE(\lambda)$ in units of %.

There are two types of QE: EQE and IQE. The definition of EQE and IQE has been discussed in the previous chapter 2.4. Figure 3.25 shows a simplified EQE setup. The working process of EQE includes shining a monochromatic light on a SC, detecting the number of photons of incident light by a reference photodiode and recording the number of generated electron carriers in the device.

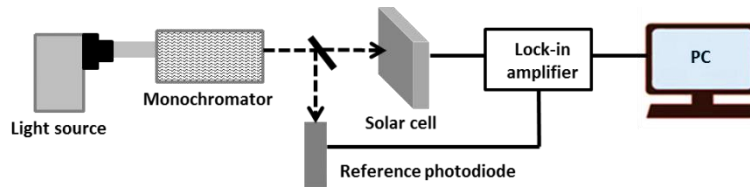


Figure 3.25 Schematic of an EQE set up.

By shining different wavelengths of light to the device, the entire curve of the relative current as a function of wavelength can then be established. The total area under the curve is equal to the total number of carriers generated by the device under the full spectrum of white light illumination. The integration of the spectra can obtain the electrical current density of the SC under the given incident light intensity. Thereby, J_{SC} can be calculated by the EQE spectra according to Equation 3.23:

$$J_{SC} = e \int EQE(\lambda) \Phi(\lambda) d\lambda \quad (3.23)$$

where e is the elementary charge of the electron and ϕ the photon flux at a given wavelength. Differing from the EQE, IQE records only the absorbed light with the exclusion of photon transmission through or reflection from the cell and absorption by the other layers.

The spectral response of studied devices was recorded from EQE for wavelengths from 375 to 900 nm, using a 250 W white light source (tungsten halogen) with a monochromator, with a computer-controlled Keithley 2636 A source meter and a calibrated Si photodiode [10].

3.4.14. Light-beam induced current (LBIC) microscopy

LBIC is a fast and easy technique for spatial characterization of the electronic properties of the SCs, which allows the identification and localization of defects on the devices [75]. It has also been widely used to study degradation effects of SCs. Figure 3.26 shows the schematic of a LBIC measurement setup. The device is positioned on a computer controlled x-y stage, and a focused beam of light, typically a laser, point by point scans over the pixel area of the SC while recording the photogenerated current under the short circuit condition. The obtained result provides the lateral distribution of photocurrent of the device in two-dimensional (X,Y) mapping. For the analysis, the obtained photocurrent map is commonly normalized to the maximized photocurrent within the device for the presentation of a better contrast variation in the LBIC image to determine the local failure and functionality of the SC. The image resolution and accuracy of the LBIC image is tunable depending on the beam-diameter of the focused laser and the scanning step distance, which can differ from several hundred μm to 1 μm or lower.

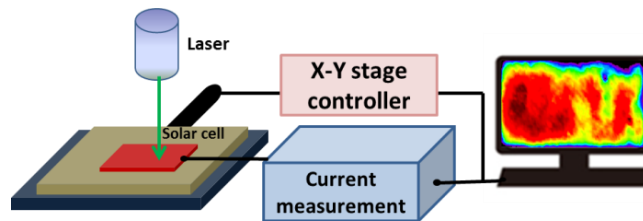


Figure 3.26 Schematic of a light-beam induced current measurement setup.

In this thesis, spatial photocurrent distribution was investigated by the LBIC technique, scanning with a computer-controlled nanomanipulator-driven XY-stage (NanoControl NC-2-3; Kleindiek Nanotechnik), and with excitation from the glass/ ITO side with a 532 nm laser (<5 mW) with a focused spot-size of $\approx 2\mu\text{m}$. For spatial photocurrent mapping, local short circuit current was scanned with a 40 μm step size across the entire photoactive pixel area of 4.0 mm \times 1.5 mm. A custom-made LabView computer program drove the stages and collected the data [10,15,17].

3.4.15. Transient photocurrent (TPC) measurement

The TPC technique is utilized to investigate the charge carrier dynamics such as charge extraction and recombination of the SC. [76-77]. This technique also reveals trapping and detrapping of the photogenerated charges, which affect carrier mobilities and lifetimes in the active layer, and the quality of contact between different layers in the device [78-79]. Figure 3.27 shows the simplified experimental setup of TPC via a pulsed light source. TPC analysis works by applying a short pulse from a LED or laser light source to the device surface for the active layer

excitation. After the excitation, the signal of photocurrent response is recorded and analyzed by an oscilloscope in form of the voltage across a low resistance resistor. The signal is recorded slightly after the light switching on and off and during the light illumination period. Figure 3.28 shows a schematic diagram of normalized TPC response. After the excitation pulse is switched on, the build-up of charges in the device can be observed. The initial current overshoot or spike at the start of the square laser pulse represents the presence of the build-up charges or trap-facilitated recombination in the device [78]. As the light pulse is switched off, the current describes the behavior of charge decay. A tail in the transient gives a hint about the presence of build-up charges or charge carrier recombination in the devices. The rise (t_{90}) and fall times (t_{10}) of the device are defined as the required time to rise the photocurrent to 90% of the steady current response and to fall to 10% of the steady current response, respectively, revealing the charge transport efficiency of the SC (see Figure 3.28). By integrating the area under the TPC curve, the extracted charge carrier density created by the light pulse can be obtained. In general, a TPC setup measures the photocurrent response close to the short-circuit condition. By biasing the external voltage across the forward and reverse bias region to the device with the TPC technique, allows the observation of voltage-dependent charge accumulation, recombination, and transport dynamics.

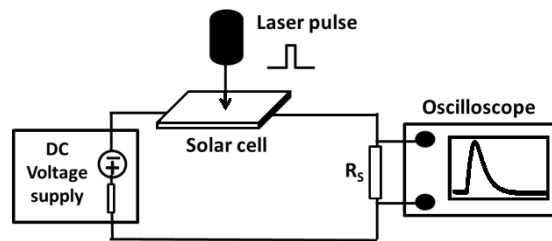


Figure 3.27 Simplified experimental setup of a photo-induced transient photocurrent.

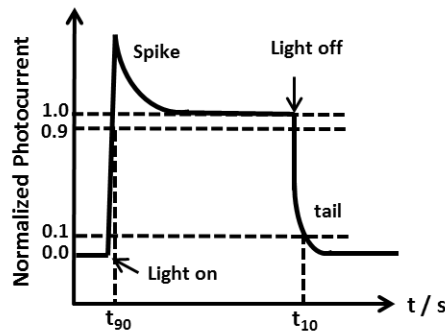


Figure 3.28 Schematic diagram of normalized transient photocurrent response.

In this thesis, a 530 nm green LED (Thorlabs, M530L2) was utilized as the light source and a 300 μ s square pulse from a function generator (HAMEG HMF 2550) at 1 kHz was used to power the LED. The photocurrent of the devices was measured by an oscilloscope (HAMEG HMO 3002 Series) with an input impedance of 50 Ω . For voltage-dependent photocurrent transients, devices were connected to a computer-controlled Keithley 2636A source meter operating in DC mode [15].

3.5 References

- [1] Brinker, C. J.; Scherer, G. W., Eds. *Sol-gel science: The Physics and Chemistry of Sol-Gel Processing*; Academic Press: Boston, 1990.
- [2] Fu, Q.; Chen, J.; Shi, C.; Ma, D. Room-Temperature Sol-Gel Derived Molybdenum Oxide Thin Films for Efficient and Stable Solution-Processed Organic Light-Emitting Diodes. *ACS applied materials & interfaces* **2013**, *5*, 6024–6029.
- [3] Sun, Y.; Seo, J. H.; Takacs, C. J.; Seifert, J.; Heeger, A. J. Inverted Polymer Solar Cells Integrated with a Low-Temperature-Annealed Sol-Gel-Derived ZnO Film as an Electron Transport Layer. *Advanced materials (Deerfield Beach, Fla.)* **2011**, *23*, 1679–1683.
- [4] Brinker C. J.; Hurd A. J.; Schunk P. R.; Ashely C. S.; Cairncross R. A.; Samuel J.; Chen K. S.; Scotto C.; Schwartz R. A.. *Metallurgical and Ceramic Protective Coatings*; Stern, K. H., Ed.; Springer Netherlands: Dordrecht, 1996.
- [5] Lévy, D.; Zayat, M., Eds. *The Sol-Gel Handbook: Synthesis, Characterization and Applications*; Wiley-VCH: Weinheim, 2015.
- [6] Danks, A. E.; Hall, S. R.; Schnepf, Z. The Evolution of ‘Sol–Gel’ Chemistry as a Technique for Materials Synthesis. *Mater. Horiz.* **2016**, *3*, 91–112.
- [7] Attia, S.M.; WANG, J.; WU, G.; SHEN, J.; MA, J. Review on Sol-Gel Derived Coatings: Process, Techniques and Optical Applications. *J Mater Sci Technol*, **2002**, *18(03)*, 211-217.
- [8] Melde, B. J.; Johnson, B. J.; Charles, P. T. Mesoporous Silicate Materials in Sensing. *Sensors* **2008**, *8*, 5202–5228.
- [9] Zilberberg, K.; Gharbi, H.; Behrendt, A.; Trost, S.; Riedl, T. Low-Temperature, Solution-Processed MoO_x for Efficient and Stable Organic Solar Cells. *ACS applied materials & interfaces* **2012**, *4*, 1164–1168.
- [10] Chien, H.-T.; Pözl, M.; Koller, G.; Challinger, S.; Fairbairn, C.; Baikie, I.; Kratzer, M.; Teichert, C.; Friedel, B. Effects of Hole-Transport Layer Homogeneity in Organic Solar Cells – A Multi-Length Scale Study. *Surfaces and Interfaces* **2017**, *6*, 72–80.
- [11] Dong, X.; Liu, J.; Yan, J.; Wang, J.; Hong, G. Study of Preparation and Photo Chromism of MoO₃ Nanoparticles Hydrosol, *Rare Met. Mater. Eng.* **2005**, *34*, 421–424.
- [12] Liu, F.; Shao, S.; Guo, X.; Zhao, Y.; Xie, Z. Efficient Polymer Photovoltaic Cells Using Solution-Processed MoO₃ as Anode Buffer Layer. *Solar Energy Materials and Solar Cells* **2010**, *94*, 842–845.
- [13] Schlaf, R.; Murata, H.; Kafafi, Z. Work Function Measurements on Indium Tin Oxide Films. *Journal of Electron Spectroscopy and Related Phenomena* **2001**, *120*, 149–154.
- [14] Bermudez, V. M.; Berry, A. D.; Kim, H.; Piqué, A. Functionalization of Indium Tin Oxide. *Langmuir: the ACS journal of surfaces and colloids* **2006**, *22*, 11113–11125.
- [15] Chien, H.-T.; Pilat F.; Griesser T.; Fitzek H.; Poelt P.; Friedel B.; Influence of Environmentally Affected Hole Transport Layers on Spatial Homogeneity and Charge Transport Dynamics of Organic Solar Cells. (under revision in *ACS Appl. Mater. Interfaces*)
- [16] Kim, Y.; Cook, S.; Tuladhar, S. M.; Choulis, S. A.; Nelson, J.; Durrant, J. R.; Bradley, D. D. C.; Giles, M.; McCulloch, I.; Ha, C.-S.; Ree M. A Strong Regioregularity Effect in Self-Organizing Conjugated Polymer Films and High-Efficiency Polythiophene: Fullerene Solar Cells. *Nature Mater* **2006**, *5*, 197–203.

- [17] Chien, H.-T.; Zach, P. W.; Friedel, B. Short-Term Environmental Effects and Their Influence on Spatial Homogeneity of Organic Solar Cell Functionality. *ACS applied materials & interfaces* **2017**, *9*, 27754–27764.
- [18] Binnig; Quate; Gerber. Atomic Force Microscope. *Physical review letters* **1986**, *56*, 930–933.
- [19] Ducker, W. A.; Senden, T. J.; Pashley, R. M. Direct Measurement of Colloidal Forces Using an Atomic Force Microscope. *Nature* **1991**, *353*, 239–241.
- [20] Schulz, M. J.; Shanov, V. N.; Yun, Y., Eds. *Nanomedicine Design of Particles, Sensors, Motors, Implants, Robots, and Devices*; Engineering in medicine & biology; Artech House: Boston, Mass., 2009.
- [21] Molhave K. Open Source Handbook of Nanoscience and Nanotechnology. (accessed 20/02/2018). URI:https://commons.wikimedia.org/wiki/File:AFM_contact_ICM_and_NCM.jpg.
- [22] Collins, D. Scanning Tunneling Microscopy and Atomic Force Microscopy. (accessed 20/02/2018). URI: <http://slideplayer.com/slide/6856881/>.
- [23] Mukherjee, R.; Chaudhury, K.; Das, S.; Sengupta, S.; Biswas, P. Posterior Capsular Opacification and Intraocular Lens Surface Micro-Roughness Characteristics: An Atomic Force Microscopy Study. *Micron* **2012**, *43*, 937–947.
- [24] AFM Different Mode Definition, (accessed 20/02/2018). URI:<http://www.chembio.uoguelph.ca/educmat/chm729/afm/details.htm>.
- [25] Kozlova, E. K.; Chernysh, A. M.; Moroz, V. V.; Kuzovlev, A. N. Analysis of Nanostructure of Red Blood Cells Membranes by Space Fourier Transform of AFM Images. *Micron* **2013**, *44*, 218–227.
- [26] Nonnenmacher, M.; O'Boyle, M. P.; Wickramasinghe, H. K. Kelvin Probe Force Microscopy. *Appl. Phys. Lett.* **1991**, *58*, 2921–2923.
- [27] Melitz, W.; Shen, J.; Kummel, A. C.; Lee, S. Kelvin Probe Force Microscopy and its Application. *Surface Science Reports* **2011**, *66*, 1–27.
- [28] Sadewasser, S.; Jelinek, P.; Fang, C.-K.; Custance, O.; Yamada, Y.; Sugimoto, Y.; Abe, M.; Morita, S. New Insights on Atomic-Resolution Frequency-Modulation Kelvin-Probe Force-Microscopy Imaging of Semiconductors. *Physical review letters* **2009**, *103*, 266103.
- [29] Tanimoto, M. Kelvin Probe Force Microscopy for Characterization of Semiconductor Devices and Processes. *J. Vac. Sci. Technol. B* **1996**, *14*, 1547.
- [30] Leung, C.; Maradan, D.; Kramer, A.; Howorka, S.; Mesquida, P.; Hoogenboom, B. W. Improved Kelvin Probe Force Microscopy for Imaging Individual DNA Molecules on Insulating Surfaces. *Appl. Phys. Lett.* **2010**, *97*, 203703.
- [31] Li, C.; Minne, S.; Hu, Y.; Ma, J.; He, J.; Mittel, H.; Kelly, V.; Erina, N.; Guo, S.; Mueller, T. PeakForce Kelvin Probe Force Microscopy, Bruker Nano Surfaces Division, 2013. (accessed 20/02/2018). URI:https://www.nanowerk.com/nanocatalog/productimages/1493676404AN140-RevA1-PeakForce_KPFM-AppNote.pdf.
- [32] Takihara, M. Kelvin Probe Force Microscopy (KFM). (accessed 20/02/2018). URI: http://www.spm.iis.u-tokyo.ac.jp/takihara/Kelvin%20probe%20force%20microscopy_e.html.
- [33] Photoemission Spectroscopy. (accessed 20/02/2018). URI:https://en.wikipedia.org/wiki/Photoemission_spectroscopy.
- [34] Nalwa, H. S., Ed. *Handbook of Surfaces and Interfaces of Materials: Five-Volume Set*; Elsevier: Burlington, 2001.
- [35] Takayama, A., Ed. *High-Resolution Spin-Resolved Photoemission Spectrometer and the Rashba*

Effect in Bismuth Thin Films; Springer Theses; Springer Japan: Tokyo, 2015.

[36] Castle, J. E. Practical Surface Analysis by Auger and X-ray Photoelectron Spectroscopy. Briggs, D. and Seah, M. P., Eds. John Wiley and Sons Ltd, Chichester, 1983, 533 pp. *Surf. Interface Anal.* **1984**, *6*, 302.

[37] AUGUSTINE, B. Efficiency and Stability Studies for Organic Bulk Heterojunction Solar Cells, PhD Dissertation, 2016. (accessed 20/02/2018). URI:<http://jultika.oulu.fi/files/isbn9789526214436.pdf>.

[38] Baikie, I. D.; Grain, A. C.; Sutherland, J.; Law, J. Ambient Pressure Photoemission Spectroscopy of Metal Surfaces. *Applied Surface Science* **2014**, *323*, 45–53.

[39] KP Technology Ltd, APS Technique. (accessed 21/02/2018). URI:http://www.kelvinprobe.com/products_info.php?ind=1.

[40] Fowler, R. H. The Analysis of Photoelectric Sensitivity Curves for Clean Metals at Various Temperatures. *Phys. Rev.* **1931**, *38*, 45–56.

[41] Baikie, I. D.; Grain, A.; Sutherland, J.; Law, J. Near Ambient Pressure Photoemission Spectroscopy of Metal and Semiconductor Surfaces. *Phys. Status Solidi C* **2015**, *12*, 259–262.

[42] Tompkins, H. G.; and Irene, E. A. Eds. *Handbook of Ellipsometry*; William Andrew: New York, 2005.

[43] Fujiwara, H., Ed. *Spectroscopic Ellipsometry: Principles and Applications*; John Wiley: Chichester, 2007.

[44] Polarization by Reflection, Brewster's Angle Definition, (accessed 21/02/2018). URI:http://physics.bu.edu/~duffy/semester2/c27_brewster.html.

[45] Azzam, R. M. A.; Bashara, N. M. *Ellipsometry and polarized light*; North-Holland: Amsterdam, Oxford, 1977.

[46] Hecht, E. *Optics*; Addison-Wesley: Reading Mass., 2002.

[47] Langereis, E.; Heil, S. B. S.; van de Sanden, M. C. M.; Kessels, W. M. M. In Situ Spectroscopic Ellipsometry Study on the Growth of Ultrathin TiN Films by Plasma-Assisted Atomic Layer Deposition. *Journal of Applied Physics* **2006**, *100*, 23534.

[48] Nanoscience Instruments. Optical Profilometry. (accessed 21/02/2018). URI:<http://www.nanoscience.com/technology/optical-profiler-technology/how-profilometer-works/>.

[49] Profilometer. (accessed 21/02/2018). URI: <https://en.wikipedia.org/wiki/Profilometer>.

[50] X-ray Scattering Techniques. (accessed 21/02/2018). URI:https://en.wikipedia.org/wiki/X-ray_scattering_techniques.

[51] X-ray Powder Diffraction. (accessed 21/02/2018). URI:https://serc.carleton.edu/research_education/geochemsheets/techniques/XRD.html.

[52] Bragg's Law. (accessed 21/02/2018). URI: https://en.wikipedia.org/wiki/Bragg%27s_law.

[53] Speakman, S. A. Basics of X-Ray Powder Diffraction, (accessed 21/02/2018). URI:<http://prism.mit.edu/xray/oldsite/1%20Basics%20of%20X-Ray%20Powder%20Diffraction.pdf>.

[54] Chalmers, J. M.; Edwards, H. G. M.; Hargreaves, M. D. *Infrared and Raman Spectroscopy in Forensic Science*; John Wiley & Sons, Ltd: Chichester, UK, 2012.

[55] Raman Spectroscopy. (accessed 21/02/2018). URI:<https://www.sas.upenn.edu/~crulli/RamanBasics.html>.

[56] Skoog, D. A.; Holler, F. J.; Crouch, S. R., Eds. *Principles of Instrumental Analysis*; Brooks/Cole, Cengage Learning, 2007.

- [57] Andersen, M. E.; Muggli, R. Z. Microscopical Techniques in the Use of the Molecular Optics Laser Examiner Raman Microprobe. *Anal. Chem.* **2002**, *53*, 1772–1777.
- [58] Franck–Condon Principle. (accessed 21/02/2018). URI: https://en.wikipedia.org/wiki/Franck%E2%80%93Condon_principle
- [59] Swinehart, D. F. The Beer-Lambert Law. *J. Chem. Educ.* **1962**, *39*, 333.
- [60] Lakowicz, J. R. *Principles of fluorescence spectroscopy*; Springer: New York, 2006.
- [61] Thermo Fisher Scientific Inc, Fluorescence Fundamentals. (accessed 21/02/2018). URI: <https://www.thermofisher.com/at/en/home/references/molecular-probes-the-handbook/introduction-to-fluorescence-techniques.html>.
- [62] Fluorescence. (accessed 21/02/2018). URI: <https://en.wikipedia.org/wiki/Fluorescence>.
- [63] Stokes shift. (accessed 21/02/2018). URI: https://en.wikipedia.org/wiki/Stokes_shift.
- [64] Emery, K.; Myers, D.; Rummel, S. Solar Simulation-Problems and Solutions, *Conference Record of the Twentieth IEEE Photovoltaic Specialists Conference*; IEEE, 1988, 1087-1091.
- [65] Shockley, W.; Queisser, H. J. Detailed Balance Limit of Efficiency of p-n Junction Solar Cells. *Journal of Applied Physics* **1961**, *32*, 510–519.
- [66] Servaites, J. D.; Ratner, M. A.; Marks, T. J. Organic solar cells: A new look at traditional models. *Energy Environ. Sci.* **2011**, *4*, 4410.
- [67] Streetman, B. G.; Banerjee, S. *Solid State Electronic Devices*; Pearson: Boston, 2015.
- [68] Street, R. A.; Schoendorf, M.; Roy, A.; Lee, J. H. Interface State Recombination in Organic Solar Cells. *Phys. Rev. B* **2010**, *81*, 205307.
- [69] Moiz, S. A.; Khan, I. A.; Younis, W. A.; Karimov, K. S. Space Charge–Limited Current Model for Polymers, *Conducting Polymers*; Yilmaz, F., Ed.; InTech, 2016.
- [70] Stallinga, P., Ed. *Electrical Characterization of Organic Electronic Materials and Devices*; John Wiley & Sons, Ltd: Chichester, UK, 2009.
- [71] Friedel, B.; McNeill, C. R.; Greenham, N. C. Influence of Alkyl Side-Chain Length on the Performance of Poly(3-alkylthiophene)/Polyfluorene All-Polymer Solar Cells. *Chem. Mater.* **2010**, *22*, 3389–3398.
- [72] Lampert, M. A. Simplified Theory of Space-Charge-Limited Currents in an Insulator with Traps. *Phys. Rev.* **1956**, *103*, 1648–1656.
- [73] Murgatroyd, P. N. Theory of Space-Charge-Limited Current Enhanced by Frenkel Effect. *J. Phys. D: Appl. Phys.* **1970**, *3*, 151–156.
- [74] Shrotriya, V.; Li, G.; Yao, Y.; Moriarty, T.; Emery, K.; Yang, Y. Accurate Measurement and Characterization of Organic Solar Cells. *Adv. Funct. Mater.* **2006**, *16*, 2016–2023.
- [75] Kroon, J. M.; Wienk, M. M.; Verhees, W.; Hummelen, J. C. Accurate Efficiency Determination and Stability Studies of Conjugated Polymer/Fullerene Solar Cells. *Thin Solid Films* **2002**, *403-404*, 223–228.
- [76] Pivrikas, A.; Sariciftci, N. S.; Juška, G.; Österbacka, R. A Review of Charge Transport and Recombination in Polymer/Fullerene Organic Solar Cells. *Prog. Photovolt: Res. Appl.* **2007**, *15*, 677–696.
- [77] McNeill, C. R.; Hwang, I.; Greenham, N. C. Photocurrent Transients in All-Polymer Solar Cells: Trapping and detrapping effects. *Journal of Applied Physics* **2009**, *106*, 24507.
- [78] Hwang, I.; McNeill, C. R.; Greenham, N. C. Drift-Diffusion Modeling of Photocurrent Transients in Bulk Heterojunction Solar Cells. *Journal of Applied Physics* **2009**, *106*, 94506.
- [79] C. Main. In Amorphous and Microcrystalline Silicon Technology-1997, Proceedings of MRS

symposium A; Hack, M.; Schiff, E. A.; Wagner, S.; Matsuda, A.; Schropp, R., Eds., MRS, Warrendale, PA, 1997; vol. 467, p. 167 (Ch. 143).

Results and Publications

4.1. Effects of Hole-Transport Layer Homogeneity in Organic Solar Cells—A Multi-Length Scale Study. *Surfaces and Interfaces*

Huei-Ting Chien, Markus Pölzl, Georg Koller, Susanna Challinger, Callum Fairbairn, Iain Baikie, Markus Kratzer, Christian Teichert, Bettina Friedel
Surfaces and Interfaces, 2017, 6, 72

4.2. Influence of Environmentally Affected Hole Transport Layers on Spatial Homogeneity and Charge Transport Dynamics of Organic Solar Cells.

Huei-Ting Chien, Florian Pilat, Thomas Griesser, Harald Fitzek, Peter Poelt, Bettina Friedel,
(accepted in *ACS Appl. Mater. Interfaces*)

4.3. Short-Term Environmental Effects and Their Influence on Spatial Homogeneity of Organic Solar Cell Functionality.

Huei-Ting Chien, Peter W. Zach, Bettina Friedel
ACS Appl. Mater. Interfaces, 2017, 9, 27754

4.1. Effects of Hole-Transport Layer Homogeneity in Organic Solar Cells—A Multi-Length Scale Study. Surfaces and Interfaces

Huei-Ting Chien, Markus Pölzl, Georg Koller, Susanna Challinger, Callum Fairbairn, Iain Baikie, Markus Kratzer, Christian Teichert, Bettina Friedel

Author Contributions

The author defined the research plan, executed the experiments, prepared the samples for HTL characterization, fabricated the SCs and measured the device physics. Markus Pölzl did the Labview programming for the LBIC measurement setup. The XPS measurements were done by Georg Koller. The absolute work function results and surface CPD distribution maps of complete SC pixel areas were carried out by Susanna Challinger, Callum Fairbairn, and Iain Baikie. The AFM and local contact potential difference maps of $3\ \mu\text{m} \times 3\ \mu\text{m}$ areas were measured by Markus Kratzer and Christian Teichert. The author did the literature review, analyzed the results and wrote the manuscript. The work was supervised by Bettina Friedel.



Effects of hole-transport layer homogeneity in organic solar cells – A multi-length scale study



Huei-Ting Chien^a, Markus Pölzl^a, Georg Koller^b, Susanna Challinger^c, Callum Fairbairn^c, Iain Baikie^c, Markus Kratzer^d, Christian Teichert^d, Bettina Friedel^{a,*}

^aInstitute of Solid State Physics, Graz University of Technology, Austria

^bInstitute of Experimental Physics, Graz University, Austria

^cKP Technology Ltd., Scotland, United Kingdom

^dInstitute of Physics, Montanuniversitaet Leoben, Austria

ARTICLE INFO

Article history:

Received 5 September 2016

Revised 18 November 2016

Accepted 20 November 2016

Available online 8 December 2016

Keywords:

Colloidal films

Spatial inhomogeneity

Organic solar cells

Hole-transport layer

Surface potential distribution

Photocurrent mapping

ABSTRACT

Irreproducibility is a serious issue in thin film organic photovoltaic (OPV) devices, as smallest local inhomogeneities can change the entire behaviour of identically built devices without showing obvious failure. Inhomogeneities can occur at various steps of device preparation and appear in all layers with different length scales and impact. The hole-transport interlayer (HTL) in OPV devices blocks unwanted electron diffusion to the anode and corrects energetic mismatch between oxide electrode and organic semiconductor. Most commonly used is commercial ink based on poly(3,4-ethylenedioxythiophene):poly(styrenesulfonate) (PEDOT:PSS) colloidal particles. However, exactly these are suspected to cause microscopic inhomogeneities, causing known irreproducibility of device characteristics. Considering PEDOT:PSS' acidity-caused electrode corrosion, it is questionable how much impact colloids have on device homogeneity. In this report, we give proof that a colloidal HTL does not necessarily cause device inhomogeneity and decreased efficiency, by comparing OPV devices with different HTLs, namely from commercial PEDOT:PSS ink and from MoO₃, obtained from two liquid precursors, leading to quasi-continuous or colloidal layers. With a combination of X-ray diffraction, atomic force and Kelvin probe microscopy, photoelectron and ambient air photoemission spectroscopy, we discuss the layers' properties from nano- to macroscale and demonstrate their impact upon implementation into OPV devices, via spatially-resolved characterization.

© 2016 Published by Elsevier B.V.

1. Introduction

Organic photovoltaic (OPV) cells have received considerable attention as a potential source of renewable energy due to their advantages of easy fabrication, light weight, low manufacturing cost and mechanical flexibility. Typically, an OPV device consists of a transparent conductive indium tin oxide (ITO) anode, a donor-acceptor bulk-heterojunction photoactive layer and a low-work-function metallic cathode [1–4]. To enhance the collection of photogenerated charges [5] and decrease leakage currents [6] a hole-transport layer (HTL) is commonly used between ITO and the active layer.

However, despite the fact that this type of devices reaches good efficiencies (presently best known 11% [7]), a major problem of organic thin film diodes is the significant batch-to-batch and device-

to-device variation. Behaviour and performance of nominally identically built devices can differ considerably and so the research results published for identical systems. It is speculated that even device sets prepared at a time by the same experimentalist show not seldomly variations in performance of up to 10%.

Fact is that the physics of thin film diodes is naturally highly sensitive to smallest variations due to their limited lateral extension. These can be e.g. subtle differences in height, local composition, interface or contact properties, and the presence of impurities or grain boundaries. Such effects have been widely shown in the past for inorganic thin film solar cells [8]. In some cases the physical processes at such inhomogeneities were considerably altered from the expected device physics. Thereby the entire device may show a different behaviour to others of nominally identical built and not necessarily imply a clear device failure.

However, while organic devices are extensively studied on the nanoscale regarding their crucial donor-acceptor domain morphology, other rather microscopic variations originating from inhomogeneities of the electrode are often neglected. The few

* Corresponding author.

E-mail address: bfriedel@tugraz.at (B. Friedel).

publications on this topic show its relevance, as the extensive study on organic solar cell degradation published by Hoppe et al [9], and on microscale inhomogeneities in organic solar cells and modules been published by Revière et al [10]. Both show that the effects are versatile, originating from surface roughness, work function fluctuations, activity/non-activity patches, grain boundaries, agglomerate formation, delamination, chemical reactions. And these rather intermediate-scale effects might not be visible via standard nanoprobe snapshots. In particular the poly(3,4-ethylenedioxythiophene): poly(styrenesulfonate) (PEDOT: PSS) electrode interlayer, widely used for its high conductivity, high transparency and solution processibility [11–12] is known to generate instability and shorter life times of devices especially at exposure to humidity, due to acidity and hygroscopicity of PSS [13–14]. Additionally, originating from synthesizing the insoluble PEDOT in presence of water-soluble PSS for better handling, [15] PEDOT: PSS is forming gel-like colloidal particles, which consist of a PEDOT-rich core covered by a PSS-rich shell, [16–18]. This colloidal form is suspected to be responsible for spatial inhomogeneities and irreproducibility [19].

Here, we suggest that the local microscopic inhomogeneities in solar cells caused by the PEDOT: PSS hole-conducting interlayer are independent of the colloidal film morphology. This is demonstrated by comparison of microscopic spatial characteristics in thin film OPV devices comprising HTLs of PEDOT: PSS and of sol-gel processed MoO_3 with either colloidal form comparable to PEDOT: PSS or a quasi-continuous featureless layer.

It has been demonstrated in the past that high work-function metal-oxides, such as NiO [20–21], WO_3 [22], V_2O_5 [23–25] and MoO_3 [5–6, 25–29] might be suitable alternatives for PEDOT: PSS, especially MoO_3 , with its large bandgap between 2.9 and 3.1 eV and high work function 5.5 eV [25–26, 29–30]. In the present case, MoO_3 films are conveniently deposited from solution, equal to PEDOT: PSS. For that purpose sol-gel processing was used, allowing derivation of nano- to micron sized MoO_3 particle formulations from liquid precursors [5–6, 27–28]. Thereby the morphology, electrical properties and surface physics of the HTLs are shown with X-ray diffraction, atomic force and Kelvin probe microscopy, photoelectron and ambient air photoemission spectroscopy, and their influence on OPV device physics demonstrated, by integrated device measurements and with spatially resolved photocurrent maps from nano- to macroscale. The architecture of the studied devices is shown in Fig. 1. Herein, we use a blend of poly(3-hexylthiophene-2,5-diyl) (P3HT) and [6,6]-phenyl- C_{61} -butyric acid methyl ester (PC_{60}BM), a well-studied standard photoactive layer.

2. Experimental

2.1. Materials

Poly(3-hexylthiophene) (P3HT) was supplied by Rieke Metals Inc. (M_w 50,000–70,000 g mol^{-1} , regioregularity 91–94%). [6,6]-Phenyl- C_{61} -butyric acid methyl ester (PC_{60}BM) was purchased from Nano-C Inc. (99.5% purity). The formulation of poly(3,4 ethylenedioxythiophene): poly(4-styrenesulfonate) (PEDOT: PSS) was purchased from Heraeus Deutschland GmbH & Co. KG (Clevis P Jet (OLED)). Ammonium molybdate ($(\text{NH}_4)_2\text{MoO}_4$ ($\geq 99.98\%$) was purchased from Sigma Aldrich. Hydrochloric acid HCl ($\geq 37\%$) and bis(acetylacetonato)dioxomolybdenum(VI) ($\text{MoO}_2(\text{acac})_2$) were bought from Sigma-Aldrich. Isopropanol was purchased from VWR International LLC. All the materials were used as received. ITO substrates ($20 \Omega/\text{square}$, Ossila) were cleaned by sonication in acetone and isopropanol and followed by O_2 -plasma etching (100 W for 30 min) briefly before use.

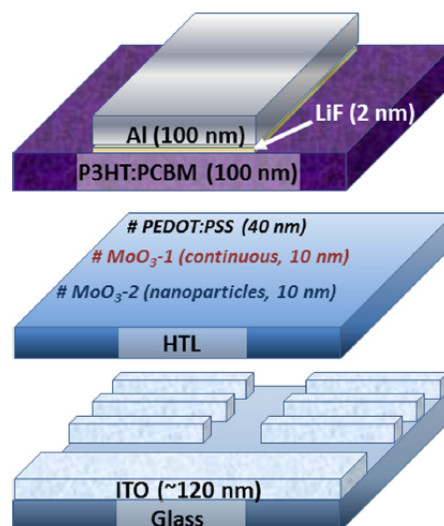


Fig. 1. Device architecture of the studied solar cells, with according layer thicknesses noted.

2.2. Preparation of the MoO_3 and PEDOT:PSS HTLs

Two different MoO_3 precursor formulations were used. The precursor leading to *continuous* films ($\text{MoO}_3\text{-1}$) was synthesized as follows: MoO_3 solution was prepared according to the procedure reported by K. Zilberberg et al. [27]. Here, $\text{MoO}_2(\text{acac})_2$ was dissolved in isopropanol to form a 0.5% (w/v) solution. The precursor formulation resulting in *nanoparticle* films ($\text{MoO}_3\text{-2}$) was prepared by hydration method in aqueous solution as reported by Liu et al. [6]. Here, $(\text{NH}_4)_2\text{MoO}_4$ was dissolved in distilled water to form a 0.005 mol/L solution. Then 2 mol/L aqueous hydrochloric acid (HCl) was added drop-wise under stirring until the pH value of the solution was between 1 and 1.5. MoO_3 precursor formulations and PEDOT: PSS, were both filtered by $0.22 \mu\text{m}$ PVDF membrane filters (Sigma Aldrich) and spin-coated onto ITO substrates at 4000 rpm for PEDOT: PSS and 3000 rpm for MoO_3 for 40 s, respectively. The layer of $\text{MoO}_3\text{-1}$ was kept at ambient air for 1 h for hydrolysis at room temperature and then annealed at 160°C for 20 min. The $\text{MoO}_3\text{-2}$ film was directly annealed at 160°C in air (20 min). The PEDOT: PSS anode buffer layers were annealed at 160°C for 20 min under Argon (Ar) flow.

2.3. Device fabrication

Solar cells with P3HT: PCBM active layer according to the architecture in Fig. 1 were prepared using different HTLs based on continuous MoO_3 ($\text{MoO}_3\text{-1}$), nanoparticle MoO_3 ($\text{MoO}_3\text{-2}$) and PEDOT: PSS, or were prepared without HTL (= ITO). For the devices, where applicable, hole-conduction layers were deposited on patterned ITO glass substrates and treated as described in 2.2. The active layer was applied in an argon atmosphere by spin-coating from a solution of P3HT and PCBM (1:1 weight ratio, each 18 mg/mL) in 70°C chlorobenzene at 2500 rpm for 60 s, followed by annealing at 120°C for 10 min. The film thickness obtained is around 150 nm. The cathode was thermally evaporated as a bilayer of LiF (2 nm)/ Al (100 nm).

2.4. Characterization

Material structure and film morphologies were analysed by atomic force microscopy (AFM) using two systems: For $1 \mu\text{m} \times 1 \mu\text{m}$ a Nanosurf, EasyScan2, and for $3 \mu\text{m} \times 3 \mu\text{m}$ and

100 $\mu\text{m} \times 100 \mu\text{m}$ a MFP 3D AFM System from Asylum Research. The images with the EasyScan2 were taken in tapping mode using a Tap190 cantilever (Budgetsensors, Bulgaria) with a nominal frequency of 190 kHz. The MFP 3D AFM was operated in intermittent contact mode using SSS NCHR AFM probes from APPNano with typical tip radii below 2 nm. Local contact potential difference (CPD) maps of 3 $\mu\text{m} \times 3 \mu\text{m}$ areas were measured by Kelvin probe force microscopy (KPFM) using the MFP3D system with Pt coated ACCESS EFM probes from APPNano. The AFM topography, according particle size distribution and contact potential difference (CPD) data were visualized and analysed using the Gwyddion 2.40 software.

Surface CPD distribution maps of complete solar cell pixels (4 mm \times 1.5 mm) area were examined by the SKP5050 Scanning Kelvin probe (KP Technology Ltd.). Work function results were obtained by Ambient Pressure Photoemission Spectroscopy System (APS) (APS02, KP Technology Ltd.) [31] under UV light source and ambient conditions with an excitation range of 3.3–6.8 eV. The thickness of the MoO₃ and PEDOT: PSS films was determined by variable angle spectroscopic ellipsometry (M-2000 V, J.A. Woolam). The measurements were performed at three different angles (65°, 70°, and 75°) in the wavelength range of 200–1000 nm under three-layer optical model, silicon substrate, the native SiO₂ layer (1.7 nm), and the film bulk layer by the Cauchy function. The X-ray powder diffraction profiles were obtained on a Siemens D 501 diffractometer in Bragg–Brentano geometry using CuK α radiation ($\lambda = 1.54178 \text{ \AA}$) and a graphite monochromator at the secondary side. Data were fitted using EVA X-ray diffraction analysis software. X-ray photoelectron spectroscopy (XPS) measurements were performed on a commercial spectrometer (HR-XPS, SPECS Surface Nano Analysis GmbH), using monochromatic Mg K α radiation ($h\nu = 1253.6 \text{ eV}$). The illuminated current density–voltage (J–V) characteristics of the PV cells were measured using a computer-controlled Keithley 2636A source meter under AM1.5 G illumination (100 mW/cm²) from a solar simulator (Model 10,500, ABET Technologies, rated ABB). Their external quantum efficiency (EQE) was recorded for wavelengths from 375 to 900 nm, using 250 W white light source (tungsten halogen) with monochromator, a computer-controlled Keithley 2636A source meter and a calibrated silicon photodiode. Spatial photocurrent distribution was scanned with a computer-controlled nano-manipulator-driven xy-stage (Kleindiek Nanotechnik, NanoControl NC-2-3) and excitation with a 532 nm laser (<5 mW) with a focused spot-size of $\approx 2 \mu\text{m}$.

3. Results

3.1. Properties of the hole-transport materials and interlayers

To study the pure colloidal effects of the hole-transport interlayer on the OPV device homogeneity and performance, commercial PEDOT: PSS was compared with two different types of hydrothermally grown MoO₃ particles, **MoO₃-1** as a continuous layer and **MoO₃-2** as a nanoparticle layer with a particle size comparable with PEDOT: PSS. XRD diffraction patterns of both MoO₃ films (see Fig. 2) show a large number of diffraction peaks, the most prominent ones at $2\theta = 9.7^\circ$, 19.5° , 25.8° , 29.4° , 35.5° and 45.5° , corresponding to the (100), (200), (210), (300), (310) and (410) crystal planes of the hexagonal MoO₃ phase (JCPDS Card No.21-0569, h-MoO₃), which is predominantly present in low-temperature syntheses [32–33]. The intensity distribution is not completely in agreement with the expected powder pattern according to the reference and also varies between the two film types. It can be assumed that there might be a small degree of preferential orientation in the films. Only two peaks, at $2\theta = 32.8^\circ$ and 40.0° , merely occurring in the continuous film **MoO₃-1**, could not be assigned to this MoO₃ phase, nor identified as another or precursor residues.

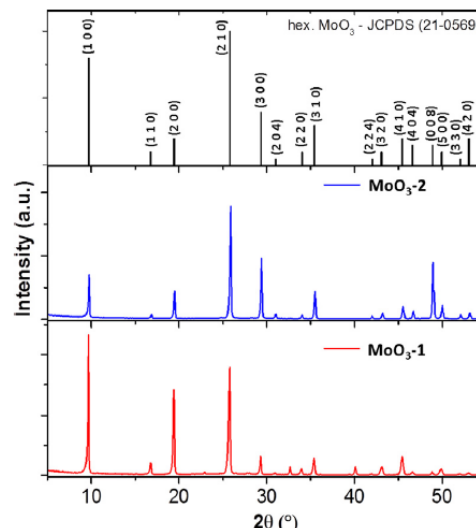


Fig. 2. X-ray diffraction patterns of solution-processed continuous **MoO₃-1** (red line) and nanoparticle (blue line) **MoO₃-2** films in comparison with the reference pattern of hexagonal MoO₃ (black bars, JCPDS 21-0569). For interpretation of the references to colour in this figure legend, the reader is referred to the web version of this article.

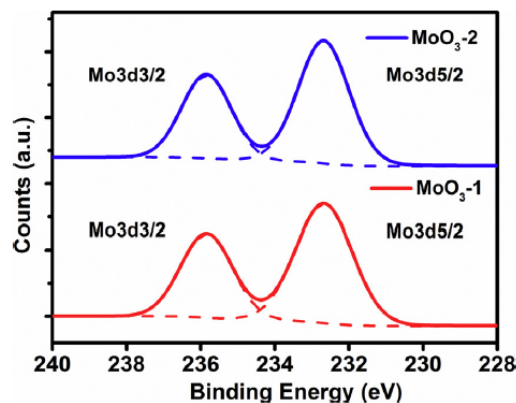


Fig. 3. XPS spectra of different solution processed continuous **MoO₃-1** and nanoparticle **MoO₃-2** film, showing the Mo 3d core level spectra with the Mo 3d 3/2 and Mo 3d 5/2 peak doublet.

X-ray photoelectron spectra (XPS) measurements were performed to confirm that both MoO₃ films have comparable surface chemistry. Fig. 3 shows detail scans of the Mo 3d core level region of both MoO₃ films showing the characteristic Mo 3d_{3/2} (high binding energy) and Mo 3d_{5/2} (low binding energy) doublet. The doublet could be fitted with two peaks, one centred at 232.7 eV for Mo 3d_{5/2} and the other at 235.8 eV for Mo 3d_{3/2}, respectively. These binding energies are consistent with literature values of Mo⁶⁺ oxidation state of MoO₃ [34–36]. The thicknesses of **MoO₃-1** and **MoO₃-2** films is in both cases around 10 nm and for PEDOT: PSS films around 40 nm, as measured by ellipsometry (not shown). The absolute work function of the HTLs on ITO substrates and of bare ITO was determined by APS [31]. Fig. 4(a) shows the according square-roots of photoemission of the various hole-conduction layers and ITO. Their work functions have been estimated from the offset of photoemission and found to be around 5.0 eV for PEDOT: PSS, **MoO₃-1** and **MoO₃-2** and around 4.6 eV for ITO. These results indicate presence of equal potential steps for hole collection from P3HT's highest occupied molecular orbital (HOMO) and transfer to

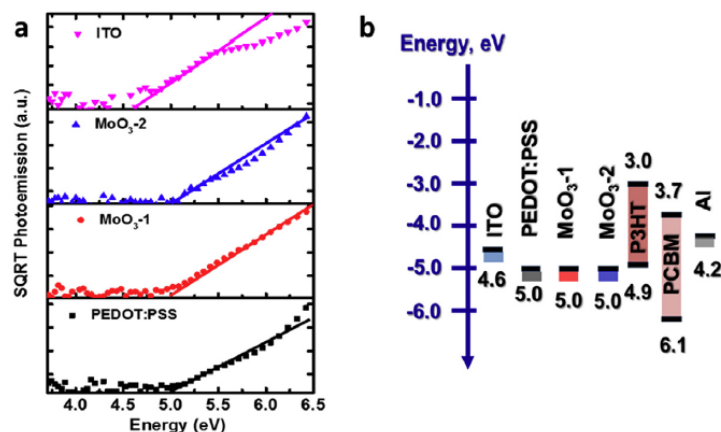


Fig. 4. Intensity corrected normalized square-root of the air photoemission response of ITO and the different HTL films (a). Schematic energy level diagram with the accordingly derived work functions, and energies of additional components of the OPV structure, such as the HOMO/LUMO energies of P3HT and PCBM and the work function of Al from literature [6] (b).

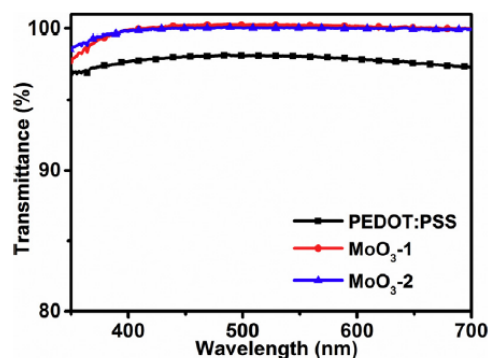


Fig. 5. UV-Vis transmission spectra of different HTLs.

the ITO anode for any of the three hole conductors, as depicted in the energy level diagram in Fig. 4(b), showing the APS-derived work functions and reported molecular orbital energies of P3HT, PCBM and work function of Al [6]. In the wavelength spectral region relevant for solar cells (>350 nm), the optical transmission of the three HTLs is quite comparable with values close to 100%, as shown in Fig. 5. Film morphology of the three HTL materials was investigated by AFM. Fig. 6 shows AFM height images of ITO on glass and of PEDOT: PSS in comparison with the continuous and nanoparticle MoO₃ films deposited on polished Si substrates. The ITO surface (Fig. 6a) shows the typical multicrystalline structure with quite high roughness of $RMS = 3.54$ nm. The PEDOT: PSS film (Fig. 6b) shows a colloidal structure of almost spherical particles and considerable amount of agglomerates thereof resulting in an apparently quite broad particle size distribution with a mean diameter of 30 nm (Fig. 6e) and film roughness of $RMS = 0.95$ nm (note: supplier gives 25 nm average size). The MoO₃-1 film (Fig. 6c) is the least rough one with $RMS = 0.27$ nm and shows the smallest sized particles (resolution was not sufficient to determine the shape) with a mean diameter of 6 nm and the most narrow size distribution (Fig. 6e). Layers deposited from these particles are microscopically smooth compared to the other two materials, therefore in the following referred to as quasi-continuous. However, the present dark spots in the film indicate pin holes which were caused already during deposition by spin coating by evaporation of the solvent. The MoO₃-2 film (Fig. 6d) shows spherical particles with an average diameter of 18 nm, therewith slightly smaller than

Table 1

Mean particle size and film roughness of different HTL materials and films on Si and on ITO surface, as derived from AFM (Fig. 6 and Fig. 7a–d).

| HTLs | Mean Diameter (nm) | RMS _{Si} (nm) | RMS _{ITO} (nm) |
|---------------------|--------------------|------------------------|-------------------------|
| ITO | – | – | 3.5 |
| PEDOT:PSS | 30 | 1.0 | 1.1 |
| MoO ₃ -1 | 6 | 0.3 | 1.4 |
| MoO ₃ -2 | 18 | 0.4 | 1.3 |

for PEDOT: PSS, also due to absence of aggregation, but shows a broader distribution of the primary particle size (Fig. 6e) compared to MoO₃-1, which induced higher $RMS = 0.36$ nm. A summary of mean particle size of the materials and roughness of the according HTL on silicon and on ITO (as described further below) can be found in Table 1.

The appearance of these structures on a larger scale, when applied on the transparent ITO electrode can be seen from Fig. 7 showing AFM topography images of bare ITO and the different HTL coatings on ITO substrates. Expectedly, bare ITO (Fig. 7a) exhibits strong surface roughness with RMS of 3.5 nm, caused by its multicrystalline structure. This roughness is well-known to induce difficulties and inhomogeneities for further deposition of the organic active layer. PEDOT: PSS is commonly used for its properties not only as HTL but also for establishing a more flat topography on rough ITO. In present case, with 40 nm of PEDOT: PSS deposited on ITO, the structure appears softened by the particles, leading to a reduced RMS of 1.1 nm, but the original crystal pattern is still visible (Fig. 7b). In the case of MoO₃ HTLs, the film thickness must be much less than for PEDOT: PSS to avoid decreased photocurrent by optical absorption losses [27]. Therefore, the according films have no significant padding effect on the ITO structure, as can be seen for MoO₃-1 (Fig. 7c) and MoO₃-2 films on ITO substrate (Fig. 7d). In both cases, the rough ITO surface pattern is apparent, the MoO₃ hardly noticeable at this magnification. Thereby the roughness of ITO/MoO₃-1 is with RMS of 1.4 nm still larger than for ITO/MoO₃-2 is with RMS of 1.3 nm, probably because the continuous film rather replicates the underlying surface, while particles manage to fill “valleys”. Potential work-function fluctuations depending on a colloidal or continuous HTL structure across the device area on the nano- and microscale might have effects on the spatially resolved and integral device function. This was investigated on ITO and various ITO/HTL configurations on different length scales and (where applicable) compared to according spatially resolved photocurrent maps of respective P3HT: PCBM solar cells with this HTL configura-

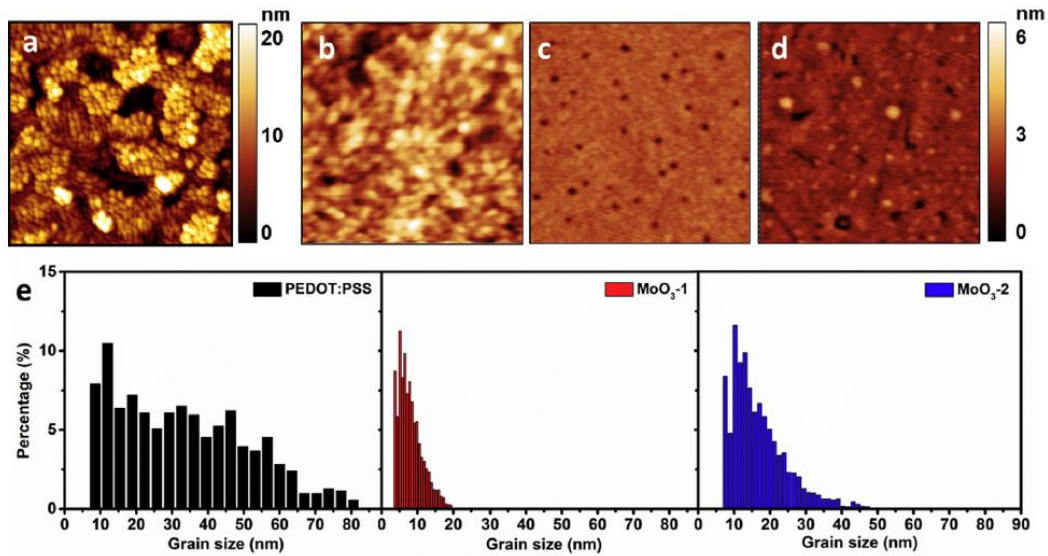


Fig. 6. AFM topography images ($1\ \mu\text{m} \times 1\ \mu\text{m}$ area) of ITO on glass (a) and different HTL films on Si wafer substrates: PEDOT:PSS (b), MoO_3 -1 (continuous) (c) and MoO_3 -2 (nanoparticles) (d). Size distribution for PEDOT:PSS, MoO_3 -1 and MoO_3 -2, as derived from AFM image particle analysis (e).

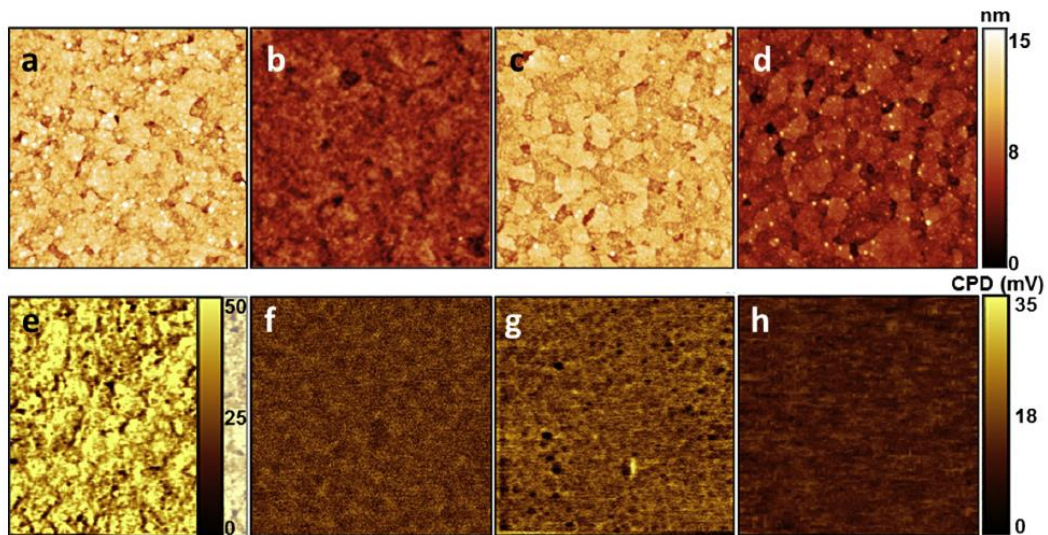


Fig. 7. $3\ \mu\text{m} \times 3\ \mu\text{m}$ area images. AFM topography images (upper row) and the respective relative surface potential maps (bottom row) of ITO (a + e), ITO/PEDOT:PSS (b + f), ITO/ MoO_3 -1 (continuous) (c + g) and ITO/ MoO_3 -2 (nanoparticles) (d + h).

ration. The nanoscale contact potential difference between AFM probe and surface ($V_{CPD} = (\Phi_{Sample} - \Phi_{Tip})/e$) has been measured by KPFM across $3\ \mu\text{m} \times 3\ \mu\text{m}$ areas, alongside with the aforementioned AFM topography images. The maps in Fig. 7e–h show the relative changes in contact potential across the surface (for better visibility ITO scaled separately, HTLs scaled to the maximum change among samples). All samples show spatial inhomogeneities of surface potential, expectedly the strongest fluctuations are shown by the bare ITO film (Fig. 7e), with feature sizes correlating with the topographic features (Fig. 7a). The large contrast of the pseudo colour image, compared to any of the HTL configurations, also indicates quite high amplitude of these spatial fluctuations and found to be 50 mV, determined from maximum CPD peak-to-peak difference, which is consistent with previous KPFM measurements performed on ITO/Glass [37]. The samples with HTLs also show distinct features in the CPD maps but

with considerably lower amplitude, being 20 mV for ITO/PEDOT:PSS, 22 mV for ITO/ MoO_3 -1 and 15 mV for ITO/ MoO_3 -2. In the case of ITO/PEDOT:PSS (Fig. 7f) the CPD map shows a pattern of lighter and darker regions, which is similar, but not entirely corresponding to the associated topography (Fig. 7b), suggesting that there are additional variations caused by non-uniform surface potential of the PEDOT:PSS particle agglomerates themselves. The continuous MoO_3 film sample ITO/ MoO_3 -1 (Fig. 7g), does not reflect any features from the underlying ITO topographic structure (Fig. 7c) in the CPD map, but shows a subtle fine pattern of slightly different potential regions and additionally some peculiar dark spots, i.e. localized circular areas of low potential. The latter might arise from aforementioned pin holes in the MoO_3 thin film, which were not even visible in the associated topography image. The fact that these pin holes appear to have a larger dimension on ITO than in the topography image on Si (Fig. 6b) is plausible, because the gran-

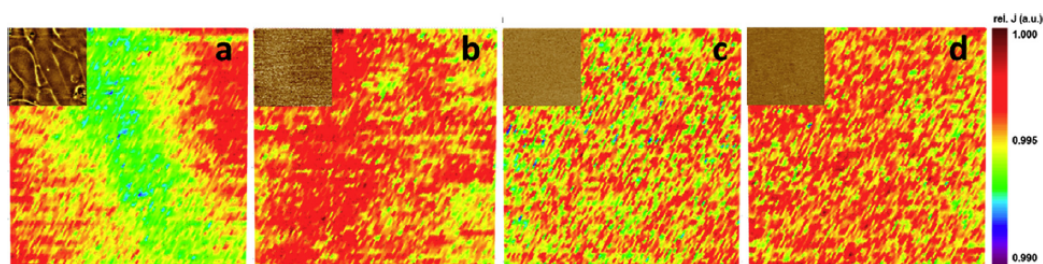


Fig. 8. Relative photocurrent maps on the microscale ($100\ \mu\text{m} \times 100\ \mu\text{m}$ working area) of P3HT:PCBM solar cells without HTL (a) or with PEDOT:PSS (b), MoO_3 -1 (continuous), (c) MoO_3 -2 (nanoparticles) (d). Inset shows according underlying surface potential distribution map ($30\ \mu\text{m} \times 30\ \mu\text{m}$).

ular surface structure of ITO works as local seed point for solvent evaporation. The difference between the pin holes' potential (on ITO potential) and the MoO_3 film surface causes a nominally higher CPD difference, than the film would have otherwise. The CPD map of the MoO_3 nanoparticle film sample ITO/ MoO_3 -2 (Fig. 7h) shows clearly the lowest amplitude of fluctuations in surface potential and the subtle brighter and darker areas in the film barely reflect the underlying ITO pattern (Fig. 7d). From the results it can be seen that the amplitude of spatial potential fluctuations is generally reduced if any HTL is deposited, indicating that the lacking uniformity of the underlying ITO anode can be thereby greatly improved. Further it can be concluded that the spatial variations of CPD seem to be independent of the padding effect an HTL material has on the underlying rough ITO structure. However, the surface coverage, as thin as it might be, seems to play an important role, as can be seen from the effect of pin holes for ITO/ MoO_3 -1. The fact that ITO/PEDOT: PSS shows the highest amplitude of surface potential fluctuations, despite the fact that it shows neither significant pores or reflects morphological features of underlying ITO surface or colloidal agglomerates, leads to the suspicion that the PEDOT: PSS material itself is non-uniform regarding its surface properties. This has been suggested in the past and based on observed conductivity anisotropy, PSS segregation or agglomerate formation [17–18, 38–39]. While photoconductive AFM allows visualization of nanoscale photocurrent distribution, this would be clearly dominated by features of donor/acceptor domains in the photoactive layer blend and not allow any further conclusions on the HTL effects [40–41]. A sub-microscale comparison of HTL surface potential with the photocurrent distribution, as derived by laser-beam-induced current mapping, was conducted. Fig. 8 shows relative photocurrent density (J) maps of P3HT:PCBM solar cells with ITO, PEDOT: PSS, MoO_3 -1 and MoO_3 -2 with a scanning area of $100\ \mu\text{m} \times 100\ \mu\text{m}$ and for comparison a CPD map inset of equal magnification with a scanning area of $30\ \mu\text{m} \times 30\ \mu\text{m}$. For the device with only ITO (Fig. 8a), it can be seen that the observed nanoscale inhomogeneity of the ITO surface potential propagates also into larger scale (see inset) and seems to have detrimental effects on the photocurrent, because the cell shows large regions (about half the size of the scan area) of lower current output than in the rest of the area, with a difference in current density amplitude between these regions of about 0.5%. When any HTL is applied in the solar cell, the surface potential fluctuations (insets) are considerably reduced compared to ITO-only, as seen before on small scale. The device with PEDOT: PSS as HTL (Fig. 8b) exhibits larger continuous areas of high current output with scattered small regions of low output, whereas the current amplitude between these areas changes again by 0.5%. In comparison, the cells with continuous HTL MoO_3 -1 (Fig. 8c) and nanoparticle HTL MoO_3 -2 (Fig. 8d) show a very different pattern. Despite the fact that no significant changes in surface potential are visible on this scale (insets) for either of them, the photocurrent map shows a small scale pattern of strongly scat-

tered regions of extremely high, medium and very low current output with changes in current amplitude of 1% across the small area. Hereby the fractions of high photocurrent output make up 40% of the area for MoO_3 -1 and 60% for MoO_3 -2 cells, the very low output regions make up about 5% and <1% of the device area, respectively. The very localized regions of extremely low output for the MoO_3 -1 cell might be caused by the pin hole effect which has been mentioned earlier. All-in-all within the four conditions, the device with the HTL of MoO_3 -2 has the best photocurrent homogeneity and highest density of high-output regions, indicating that the particles of MoO_3 are well distributed across the ITO, shielding its inhomogeneities very effectively despite the small nominal thickness and promoting efficient charge transfer at the electrode interface. Which consequences these local effects have on the entire device area is finally investigated in terms of photocurrent distribution on the complete pixel area of $4.0\ \text{mm} \times 1.5\ \text{mm}$ size of a P3HT:PCBM solar cell and compared with equally large area CPD (measured by scanning Kelvin probe) of the associated ITO/HTL configurations, shown in Fig. 9. The bare ITO electrode (Fig. 9a), shows a very strong gradient in surface potential across the entire area with a maximum difference of 65.5 mV in a similar range, compared to the values from small area. For the photocurrent distribution this inhomogeneity causes equally strong fluctuations, whereas a large area of strong output is found in the centre of the solar cell pixel and clearly decreasing outwards. Thereby the photocurrent density (J) amplitude changes by 12% across the pixel area. When PEDOT: PSS is used as HTL (Fig. 9b), the fluctuations in surface potential across the area get much more refined and fluctuations less intense with a maximum difference of only 47.4 mV. In consequence, the photocurrent distribution of the according solar cells is much more uniform, showing a large almost homogenous area of reasonable but not extremely high output, with few negligible pixel edge effects, with changes in current amplitude of only 5%. However, there are clearly no high output areas on the PEDOT: PSS cell. The MoO_3 -HTLs samples draw a different picture. ITO/ MoO_3 -1 (Fig. 9c) and ITO/ MoO_3 -2 (Fig. 9d) show both a similarly scattered pattern in their surface potential distribution, comparable to ITO/PEDOT: PSS. Thereby MoO_3 -1 shows still some areas of higher uniformity. The maximum fluctuations however, are with of 55.5 mV for MoO_3 -1 and 48.5 mV for MoO_3 -2, also quite similar to PEDOT: PSS. This is a different trend than recorded on the small length scale. But though the surface potential distribution of the three HTL configurations on this length scale is similar, the output pattern of the solar cells with MoO_3 HTL are very different to the one with PEDOT: PSS. The photocurrent of the cell with MoO_3 -1 shows one large homogeneous area of high to very high output, with photocurrent amplitude fluctuation of only 2%. Thereby the minor defects (spots of low output), probably caused by aforementioned pin holes, were neglected. The MoO_3 -2 cell, shows equal behaviour, but without defects, showing one large homogeneous area of high to very high current output, again with a maximum change in amplitude of 2%.

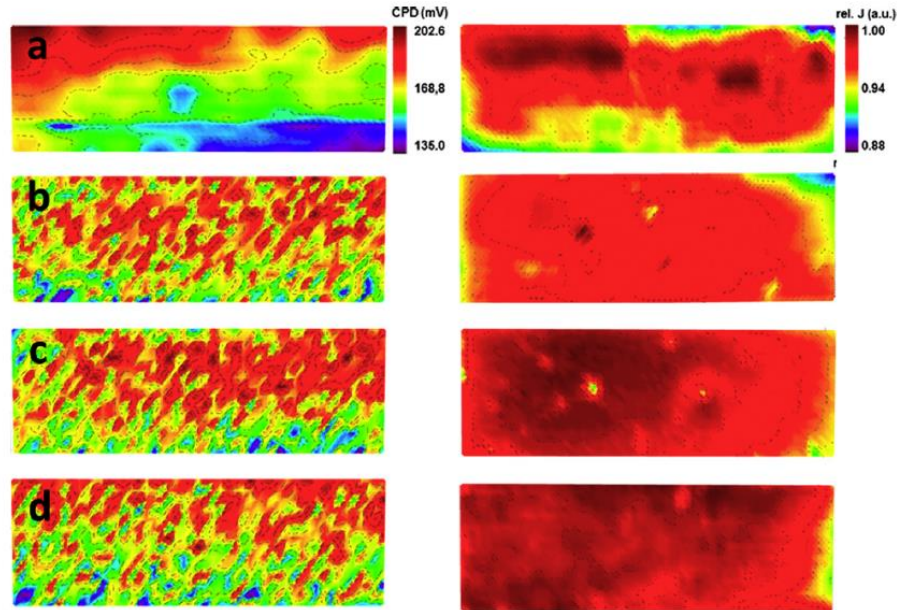


Fig. 9. Large area surface potential (CPD) contrast of ITO/HTL films (left) and relative photocurrent map of according P3HT:PCBM solar cell pixel (right) for the configurations: bare ITO (a), ITO/PEDOT:PSS (b), ITO/MoO₃-1 (c) and ITO/MoO₃-2 (d). 4.0 mm × 1.5 mm scan area.

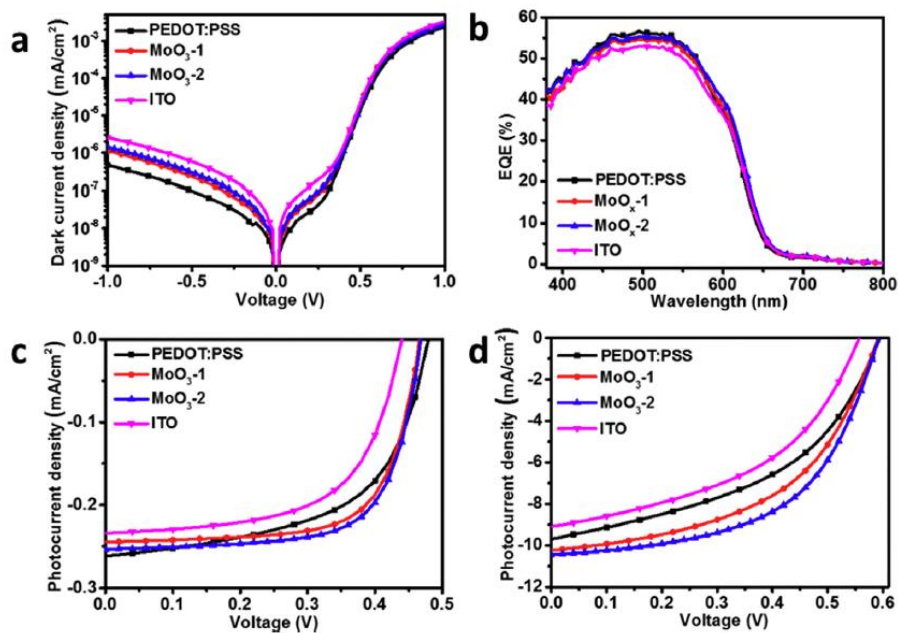


Fig. 10. Electrical performances of the OPV devices with only ITO and with different HTLs. J–V characteristics in the dark (a). EQE (b) and J–V characteristics under monochromatic 550 nm illumination (c) at low light intensity of ~ 3.5 mW/cm². J–V characteristics under simulated solar illumination according to AM1.5 G (d).

3.2. Device performance of solar cells

The integrated solar cell characteristics of P3HT:PCBM devices with the different electrode/HTL configurations ITO, ITO/PEDOT:PSS, ITO/MoO₃-1 and ITO/MoO₃-2, have been determined by standard methods, to confirm the findings from the area sensitive characterization. Fig. 10a shows a semi-logarithmic plot of the dark current density of the four systems. The device with only ITO shows clearly the largest leakage current, roughly one order of magnitude higher than the device with PEDOT:PSS. The two MoO₃ sys-

tems are located in-between, with about half an order of magnitude lower leakage current than for the ITO-only device. At higher forward bias, all four devices show an identical character, which can be expected as this part is dominated by bulk charge transport in the active layer, which is the same for all devices. Also the spectral response of the device is mostly determined by the active layer, as visible from the identical shape of the external quantum efficiency (EQE) of the devices shown in Fig. 10b. Its amplitude however, differs slightly between the four cells, with the highest value for ITO/PEDOT:PSS with 57% EQE and the lowest for ITO

Table 2
Summary of photovoltaic parameters of OPV cells with only ITO and with different HTLs, as derived from characteristics in Fig. 9d.

| HTLs | η (%) | FF | V_{OC} (V) | J_{SC} (mA/cm ²) |
|---------------------|------------|------|--------------|--------------------------------|
| ITO | 2.32 | 0.46 | 0.560 | 9.10 |
| PEDOT:PSS | 2.64 | 0.46 | 0.594 | 9.70 |
| MoO ₃ -1 | 3.05 | 0.50 | 0.591 | 10.24 |
| MoO ₃ -2 | 3.38 | 0.55 | 0.592 | 10.45 |

with 51% EQE. As the EQE is determined by the short-circuit current (J_{SC}) per wavelength, its trend correlates directly with that of the J_{SC} seen in the photocurrent characteristic recorded at 550 nm (close to the wavelength of maximum EQE) at same light intensity, as shown in Fig. 10c. Also the open-circuit voltages (V_{OC}) of the four cells vary, with lowest value for the ITO device with 0.440 V, highest V_{OC} for ITO/PEDOT: PSS with 0.479 V, and the values of ITO/MoO₃-1 and ITO/MoO₃-2 equal with 0.467 V in-between. This poor V_{OC} of the ITO device can be easily explained by voltage losses at the shunts, which were confirmed by the dark current characteristics. An additional observation is the lower rectangularity of the photocurrent curve of ITO/PEDOT: PSS compared to those of ITO/MoO₃-1 and ITO/MoO₃-2, as visible from the lower fill factor (FF) of 0.57 for ITO/PEDOT: PSS, compared to 0.68 for ITO/MoO₃-1 and 0.69 for ITO/MoO₃-2. This behaviour can indicate interfacial barriers for charge transfer at the electrode interface or bad transport, which lead to accumulation of charges. The fact that this is already prominent at low light intensities, as they were used for EQE and monochromatic photocurrent measurement ($P_{\text{monochr}} \sim 3.5 \text{ mW/cm}^2$), strongly suggests that worse performance of the device can be expected at high light intensities, when a higher density of charges is created in the device. Photocurrent characteristics of the devices at high light intensities have been recorded under simulated solar conditions, i.e. white light AM1.5 G illumination with $P = 100 \text{ mW/cm}^2$, as presented in Fig. 10d. A summary of characteristic solar cell values is given in Table 2. The ITO device still shows the lowest J_{SC} and V_{OC} compared to the other systems, with 9.1 mA/cm² and 0.56 V, respectively. Main reason for that is the unfavourable potential barrier between ITO and P3HT (Fig. 4b). With 9.7 mA/cm², the ITO/PEDOT: PSS device exhibits a considerably lower J_{SC} than ITO/MoO₃-1 with 10.3 mA/cm² and ITO/MoO₃-2 with 10.5 mA/cm², while their V_{OC} is identical with 0.59 V. As predicted, ITO/PEDOT: PSS exhibits an even more decreased FF at this light intensity of 0.46, similar to that of the ITO device. Both MoO₃ systems show higher FF of 0.50 for MoO₃-1 and 0.55 for MoO₃-2. The lower value for the cell with continuous MoO₃-1 HTL could be caused by charge transfer issues in regions with pin holes. Altogether, this leads to the maximum power conversion efficiency η for the ITO/MoO₃-2 device with 3.38%, followed by ITO/MoO₃-1 with 3.05%, 2.64% for the ITO/PEDOT: PSS and 2.32% for the ITO device.

4. Discussion

It is obvious that the PV performance of a conventional organic solar cell is generally greatly improved by presence of a HTL, indicated by the fact that lower work function of ITO and direct contact between ITO and the organic semiconductor layer P3HT: PCBM cause charge blocking at the interface and large leakage currents within the cell. Comparing the colloidal PEDOT: PSS as HTL with two different MoO₃-HTLs of identical physical and morphological material properties, except for their form, continuous vs. nanoparticle colloidal layer, interesting observations: Despite the fact that a continuous layer with pin holes and a thin colloidal layer with potential voids both should show some sort of “porosity” allowing

effects from the underlying ITO to shine through to the surface, the MoO₃-2 nanoparticle HTL samples show most homogeneous surface potential and photocurrent distribution on small length scales, highest and most homogeneous photocurrent on the full device area, best integral device performance. The continuous MoO₃-1 HTL configuration delivered also homogeneous potential and output, except for the regions with pin holes, visualized as localized spots of potential drops and low photocurrent output and in consequence slightly lower overall performance. PEDOT: PSS on the other hand, the long-term favourite among OPV HTLs, shows inhomogeneities in surface potential even on a very small scale, despite the fact that the thicker layer (of 40 nm) is efficiently padding the rough ITO surface (RMS 3.5 nm \rightarrow 1.1 nm), indicating the variations arising from the material properties itself, e.g. aggregation, degradation (with In migration) or excess PSS segregation at the film surface [17,18]. In a solar cell, this effect causes patchy performance fluctuations on a small length scale, which seem to develop into charge transfer barriers on the large scale, as reflected in homogeneous but considerably lower output of the cells and finally low device efficiency at standard AM1.5 G conditions. In summary, well distributed small particles of MoO₃ as HTLs in organic solar cells lead to a better spatially uniform photocurrent distribution and best PV cell electrical performance with an overall efficiency η reaching 3.38%. From the presented results it can be assumed that the two MoO₃ HTLs would lead to entirely identical performance in absence of the pin-holes. Therefore it is suggested that the failure of PEDOT: PSS device homogeneity and performance cannot be deduced from its colloidal state or surface coverage, but rather its chemical properties, such as PSS segregation or acidity-caused electrode corrosion.

5. Conclusions

We compared the surface and device inhomogeneity of P3HT: PCBM bulk heterojunction PV cells influenced by three different solution-processed colloidal HTLs, one PEDOT: PSS, one continuous MoO₃ and one nanoparticle MoO₃ film, and compared them with ITO only devices. This was supported by the comparison of the morphology and contact potential difference distribution of HTL layers and spatial photocurrent distribution of the OPV devices at different resolutions from the nano- to the micrometer scale. This has been discussed in relation to the difference in integral device characteristics and performance between those different OPV cells. The results showed anode film homogeneity and device performance greatly improved by presence of any HTL. Regardless of continuous or nanoparticle layers, MoO₃ HTLs lead to entirely identical performance excluding the pin-hole effect, which induced slightly lower performance and uniformity. In contrast to the MoO₃ HTLs, PEDOT: PSS HTL showed spatial inhomogeneities and device charge transfer barriers, which may be caused by its chemical characteristics. Independent of colloidal or continuous form, MoO₃ proves as a better candidate for anode buffer layers, leading to higher performance, higher homogeneity, and also lower cost, in solution-processed organic solar cells.

Acknowledgement

H.-T. C. and B.F. are grateful to the Austrian Science Fund (FWF) for financial support (Project No. P 26066) and to Dr Anna Coclite (TU Graz) for providing the ellipsometry measurements.

References

- [1] S. Gunes, H. Neugebauer, N.S. Sariciftci, Conjugated polymer-based organic solar cells, *Chem. Rev.* 107 (2007) 1324–1338.
- [2] M.C. Scharber, N.S. Sariciftci, Efficiency of bulk-heterojunction organic solar cells, *Prog. Polymer Sci.* 38 (2013) 1929–1940.

- [3] G. Yu, J. Gao, J.C. Hummelen, F. Wudl, A.J. Heeger, Polymer photovoltaic cells: enhanced efficiencies via a network of internal donor-acceptor heterojunctions, *Science* 270 (1995) 1789–1791.
- [4] J.J.M. Halls, C.A. Walsh, N.C. Greenham, E.A. Marseglia, R.H. Friend, S.C. Moratti, A.B. Holmes, Efficient photodiodes from interpenetrating polymer networks, *Nature* 376 (1995) 498–500.
- [5] J. Meyer, R. Khalandovsky, P. Gorrrn, A. Kahn, MoO₃ films spin-coated from a nanoparticle suspension for efficient hole-injection in organic electronics, *Adv. Mater.* 23 (2011) 70–73.
- [6] F. Liu, S. Shao, X. Guo, Y. Zhao, Z. Xie, Efficient polymer photovoltaic cells using solution-processed MoO₃ as anode buffer layer, *Solar Energy Mater. Solar Cells* 94 (2010) 842–845.
- [7] M.A. Green, K. Emery, Y. Hishikawa, W. Warta, E.D. Dunlop, Solar cell efficiency tables (Version 45), *Prog. Photovolt: Res. Appl.* 23 (2015) 1–9.
- [8] V.G. Karpov, A.D. Compaan, D. Shvydka, Random diode arrays and mesoscale physics of large-area semiconductor devices, *Phys. Rev. B* 69 (2004) 045325.
- [9] B.Zimmermann Galagan, U. Würfel, M. Hösel, H.F. Dam, S.A. Gevorgyan, S. Kudret, W. Maes, L. Lutsen, D. Vanderzande, R. Andriessen, G. Teran-Escobar, M. Lira-Cantu, A. Rivaton, G.Y. Uzunoğlu, D. Germack, B. Andreasen, M.V. Madsen, K. Norrman, H. Hoppe, F.C. Krebs, Investigation of the degradation mechanisms of a variety of organic photovoltaic devices by combination of imaging techniques—the ISOS-3 inter-laboratory collaboration, *Energy Environ. Sci.* 5 (2012) 6521–6540.
- [10] G.A. Rivière, J.-J. Simon, L. Escoubas, W. Vervisch, M. Pasquinielli, Photo-electrical characterizations of plastic solar modules, *Solar Energy Mater. Solar Cells* 102 (2012) 19–25.
- [11] Y. Cao, G. Yu, C. Zhang, R. Menon, A. Heeger, Polymer light-emitting diodes with polyethylene dioxythiophene–polystyrene sulfonate as the transparent anode, *Synthetic Metals* 87 (1997) 171–174.
- [12] D. Heithecker, A. Kammoun, T. Dobbertin, T. Riedl, E. Becker, D. Metzendorf, D. Schneider, H.-H. Johannes, W. Kowalsky, Low-voltage organic electroluminescence device with an ultrathin, hybrid structure, *Appl. Phys. Lett.* 82 (2003) 4178.
- [13] M.P. de Jong, L.J. van Ijzendoorn, M.J.A. de Voigt, Stability of the interface between indium-tin-oxide and poly(3,4-ethylenedioxythiophene)/poly(styrenesulfonate) in polymer light-emitting diodes, *Appl. Phys. Lett.* 77 (2000) 2255.
- [14] F. So, D. Kondakov, Degradation mechanisms in small-molecule and polymer organic light-emitting diodes, *Adv. Mater.* 22 (2010) 3762–3777.
- [15] S. Kirchmeyer, K. Reuter, Scientific importance, properties and growing applications of poly(3,4-ethylenedioxythiophene), *J. Mater. Chem.* 15 (2005) 2077–2088.
- [16] G. Greczynski, T. Kugler, M. Keil, W. Osikowicz, M. Fahlman, W. Salaneck, Photoelectron spectroscopy of thin films of PEDOT–PSS conjugated polymer blend: A mini-review and some new results, *J. Electron Spectrosc. Relat. Phenom.* 121 (2001) 1–17.
- [17] B. Friedel, T.J. Brenner, C.R. McNeill, U. Steiner, N.C. Greenham, Influence of solution heating on the properties of PEDOT: PSS colloidal solutions and impact on the device performance of polymer solar cells, *Organic Electron.* 12 (2011) 1736–1745.
- [18] B. Friedel, P.E. Keivanidis, T.J.K. Brenner, A. Abrusci, C.R. McNeill, R.H. Friend, N.C. Greenham, Effects of layer thickness and annealing of pedot: PSS layers in organic photodetectors, *Macromolecules* 42 (2009) 6741–6747.
- [19] M. Kemerink, S. Timpanaro, M.M. de Kok, E.A. Meulenkaamp, F.J. Touwslager, Three-dimensional inhomogeneity in PEDOT: PSS films, *J. Phys. Chem. B* 108 (2004) 18820–18825.
- [20] K.X. Steirer, J.P. Chesin, N.E. Widjonarko, J.J. Berry, A. Miedaner, D.S. Ginley, D.C. Olson, Solution deposited NiO thin-films as hole transport layers in organic photovoltaics, *Organic Electron.* 11 (2010) 1414–1418.
- [21] K.X. Steirer, P.F. Ndione, N.E. Widjonarko, M.T. Lloyd, J. Meyer, E.L. Ratcliff, A. Kahn, N.R. Armstrong, C.J. Curtis, D.S. Ginley, J.J. Berry, D.C. Olson, Enhanced efficiency in plastic solar cells via energy matched solution processed NiOx interlayers, *Adv. Energy Mater.* 1 (2011) 813–820.
- [22] C. Tao, S. Ruan, G. Xie, X. Kong, L. Shen, F. Meng, C. Liu, X. Zhang, W. Dong, W. Chen, Role of tungsten oxide in inverted polymer solar cells, *Appl. Phys. Lett.* 94 (2009) 43311.
- [23] K. Zilberberg, S. Trost, H. Schmidt, T. Riedl, Solution processed vanadium pentoxide as charge extraction layer for organic solar cells, *Adv. Energy Mater.* 1 (2011) 377–381.
- [24] K. Takanezawa, K. Tajima, K. Hashimoto, Efficiency enhancement of polymer photovoltaic devices hybridized with ZnO nanorod arrays by the introduction of a vanadium oxide buffer layer, *Appl. Phys. Lett.* 93 (2008) 63308.
- [25] V. Shrotriya, G. Li, Y. Yao, C.-W. Chu, Y. Yang, Transition metal oxides as the buffer layer for polymer photovoltaic cells, *Appl. Phys. Lett.* 88 (2006) 73508.
- [26] J. Meyer, A. Shu, M. Kröger, A. Kahn, Effect of contamination on the electronic structure and hole-injection properties of MoO₃/organic semiconductor interfaces, *Appl. Phys. Lett.* 96 (2010) 133308.
- [27] K. Zilberberg, H. Gharbi, A. Behrendt, S. Trost, T. Riedl, Low-temperature, solution-processed MoO₃ for efficient and stable organic solar cells, *ACS Appl. Mater. Interfaces* 4 (2012) 1164–1168.
- [28] S. Murase, Y. Yang, Solution processed MoO₃ interfacial layer for organic photovoltaics prepared by a facile synthesis method, *Adv. Mater.* (Deerfield Beach, Fla.) 24 (2012) 2459–2462.
- [29] Y. Sun, C.J. Takacs, S.R. Cowan, J.H. Seo, X. Gong, A. Roy, A.J. Heeger, Efficient, air-stable bulk heterojunction polymer solar cells using MoO₃ as the anode interfacial layer, *Adv. Mater.* 23 (2011) 2226–2230.
- [30] C.J. Brinker, G.W. Scherer, *Sol-Gel Science: The Physics And Chemistry Of Sol-Gel Processing*, Academic Press, Boston, 1990.
- [31] I.D. Baikie, A.C. Grain, J. Sutherland, J. Law, Ambient pressure photoemission spectroscopy of metal surfaces, *Appl. Surface Sci.* 323 (2014) 45–53.
- [32] A. Chithambararaj, N. Rajeswari Yogamalar, A.C. Bose, Hydrothermally synthesized h-MoO₃ and α-MoO₃ nanocrystals: new findings on crystal-structure-dependent charge transport, *Cryst. Growth Des.* 16 (2016) 1984–1995.
- [33] Z. Zhang, R. Yang, Y. Gao, Y. Zhao, J. Wang, L. Huang, J. Guo, T. Zhou, P. Lu, Z. Guo, Q. Wang, Novel Na₂Mo₄O₁₃/α-MoO₃ hybrid material as highly efficient CWO catalyst for dye degradation at ambient conditions, *Sci. Reports* 4 (2014) 6797.
- [34] G.D. Khattak, M.A. Salim, A.S. Al-Harathi, D.J. Thompson, L.E. Wenger, Structure of molybdenum-phosphate glasses by X-ray photoelectron spectroscopy (XPS), *J. Non-Crystalline Solids* 212 (1997) 180–191.
- [35] F. Werfel, E. Minni, Photoemission study of the electronic structure of Mo and Mo oxides, *J. Phys. C: Solid State Phys.* 16 (1983) 6091–6100.
- [36] R. Kleyna, H. Mex, M. Voß, D. Borgmann, L. Viscido, J.M. Heras, Modification of MoO₃ surfaces by vapour-deposited cobalt atoms, *Surface Sci.* 433–435 (1999) 723–727.
- [37] Y. Udum, P. Denk, G. Adam, D.H. Apaydin, A. Nevesad, C. Teichert, M.S. White, N.S. Sariciftci, M.C. Scharber, Inverted bulk-heterojunction solar cell with cross-linked hole-blocking layer, *Organic Electron.* 15 (2014) 997–1001.
- [38] A.M. Nardes, M. Kemerink, R.A.J. Janssen, Anisotropic hopping conduction in spin-coated PEDOT: PSS thin films, *Phys. Rev. B* 76 (2007).
- [39] A.M. Nardes, M. Kemerink, R.A.J. Janssen, J.A.M. Bastiaansen, N.M.M. Kiggen, B.M.W. Langeveld, A.J.J.M. van Breemen, M.M. de Kok, Microscopic understanding of the anisotropic conductivity of PEDOT: PSS thin films, *Adv. Mater.* 19 (2007) 1196–1200.
- [40] D.C. Coffey, O.G. Reid, D.B. Rodovsky, G.P. Bartholomew, D.S. Ginger, Mapping local photocurrents in polymer/fullerene solar cells with photoconductive atomic force microscopy, *Nano Lett.* 7 (2007) 738–744.
- [41] B. Friedel, B. Ehrler, S. Huettnner, N.C. Greenham, Enhanced nanoscale imaging of polymer blends by temperature-controlled selective dissolution, *Small* 8 (2012) 237–240.

4.2. Influence of Environmentally Affected Hole Transport Layers on Spatial Homogeneity and Charge Transport Dynamics of Organic Solar Cells.

Huei-Ting Chien, Florian Pilat, Thomas Griesser, Harald Fitzek, Peter Poelt, Bettina Friedel

Author Contributions

The author defined the research plan, executed the experiments, prepared the samples for HTL characterization, fabricated the SCs and measured the device physics. The dynamic TPC measurements were done by Florian Pilat. The XPS measurements were done by Thomas Griesser. The Raman measurements were carried out by Harald Fitzek and Peter Poelt. The author did the literature review, analyzed the results and wrote the manuscript. The work was supervised by Bettina Friedel.

Influence of Environmentally Affected Hole Transport Layers on Spatial Homogeneity and Charge Transport Dynamics of Organic Solar Cells.

Huei -Ting Chien^{1*}, Florian Pilat¹, Thomas Griesser², Harald Fitzek³, Peter Poelt^{3,4}, Bettina Friedel^{1,5}

¹*Institute of Solid State Physics, Graz University of Technology, Austria;*

²*Chair of Chemistry of Polymeric Materials, University of Leoben, Austria;*

³*Institute of Electron Microscopy and Nanoanalysis, Graz University of Technology, Austria;*

⁴*Graz Centre for Electron Microscopy, Austria*

⁵*illwerke vkw Endowed Professorship for Energy Efficiency, Energy Research Center, Vorarlberg University of Applied Sciences, Austria*

*Email: hchien@tugraz.at

KEYWORDS: organic solar cells; spatial homogeneity; photocurrent mapping; environmental degradation; colloidal films; hole-transport layer

ABSTRACT

After the efficiency of organic photovoltaic (OPV) cells achieved more than 10%, the control of stability and degradation mechanisms of solar cells became a prominent task. The improvement of device efficiency due to incorporation of a hole-transport layer (HTL) in bulk-heterojunction solar cells has been extensively reported. However, the most widely used HTL material, poly(3,4-ethylenedioxythiophene):poly(styrenesulfonate) (PEDOT:PSS) is frequently suspected to be the dominating source for device's instability under environmental conditions. Thereby effects like photooxidation and electrode corrosion are often reported to shorten device lifetime. However, often in environmental device studies, the source of degradation, whether being from the HTL, the active layer or the metal cathode are rather difficult to distinguish, because the external diffusion of oxygen and water affects all components. In this study, different HTLs, namely prepared from traditional PEDOT:PSS and also two types of molybdenum trioxide (MoO_3), are exposed to different environments such as oxygen, light or humidity, prior to device finalization under inert conditions. This allows investigating any effects within the HTL and from reactions at its interface to the indium-tin-oxide electrode or the active layer. The surface and bulk chemistry of the exposed HTL has been monitored and discussed in context to the observed device physics, dynamic charge transport and spatial performance homogeneity of the according OPV device. The results show that merely humidity-exposure of the HTL leads to decreased device performance for PEDOT:PSS, but also for one type of the tested MoO_3 . The losses are related to the amount of absorbed water in the HTL, inducing loss of active area in terms of interfacial contact. The device with PEDOT:PSS HTL after humid air exposure showed seriously decreased photocurrent by micro-delamination of swelling/shrinkage of the hygroscopic layer. The colloidal MoO_3 with water-based precursor solution presents slight decay of solar cell performance, also here caused by swelling/shrinking reaction, but by a combination of in-plane particle contact and resistance scaling with particle expansion. However, the device with quasi-continuous and alcohol-based MoO_3 showed unharmed stable electrical performance.

INTRODUCTION

The research on organic photovoltaics (OPV) reached remarkable growth due to their potential for realization of flexible, large-area and light-weight devices, categorized by environmental friendliness, low thermal budget and low-cost production e.g. via roll-to-roll printing.¹⁻⁴ The power conversion efficiency (PCE) of OPVs has been greatly improved by introducing the bulk-heterojunction (BHJ) concept by the combination of organic donor and acceptor on the nanoscale.^{1,5} The most prominent system here is the donor-acceptor couple of the conjugated polymer poly(3-hexylthiophene) (P3HT) and the fullerene derivative phenyl- C_{61} -butyric acid methyl ester (PCBM).⁶⁻⁷ Best systems currently reach up to 12% efficiency.⁸⁻⁹ Typical BHJ OPVs require a selective hole-transport layer (HTL) to block electrons and enhance hole-transfer to the anode, further to stabilize the anode's work function and reducing its surface roughness.¹⁰⁻¹¹ The most commonly used material for the anode interlayer is poly(3,4-ethylenedioxythiophene):poly(styrenesulfonate) (PEDOT:PSS) due to its benefits such as high conductivity, high transparency and good solution processibility.¹²⁻¹³ However, beside high

efficiencies and cost-effective processing, also long device lifetimes are desirable for OPVs.¹⁴ Plenty of research has been focusing on environmentally induced mechanisms leading to device degradation, based on various approaches and techniques.^{15–20} This is not exclusively caused by environments like air, light and humidity, even solvent vapors which are present during fabrication or even testing, can affect the device performance considerably.²¹ But exactly the long-term stability is a concern when using PEDOT:PSS, since the strongly hygroscopic polysulfonic acid dissociates under the influence of humidity, suspected to induce corrosion in the device.^{14–20,22} To overcome this problem, high-work function transition metal oxides, such as NiO_x,^{23–24} WO₃²⁵ and MoO₃^{26–28} have been introduced as alternatives to PEDOT:PSS in OPVs. Still, it is not clear if those materials are entirely inert against environmental influence. Spatially resolved methods such as conductive atomic force microscopy²⁹, near-field scanning optical microscopy³⁰, lock-in thermography³¹, photo- and electroluminescence³² and light-beam induced current (LBIC)^{28,32} have been applied as tools to characterize surface and device performance of OPVs. In particular, laser beam induced current (LBIC) has been widely used to investigate degradation and efficiency losses by spatial homogeneity across the entire photoactive pixel area.^{20,33–35} Further, transient photocurrents (TPC) have been used to gain knowledge about the dynamics of charge separation, determine mobilities, to describe the build-up of trapped charges and the dynamics of recombination of OPVs.^{36–42}

Aim of this work is to distinguish the environmental effects solely induced by exposition of the HTL, without the impact of a total device exposure. Therefore three different types of solution processed HTLs have been compared: (1) deposited from commercial PEDOT:PSS ink, (2) a quasi-continuous MoO₃ nanolayer obtained from deposition of an acetylacetonate precursor in alcohol and hydrolysis in air and (3) a MoO₃ layer of colloidal particles obtained from hydrolysis and condensation of a molybdate precursor in acidic aqueous solution. The two different precipitation methods for MoO₃ were chosen to see eventual effects of an acid presence. The as-prepared HTLs on indium-tin-oxide (ITO) glass substrates are exposed to dry air, humid air in the dark or with illumination, before further processing of the ITO/HTL/P3HT:PCBM/LiF/Al device stack in inert atmosphere. Surface and local bulk chemistry of the exposed HTLs have been investigated by X-ray photoelectron spectroscopy (XPS) and Raman microscopy, respectively. Finalized devices are characterized regarding their general device performance and scanned regarding their photocurrent homogeneity and local device characteristics by LBIC. The dynamic behavior of charge transport in the devices was studied by TPC. Altogether, these results allow conclusions on device changes/degradation solely connected to chemical/photochemical reactions of the HTL itself or at the closest interfaces in consequence.

EXPERIMENTAL SECTION

Materials

P3HT was supplied by Rieke Metals Inc. (MW 50–70 kg mol⁻¹, regioregularity 91–94%). PC₆₀BM was purchased from Nano-C Inc. (99.5% purity). Anhydrous chlorobenzene (99.8%) as solvent for the organic semiconductors, was purchased from Acros Organics. The aqueous

formulation of PEDOT: PSS ink was purchased from Heraeus Deutschland GmbH & Co. KG (Clevios P Jet (OLED)). Ammonium molybdate ((NH₄)₂MoO₄) (≥99.98%), hydrochloric acid (HCl) (≥37%) and bis(acetylacetonato)dioxomolybdenum(VI) (MoO₂(acac)₂) were purchased from Sigma-Aldrich. Isopropanol (99.9%) was purchased from VWR International LLC. All substances were used as received. ITO substrates (20 Ω /square, Ossila) were cleaned by sonication in acetone and isopropanol, followed by O₂ plasma etching (100 W for 30 min) briefly before further processing.

Preparation of the MoO₃ and PEDOT:PSS HTLs

Two different formulations were used to generate the MoO₃ films. The quasi-continuous films, consisting of a nanosized network with particle mean diameter of 6 nm,²⁸ are referred to in the following as **MoO₃-1**. For their preparation, following a procedure reported by K. Zilberberg et al.,²⁶ MoO₂(acac)₂ was dissolved in isopropanol to form a 0.5% (w/v) precursor solution. The colloidal films, comprising a layer of separated particles (10-30 nm),²⁸ are referred to as **MoO₃-2** in this study and were prepared as reported by Liu et al..²⁷ Here, (NH₄)₂MoO₄ was dissolved in distilled water to form a 0.005 mol/L solution. Then 2 mol/L aqueous HCl solution as catalyst was added drop-wise under stirring until the pH value of the solution was between 1 and 1.5. Particles of MoO₃ start forming already in solution by hydrolysis and condensation, thus generating a suspension. All three formulations, PEDOT:PSS, MoO₃-1 and MoO₃-2, were filtered by 0.22 μm PVDF membrane filters (Sigma Aldrich) prior to deposition and spin-coated onto ITO substrates at 4000 rpm for PEDOT: PSS and 3000 rpm for MoO₃ for 40s, respectively. The layers of MoO₃-1 and MoO₃-2 were kept in ambient air at room temperature for 1 h for hydrolysis of the precursor. Finally, films were annealed at 160 °C for 20 min to dry and promote oxide formation. The PEDOT: PSS layers were merely heated to 160 °C for 20 min under Argon (Ar) flow for removal of water. The film thickness of PEDOT:PSS is around 40 nm, MoO₃-1 and MoO₃-2 are both around 10 nm. The as-prepared HTLs were either used immediately for device fabrication (referred to as ***/Fresh**) or underwent selected exposure before. For this purpose films were submitted to dry air with <20% relative humidity (***/Air**) or humid air with >80% relative humidity (***/H₂O**) without any illumination, or to dry air under white light illumination (tungsten halogen) at 10% equivalent of AM1.5G (***/Air&light**), respectively. For each condition, the temperature was 25°C and the duration of exposure was 18 hours. Devices were fabricated immediately after exposure. Samples for XPS investigation were prepared with the same procedure on unpatterned ITO substrates. Different to the standard process, samples for Raman spectroscopy were prepared on ITO substrates for PEDOT:PSS and on Si substrates for MoO₃-1 and MoO₃-2 by drop casting method to obtain thicker layers (~80nm) to increase the weak signal intensity.

Device fabrication

Standard solar cells with P3HT:PCBM photoactive layer according to the architecture shown in Figure 1 were assembled in inert gas atmosphere, using named HTLs of **MoO₃-1**, **MoO₃-2** and **PEDOT: PSS** directly after different environments exposures. The active layer was applied on the according ITO/HTL substrate by spin-coating from a solution of P3HT and PCBM (1:1 weight ratio, 18 mg/mL each) in 70°C chlorobenzene at 1500 rpm for 60 s, followed by annealing at 120° C for 5 min. The film thickness obtained is around 150 nm. The cathode was thermally evaporated as a bilayer of LiF (2nm) and Al (100 nm). The nominal active area of the

devices is 6 mm^2 (pixel size $1.5 \text{ mm} \times 4.0 \text{ mm}$).

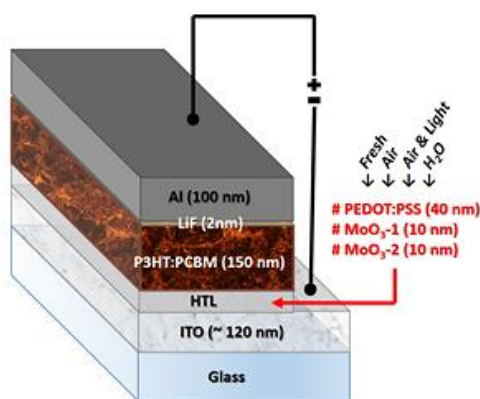


Figure 1. Investigated device architecture with the focus on different hole-transport layers and their environmental exposure conditions.

Characterization

The surface chemistry of HTLs was characterized by XPS and local bulk chemistry by Raman spectroscopy. The XPS (Thermo Fischer Scientific, Waltham, MA USA) is equipped with a monochromatic Al $K\alpha$ X-ray source (1486.6 eV). All scans were performed at room temperature. The peaks were fitted using a Gaussian/Lorentzian mixed function employing Shirley background correction (Software XPSPEAK41). Raman measurements were performed with a Horiba Jobin Yvon LabRam 800 HR spectrometer equipped with a 1024×256 CCD (Peltier-cooled) and an Olympus BX41 microscope. All scans were done using a laser wavelength of 532 nm (50 mW), an x50 Olympus LMPlanFLN (N.A. 0.5) objective and a 300 l/mm grating (spectral resolution of 3 cm^{-1}). Spatial Raman spectroscopy characteristics for point-to-point analysis were taken in line-scans along $100 \mu\text{m}$ scanning area with $2 \mu\text{m}$ step size for PEDOT:PSS, and with $4 \mu\text{m}$ for $\text{MoO}_3\text{-1}$ and $\text{MoO}_3\text{-2}$, respectively. In order to avoid damage to the sample, the laser intensity was reduced to 10 % for the measurements of PEDOT:PSS and $\text{MoO}_3\text{-2}$ and to 1 % for the measurements of $\text{MoO}_3\text{-1}$. The photocurrent density–voltage (J–V) characteristics of the OPV cells were recorded using a computer-controlled Keithley 2636A source meter and AM1.5G illumination ($100 \text{ mW}/\text{cm}^2$) from a solar simulator (Model 10500, ABET Technologies, rated ABB). Spatial photocurrent distribution was determined by laser beam induced current (LBIC) method, scanning with a computer-controlled nano-manipulator-driven xy-stage (Kleindiek Nanotechnik, NanoControl NC-2-3) and excitation with a 532 nm laser (<5mW) with a focused spot-size of $\approx 2 \mu\text{m}$. Spatial photocurrent mappings were scanned with $40 \mu\text{m}$ step size across the entire photoactive pixel area of $4.0 \text{ mm} \times 1.5 \text{ mm}$ (Figure 1). Local photocurrent-voltage characteristics for point-to-point analysis were taken in line-scans along the long side of each pixel, scanning from the left (0 mm) to the right (4 mm) with $160 \mu\text{m}$ step size. For transient photocurrent measurements, a 530 nm green LED (Thorlabs, M530L2) was used as the light source and a 300 μs square pulse from a function generator (HAMEG HMF 2550) at 1 kHz was used to power the LED. The photocurrent of the devices was measured by an oscilloscope (HAMEG HMO 3002 Series) with input impedance of 50Ω . For voltage-dependent photocurrent transients, devices were connected to a computer-controlled Keithley 2636A source meter operating in DC mode.

RESULTS AND DISCUSSION

To investigate how the environmental conditions such as air, illumination and humidity affect the HTLs and in consequence lead to degradation of the OPV devices, solar photocurrent density-voltage (J-V) characteristics were recorded, shown in Figure 2.

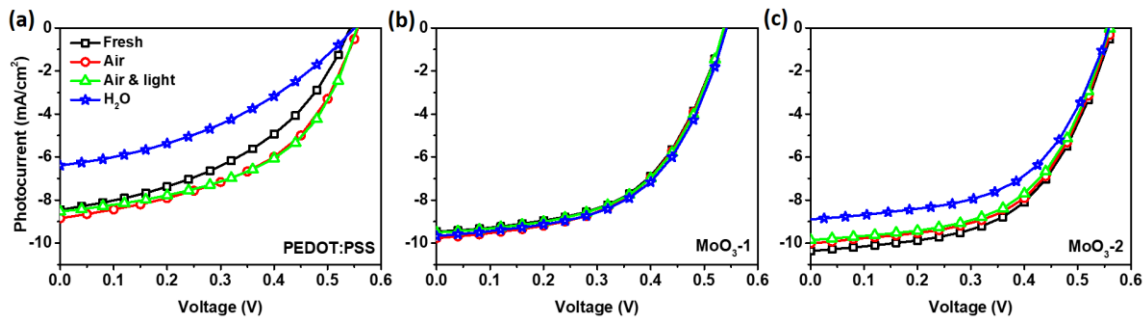


Figure 2. Photocurrent characteristics under AM1.5G of devices with fresh prepared HTLs and after different environmental exposures (a) PEDOT:PSS (b) MoO₃-1 (c) MoO₃-2.

In every case the “fresh” condition acts as blind sample in this study, to account for environment-independent relaxation, aging or measurement-related changes of the materials. Figure 2(a) shows the J-V-characteristics of devices with exposed PEDOT:PSS HTLs. It can be seen that *PEDOT:PSS/Air* and *PEDOT:PSS/Air&light* present the best performance of the 4 conditions, with the highest rectangularity indicated by fill factors (FF) of 0.49 and 0.50, respectively. *PEDOT:PSS/Fresh* on the other hand, shows equal short-circuit current (J_{SC}) of around -8.6 mA/cm^2 and open-circuit voltage (V_{OC}) of around 0.54, but considerably lower fill factor of only 0.44. However, the by far lowest performance is shown by *PEDOT:PSS/H₂O*, which exhibits lower rectangularity with FF of 0.39 and additionally greatly reduced photocurrent of J_{SC} of -6.4 mA/cm^2 , but stable V_{OC} of 0.55. The behaviour of the fresh sample compared to the air- and light-exposed ones can be explained by reduced interfacial charge transport efficiency between PEDOT:PSS and neighboring layers and an associated higher series resistance of the device, indicated by low FF and the change in slope around the V_{OC} , respectively. The reason for the lack in interfacial transfer is the non-equilibrium condition the PEDOT:PSS layer is in when it is processed into a device right away. In that case, a certain degree of aging is necessary for relaxation of the polymer and its surface groups to make better contact to the ITO electrode and the active layer. The low FF accompanied by reduced photocurrent in *PEDOT:PSS/H₂O* on the other hand, is a sign for loss of active area, in the sense of ITO corrosion producing insulating islands or local (photo)degradation of the adjacent active area facilitated by the absorbed water diffusing from the exposed PEDOT:PSS layer.⁴³⁻⁴⁵ Figure 2(b) shows the solar J-V curve of devices with MoO₃-1 HTL after different environmental exposures. All four samples, *MoO₃-1/Fresh*, *MoO₃-1/Air*, *MoO₃-1/Air&light* and *MoO₃-1/H₂O* show identical unaltered performance irrespective of the exposure of the HTL, with J_{SC} of about -9.5 mA/cm^2 , a V_{OC} of 0.54 and a quite high fill factor of 0.54. This suggests that MoO₃-1 is a considerably stable HTL material with unalterable surface chemistry, morphology or electric properties. Figure 2(c) shows the solar photocurrent characteristics of devices comprising fresh or exposed MoO₃-2 HTLs. Three of the samples, *MoO₃-2/Fresh*, *MoO₃-2/Air* and *MoO₃-2/Air&light* exhibit very similar characteristics with J_{SC} around -10.3 mA/cm^2 , V_{OC} of 0.56

and FF of 0.55. Only the photocurrent output of the humidity-exposed sample MoO_3-2/H_2O is significantly lower with J_{SC} of -8.9 mA/cm^2 , while neither the FF nor the V_{OC} are affected. The fact that FF and series resistance (indicated by the slope near V_{OC}) do not change compared to the other samples, but only the current, indicates that the loss of photocurrent is caused by loss of photoactive area contributions, either by local insulating areas due to corrosion of the ITO electrode interface or by degradation of the adjacent organic semiconductor. Though the current slopes in V_{OC} look quite parallel for MoO_3-2/H_2O compared to the other exposure conditions, there is a difference in series resistance with an increase of around 9 %, implying that the bulk or interfacial charge transport is slightly affected.

To differentiate any effects caused by the devices' charge transport ability and potential trapping phenomena, charge transport dynamics were studied via TPC. Complete sets of biased photocurrent transients following 300 μs square laser pulses for devices with exposed HTLs, for all conditions are shown in the Supporting Information with relative (Figure S1) and normalized currents (Figure S2). Selected normalized transient photocurrents are displayed in Figure 3, for devices of exposed PEDOT:PSS HTL (all conditions) and for the humidity-exposed MoO_3 HTLs. Comparing the device response of *PEDOT:PSS/Fresh*, *PEDOT:PSS/Air*, *PEDOT:PSS/Air&light* and *PEDOT:PSS/H₂O* in Figure 3 (a)-(d), one particular feature can be noticed, that is a current-overshoot of the device at the start of the square light pulse for some samples.

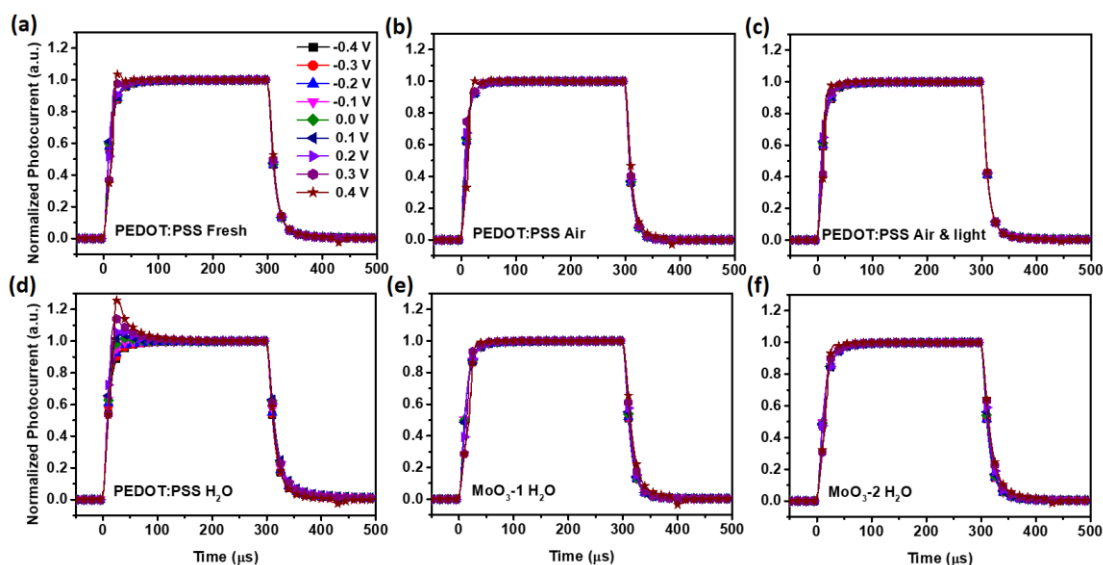


Figure 3. Normalized TPC (normalized by the steady state photocurrent at 300 μs) at different applied bias of selected devices with different environmentally exposed HTLs, namely (a) freshly prepared PEDOT:PSS (b) PEDOT:PSS after air exposure in the dark (c) PEDOT:PSS after air with illumination (d) PEDOT:PSS after humid air exposure in the dark (e) MoO_3-1 after humid air exposure in the dark (f) MoO_3-2 after humid air exposure in the dark.

For *PEDOT:PSS/Fresh* this feature occurs quite weakly and merely for higher positive voltages. For *PEDOT:PSS/H₂O* on the other hand the effect is present starting from -0.2 V and gets more pronounced the more positive the voltage. *PEDOT:PSS/Air* and *PEDOT:PSS/Air&light* do not show this behavior. Otherwise the transient characteristics of the devices with exposed PEDOT:PSS are quite similar with rise (t_{90}) of $t_{90}(\text{PEDOT:PSS}) = 25 \pm 2 \mu\text{s}$ and fall times (t_{10}) of $t_{10}(\text{PEDOT:PSS}) = 25 \pm 2$

μs , respectively. With one exception, PEDOT:PSS/H₂O has slightly extended rise and fall times of $t_{90}(\text{PEDOT:PSS/H}_2\text{O}) = 27 \mu\text{s}$ and $t_{10}(\text{PEDOT:PSS/H}_2\text{O}) = 33 \mu\text{s}$. In devices with MoO₃ HTL current shoots are not observed for any condition. Exemplarily, the photocurrent transients of **MoO₃-1/H₂O** and **MoO₃-2/H₂O** are shown in Figure 3 (e) and (f). The transients of the MoO₃ HTL devices behave quite similar for any of the exposure conditions or bias voltage (see also Supplemental Information Figure S2) with rise and fall times of around $t_{90}(\text{MoO}_3\text{-1}) = 29 \pm 1 \mu\text{s}$ and $t_{10}(\text{MoO}_3\text{-1}) = 30 \pm 1 \mu\text{s}$, and of around $t_{90}(\text{MoO}_3\text{-2}) = 27 \pm 1 \mu\text{s}$ and $t_{10}(\text{MoO}_3\text{-2}) = 26 \pm 1 \mu\text{s}$, respectively. With one exception, MoO₃-2/H₂O has slightly extended rise and fall times of $t_{90}(\text{MoO}_3\text{-2/H}_2\text{O}) = 30 \mu\text{s}$ and $t_{10}(\text{MoO}_3\text{-2/H}_2\text{O}) = 30 \mu\text{s}$. The slight homogeneous increase of charge extraction times when the applied bias is varied from -0.4 V to 0.4 V, is directly assigned to the influence of decreased internal electric field. Lack of heavy or abrupt changes to the rise and fall times and absence of any overshoot behavior are signs for stable, unhindered and well balanced transport in the devices.⁴⁶ Especially the biasing is a valuable tool to identify energetic barriers or traps in a device, as the applied voltage depending on polarity and strength helps photogenerated charges to overcome barriers, getting released from traps and swept out of the device.^{41,47} In the case of MoO₃-HTL device sets, where divergent behavior could have been expected after the general J-V characteristics, transients show no signs of delayed charges or blocking behaviour. Only **MoO₃-2/H₂O** shows slightly longer rise and fall times, indicating a lower charge transport efficiency of solar cell influenced by the HTL's or interfacial contact resistance. The case of PEDOT:PSS is there somehow more complex. While the air- and air/light exposure shows no signs for blocking of delayed transport either, the fresh and the humidity-exposed film seem to induce a build-up of charges in the device upon switch-on, seen as the overshoot of current at the start of the square laser pulse. This is clearly a consequence of an interface issue near the ITO electrode or near the active layer. The fact that for the fresh one this only happens weakly and only for high positive voltages, reducing the internal electric field of the device, supports the aforementioned theory of an unrelaxed PEDOT:PSS layer. When the bias is strong enough to overcome this eventual layer contact problem, the device transport is normal. For the humidity-exposed PEDOT:PSS layer the consequences seem to be more severe, as the charge build-up already takes effect from negative biases and builds up fast when reducing the device's internal field. This behavior is typical for traps in a device.^{41,47} Merely for negative voltages exceeding -0.3 V the charge transport is unhindered, giving an idea about the strength/depth of the charge traps in these devices. The longer rise and fall times also imply a lower charge transport efficiency of solar cell. Thereby the rising relative magnitude of the overshoot transient peaks to the steady state photocurrent with increasing applied voltage, correlates with trap-facilitated recombination.³⁸ In this case their origin could be migrated indium or oxidation sites in the organic active layer, or at surface defects (e.g. dangling bonds) of the corroded inorganic ITO.³⁷ The build-up of trapped charges in the device may hereby lead to increased recombination rates either directly through trap-assisted recombination routes such as Shockley-Read-Hall recombination, or through space charge mediating increases in bimolecular recombination and/or decreases in charge separation efficiency.³⁸ When the overshoot transient peaks are not observed in the reversed bias region this indicates that the larger internal electric field in the device inhibits trap-mediated recombination.⁴⁷

XPS and Raman spectroscopy were investigated to understand changes in surface

chemistry and local bulk chemistry of HTL films after different environmental exposure, which might explain their impact on the adjacent layers within the solar cell stack. The films' XPS core level spectra of atoms relevant to the respective material are shown in Figure 4.

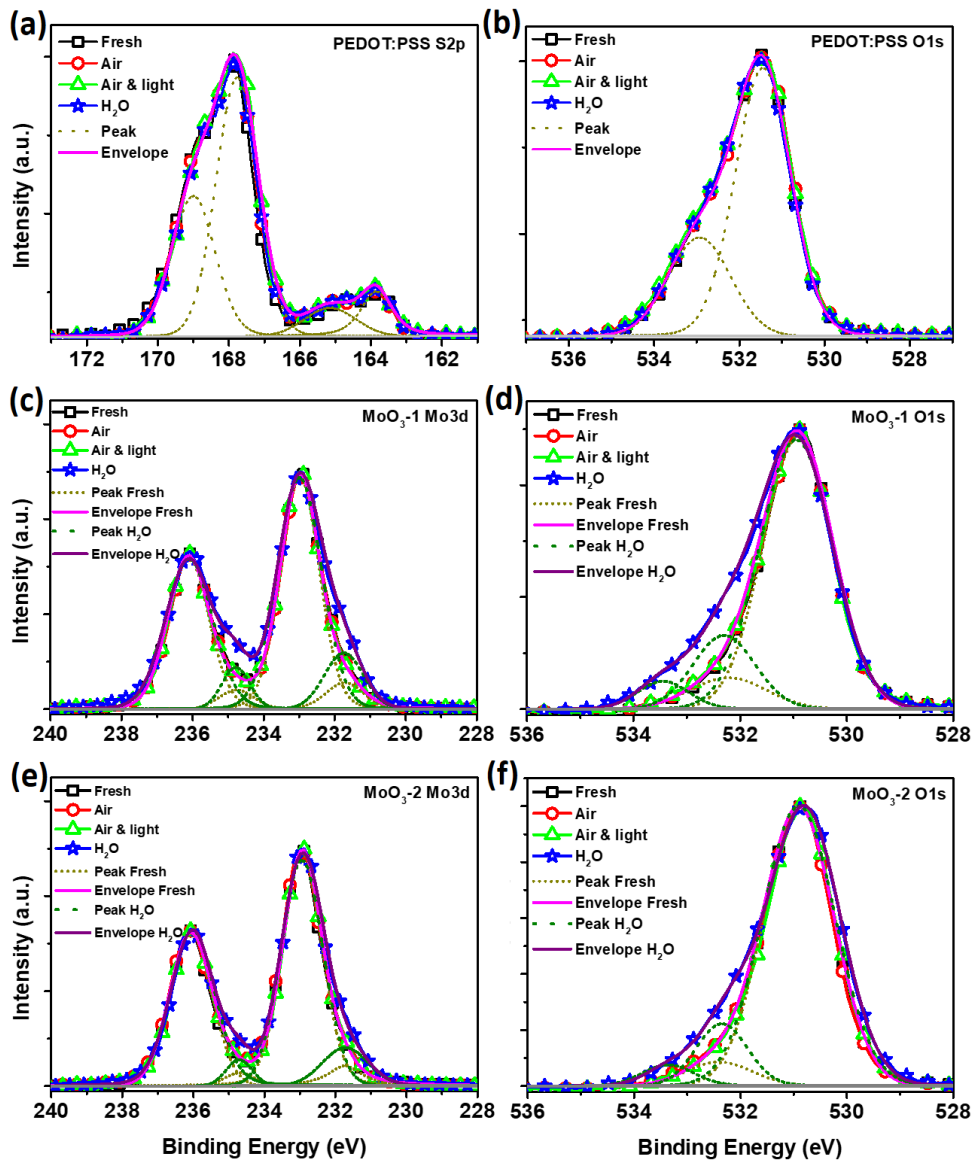


Figure 4. XPS spectra of different HTL films after selected environmental exposures: (a) S 2p core level of PEDOT:PSS (b) O 1s core level of PEDOT:PSS (c) Mo 3d core level of MoO₃-1 (d) O 1s core level of MoO₃-1 (e) Mo 3d core level of MoO₃-2 (f) O 1s core level of MoO₃-2.

The S 2p and O 1s core level spectra in *PEDOT:PSS* HTLs for different exposure conditions are presented in Figure 4(a) and (b), respectively. In the S 2p signal of PEDOT:PSS (Figure 4a), two weak low-binding energy peaks appear at approximately 165.1 eV and 163.9 eV, corresponding to the spin-split components of the sulfur atoms in the PEDOT, while the stronger high-binding energy peaks at 169.0 eV and 167.8 eV correspond to the sulfur atoms in PSS.⁴⁸⁻⁴⁹ The intensity relation between PEDOT and PSS contributions is typical, because the PEDOT:PSS particles and films thereof are covered with PSS, therefore diminishing the PEDOT signal. However, no clear difference is seen for different exposure scenarios. Figure 4(b) shows the XPS spectra of O 1s core

level, a main peak at 531.5 eV that originates from SO_3^{2-} acid groups of PSS, and a weaker shoulder at 533.0 eV due to C-O bonds of PEDOT.⁵⁰ Also these spectra exhibit no clear changes on surface chemistry of PEDOT:PSS HTLs. It should be mentioned though that water eventually adsorbed by PSS in humidity-exposed films might have been released in the XPS's high vacuum chamber before measurement was initialized. Figure 4 (c) and (e) show the *Mo 3d* doublet core level spectra of **MoO₃-1** and **MoO₃-2** films. Both materials demonstrate comparable results for fresh films and for air and air with illumination exposures. The doublet peaks show a slight asymmetric line shape, suggesting the presence of mixed oxidation states of Mo, which slightly shift their energy. The major contribution comes from Mo^{6+} oxidation states with the *3d_{3/2}* peak at 236.0 eV and *3d_{5/2}* at 232.8 eV, while the minor underlying peaks centered at 234.7 eV and 231.7 eV are assigned to the 3d orbital doublet of Mo^{5+} .⁵¹⁻⁵² In both, MoO₃-1 and MoO₃-2 films, the intensity of the peaks belonging to Mo^{5+} oxidation state get stronger after humid-air exposure, visible a tail of the peaks on the low-energy side. Since for preparation of both materials hydrolysis reactions with a molybdenum precursor are involved, it is suggested absorbed humidity triggered according chemical reactions with Mo atoms in the film, leading to this shift. Figure 4(d) and (f) depict the *O 1s* core level spectra for MoO₃-1 and MoO₃-2 HTL after exposure. Again here fresh, air- and illuminated air-exposed samples are very similar, showing a main peak at 530.9 eV assigned to the O^{2-} in the oxide⁵³ and a weak second component at 532.4 eV attributed to hydroxyl groups.⁵³ With humidity-exposure a significant increase of surface hydroxyl groups is observed and additionally a further signal appears at 533.4 eV, which can be assigned to adsorbed molecular water.⁵⁴⁻⁵⁵ This confirms an ongoing hydrolysis and condensation reaction of molybdenum oxide in the film upon humidity exposure. However, none of the surface chemical observations can explain the behavior of the films in the device.

Raman spectroscopy provides more detailed information related to the chemical properties of the bulk and is not recorded under vacuum, allowing the exposed films to maintain their chemical surface composition during the measurement. In the present experiment, spatially resolved Raman measurements were performed which allow a point-to-point analysis of the film's chemistry, completing the highly accurate surface sensitive but area-integrated information of XPS. Figure 5 a-c present the averaged spectra of the area scans for all exposition scenarios for PEDOT:PSS, MoO₃-1, and MoO₃-2, respectively. The complete sets of the corresponding spatially resolved Raman spectra sequences obtained by Raman microscopy scans for all exposure conditions can be found in the Supplemental Information in Figure S3. As the humidity-exposed films seem to exhibit the most relevant changes, these are shown exemplarily for each of the materials in Figure 5 d-f. Figure 5(a) shows the average spectra of point-to-point Raman analysis of **PEDOT:PSS** HTLs after different environmental exposures (see from Figure 5 (s) for humid air exposure and Figure S3 in supplement for fresh, air, and air with illumination exposures). All spectra of PEDOT:PSS HTLs after different environmental exposures show nearly identical bands, suggesting no clear chemical composition changes on PEDOT:PSS film after exposure. Those curves exhibit the main peak at 1442 cm^{-1} , corresponding to the C=C symmetrical stretching vibration of PEDOT and the band near 1370 cm^{-1} is associated with the C-C stretching.⁵⁶ The peaks at 1508 and 1570 cm^{-1} have been associated with the C=C asymmetric stretching vibrations that correspond to thiophene rings in the middle and at the end of the chains, respectively.⁵⁷ The band located at 1540 cm^{-1} is related to the splitting of these asymmetrical stretching

vibrations.⁵⁸⁻⁵⁹ All the other bands observed at 440, 578, 701, 854, 991, 1097, 1367, 1255, 1367, 1505, 1539 and 1569 cm^{-1} are also associated with PEDOT on the basis of the spectrum of PEDOT.⁵⁶⁻⁵⁷ Figure 5 (d) demonstrates spatially resolved Raman spectra from the PEDOT: PSS HTL after humid air exposure. The spectra present equal chemical composition across scanning area, merely varying by intensities with film thickness, which corresponds to the bubble feature displayed in the corresponding optical microscopy picture (Fig. 5d inset). These bubbles were exclusively found in humidity-exposed PEDOT:PSS films. It is suggested that the bubbles form as a consequence of film swelling upon water uptake by the hygroscopic polymer PSS. This means that the water exposure does not induce irreversible chemical changes in the PEDOT:PSS layer, but merely reversible water uptake, with eventual effect on morphology.

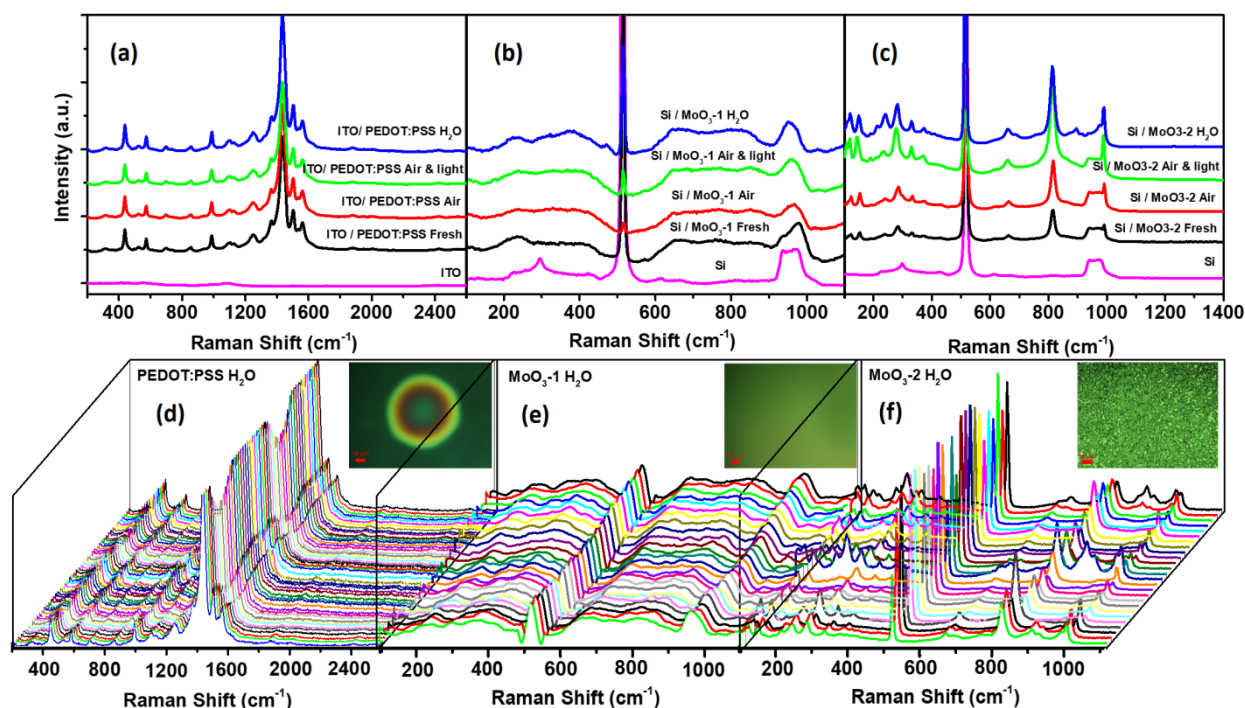


Figure 5. Area-averaged spectra of spatially resolved Raman characteristics of PEDOT:PSS (a), MoO_3 -1 (b) and MoO_3 -2 (c) films after different exposures scenarios. Spatially resolved sequences of Raman spectra for humidity-exposed PEDOT:PSS (d), MoO_3 -1 (e) and MoO_3 -2 (f).

The average spectra of ***MoO₃-1*** HTLs for freshly prepared, air, air with illumination and humid air exposures are shown Figure 5 (b). These spectra present identical features for all different conditions, indicating no obvious chemical composition transformation on the bulk MoO_3 -1 HTL films. The broad band features in the spectral are consistent with the previous literatures.⁶⁰⁻⁶² Thereby the Raman band usually appearing in the 500–1000 cm^{-1} and 200–400 cm^{-1} regions stands for the stretching (ν) and bending (δ) vibration of the structure of MoO_3 .⁶¹ Here, the broad Raman bands at about 640, 850, 950, and 989 cm^{-1} , are explained by a wide distribution of different Mo-O bond length.⁶⁰ Bands in the range of 920–1000 cm^{-1} are associated with stretching modes of the Mo=O terminal.⁶³ Looking at the spatially resolved spectra of humidity exposed MoO_3 -1 (Figure 5 (e)), all spectra exhibit high homogeneity of peaks and intensities across the scanning area, implying a great chemical stability of MoO_3 -1 HTL. The microscopic

pictures given in the inset of the diagram show a widely continuous and homogeneous film. Figure 5(c) demonstrates average Raman spectra from the four different conditions of **MoO₃-2** HTL films. The spectra of fresh MoO₃ HTL and after air and air with illumination exposures show identical Raman bands, suggesting the considerably comparable chemical composition in those films. The peaks at 152, 280, 660, 819, and 995 cm⁻¹ are associated with the thermodynamically stable α -MoO₃ crystalline phase.⁶⁴ The vibration modes, which appear in the frequency ranges of 1000–600 cm⁻¹ and 600–200 cm⁻¹, are corresponding to the stretching and deformation modes, respectively.⁶⁵⁻⁶⁶ The Raman peaks at 994 and 819 cm⁻¹ are the stretching vibration of the terminal double bonds (Mo=O).⁶⁷ The wave number range, between 150 and 400 cm⁻¹, are associated to the Mo-O modes type scissor, wagging, twist and rotational/translational rigid MoO₄ chain mode.⁶⁷ Figure 5(f) shows the sequence of spatially resolved Raman spectra of MoO₃-2 HTL after humid air exposure. Unlike the PEDOT:PSS and MoO₃-1 HTLs after humid air exposure, which present spatially homogeneous chemical composition, MoO₃-2 HTLs present considerably inhomogeneous spectra across the scanning area after humid air exposure. These inhomogeneities are not limited to thickness related intensity variations but also different new peaks appearing around 900–1000 cm⁻¹ in some local spectra. These additional peaks at 691, 901, 912, and 978 cm⁻¹ can be correlated to an h-MoO₃ crystalline phase, which has been previously reported.⁶⁸⁻⁶⁹ The peaks in the range of 880–987 cm⁻¹ are due to Mo=O bond and the band at 691 cm⁻¹ is corresponding to O–Mo–O vibrations. Most spectra of humidity-exposed MoO₃-2 show the peaks of α -MoO₃, which is the same phase as seen for all other exposure conditions, but some local spectra display mixed peaks of α -MoO₃ and h-MoO₃ in one spectrum, implying that water induces a phase transition in the MoO₃-2 HTL from α -MoO₃ to h-MoO₃. From the optical microscopy image, which is shown in the inset Figure 5(f), the film exhibits a granular structure, which is also present in freshly prepared MoO₃-2 HTLs and after air and air/illumination exposure. However, upon humidity exposure, these particles seem to swell by absorption of water from around 50 nm for other conditions to about 200 nm. This swelling and also the different MoO₃-phase alters the grain boundaries and charge transport properties of the film and thus may lead to lower conductivity of the MoO₃-2 HTL film.

To investigate how altered surface and bulk properties of environmentally exposed HTLs and their local homogeneities affect OPV devices they have been integrated in, microscale laser-beam-induced photocurrent mapping was conducted. Figure 6 shows relative photocurrent density (J) maps of P3HT:PCBM solar cells with PEDOT:PSS, MoO₃-1 and MoO₃-2 HTLs after different environmental exposures with a scanning area of 1500 μ m x 4000 μ m. On the given length scale, the photocurrent map of **PEDOT:PSS/Fresh** exhibits only subtle wave-like fluctuations across the area of around 5% of highest photocurrent amplitude, except for some considerably lower current near the pixel edges. Further, some very defined spots of 100 μ m with slightly lower performance are visible. In comparison, both **PEDOT:PSS/Air** and **PEDOT:PSS/Air&light**, show slightly more homogeneous photocurrent distribution as **PEDOT:PSS/Fresh**, with similar current gradient, but without visible pattern and without mentioned edge effects. For humidity-exposed PEDOT:PSS this changes drastically. **PEDOT:PSS/H₂O** shows a highly inhomogeneous photocurrent output, with a wave-like pattern across the surface like **PEDOT:PSS/Fresh**, wherein only 20% of the output area shows unchanged high performance, while for about 2/3 of the area photocurrent output is reduced by 15%, for about 1/10 by 25%

photocurrent and output is basically negligible for the remaining area.

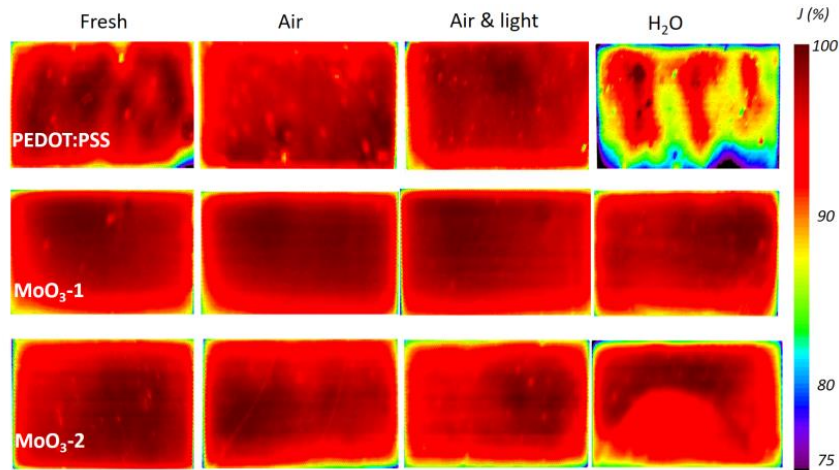


Figure 6. Relative photocurrent density maps of P3HT:PCBM solar cells with PEDOT:PSS, MoO₃-1 and MoO₃-2 HTLs after different environmental exposures with a scanning area of 1500 μm x 4000 μm.

The fact that air exposure of the HTL neither with nor without illumination has an effect on homogeneity of photocurrent distribution, indicates that PEDOT:PSS itself is not affected by the treatment and also does not trigger defects in the device later. The localized lower photocurrent output spots, which are visible in all the devices with PEDOT:PSS HTLs are assigned to the aggregation of colloidal particles, which has been proven in a previous report²⁸ and do not show this edge effects due to the longer relaxation time (during exposure) before device fabrication. The edge effects visible for the fresh device may be caused by aforementioned non-equilibrium interface between ITO and PEDOT:PSS, which affects the film most near the crossover between the ITO pixel patch and the glass substrate. The humidity-exposed device shows the worst performance along the pixel edges for a similar reason. In this case, the moisture uptake makes the PEDOT:PSS film expand. As the film is confined to the substrate dimensions, this leads to folding of the film, thereby creating wave-like current fluctuations. At the crossover between ITO and glass this may lead to partial delamination and thus contact loss. Devices with MoO₃-1 HTLs show remarkably comparable homogenous photocurrent distributions for all different environmental exposures *MoO₃-1/Fresh*, *MoO₃-1/Air*, *MoO₃-1/Air&light* and *MoO₃-1/H₂O*, merely with a mild smooth photocurrent gradient of less than 5% across the pixel area. This means that the subtle changes in surface chemistry of *MoO₃-1/H₂O*, which have been observed in XPS, are negligible for the photocurrent homogeneity. This is slightly different for solar cells with MoO₃-2 HTLs. They exhibit quite identical homogeneous photocurrent maps for three of the conditions *MoO₃-2/Fresh*, *MoO₃-2/Air* and *MoO₃-2/Air&light*, with a smooth photocurrent gradient of less than 5%, but compared to MoO₃-1, with a smaller area fraction of highest output. The homogeneous spatial photocurrent is consistent with the highly homogeneous surface and bulk chemical composition seen from XPS and Raman spectroscopic spectra. In contrast, *MoO₃-2/H₂O* demonstrates slight inhomogeneities in photocurrent, at the pixel edges, where photocurrent output is decreased down to 85%. From this outcome three possible scenarios can be considered

following the absorption of water vapor by the film: swelling of $\text{MoO}_3\text{-2}$ particles causing lower conductivity of the film (mentioned earlier in context of microscopy), loss of inter-particle/interfacial contact from swelling/shrinking of the particles or from potential ITO corrosion by the remaining acidity in the film, diminishing the conductivity of the actual electrode.

To gain a deeper understanding of the roots for local photocurrent losses in the devices, point-to-point J-V analyses across pixel sections have been conducted, to investigate their device physics. Different from the integrated J-V performance measured under simulated solar conditions (AM1.5G), local photocurrents were measured at 532 nm wavelength, which is at the spectral response maximum of the P3HT:PCBM active layer blend. Figure 7 shows the local photo-J-V curves of devices with the different HTLs after humidity-exposure, recorded along a central scanning line along the long-side of device pixel. These samples have been selected here because merely humidity-exposure displays significant features in the local photocurrent scans, while other conditions *fresh*, *air* and *air&light* are characterized by extraordinary conformity. Complete sets of according scans for all studied conditions of the three materials are presented in Figure S4 of the Supporting Information. For better visibility of any performance variance between local J-V characteristics across a device area, the curves have been color-coded (analogous to the relative photocurrent of the maps in Figure 6) in order of their achieved short-circuit current.

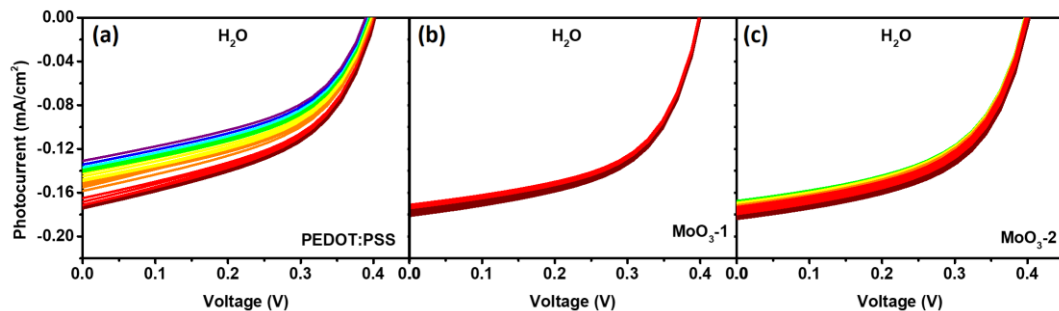


Figure 7. Local photo-J-V curves from a central line-scan along the long-side of devices with different HTL materials after humid air in the dark exposure (a) PEDOT:PSS (b) $\text{MoO}_3\text{-1}$ (c) $\text{MoO}_3\text{-2}$.

Figure 7(a) shows the point-to-point analysis J-V curves of *PEDOT:PSS/H₂O*. All characteristics show consistent slopes at the intersection with V_{OC} and good rectangularity with slight deviation of FF between 0.45 and 0.48, indicating that neither significant series resistance nor interfacial charge transport are affected by humidity in PEDOT:PSS or reactions thereof with adjacent layers. Further, the V_{OC} fluctuates only minorly between 0.40 V to 0.38 V across the device area and the curves exhibit unchanged parallel slopes at the intersection with the current-density axis (J_{SC} region), suspending leakage currents as reason for decreased photocurrent, as the parallel resistance is stable. This is in good agreement with the results from integral device characterization. Therefore the origin for the fluctuating photocurrent across the device area, with J_{SC} varying by 28 % between -0.18 mA/cm^2 at optimum performance and 0.13 mA/cm^2 , is loss of

active area. As not leakage, barriers or charge transfer limitations are obvious, photocurrent loss is most likely caused by either local degradation of the active layer by reaction with absorbed water from PSS or by local loss of contact area at the ITO/HTL or HTL/active layer interface. The latter could arise from delamination of the swelling/shrinking PEDOT:PSS layer during water uptake/release during/after device fabrication. Another reason could be failing interfacial wetting during device fabrication upon changes of the HTL's surface chemistry. Figure 7(b) shows the local J-V characteristics of **MoO₃-1/H₂O**. Here, considerably uniform J-V curves are visible, which are very similar to the ones of **MoO₃-1/Fresh**, **MoO₃-1/Air**, **MoO₃-1/Air&light** shown in the Supporting Information (Figure S4). **MoO₃-1/H₂O** exhibits exclusively constant V_{OC} of 0.4V, J_{SC} of -0.18 mA/cm² and FF of 0.57 across the device area. This is in good agreement with their integral device performance and the high homogeneity shown in the photocurrent maps. The minor deviation of photocurrent (around 5% compared to maximum) across the device area is suspected to originate from regular morphological inhomogeneities of the devices²⁸ and not related to the treatment. Figure 7(c) demonstrates the local variations of J-V curves of **MoO₃-2/H₂O**. Different to the previous MoO₃-1, here fluctuations across the device area are visible. The curves exhibit consistent parallel slopes at the intersection with J_{SC} and with V_{OC} and constant rectangularity with a FF of 0.55, indicating that neither parallel resistance nor series resistance of interfacial charge transfer are affected by humidity from the HTL. In addition, the variation of V_{OC} between 0.39 V and 0.40 V is negligible. Merely the fluctuation of photocurrent between -0.18 mA/cm² at maximum and lowest of -0.16 mA/cm² is significant. Thereby this fluctuation of 11% is less than for **PEDOT:PSS/H₂O** but considerably stronger than for **MoO₃-1/H₂O**. As similar for **PEDOT:PSS/H₂O** also here it is obvious that this effect is caused by a loss of active area, as suggested either from active layer degradation⁷⁰ or by loss of interfacial contact of the HTL with adjacent layers. This would not be unlikely because particle swelling of MoO₃-2 upon water-exposure was observed earlier. Thereby it can be speculated that the difference in intensity of this device "degradation" effect between **PEDOT:PSS/H₂O** and **MoO₃-2/H₂O** is related to the amount absorbed water and thus volume fluctuation of the layer.

For a complete overview with greater detail on all HTLs and conditions, the solar cell parameters were extracted/calculated from the respective photo-J-V characteristics in Figure 7 and in the Supplemental Information Figure S4. They are plotted in Figure 8 for J_{SC} (a), V_{OC} (b), FF (c) and R_S (d). As expected from photocurrent maps and their local device-physical analysis, devices with MoO₃-1 HTL exhibit clearly the highest spatial homogeneity and stability regarding electrical performance independent of different environmental exposures, with very narrow distribution of less than 5% deviation of the values for J_{SC}, V_{OC}, FF and R_S. In contrast, the devices with PEDOT:PSS HTL present most strongly fluctuating performance and inhomogeneity of local output of J_{SC}, V_{OC}, FF and R_S for different environmental exposures. In the worst case, which is humidity exposure reflected by **PEDOT:PSS/H₂O**, the deviation is up to 28% for J_{SC} photocurrent and around 6% for its V_{OC}, FF and R_S. For **PEDOT:PSS/Fresh**, **PEDOT:PSS/Air**, **PEDOT:PSS/Air&light**, all parameters show a more narrow and very similar distribution, with deviations as high as around 8 % for J_{SC} and between 5 and 6 % for V_{OC}, FF and R_S, indicating that air and illumination (equivalent of 10% of AM1.5G) do not cause obviously localized surface and electric property changes of the HTL. **MoO₃-2/Fresh**, **MoO₃-2/Air**, and **MoO₃-2/Air&light** present all a quite narrow distribution of solar cell parameters with deviations around 5 % for J_{SC} and less than 3 % for V_{OC},

FF and R_s . MoO_3-2/H_2O on the other hand, exhibits a wider distribution of J_{SC} with a deviation of 10% and less than 4% for V_{OC} , FF and R_s , however, no inhomogeneity effect on R_s in comparison with other environmental exposures of MoO_3-2 HTL. These results clearly show that the values of PEDOT:PSS HTLs are spreading towards lower J_{SC} , slightly lower V_{OC} , slightly lower FF and higher series resistance upon HTL contact with humidity. For the MoO_3 HTLs, MoO_3-1 shows no scattering of the values independent of the exposure condition, while for MoO_3-2 , clearly a subtle shift in J_{SC} and V_{OC} is noted but with relatively not much increased scattering. Since merely representative data have been selected for display in the main text for the sake of better visibility, statistical data on the devices' variations in performance are presented in the Supplemental Information Figure S5 for completion.

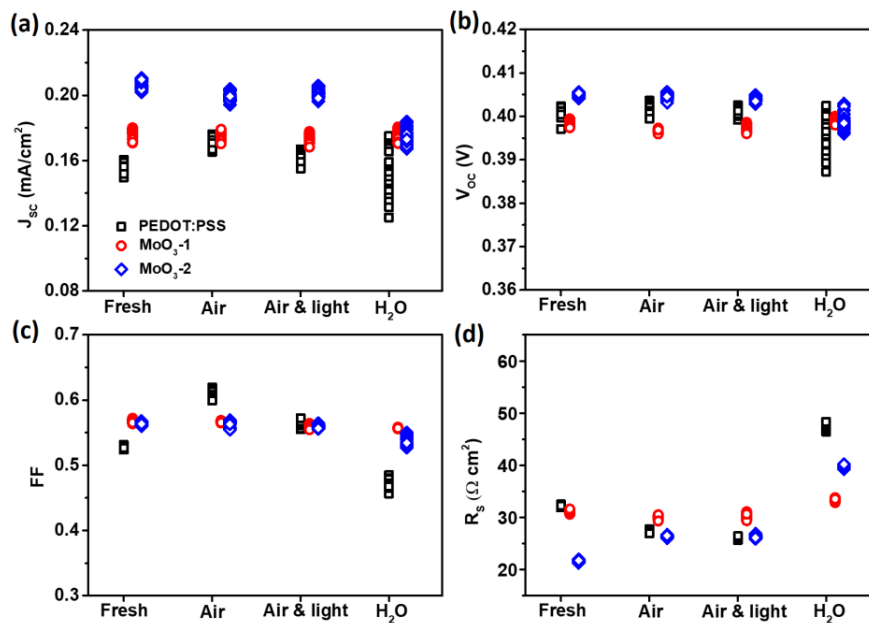


Figure 8. Solar cell parameters as extracted/calculated from the local photo-J-V curves recorded at different points along the long-side (4 mm) of a device pixel, showing (a) J_{SC} , (b) V_{OC} , (c) FF and (d) R_s .

Discussion

The presented results show clearly that PEDOT:PSS as HTL induces the most unstable, fluctuating and inhomogeneous performance in standard OPV devices, compared to the two MoO_3 HTLs. Thereby humidity-exposure of PEDOT:PSS before device completion strongest affects electrical performance, despite the fact the XPS and Raman spectra show no change in surface and bulk chemistry of the layer, suspending ITO corrosion as a potential reason and strengthening the argument of layer delamination by consecutive swelling and shrinking of the film upon water uptake or release. A significant current-overshoot and extended charge extraction times seen in the transients confirm less efficient charge transport near the electrode, leading to an accumulation of charges at high light intensities/ current densities. A highly inhomogeneous spatial photocurrent output with a wave-like pattern across the surface supports the idea of

interfacial contact issues from partial delamination of PEDOT:PSS from ITO or/and active layer. This in consequence leads to a general lower photocurrent in the device. The good rectangularity with constant FF, minor V_{OC} fluctuation and stable parallel resistance from point-to-point J-V analysis, showing no significant changes of the cell parameters except for photocurrent and series resistance, again confirms this assumption. Another condition which surprisingly causes performance changes, is the immediate use of a freshly deposited and dried PEDOT:PSS layer, leading to equal J_{SC} and V_{OC} of, but considerably lower fill factor and an associated higher series resistance of the device, compared to the ones containing air or illumination exposed PEDOT:PSS. The reason is suspected to be from limited interfacial charge transport between the PEDOT:PSS and neighboring layers due to the unrelaxed PEDOT:PSS film. This argument is supported by the fact that any form of short storage before device completion improves the device and further by the observation of a weak current overshoot in the transients at high positive bias and subtle wave-like fluctuations in the spatial photocurrent. Dry air or light exposure of the PEDOT:PSS does not lead to significant changes of the actual layer, indicating that PEDOT:PSS itself is not affected by the treatment, nor to changes of the device, confirming that also no defects are triggered later in the device. **MoO₃-1** demonstrates the most stable electrical device performance among the tested materials, with unaltered J_{SC} , V_{OC} , high fill factor and comparable homogeneous spatial photocurrent distributions for fresh, air, air with illumination and humidity exposures. This reflects also in stable charge transport dynamics seen in the transients and bulk chemical stability seen from Raman spectra. The surface chemistry shows a significant increase of surface hydroxyl groups upon humidity exposure, visible from stronger Mo⁵⁺ contribution in XPS, which seems not to affect the film properties or the device performance. **MoO₃-2** is reasonably stable for fresh films and after exposure to air or illumination, exhibiting comparable output of all solar cell parameters, J_{SC} , V_{OC} , FF, and R_s , as well as highly homogeneous spatial photocurrent output. However, upon humidity exposure, according devices show lower photocurrent output, obviously induced by a slightly increased series resistance, while other parameters are barely affected. Together with the microscopic observation of **MoO₃-2** particle swelling/shrinking upon water uptake/release, this can be explained by decreased interparticle-contact, detachment from the ITO surface or increased resistance of the actual swollen particle due to the hydrated (thus insulating) outer shell. A slightly longer charge extraction time in the photocurrent transients but missing overshoot, supports this theory and confirms that the effect on charge transport efficiency is not as strong as for **PEDOT:PSS**. This is further supported by a homogeneously slightly increased series resistance visible from local variations of J-V curves. A subtle decrease in photocurrent along the pixel edge suggests detachment of the particles at the transition between glass and ITO on the substrate, thus similar but not the same phenomenon as observed for humidity-exposed PEDOT:PSS. The observed phase transition from α -MoO₃ to h-MoO₃ in the Raman spectra is not relevant to lower charge transport efficiency due to the actual higher conductivity of h-MoO₃ compared to α -MoO₃.⁷¹ However, it cannot be excluded that the recrystallization changed interparticle or particle/ITO contact.

CONCLUSIONS

We compared the surface and device inhomogeneity of P3HT:PCBM bulk heterojunction

PV cells influenced by three different solution-processed colloidal HTLs with various environmental exposures, one PEDOT:PSS, one continuous MoO₃ and one nanoparticle MoO₃ film. HTLs are exposed to the air in the dark, air with equivalent 10% AM1.5G solar illumination, and humidity in the dark, and compare them with fresh samples, respectively, to gain the information about potentially occurring degradation mechanisms influenced by HTLs with different environmental effects. Standard OPV device investigation is accompanied by the comparison of surface and bulk chemistry of the HTLs, along with the devices' charge transport dynamics, spatial photocurrent distribution and local device physics. By this exposure procedure limited to the actual HTL, the environmental effects caused directly on the HTL and potential late effects within the device structure could be distinguished without affecting the entire device stack, different to studies with exposure of the complete device. Here we could clearly show that humidity exposure of PEDOT:PSS does not actually lead to device failure by the suspected ITO corrosion or humidity diffusion into the active layer with associated degradation, but instead merely signs for partial interfacial contact loss were found. These are caused by the consecutive swelling and shrinking of the layer on top of the ITO substrate and after incorporation within the device stack. Also fresh PEDOT:PSS layers which are immediately incorporated into devices present interfacial resistance, but, in that case because the layer is in a completely dry rigid non-equilibrium state at use. Any form of relaxation time leads to improvement. The two investigated solution processed molybdenum oxide films show extremely stable unchanging electrical behavior and homogeneity for any condition, except for humidity exposure of the particle layer. In that case humidity treatment leads to swelling of the particles, similar to PEDOT:PSS, but due to the thin non-continuous layer, the effect leads to generally higher series resistance and thus lower current by either detachment of particles from the other layers or increased resistance of the particles themselves by the insulating hydrate shell. In no condition and for no material any material degradation was found for the HTL itself or the device they were incorporated in. The observation of decreased device performance merely by the loss of interfacial contact upon water-uptake induced swelling is a completely new view on the matter.

ASSOCIATED CONTENT

Supporting Information

The Supporting Information contains complete sets of relative and normalized transient photocurrents, spatially resolved sequences of Raman spectra, statistical data on the solar cell performance and sets of local photo-J-V curves across the device for different hole-transportation layer materials after various environmental exposures.

AUTHOR INFORMATION

Corresponding Author

*Email: hchien@tugraz.at

Notes

The authors declare no competing financial interest.

ACKNOWLEDGMENT

H.-T. C. and B.F. are grateful to the Austrian Science Fund (FWF) for financial support (Project No. P 26066)

REFERENCES

- (1) Yu, G.; Gao, J.; Hummelen, J. C.; Wudl, F.; Heeger, A. J. Polymer Photovoltaic Cells: Enhanced Efficiencies via a Network of Internal Donor-Acceptor Heterojunctions. *Science* **1995**, *270*, 1789–1791.
- (2) Thompson, B. C.; Fréchet, J. M. J. Polymer-Fullerene Composite Solar Cells. *Angewandte Chemie (International ed. in English)* **2008**, *47*, 58–77.
- (3) Hoppe, H.; Sariciftci, N. S. Polymer Solar Cells. In *Photoresponsive Polymers II*; Marder, S. R., Lee, K.-S., Eds.; Springer Berlin Heidelberg: Berlin, Heidelberg, 2008; pp 1–86.
- (4) Brabec, C. J.; Gowrisanker, S.; Halls, J. J. M.; Laird, D.; Jia, S.; Williams, S. P. Polymer-Fullerene Bulk-Heterojunction Solar Cells. *Advanced materials (Deerfield Beach, Fla.)* **2010**, *22*, 3839–3856.
- (5) Sariciftci, N. S.; Smilowitz, L.; Heeger, A. J.; Wudl, F. Photoinduced Electron Transfer From a Conducting Polymer to Buckminsterfullerene. *Science* **1992**, *258*, 1474–1476.
- (6) Li, G.; Shrotriya, V.; Huang, J.; Yao, Y.; Moriarty, T.; Emery, K.; Yang, Y. High-Efficiency Solution Processable Polymer Photovoltaic Cells by Self-Organization of Polymer Blends. *Nat Mater* **2005**, *4*, 864–868.
- (7) Ma, W.; Yang, C.; Gong, X.; Lee, K.; Heeger, A. J. Thermally Stable, Efficient Polymer Solar Cells with Nanoscale Control of the Interpenetrating Network Morphology. *Adv. Funct. Mater.* **2005**, *15*, 1617–1622.
- (8) Green, M. A.; Emery, K.; Hishikawa, Y.; Warta, W.; Dunlop, E. D. Solar Cell Efficiency Tables (version 46). *Prog. Photovolt: Res. Appl.* **2015**, *23*, 805–812.
- (9) Dennler, G.; Scharber, M. C.; Ameri, T.; Denk, P.; Forberich, K.; Waldauf, C.; Brabec, C. J. Design Rules for Donors in Bulk-Heterojunction Tandem Solar Cells?: Towards 15 % Energy-Conversion Efficiency. *Adv. Mater.* **2008**, *20*, 579–583.
- (10) Kim, J. Y.; Kim, S. H.; Lee, H.-H.; Lee, K.; Ma, W.; Gong, X.; Heeger, A. J. New Architecture for High-Efficiency Polymer Photovoltaic Cells Using Solution-Based Titanium Oxide as an Optical Spacer. *Adv. Mater.* **2006**, *18*, 572–576.
- (11) Chan, M. Y.; Lee, C. S.; Lai, S. L.; Fung, M. K.; Wong, F. L.; Sun, H. Y.; Lau, K. M.; Lee, S. T. Efficient Organic Photovoltaic Devices Using a Combination of Exciton Blocking Layer and Anodic Buffer Layer. *Journal of Applied Physics* **2006**, *100*, 94506.
- (12) Cao, Y.; Yu, G.; Zhang, C.; Menon, R.; Heeger, A. Polymer Light-Emitting Diodes with Polyethylene Dioxythiophene–Polystyrene Sulfonate as the Transparent Anode. *Synthetic Metals* **1997**, *87*, 171–174.
- (13) Heithecker, D.; Kammoun, A.; Dobbertin, T.; Riedl, T.; Becker, E.; Metzendorf, D.; Schneider, D.; Johannes, H.-H.; Kowalsky, W. Low-Voltage Organic Electroluminescence Device with an Ultrathin, Hybrid Structure. *Appl. Phys. Lett.* **2003**, *82*, 4178–4180.
- (14) Jørgensen, M.; Norrman, K.; Krebs, F. C. Stability/Degradation of Polymer Solar Cells. *Solar*

Energy Materials and Solar Cells **2008**, *92*, 686–714.

(15) Schafferhans, J.; Baumann, A.; Wagenpfahl, A.; Deibel, C.; Dyakonov, V. Oxygen Doping of P3HT:PCBM Blends: Influence on Trap States, Charge Carrier Mobility and Solar Cell Performance. *Organic Electronics* **2010**, *11*, 1693–1700.

(16) Seemann, A.; Egelhaaf, H.-J.; Brabec, C. J.; Hauch, J. A. Influence of Oxygen on Semi-Transparent Organic Solar Cells with Gas Permeable Electrodes. *Organic Electronics* **2009**, *10*, 1424–1428.

(17) Hermenau, M.; Riede, M.; Leo, K.; Gevorgyan, S. A.; Krebs, F. C.; Norrman, K. Water and Oxygen Induced Degradation of Small Molecule Organic Solar Cells. *Solar Energy Materials and Solar Cells* **2011**, *95*, 1268–1277.

(18) Rivaton, A.; Chambon, S.; Manceau, M.; Gardette, J.-L.; Lemaître, N.; Guillerez, S. Light-Induced Degradation of the Active Layer of Polymer-Based Solar Cells. *Polymer Degradation and Stability* **2010**, *95*, 278–284.

(19) Ecker, B.; Nolasco, J. C.; Pallarés, J.; Marsal, L. F.; Posdorfer, J.; Parisi, J.; Hauff, E. von. Degradation Effects Related to the Hole Transport Layer in Organic Solar Cells. *Adv. Funct. Mater.* **2011**, *21*, 2705–2711.

(20) Chien, H.-T.; Zach, P. W.; Friedel, B. Short-Term Environmental Effects and Their Influence on Spatial Homogeneity of Organic Solar Cell Functionality. *ACS applied materials & interfaces* **2017**, *9*, 27754–27764.

(21) Wang, W.; Guo, S.; Herzig, E. M.; Sarkar, K.; Schindler, M.; Magerl, D.; Philipp, M.; Perlich, J.; Müller-Buschbaum, P. Investigation of morphological degradation of P3HT:PCBM bulk heterojunction films exposed to long-term host solvent vapor. *J. Mater. Chem. A* **2016**, *4*, 3743–3753

(22) Jong, M. P. de; van Ijzendoorn, L. J.; Voigt, M. J. A. de. Stability of the Interface between Indium-Tin-Oxide and Poly(3,4-ethylenedioxythiophene)/Poly(styrenesulfonate) in Polymer Light-Emitting Diodes. *Appl. Phys. Lett.* **2000**, *77*, 2255–2257.

(23) Irwin, M. D.; Buchholz, D. B.; Hains, A. W.; Chang, R. P. H.; Marks, T. J. P-Type Semiconducting Nickel Oxide as an Efficiency-Enhancing Anode Interfacial Layer in Polymer Bulk-Heterojunction Solar Cells. *Proceedings of the National Academy of Sciences* **2008**, *105*, 2783–2787.

(24) Steirer, K. X.; Chesin, J. P.; Widjonarko, N. E.; Berry, J. J.; Miedaner, A.; Ginley, D. S.; Olson, D. C. Solution Deposited NiO Thin-Films as Hole Transport Layers in Organic Photovoltaics. *Organic Electronics* **2010**, *11*, 1414–1418.

(25) Meyer, J.; Kröger, M.; Hamwi, S.; Gnam, F.; Riedl, T.; Kowalsky, W.; Kahn, A. Charge Generation Layers Comprising Transition Metal-Oxide/Organic Interfaces: Electronic Structure and Charge Generation Mechanism. *Appl. Phys. Lett.* **2010**, *96*, 193302.

(26) Zilberberg, K.; Gharbi, H.; Behrendt, A.; Trost, S.; Riedl, T. Low-Temperature, Solution-Processed MoO(x) for Efficient and Stable Organic Solar Cells. *ACS applied materials & interfaces* **2012**, *4*, 1164–1168.

(27) Liu, F.; Shao, S.; Guo, X.; Zhao, Y.; Xie, Z. Efficient Polymer Photovoltaic Cells Using Solution-Processed MoO₃ as Anode Buffer Layer. *Solar Energy Materials and Solar Cells* **2010**, *94*, 842–845.

(28) Chien, H.-T.; Pözl, M.; Koller, G.; Challinger, S.; Fairbairn, C.; Baikie, I.; Kratzer, M.; Teichert, C.; Friedel, B. Effects of Hole-Transport Layer Homogeneity in Organic Solar Cells – A Multi-Length

Scale Study. *Surfaces and Interfaces* **2017**, *6*, 72–80.

(29) Coffey, D. C.; Reid, O. G.; Rodovsky, D. B.; Bartholomew, G. P.; Ginger, D. S. Mapping Local Photocurrents in Polymer/Fullerene Solar Cells with Photoconductive Atomic Force Microscopy. *Nano letters* **2007**, *7*, 738–744.

(30) McNeill, C. R.; Frohne, H.; Holdsworth, J. L.; Furst, J. E.; King, B. V.; Dastoor, P. C. Direct Photocurrent Mapping of Organic Solar Cells Using a Near-Field Scanning Optical Microscope. *Nano letters* **2004**, *4*, 219–223.

(31) Breitenstein, O.; Warta, W.; Langenkamp, M. *Lock-in Thermography: Basics and Applications to Functional Diagnostics of Electronic Components*; Springer series in advanced microelectronics 10; Springer: Berlin, London, 2011.

(32) Krebs, F. C.; Søndergaard, R.; Jørgensen, M. Printed Metal Back Electrodes for R2R Fabricated Polymer Solar Cells Studied Using the LBIC Technique. *Solar Energy Materials and Solar Cells* **2011**, *95*, 1348–1353.

(33) Rösch, R.; Tanenbaum, D. M.; Jørgensen, M.; Seeland, M.; Bärenklau, M.; Hermenau, M.; Voroshazi, E.; Lloyd, M. T.; Galagan, Y.; Zimmermann, B.; Würfel, U.; Hösel, M.; Dam, H. F.; Gevorgyan, S. A.; Kudret, S.; Maes, W.; Lutsen, L.; Vanderzande, D.; Andriessen, R.; Teran-Escobar, G.; Lira-Cantu, M.; Rivaton, A.; Uzunoğlu, G. Y.; Germack, D.; Andreasen, B.; Madsen, M. V.; Norrman, K.; Hoppe, H.; Krebs, F. C. Investigation of the Degradation Mechanisms of a Variety of Organic Photovoltaic Devices by Combination of Imaging Techniques—the ISOS-3 Inter-Laboratory Collaboration. *Energy Environ. Sci.* **2012**, *5*, 6521.

(34) Krebs, F. C. *Stability and Degradation of Organic and Polymer Solar Cells*; Wiley: Chichester, 2012.

(35) Jeranko, T.; Tributsch, H.; Sariciftci, N.; Hummelen, J. Patterns of Efficiency and Degradation of Composite Polymer Solar Cells. *Solar Energy Materials and Solar Cells* **2004**, *83*, 247–262.

(36) Christ, N.; Kettlitz, S.; Mescher, J.; Valouch, S.; Lemmer, U. Dispersive Transport in the Temperature Dependent Transient Photoresponse of Organic Photodiodes and Solar Cells. *Journal of Applied Physics* **2013**, *113*, 234503.

(37) McNeill, C. R.; Hwang, I.; Greenham, N. C. Photocurrent Transients in All-Polymer Solar Cells: Trapping and detrapping effects. *Journal of Applied Physics* **2009**, *106*, 24507.

(38) Hwang, I.; McNeill, C. R.; Greenham, N. C. Drift-Diffusion Modeling of Photocurrent Transients in Bulk Heterojunction Solar Cells. *Journal of Applied Physics* **2009**, *106*, 94506.

(39) Shuttle, C. G.; Treat, N. D.; Douglas, J. D.; Fréchet, J. M. J.; Chabynyc, M. L. Deep Energetic Trap States in Organic Photovoltaic Devices. *Adv. Energy Mater.* **2012**, *2*, 111–119.

(40) Kniepert, J.; Schubert, M.; Blakesley, J. C.; Neher, D. Photogeneration and Recombination in P3HT/PCBM Solar Cells Probed by Time-Delayed Collection Field Experiments. *J. Phys. Chem. Lett.* **2011**, *2*, 700–705.

(41) Tress, W.; Corvers, S.; Leo, K.; Riede, M. Investigation of Driving Forces for Charge Extraction in Organic Solar Cells: Transient Photocurrent Measurements on Solar Cells Showing S-Shaped Current-Voltage Characteristics. *Adv. Energy Mater.* **2013**, *3*, 873–880.

(42) Zhou, H.; Zhang, Y.; Seifert, J.; Collins, S. D.; Luo, C.; Bazan, G. C.; Nguyen, T.-Q.; Heeger, A. J. High-Efficiency Polymer Solar Cells Enhanced by Solvent Treatment. *Advanced materials (Deerfield Beach, Fla.)* **2013**, *25*, 1646–1652.

(43) Crispin, X.; Marciniak, S.; Osikowicz, W.; Zotti, G.; van der Gon, A. W. D.; Louwet, F.; Fahlman,

M.; Groenendaal, L.; Schryver, F. de; Salaneck, W. R. Conductivity, Morphology, Interfacial Chemistry, and Stability of Poly(3,4-ethylene dioxythiophene)-Poly(styrene sulfonate): A Photoelectron Spectroscopy Study. *J. Polym. Sci. B Polym. Phys.* **2003**, *41*, 2561–2583.

(44) Marciniak, S.; Crispin, X.; Uvdal, K.; Trzcinski, M.; Birgersson, J.; Groenendaal, L.; Louwet, F.; Salaneck, W. Light Induced Damage in Poly(3,4-ethylenedioxythiophene) and its Derivatives Studied by Photoelectron Spectroscopy. *Synthetic Metals* **2004**, *141*, 67–73.

(45) Rannou, P.; Nechtschein, M. Ageing of Poly(3,4-ethylenedioxythiophene): Kinetics of Conductivity Decay and Lifespan. *Synthetic Metals* **1999**, *101*, 474.

(46) Li, Z.; Gao, F.; Greenham, N. C.; McNeill, C. R. Comparison of the Operation of Polymer/Fullerene, Polymer/Polymer, and Polymer/Nanocrystal Solar Cells: A Transient Photocurrent and Photovoltage Study. *Adv. Funct. Mater.* **2011**, *21*, 1419–1431.

(47) Li, Z.; McNeill, C. R. Transient Photocurrent Measurements of PCDTBT: PC₇₀BM and PCPDTBT:PC₇₀BM Solar Cells: Evidence for Charge Trapping in Efficient Polymer/Fullerene Blends. *Journal of Applied Physics* **2011**, *109*, 74513.

(48) Liu, Y.; Park, H.-G.; Lee, J. H.; Seo, D.-S.; Kim, E.-M.; Heo, G.-S. Electro-Optical Switching of Liquid Crystals Sandwiched between Ion-Beam-Spurted Graphene Quantum Dots-Doped PEDOT:PSS Composite Layers. *Optics express* **2015**, *23*, 34071–34081.

(49) Park, H.; Lee, S. H.; Kim, F. S.; Choi, H. H.; Cheong, I. W.; Kim, J. H. Enhanced Thermoelectric Properties of PEDOT: PSS Nanofilms by a Chemical Dedoping Process. *J. Mater. Chem. A* **2014**, *2*, 6532–6539.

(50) Zhang, S.; Yu, Z.; Li, P.; Li, B.; Isikgor, F. H.; Du, D.; Sun, K.; Xia, Y.; Ouyang, J. Poly(3,4-ethylenedioxythiophene): Polystyrene Sulfonate Films with Low Conductivity and Low Acidity through a Treatment of Their Solutions with Probe Ultrasonication and Their Application as Hole Transport Layer in Polymer Solar Cells and Perovskite Solar Cells. *Organic Electronics* **2016**, *32*, 149–156.

(51) Zhu, Y.; Yuan, Z.; Cui, W.; Wu, Z.; Sun, Q.; Wang, S.; Kang, Z.; Sun, B. A Cost-Effective Commercial Soluble Oxide Cluster for Highly Efficient and Stable Organic Solar Cells. *J. Mater. Chem. A* **2014**, *2*, 1436–1442.

(52) Wallace Chik Ho Choy, Fengxian Xie, ChuanDaO Wang. Solution-Processed Transition Metal Oxides. US 2014/0061550 A1, 2014.

(53) Diaz-Droguett, D. E.; Fuenzalida, V. M. Gas Effects on the Chemical and Structural Characteristics of Porous MoO₃ and MoO_{3-x} Grown by Vapor Condensation in Helium and Hydrogen. *Materials Chemistry and Physics* **2011**, *126*, 82–90.

(54) Kwon, D. W.; Park, K. H.; Hong, S. C. The Influence on SCR Activity of the Atomic Structure of V₂O₅/TiO₂ Catalysts Prepared by a Mechanochemical Method. *Applied Catalysis A: General* **2013**, *451*, 227–235.

(55) Luo, Z.; Poyraz, A. S.; Kuo, C.-H.; Miao, R.; Meng, Y.; Chen, S.-Y.; Jiang, T.; Wenos, C.; Suib, S. L. Crystalline Mixed Phase (Anatase/Rutile) Mesoporous Titanium Dioxides for Visible Light Photocatalytic Activity. *Chem. Mater.* **2014**, *27*, 6–17.

(56) Garreau, S.; Louarn, G.; Buisson, J. P.; Froyer, G.; Lefrant, S. In Situ Spectroelectrochemical Raman Studies of Poly(3,4-ethylenedioxythiophene) (PEDT). *Macromolecules* **1999**, *32*, 6807–6812.

(57) Sakamoto, S.; Okumura, M.; Zhao, Z.; Furukawa, Y. Raman Spectral Changes of PEDOT–PSS in

Polymer Light-Emitting Diodes upon Operation. *Chemical Physics Letters* **2005**, *412*, 395–398.

(58) Chiu, W. W.; Travaš-Sejdić, J.; Cooney, R. P.; Bowmaker, G. A. Spectroscopic and Conductivity Studies of Doping in Chemically Synthesized Poly(3,4-ethylenedioxythiophene). *Synthetic Metals* **2005**, *155*, 80–88.

(59) Chiu, W. W.; Travaš-Sejdić, J.; Cooney, R. P.; Bowmaker, G. A. Studies of Dopant Effects in Poly(3,4-ethylenedi-oxythiophene) Using Raman Spectroscopy. *J. Raman Spectrosc.* **2006**, *37*, 1354–1361.

(60) Diskus, M.; Nilsen, O.; Fjellvåg, H.; Diplas, S.; Beato, P.; Harvey, C.; van Schrojenstein Lantman, E.; Weckhuysen, B. M. Combination of Characterization Techniques for Atomic Layer Deposition MoO₃ Coatings: From the Amorphous to the Orthorhombic α -MoO₃ Crystalline Phase. *Journal of Vacuum Science & Technology A: Vacuum, Surfaces, and Films* **2012**, *30*, 01A107.

(61) Ivanova, T.; Gesheva, K.; Szekeres, A. Structure and Optical Properties of CVD Molybdenum Oxide Films for Electrochromic Application. *Journal of Solid State Electrochemistry* **2002**, *7*, 21–24.

(62) Chelvanathan, P.; Rahman, K. S.; Hossain, M. I.; Rashid, H.; Samsudin, N.; Mustafa, S. N.; Bais, B.; Akhtaruzzaman, M.; Amin, N. Growth of MoO_x Nanobelts from Molybdenum Bi-Layer Thin Films for Thin Film Solar Cell Application. *Thin Solid Films* **2017**, *621*, 240–246.

(63) Seguin, L.; Figlarz, M.; Cavagnat, R.; Lassègues, J.-C. Infrared and Raman Spectra of MoO₃ Molybdenum Trioxides and MoO₃ · xH₂O Molybdenum Trioxide Hydrates. *Spectrochimica Acta Part A: Molecular and Biomolecular Spectroscopy* **1995**, *51*, 1323–1344.

(64) Camacho-López, M. A.; Escobar-Alarcón, L.; Picquart, M.; Arroyo, R.; Córdoba, G.; Haro-Poniatowski, E. Micro-Raman Study of the m-MoO₂ to α -MoO₃ Transformation Induced by Cw-Laser Irradiation. *Optical Materials* **2011**, *33*, 480–484.

(65) Liu, D.; Lei, W. W.; Hao, J.; Liu, D. D.; Liu, B. B.; Wang, X.; Chen, X. H.; Cui, Q. L.; Zou, G. T.; Liu, J.; Jiang, S. High-Pressure Raman Scattering and X-Ray Diffraction of Phase Transitions in MoO₃. *Journal of Applied Physics* **2009**, *105*, 23513.

(66) Kondrachova, L.; Hahn, B. P.; Vijayaraghavan, G.; Williams, R. D.; Stevenson, K. J. Cathodic Electrodeposition of Mixed Molybdenum Tungsten Oxides from Peroxo-Polymolybdotungstate Solutions. *Langmuir : the ACS journal of surfaces and colloids* **2006**, *22*, 10490–10498.

(67) Dieterle, M.; Weinberg, G.; Mestl, G. Raman Spectroscopy of Molybdenum Oxides. *Phys. Chem. Chem. Phys.* **2002**, *4*, 812–821.

(68) Atuchin, V. V.; Gavrilova, T. A.; Kostrovsky, V. G.; Pokrovsky, L. D.; Troitskaia, I. B. Morphology and Structure of Hexagonal MoO₃ Nanorods. *Inorg Mater* **2008**, *44*, 622–627.

(69) Pan, W.; Tian, R.; Jin, H.; Guo, Y.; Zhang, L.; Wu, X.; Zhang, L.; Han, Z.; Liu, G.; Li, J.; Rao, G.; Wang, H.; Chu, W. Structure, Optical, and Catalytic Properties of Novel Hexagonal Metastable h-MoO₃ Nano- and Microrods Synthesized with Modified Liquid-Phase Processes. *Chem. Mater.* **2010**, *22*, 6202–6208.

(70) Grossiord, N.; Kroon, J. M.; Andriessen, R.; Blom, P. W. Degradation Mechanisms in Organic Photovoltaic Devices. *Organic Electronics* **2012**, *13*, 432–456.

(71) Chithambararaj, A.; Rajeswari Yogamalar, N.; Bose, A. C. Hydrothermally Synthesized h-MoO₃ and α -MoO₃ Nanocrystals: New Findings on Crystal-Structure-Dependent Charge Transport. *Crystal Growth & Design* **2016**, *16*, 1984–1995.

Influence of Environmentally Affected Hole Transport Layers on Spatial Homogeneity and Charge Transport Dynamics of Organic Solar Cells.

Huei -Ting Chien^{1}, Florian Pilat¹, Thomas Griesser², Harald Fitzek³, Peter Poelt,^{3,4} Bettina Friedel^{1,5}*

¹Institute of Solid State Physics, Graz University of Technology, Austria;

²Chair of Chemistry of Polymeric Materials, University of Leoben, Austria;

³Institute of Electron Microscopy and Nanoanalysis, Graz University of Technology, Austria;

⁴Graz Centre for Electron Microscopy, Austria

⁵illwerke vkw Endowed Professorship for Energy Efficiency, Energy Research Center, Vorarlberg University of Applied Sciences, Austria

*Email: hchien@tugraz.at

Figure S1 shows complete sets of biased photocurrent transients following 300 μs square laser pulses for devices with different environmental exposed hole transport layers (HTLs), for all conditions. Only PEDOT:PSS/Fresh and PEDOT:PSS/H₂O show a current-overshoot of the device at the start of the square light pulse. The overshoot feature occurs quite weakly and merely for higher positive voltages for PEDOT:PSS/Fresh while the same effect of PEDOT:PSS/H₂O presents starting from -0.2 V and gets more considerable with increased positive voltage.

Figure S2 normalized transient photocurrents (TPCs) from Figure S1 for devices with freshly prepared MoO₃-1 and MoO₃-2 HTL and after air in the dark, air with illumination and humid air in the dark exposures. The transients of both MoO₃ HTL devices behave quite similar for any of the exposure conditions or bias voltage with rise and fall times of around t_{90} (MoO₃-1) 29 +/- 1 μs and t_{10} (MoO₃-1) 30 +/- 1 μs , and of around t_{90} (MoO₃-2) 27 +/- 1 μs and t_{10} (MoO₃-2) 26 +/- 1 μs , respectively. No any current-overshoot behaviors are observed in all these devices.

Figure S3 shows the spatially resolved Raman spectra sequences obtained by Raman microscopy scans for freshly prepared HTLs and after air in the dark, air with illumination and humid air in the dark exposures. These spectra present identical and homogeneous features for each HTL after different exposure conditions. The microscopic pictures given in the inset of the diagram also show comparable feature for each HTL films.

Figure S4 shows local photo-J-V curves from a central line-scan along the long-side of devices with freshly prepared HTL and HTL after air in the dark, air with illumination and humid air exposure in the dark. All J-V curves present considerably uniform distribution, with unaltered short-circuit current (J_{SC}), open-circuit voltage (V_{OC}) and rectangularity with constant FF across the pixel area. Devices with each HTL material after exposure conditions show similar J_{SC} and V_{OC} output. However, *PEDOT:PSS/Fresh* shows less rectangularity with FF compare to *PEDOT:PSS/Air* and *PEDOT:PSS/Air&light*, while *MoO₃-1* and *MoO₃-2* present all similar FF for all different exposure conditions.

Figure S5 shows a statistical view on the devices' variations in performance, in terms of short-circuit current density (a), open circuit voltage (b), fill factor (c), power conversion efficiency (d) and series resistance (e). These have been taken from roughly 200 devices prepared in this study. Non-functional or obviously impaired devices have been discarded and are thus not included (they make less than 7% of all devices, with no preference to a condition).

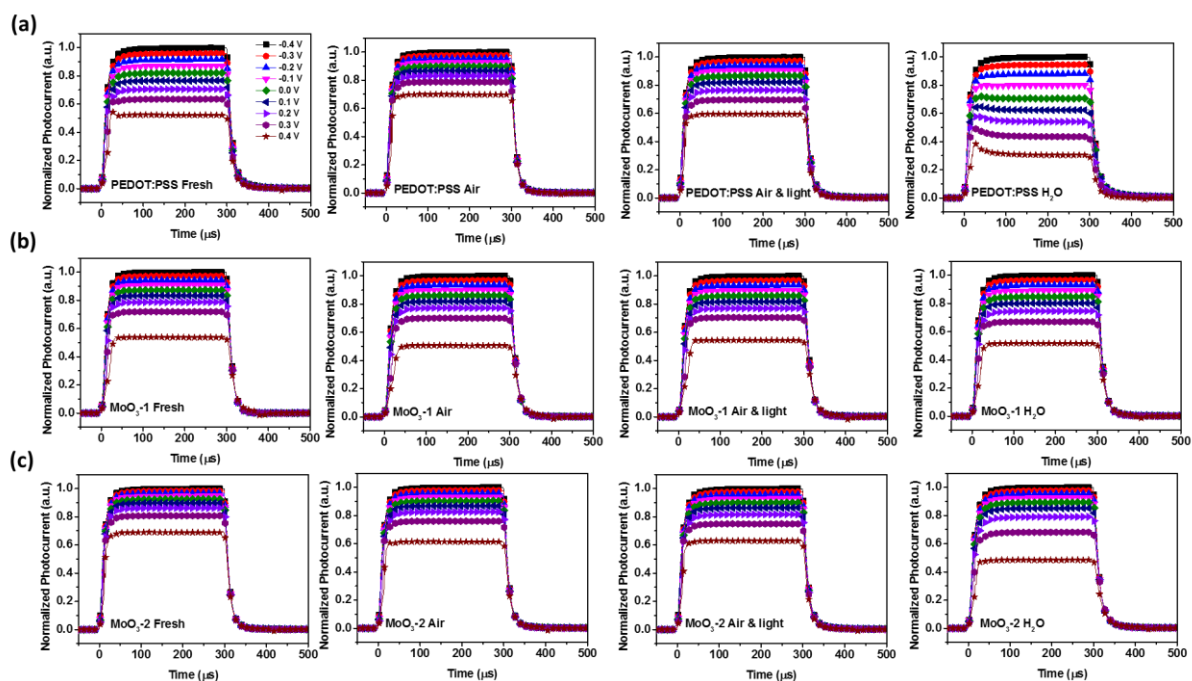


Figure S1. Relative TPC (normalized by the maximum steady state photocurrent at 300 μs for each device) at different applied bias of selected devices with freshly prepared HTL and HTL after air in the dark, air with illumination and humid air exposure in the dark (a) PEDOT:PSS (b) MoO₃-1 (c) MoO₃-2

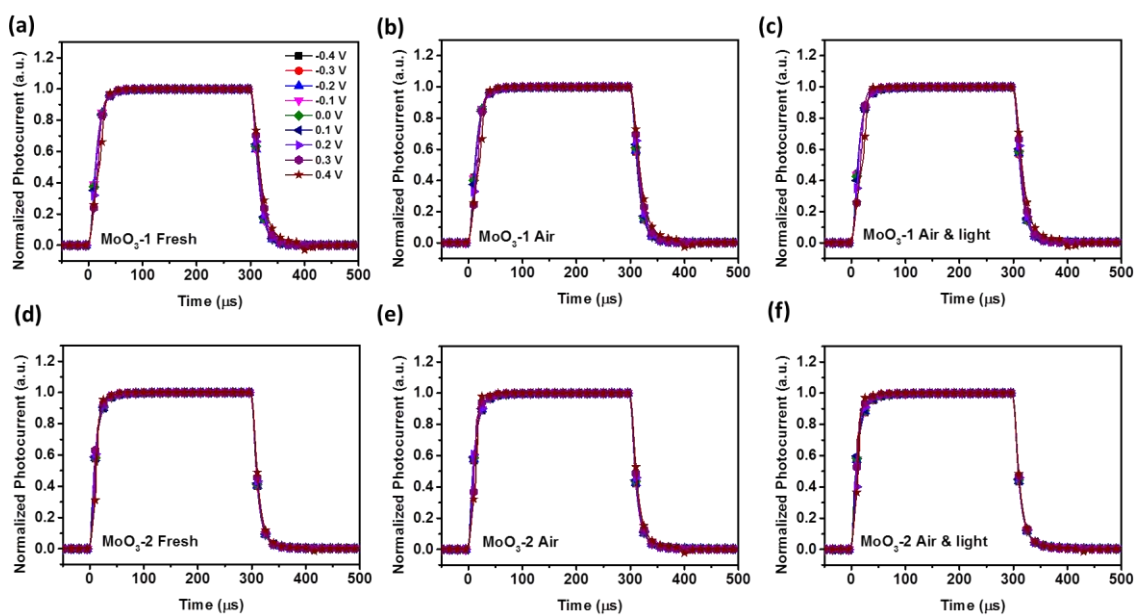


Figure S2. Normalized TPC (normalized by the steady state photocurrent at 300 μs from Figure S1) at different applied bias of selected devices with different environmentally exposed HTLs, namely (a) freshly prepared MoO₃-1 (b) MoO₃-1 after air exposure in the dark (c) MoO₃-1 after air with illumination (d) freshly prepared MoO₃-2 (e) MoO₃-2 after air exposure in the dark (f) MoO₃-2 after air with illumination.

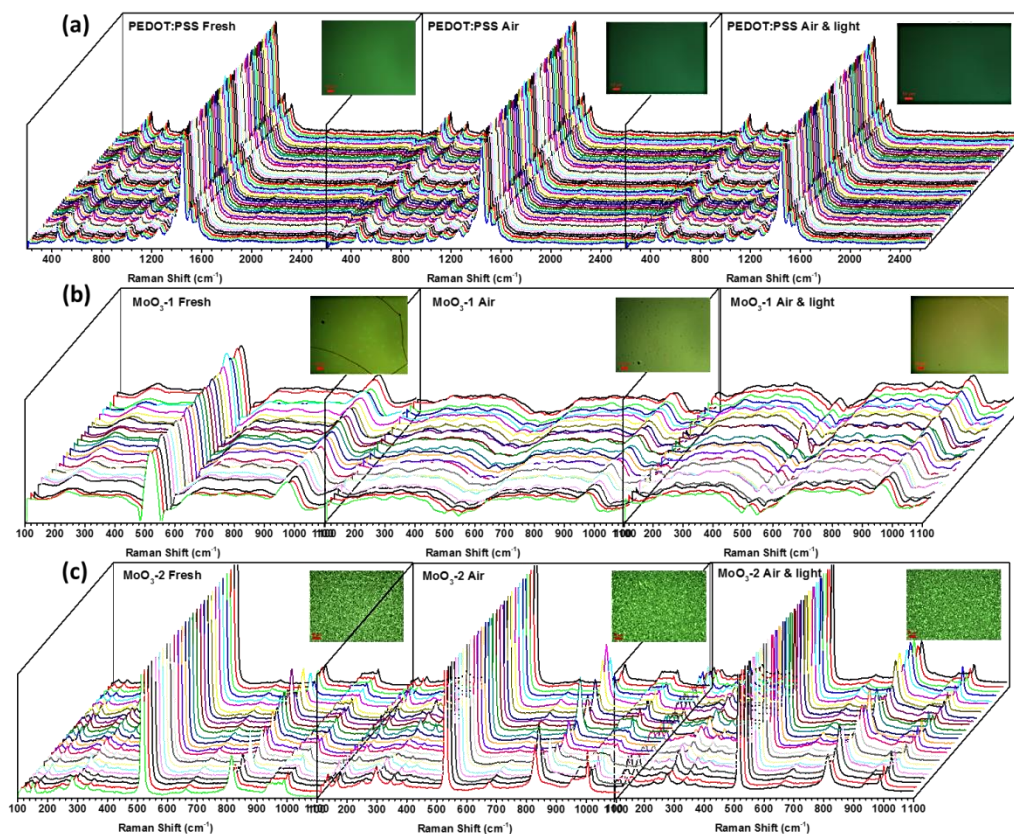


Figure S3. Spatially resolved sequences of Raman spectra for freshly prepared HTL and HTL after air in the dark, air with illumination and humid air exposure in the dark exposure (a) PEDOT:PSS (b) MoO₃-1 (c) MoO₃-2.

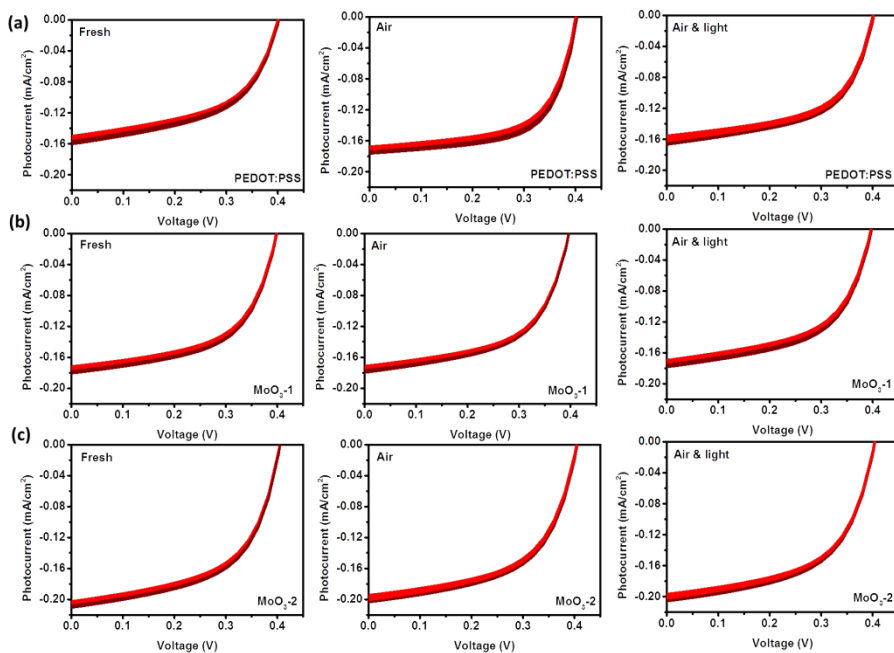


Figure S4. Local photo-J-V curves from a central line-scan along the long-side of devices with freshly prepared HTL and HTL after air in the dark, air with illumination and humid air exposure in the dark (a) PEDOT:PSS (b) MoO₃-1 (c) MoO₃-2

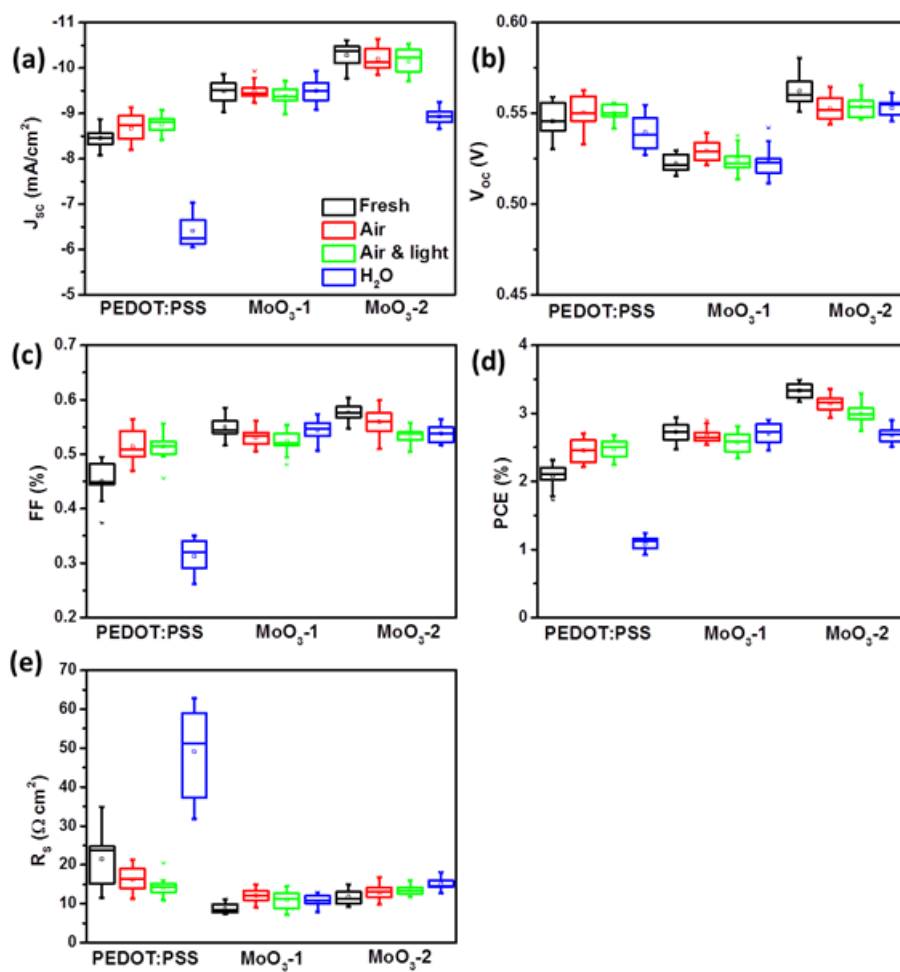


Figure S5. Statistical deviation of solar cell data as extracted/calculated from the J-V curves, showing (a) J_{sc} , (b) V_{oc} , (c) FF and (d) PCE and (e) R_s .

4.3. Short-Term Environmental Effects and Their Influence on Spatial Homogeneity of Organic Solar Cell Functionality.

Huei-Ting Chien, Peter W. Zach, Bettina Friedel

Author Contributions

The author defined the research plan, executed the experiments, fabricated the solar cells and measured the device physics. Fluorescence measurements were done by Peter W. Zach. The author did the literature review, analyzed the results and wrote the manuscript. The work was supervised by Bettina Friedel.

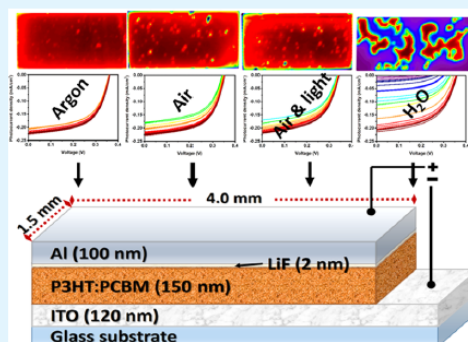
Short-Term Environmental Effects and Their Influence on Spatial Homogeneity of Organic Solar Cell Functionality

Huei-Ting Chien,^{*,†} Peter W. Zach,[‡] and Bettina Friedel^{†,§}[†]Institute of Solid State Physics and [‡]Institute of Analytical Chemistry and Food Chemistry, Graz University of Technology, 8010 Graz, Austria[§]Energy Research Center, Vorarlberg University of Applied Sciences, 6850 Dornbirn, Austria

Supporting Information

ABSTRACT: In this study, we focus on the induced degradation and spatial inhomogeneity of organic photovoltaic devices under different environmental conditions, uncoupled from the influence of any auxiliary hole-transport (HT) layer. During testing of the corresponding devices comprising the standard photoactive layer of poly(3-hexylthiophene) as donor, blended with phenyl-C₆₁-butyric acid methyl ester as acceptor, a comparison was made between the nonencapsulated devices upon exposure to argon in the dark, dry air in the dark, dry air with illumination, and humid air in the dark. The impact on the active layer's photophysics is discussed, along with the device physics in terms of integral solar cell performance and spatially resolved photocurrent distribution with point-to-point analysis of the diode characteristics to determine the origin of the observed integrated organic photovoltaic device behavior. The results show that even without the widely used hygroscopic HT layer, poly(3,4-ethylenedioxythiophene):poly(styrenesulfonate), humidity is still a major factor in the short-term environmental degradation of organic solar cells with this architecture, and not only oxygen or light, as is often reported. Different from previous reports where water-induced device degradation was spatially homogeneous and formation of Al₂O₃ islands was only seen for oxygen permeation through pinholes in aluminum, we observed insulating islands merely after humidity exposure in the present study. Further, we demonstrated with laser beam induced current mapping and point-to-point diode analysis that the water-induced performance losses are a result of the exposed device area comprising regions with entirely unaltered high output and intact diode behavior and those with severe degradation showing detrimentally lowered output and voltage-independent charge blocking, which is essentially insulating behavior. It is suggested that this is caused by transport of water through pinholes to the organic/metal interface, where they form insulating oxide or hydroxide islands, while the organic active layer stays unharmed.

KEYWORDS: organic solar cells, spatial homogeneity, photocurrent mapping, parallel microdiodes, environmental degradation



INTRODUCTION

Organic photovoltaic (OPV) cells are considered to be a promising low-cost alternative source of renewable energy compared to traditional inorganic solar cells due to their advantages of easy fabrication, low manufacturing cost, light weight, mechanical flexibility, and environmental friendliness.^{1–4} Because of the short diffusion range of photo-generated excitons in organic semiconductors, the most commonly used photoactive layer structure in OPVs is the donor/acceptor bulk-heterojunction (BHJ), basically consisting of a blend of donor and acceptor. One intensively studied BHJ system is the blend of the conjugated polymer poly(3-hexylthiophene) (P3HT) for its excellent carrier mobility and a highly ordered packing structure^{5,6} and the fullerene acceptor [6,6]-phenyl-C₆₁-butyric acid methyl ester (PCBM).^{7–9} In a typical BHJ OPV architecture, this photoactive layer is sandwiched between two electrodes, and eventually additional charge-selective interlayers in-between, to enhance collection of the photogenerated charges and decrease leakage currents.^{10–12}

To date, record efficiencies of lab-scale OPV devices have been reported in the range of 10–12%.¹³ However, irreproducibility and instability are still major problems for this type of device, and these issues lead to performance variations of up to 10% batch-to-batch on identical devices. Therein, the operation environment has been identified as playing a critical role as a potential source for OPV degradation, with four main factors primarily responsible for limiting stability: oxygen, water, light, and heat.^{14,15} Deterioration by photo-oxidation of the conjugated polymer, diffusion of foreign atoms creating charge traps and recombination centers, corrosion of the electrodes, or thermally induced morphological reorganization are only a few examples of the manifold effects occurring.^{16,17} In some cases, degradation is even accelerated by introducing certain auxiliary layers into the device architecture. A well-known example is the

Received: June 11, 2017

Accepted: August 3, 2017

Published: August 3, 2017

prominent hole-transport (HT) material poly(3,4-ethylenedioxythiophene):poly(styrenesulfonate) (PEDOT:PSS), once popular for its advantageous solution processability, high transparency, work function, and conductivity.^{18,19} When applied between the inorganic indium-tin-oxide (ITO) electrode and an organic semiconductor, its function is to block electron transport and lower the hole-extraction barrier to the anode. Unfortunately, the hygroscopic acid component PSS causes electrode corrosion in humidity, leading to indium diffusion, instability, shorter life times, and spatial inhomogeneity of devices.^{20–23} To circumvent these problems, alternative interlayers such as transition metal oxides^{24–26} have been used to substitute PEDOT:PSS as HT layers in OPVs. Despite the fact that numerous long-term degradation and stability studies with standard OPV device architectures have been reported, only a few publications have been dedicated to the study of degradation and homogeneity, free of the influence of HT layers.²⁷

This work aims to fill this gap by studying the short-term environmental effects on standard P3HT:PCBM OPV devices in the absence of any HT layers between the ITO electrode and photoactive layer. The architecture of the devices studied is shown in Figure 1. Thereby, a comparison was made between

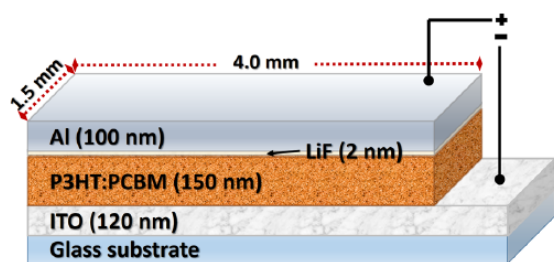


Figure 1. Illustration of the device architecture for hole-transport layer (HTL) free organic solar cells investigated in this study.

exposure to different environments: in argon, dry air, or humid air in the dark, and in dry air under illumination. Different sorts of imaging techniques have been used in the past to monitor degradation of optoelectronic devices.^{28–30} In photovoltaics, laser beam induced current (LBIC), is a prominent method for mapping the photocurrent response across the device area and thus localizing fabrication/degradation defects.^{12,31–34} Additionally, local photocurrent–voltage characteristics at different sites of the device can be used to identify the nature of the defect causing the locally diminished photocurrent. This technique was adapted from photovoltaic module testing, where the physics of the entire module is determined by the physics of assembled subdevices.³⁵ In the case of a single solar cell, the spatial distribution of heterogeneously responding areas can be seen as parallel-connected microdiodes,³⁶ which has been demonstrated for polycrystalline inorganic thin-film solar cells, for example, by Karpov et al.³⁷

By connecting global device behavior with such spatially resolved characteristics and photocurrent imaging, we can gain knowledge about the predominant factors causing initial performance loss of the devices shortly after fabrication.

EXPERIMENTAL SECTION

Materials. Poly(3-hexylthiophene) was supplied by Rieke Metals, Inc. (molecular weight 50–70 kg/mol, regioregularity 91–94%). [6,6]-Phenyl-C₆₁-butyric acid methyl ester was purchased from Nano-C Inc.

(99.5% purity). Anhydrous chlorobenzene, as solvent for the organic semiconductors, was purchased from Sigma-Aldrich. All materials were used as received. ITO-coated glass substrates (20 Ω/sq; Ossila Ltd.) were cleaned by sonication in acetone and 2-propanol, followed by O₂-plasma etching (100 W for 30 min) briefly before use.

Sample Preparation. Standard P3HT:PCBM solar cells without HT layers were fabricated with the layer structure ITO/P3HT:PCBM/LiF/Al. The active layer was applied directly onto patterned ITO glass by spin-coating from a solution of P3HT and PCBM (1:1 weight ratio, each 18 mg/mL in 70 °C chlorobenzene) at 1500 rpm for 60 s, followed by annealing at 120 °C for 5 min. The obtained active layer thickness was around 150 nm. The cathode was thermally evaporated as a bilayer of LiF (2 nm)/Al (100 nm). Active layer samples for photophysical testing were prepared as described above on spectroil quartz substrates. For mimicking the different environmental conditions, the nonencapsulated devices were exposed to static argon (Ar), dry air with <20% relative humidity (air), or humid air with >80% relative humidity (H₂O) without any illumination, and to dry air under white light illumination (tungsten halogen, 10% equivalent of AM1.5G) (air and light), respectively. Durations of exposure were varied between 0 and 240 min, and devices were characterized immediately after. Active layer samples were treated accordingly. The ambient temperature was around 25 °C for all conditions. To avoid additional effects from long-term photocurrent mapping in air, exposed devices were encapsulated before measurement.

Characterization. UV–vis optical absorbance spectra of the P3HT:PCBM active layers were recorded between 300 and 800 nm, using a Shimadzu UV-1800 UV–vis spectrophotometer. Fluorescence spectra were acquired on a Fluorolog3 spectrofluorometer (Horiba Jobin Yvon) equipped with a near-infrared-sensitive photomultiplier R2658 from Hamamatsu (300–1050 nm). Excitation wavelength was 532 nm. The absolute luminescence quantum yields were determined using an integrating sphere from Horiba. Both UV–vis absorbance spectra and fluorescence spectra were recorded in air. The photocurrent density–voltage (J – V) characteristics of the solar cells without encapsulation were measured in argon (glovebox) under simulated solar illumination (AM1.5G) at 1 sun (100 mW/cm²) (solar simulator, model 10500; Abet Technologies) using a computer-controlled Keithley 2636 A source meter. Their spectral response was recorded from external quantum efficiency (EQE) acquired for wavelengths from 375 to 900 nm, using a 250 W white light source (tungsten halogen) with monochromator, with a computer-controlled Keithley 2636 A source meter and calculated against a calibrated silicon photodiode. Spatial photocurrent distribution was determined by the laser beam induced current (LBIC) method, scanning with a computer-controlled nanomanipulator-driven xy -stage (NanoControl NC-2-3; Kleindiek Nanotechnik), and with excitation from the glass/ITO side with a 532 nm laser (<5 mW) with a focused spot-size of $\approx 2 \mu\text{m}$. For spatial photocurrent mapping, local short circuit current was scanned with a 40 μm step size across the entire photoactive pixel area of 4.0 mm \times 1.5 mm (Figure 1). Local photocurrent–voltage characteristics for point-to-point analysis were taken in line-scans along the long side of each pixel, scanning from left (0 mm) to right (4 mm) with a 200 μm step size. EQE, LBIC, and local photocurrent–voltage characteristics for point-to-point analysis were performed on encapsulated devices to prevent avertible further effects by measurement in an air atmosphere.

RESULTS AND DISCUSSION

Integral Device Behavior. To understand the type and dynamics of the effects of different environments on OPV devices, the repeatedly exposed devices were analyzed depending on duration and atmosphere. Additional short time light exposure during measurement was confirmed to be negligible with respect to the relevant effects in this study. The solar photocurrent density–voltage (J – V) characteristics of the devices after exposure sequences of 60 min up to a total

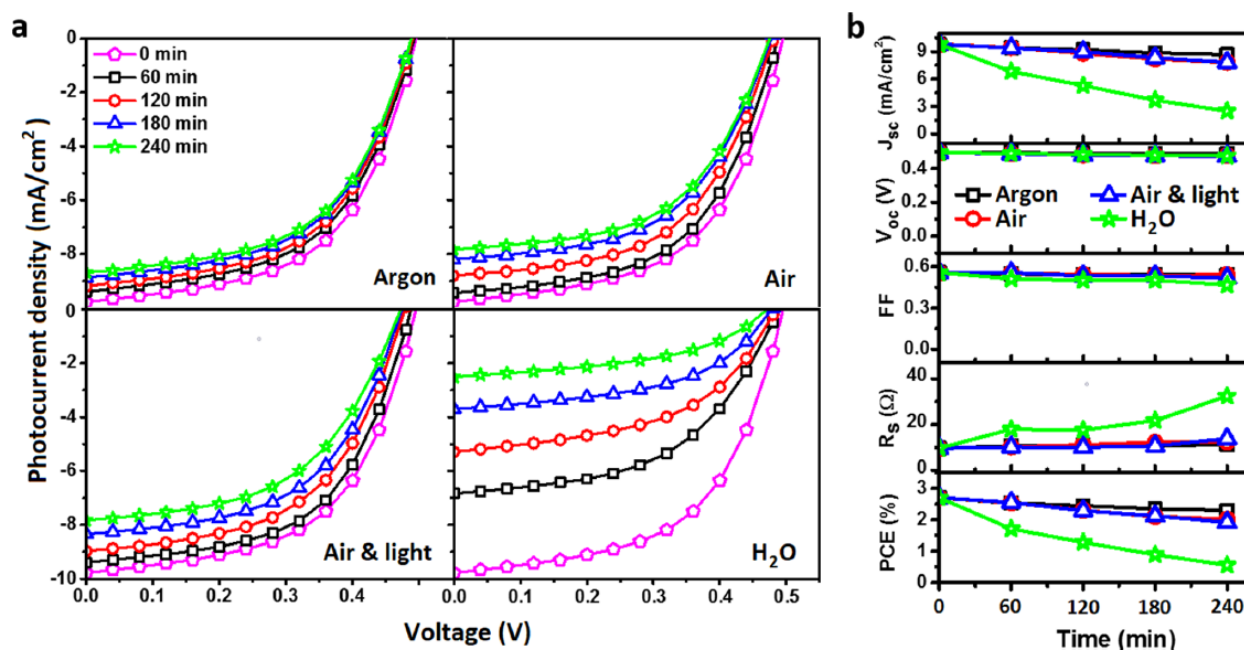


Figure 2. (a) J - V characteristics of devices changing from pristine state over repeated 60 min environmental exposure sequences up to 240 min under argon/dark, air/dark, air/light, and humidity/dark exposure. (b) Overview of solar cell key values changing with increasing exposure time at different environmental conditions.

duration of 240 min are shown in Figure 2a. The respective solar cell key values, such as short circuit current density (J_{SC}), open circuit voltage (V_{OC}), fill factor (FF), power conversion efficiency (PCE), and series resistance (R_S) were extracted/calculated from the corresponding characteristics and are summarized in a plot in Figure 2b for better visibility of even small changes. Before exposure, all devices showed identical characteristics (Figure 2a) and key values (Figure 2b), with a J_{SC} value of almost $10 \text{ mA}/\text{cm}^2$, a V_{OC} value of 0.5 V, an FF of almost 60%, and a resulting PCE of about 3%, confirming their comparability. The argon test series acted as the blind sample in this study, to account for environment-independent material relaxation and aging, but also for effects by measurement conditions. This is necessary because for P3HT:PCBM solar cells in particular, significant morphological changes to the active layer have been observed during operation,³⁸ different to the same active layer within an inverted configuration.³⁹ Accordingly, the J - V characteristics of the devices that were exposed to argon (Figure 2a) show, as expected, the least variation over exposure time, with equal shape of the curves, slopes, and V_{OC} . Only an insignificant decrease in photocurrent J_{SC} is noticeable, whose cause is suspected to be the minor decay of the active layer due to repeated applied voltage under illumination during characterization. The consequent lowered J_{SC} leads to a slightly lower PCE, whereas all other values are stable (Figure 2b, black squares).

Compared to that, nonilluminated air-exposed solar cells (Figure 2a) showed a slightly stronger reduction of photocurrent over exposure time. Looking at their key values (Figure 2b, red circles), it can be seen that the V_{OC} is weakly affected and the series resistance is slightly increased. This indicates a slightly accelerated aging process, compared to samples stored in inert gas. If devices are exposed to air under illumination, a condition commonly feared to cause detrimental photo-oxidation of the active layer, here, merely the same scale

small variations as for the air/dark sample are seen (Figure 2a). In comparison with the air/dark series, the key values of the illuminated air devices (Figure 2b, blue triangles) show identical development of J_{SC} over time, and also only minor changes to V_{OC} , but differ by presenting a small decrease in fill factor and an increase in series resistance. However, this still very similar behavior indicates that low intensity light sources (here 10% intensity of 1 sun) do not lead to further device degradation. In contrast to that, devices that were exposed to humid air without illumination show detrimental development with exposure duration. This is immediately visible from their J - V curves (Figure 2a), which show considerable reduction of photocurrent with increasing exposure time. Thereby, J_{SC} dramatically decreases by 25% within the first 60 min and continues to decay by up to 75% after 240 min of exposure. By looking at the key values of the devices of the humidity series (Figure 2b, green stars), an observation is that the significant increase in series resistance with exposure time shows the strongest direct effect on J_{SC} , whereas the related FF and V_{OC} are relatively little affected. With J_{SC} as the main humidity-responsive factor contributing to PCE, the efficiency also follows the trend of photocurrent development. The relatively small response of V_{OC} and FF to humidity implies that the effective bandgap of the active layer stays unchanged and no major leakage currents were generated after exposure. The trend of all factors (V_{OC} , J_{SC} , FF, R_S , and PCE) for the devices with Ar/dark, air/dark, and air/light exposure are relatively similar. The slight efficiency losses that occur are dominated by a drop of J_{SC} , which corresponds to the rise of series resistance (R_S). In the case of the device series with humidity exposure, R_S increases considerably, giving rise to the suspicion that humidity led either to degradation of the bulk active layer material or generation of interfacial barriers at the electrodes. To clarify which major mechanisms are responsible, further characterization was acquired and is discussed in this paper.

Numerous past publications refer to oxygen/humidity-based degradation of the organic/electrode interface in OPV devices, with quite differing arguments about the actual role of water alone. Often observed are voltage-dependent interfacial charge-transfer barriers, typically recognizable from S-shaped J - V curves with lowered fill factor and reduced V_{OC} .^{15,16,40–43} However, in the present case, the J - V curves did not deteriorate and both FF and V_{OC} were barely affected, indicating that the interfacial charge-transfer efficiency between the active layer and electrode is unaltered during exposure. Further, the J - V curves of all exposure conditions show still parallel slopes at the intersection with the current axis (J_{SC} region) with increasing aging time, implying that shunt resistance (R_{SH}) also stays unchanged, therefore treatment also had no effect on the magnitude of leakage currents of the device.

Photophysics and Photoresponse. Beside the magnitude of J_{SC} , the spectral response of a solar cell can also carry valuable information on its physical properties. The external quantum efficiency (EQE) is determined by J_{SC} per wavelength, and is a measure for the spectral response of the device. Although the total magnitude of EQE follows the trend in photocurrent as presented before, the normalized EQE spectra allow further assumptions by visualizing potential spectral deterioration. Figure 3 shows the normalized EQE spectra of the devices following 240 min exposure at different conditions.

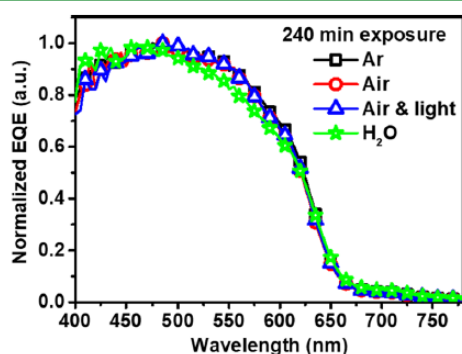


Figure 3. Normalized EQE spectra of devices following 240 min exposure in different environments.

The spectra of those solar cells exposed to Ar/dark, air/dark, and air under illumination all exhibit the congruent signature shape for EQE of the P3HT:PCBM OPV devices, which is a broad peak from 380 to 700 nm with a maximum at 500 nm and a subtle shoulder at 620 nm, basically mirroring P3HT absorption (compare also Figure 4a). Only upon humidity/dark exposure does a deviation of the EQE spectrum occur, noticeable as a flattening of the peak at the long-wavelength side. Potential reasons for this effect could be degradation either of the active layer material or the organic/electrode interface. In the first case, degradation alters the absorption spectrum of the active layer material. In the second and (as becomes clear in the following) more likely case, the flattening at long wavelength is caused by the diminishing number of charge carriers created in the back part of the solar cell, close to the LiF/Al cathode. The reason for this is that long-wavelength radiation has a larger penetration depth in P3HT:PCBM, therefore a large contribution of charges is coming from the entire volume of the active layer, whereas at 500 nm peak absorption, the penetration depth is small and thus contributions are mainly from the front of the cell, close to the ITO anode. Similar effects have been reported in the past, most prominent is the M-shape deterioration of EQE, caused, for example, by self-absorption by a too thick active layer, or in cases of degradation or barrier behavior, near the transparent anode.⁴⁴ In the present case, the loss of charge carriers at higher wavelengths could therefore indicate degradation of the active layer near the electrode or the organic/cathode interface.

Monitoring the absorption and emission behavior of conjugated polymers has proven to be useful to recognize changes, for example, due to photobleaching effects caused by photo-oxidative degradation.^{45–49} To investigate how exposure environments affect the active layer alone, its UV-vis absorption and photoluminescence (PL) properties after 240 min exposure to the respective atmospheres were investigated and compared to the pristine state. The relevant spectra are shown in Figure 4. The absorbance of the active layers (Figure 4a) shows the expected features of both blend components, which is the absorption of PCBM in the UV region below 350 nm and the characteristic P3HT peak at 500 nm with the small vibrational shoulder at 620 nm. In comparison, the spectra look identical, apart from a negligibly higher general absorption of the pristine sample. The emission behavior of a conjugated organic molecule is an even more sensitive marker to spot

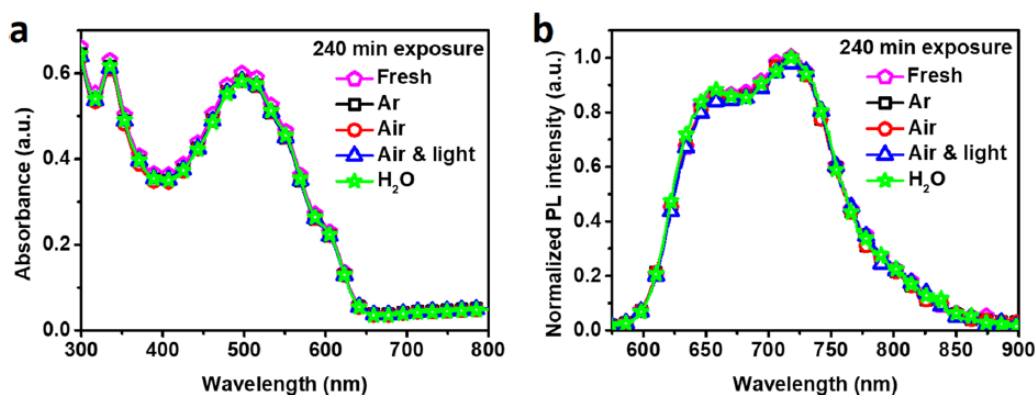


Figure 4. UV-vis absorbance (a) and normalized emission spectra (b) of P3HT:PCBM films in pristine form or after 240 min exposure to different environments.

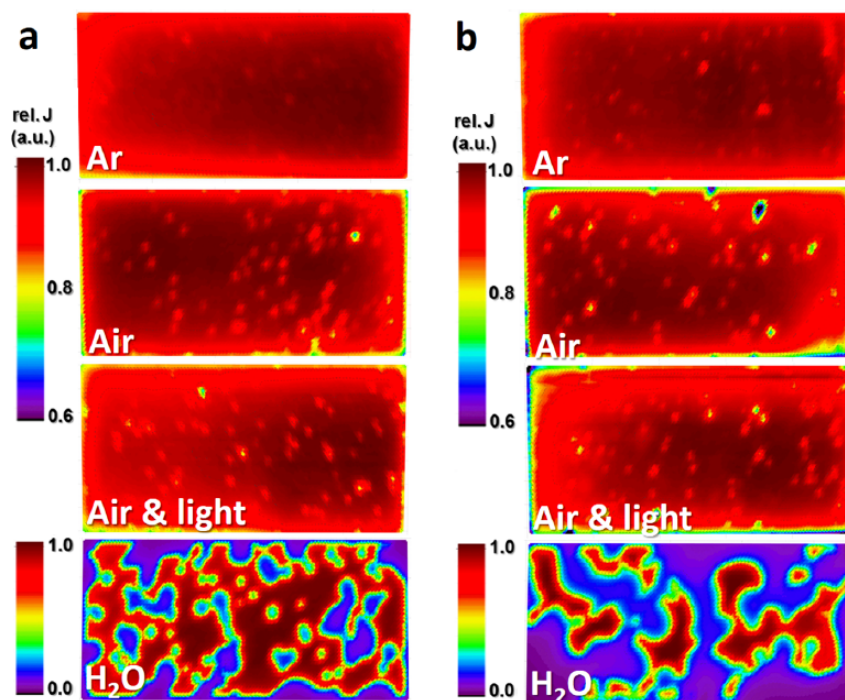


Figure 5. LBIC maps of device area (1.5 mm \times 4.0 mm) upon exposure to different atmospheres for 60 min (a) and 240 min (b).

degradation. However, looking at the shape of the normalized PL spectra (Figure 4b), again all samples exhibit the typical P3HT features in the form of the 0–0 emission at 650 nm and the 0–1 emission at 720 nm, with no significant shift of the peaks or changes of the I₀–0/I₀–1 ratio. In addition, the absolute photoluminescence quantum efficiency of the films was determined as 0.33% for the fresh samples and 0.29% for all exposed samples with no difference between argon, air, illumination, or humidity treatment. This rather small change between fresh and any aged sample, with no relation to the applied different environmental conditions, originates most likely from relaxation of the film. Therewith, the photophysical results confirm that the applied exposure processes in this study do not harm the active layer, at least if separated from the rest of the stack, that is, without contact with the electrode material.

Spatially Resolved Device Characteristics. To gain an understanding about the mechanism behind the loss of photocurrent, which seems to occur without apparent active layer degradation or interface barrier formation, the spatial homogeneity of the device physics across the solar cell area was investigated. Therefore, overview maps of the local photocurrent of respective solar cells after different environmental exposures were generated by LBIC scanning at 532 nm illumination. The normalized photocurrent density maps are shown in Figure 5 for 60 min (a) and 240 min exposure (b). For reference, a corresponding map of a fresh device before exposure is provided in Figure S1, Supporting Information. The device stored in an inert Ar atmosphere in the dark shows, as expected, a very homogeneous high output area, independent of the exposure time. Merely at the edges of the pixel area and at a few central spots (≈ 90 – 130 μm in size), the photocurrent is lowered to around 90% of the original performance, which might be due to regular morphological inhomogeneities of the devices.¹² These images represent the basic spatial performance without further environmental influence. Upon exposure to air/

dark and air under white light illumination, a very similar pattern is found: compared to the argon-stored devices, the number of low-current-spots increases by a factor of 2 for both conditions, whereas the average lateral dimension of the spots remains constant. The extent of deficiency of most spots is similar to that for the ones found in the argon samples, still reaching around 90% of the original performance, but there are also a few spots where photocurrent is reduced down to 80% after 60 min or even below after 240 min. This means that there is a small effect caused by oxygen exposure but no significant effect seen from additional illumination. A completely different picture is drawn by exposing the devices to humidity in the dark. After only 60 min exposure, the solar cell area shows spots and larger islands of failing photocurrent output, almost down to less than 10% of the original performance, whereas the other parts of the cell show an unchanged high output of 100%. The density of low-output zones was calculated to be 1/5 of the pixel area. At exposure beyond 60 min, this humidity-caused local device failure continues to propagate. After 240 min, there are only a few islands of unaltered high photocurrent output left, and the majority of the area is characterized by a quite homogeneous low-output zone with less than 10% of the original photocurrent. Here, a calculation of the low-output area corresponds to about 3/5 of the device.

The observation of island-like device failure upon humidity exposure is different to previous reports, for example, by Madogni et al.,⁴³ who showed that only on exposure to oxygen did formation of islands by growth of Al₂O₃ at the metal/organic interface occur, and instead homogeneous (photo)-degradation was caused by H₂O. However, as many studies in the past were commonly undertaken on devices containing also the hygroscopic hole-conductor PEDOT:PSS, the question is if on those occasions PSS-caused corrosion might have overshadowed other humidity effects.

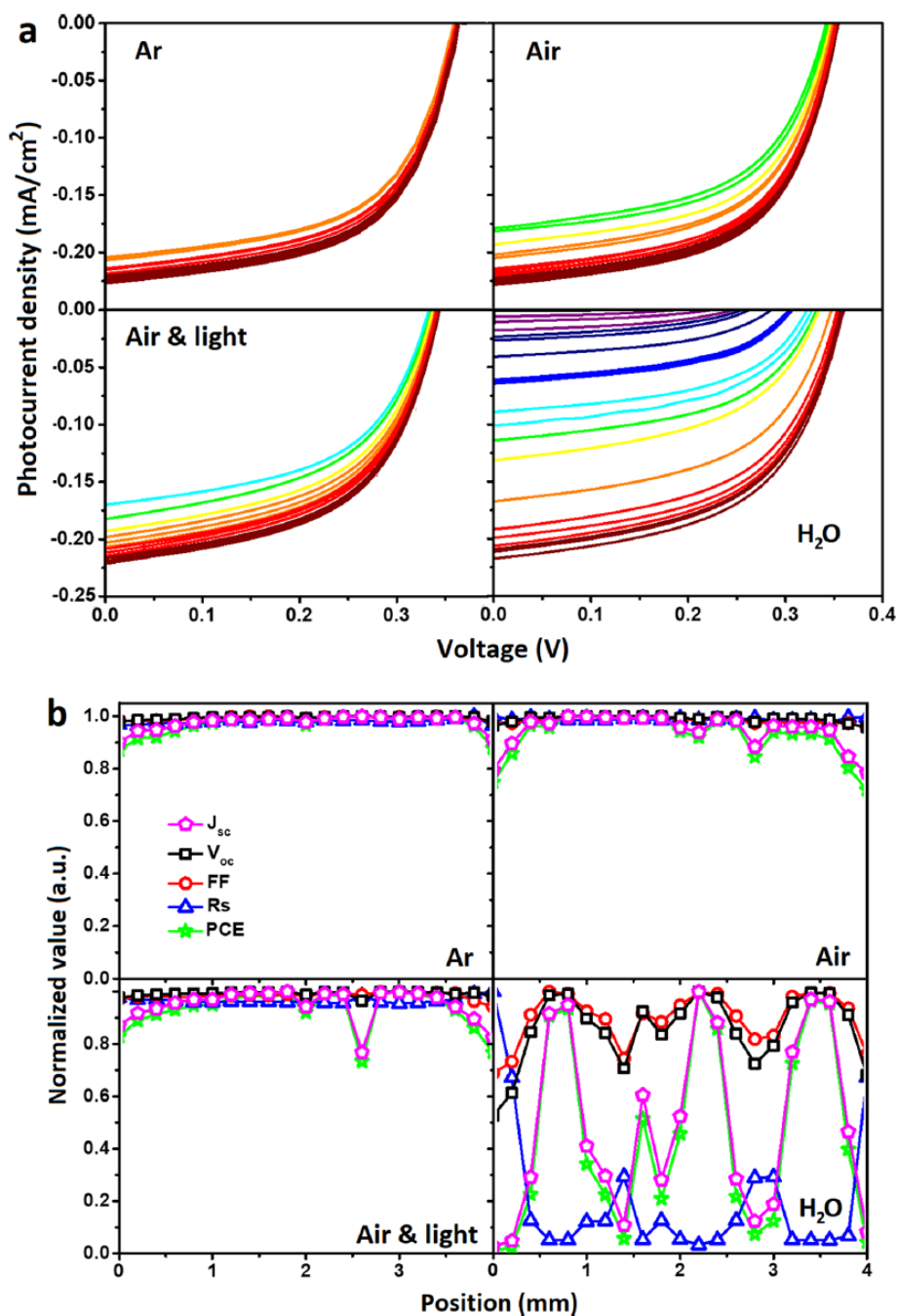


Figure 6. Local photo- J - V curves recorded at different points along the long side (4 mm) of the 240 min-exposed (Ar/dark, air/dark, air/light, and humidity/dark) solar cells (a) and the respective parameters extracted from the local photo- J - V characteristics plotted over the scan-position on the pixel (b).

Probing and comparing the local device physics in areas of high and low output might allow the cause of the locally lowered photocurrent to be isolated, and thus help to identify potential bulk material or interface degradation mechanisms connected to it. For that purpose, local photocurrent–voltage characteristics were recorded across the area of 240 min-exposed solar cells for point-to-point analysis. Figure 6a shows the local photo- J - V curves from a central line-scan along the long side of 4 mm solar cell pixels for the four conditions Ar/dark, air/dark, air/light, and humidity/dark. The solar cell

parameters J_{SC} , V_{OC} , FF, R_S , and PCE, as extracted/calculated from those photo- J - V characteristics, are plotted over their position on the pixel in Figure 6b. For better visibility of any performance scattering between local J - V characteristics across a device area (Figure 6a), the curves are color-coded in regard of their achieved photocurrent. Thereby the “devices’ best curve” is represented by a dark red line, with a J_{SC} of around -0.22 mA/cm² for all conditions, and then following the rainbow in sensible steps of decreasing J_{SC} (bright red, orange, yellow, green, turquoise, light blue, dark blue, and purple). As

expected from the photocurrent maps (Figure 5), the device stored in argon without illumination exhibits the smallest deviation from the “best curve” and also no gradual performance scattering, but a majority of points on the device with maximum performance and only a few singularities with slightly lowered photocurrent, but only down to -0.21 mA/cm^2 for the worst point. Again, air/dark and air/light exposure lead to very comparable results, with a larger deviation from the “best curve”, compared to argon/dark. Still, it is clear that the majority of the measured points deliver maximum performance and only some singularities, but more than that for Ar/dark, show lowered photocurrent, down to a J_{SC} of -0.17 mA/cm^2 . This agrees well with the impression from the photocurrent map (Figure 5). Also, for the latter three conditions, the V_{OC} remains unchanged and slopes are stable, which makes any changes to charge injection/extraction or leakage unlikely as reasons for the diminished photocurrent. Contrary to the previous conditions, exposure to humidity without illumination leads to tremendous scattering of the local J - V curves with J_{SC} varying between -0.22 and -0.01 mA/cm^2 . Thereby, also, the population of the curves with best performance is considerably decreased, and a larger number accumulates at a J_{SC} of -0.06 mA/cm^2 instead. The trend between the four conditions becomes even more obvious when comparing the normalized (to each solar cell's maximum) location-resolved plotted solar cell parameters (Figure 6b). Please also note that the resistance is normalized to the devices' overall maximum, meaning a constant “high” R_{S} does not indicate a high resistance, but merely a very small magnitude of change across the device area. As expected from photocurrent mapping (Figure 5), the Ar/dark device clearly exhibits the highest spatial homogeneity, with very constant values for J_{SC} , V_{OC} , FF, R_{S} , and PCE across the entire area, except for a slight drop of J_{SC} (and with it in PCE) at the pixel edges.

The latter is caused by the nonsharp border of the pixel area, which is defined by the dimensions of the evaporated LiF/Al electrode patch. Vapor deposition through a shadow mask is usually accompanied by formation of a small diffuse zone (gradually fading thickness) at the edges, which here might lead to gradually lower photocurrent, depending on the location at or the distance from the cathode patch.⁵⁰ Consistent with the photocurrent maps and local J - V curves, the devices exposed to air/dark and air/light also show comparable parameter plot patterns. Thereby, J_{SC} , V_{OC} , FF, R_{S} , and PCE are almost constant across the area, except for some singularities, which show a lowered photocurrent (and PCE) but with other values remaining constant. Both devices also show the edge effect observed in the argon/dark sample, even slightly more pronounced by a slightly stronger decreased photocurrent. In contrast to those three conditions, the humidity/dark exposed sample shows a dramatic pattern in the parameter plot, with strong local variations. Thereby, regions of barely affected high J_{SC} , V_{OC} , FF, and PCE, and relatively low R_{S} are neighboring areas with heavily increased resistance R_{S} , J_{SC} almost lowered to zero, and further, not as strongly affected but still lowered V_{OC} and FF. Also, after humidity exposure, edge effects are visible and seem more heavily pronounced than for the other samples. Although one might assume that this originates from humidity diffusing underneath the “impenetrable” LiF/Al patch, the photocurrent maps (Figure 5) of the humidity/dark device exhibiting barely affected regions along the edges rather suggest this is due to an overlap of the edge with a “degraded region” within the scan range. These findings correlate very well with

the observed integral device performance under the different environmental conditions (Figure 2). Despite the fact that for the integral performance, an AM1.5G standard white light source was used, and a green laser diode was used for the photocurrent scans, the trend of the overall device performance is obviously a consequence of the summarized local properties. The question is still which chemical/physical processes lead to the observed local behavior. Here, the literature gives us some known facts and options, including which parameters of a solar cell are usually affected by which kind of mechanism:^{40,43} a lower FF indicates a reduced interfacial charge-transfer efficiency between different layers, for example, the active layer and electrode interface. Higher series resistance is usually caused by either larger contact resistance at the active layer/electrode interface or by deterioration of the bulk active layer material. A decrease of V_{OC} may be a sign of a reduction of active layer/metal electrode interface, a lowered effective bandgap of the donor/acceptor couple (e.g., by material degradation), or a change in electrode work function. The drop in J_{SC} may represent degradation of the active layer, which decreases the photon absorption, and alters the charge mobility and exciton dissociation efficiency, and/or deterioration of the electrode/active layer interface, limiting charge carrier transport and collection efficiency.⁴⁰ To obtain a definite answer to whether the observed behavior comes from degraded active layer in contact with an electrode (because pure active layer degradation was already excluded earlier from photophysical characterization) or from interface degradation, the charge transport characteristics of the exposed ITO/P3HT:PCBM/LiF/Al devices were studied.

Charge Transport. Charge mobility of the devices was extracted by modeling the dark current under forward bias using the space-charge-limited expression for the current density⁵¹

$$J_{\text{SCL}} = \frac{9}{8} \epsilon \mu_0 e^{0.891\gamma} \sqrt{V_{\text{int}}/L} \frac{V_{\text{int}}^2}{L^3}$$

where μ_0 is the zero-field mobility, γ is the field activation parameter, J_{SCL} is the current density, ϵ is the permittivity, V_{int} is the internal voltage, and L is the film thickness. Assuming that the barrier for injection of electrons into the PCBM lowest unoccupied molecular orbital from the Al electrode is higher compared to the injection of holes into the P3HT HOMO from ITO, these devices will be hole-dominated under forward bias, therewith, the values are expected to be close to the hole mobilities in the P3HT:PCBM blend. Although the absolute values might be higher than those in a true hole-only device,⁵² the values will allow a relative comparison between the different exposed devices. The space-charge-limited current characteristics and the respective fits of devices after exposure to Ar/dark, air/dark, air/light, and humidity/dark are shown clearly for 240 min exposure in Figure 7.

The complete table of fitting parameters and derived charge mobilities at exposures of 60 and 240 min, respectively, is given in the Supporting Information. Beside the devices' constant parameters L and ϵ , V_{bi} and fitting parameter γ were also quite comparable between the different devices and conditions. First, the mobilities were fitted for all devices using the current density for the nominal device area of 6 mm^2 . For 60 min exposure, the zero-field mobilities were $1.29 \times 10^{-7} \text{ m}^2/(\text{V s})$ for Ar/dark, $1.24 \times 10^{-7} \text{ m}^2/(\text{V s})$ for air/dark, $1.31 \times 10^{-7} \text{ m}^2/(\text{V s})$ for air/light, and $9.5 \times 10^{-8} \text{ m}^2/(\text{V s})$ for humidity/

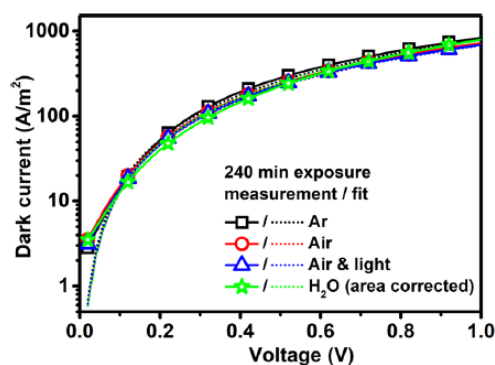


Figure 7. Current–voltage curves of 240 min-exposed ITO/P3HT:PCBM/LiF/Al devices (solid lines with symbol) with according fits to the space-charge limited model (dotted lines).

dark. Although the values for argon and air, with or without illumination, are equal within the level of accuracy and comparable with common values for P3HT:PCBM devices,⁵³ the humidity-exposed sample shows a 25% reduced charge mobility. However, following the observations from the photocurrent mapping that a fraction of 1/5 of the 60 min humidity/dark exposed device area was failing to contribute, the question is whether the material or the contact area is affected. Therefore, we repeated the fit with a corresponding area-corrected (80% of 6 mm²) current density, and obtained a mobility of $1.20 \times 10^{-7} \text{ m}^2/(\text{V s})$, therewith, within the same range of the other devices. After an exposure time of 240 min at the different conditions, the obtained mobilities were $1.46 \times 10^{-7} \text{ m}^2/(\text{V s})$ for Ar/dark, $1.24 \times 10^{-7} \text{ m}^2/(\text{V s})$ for air/dark, and $1.31 \times 10^{-7} \text{ m}^2/(\text{V s})$ for air/light, which means that for these three conditions, the longer exposure does not have a significant effect on the mobility. Only for the humidity/dark conditions was the mobility even lower than before with only $5.96 \times 10^{-8} \text{ m}^2/(\text{V s})$ for the nominal device area. However, the fit using only the intact fraction of the device area, which was estimated from photocurrent mapping with 2/5 (40% of 6 mm²), produced a mobility of $1.19 \times 10^{-7} \text{ m}^2/(\text{V s})$, which is again comparable to other exposure conditions. These results support the image of a stable and unchangeable performance of the active layer, independent of environment and duration. Therefore, the aforementioned lowered J_{SC} , V_{OC} , and increased R_{S} is not induced by active layer degradation in the present case.

Discussion. The presented results show clearly that exposure to dry air, whether illuminated or not, only induces a minor efficiency decrease of P3HT:PCBM devices without a hole-transport layer, when compared to those stored in argon in the dark. This subtle decrease is caused by singularities in the device area of slightly diminished photocurrent, whereas V_{OC} , FF, and R_{S} are not affected in these positions. As these point defects have about the same lateral dimensions as those seen for the Ar/dark devices, even if these show negligible current fluctuations in these spots, it is suspected that these are material defects present in any device, for example, foreign atoms or particles, which might act as potential reaction sites when in contact with oxygen. This is supported by the fact that the size, density, and intensity of these spots is independent of exposure time or illumination. Accordingly, also no barrier behavior, active layer photodegradation, or mobility decrease is noticeable in these devices. Exposure to humidity in the dark,

on the other hand, obviously triggers serious efficiency losses in the HTL-free solar cell. From a purely photophysical point of view, the P3HT:PCBM blend was observed to be stable under the applied conditions, even after long exposure times, which confirms the lack of any significant water-related degradation of the active layer itself. However, this does not eliminate the possibility of interface reactions of the organic donor/acceptor catalyzed by or with the electrode material. On this occasion, the EQE spectra, which join photophysics with device physics, indicated a diminished contribution of charge carriers at the LiF/Al side of the humidity-exposed device, which identified the “problem side” of the device. This is clearly different to PEDOT:PSS-containing standard solar cells, where humidity-caused degradation is majorly induced at the anode side and often ascribed to ITO corrosion by PSS and/or its hygroscopic behavior, fostering water uptake and in the cause of layer swelling, delamination. The present disturbed photocurrent generation on the aluminum side could have its origin in limited charge transfer from the organic to the LiF/Al cathode or in diminished generation/transport of charge carriers within the active layer close to it. In the literature, water-induced degradation has been associated with the formation of interfacial oxide and S-shaped current–voltage characteristics. Although we can see island-like failure areas of diminished photocurrent, and they do show a subtle drop in V_{OC} and FF in the local scan, we do not observe any classical indications for voltage-dependent barrier formation near the electrode, nor failing charge transfer, which would result in a deteriorated current–voltage characteristic. Instead, an increased series resistance in the local failure regions seems to dominate. This is also supported by the charge mobility evaluation, which clearly shows intact unchanged transport behavior, if the “failure areas” are neglected. Therefore, it is assumed that the active layer, even in contact with the cathode, is still widely intact. However, the charge carriers generated in such a region have to be transported a longer distance to an intact electrode area to be extracted, which leads to a virtually higher resistance and the noticeable but small local FF and V_{OC} decrease. In consequence, the properties of the partial contributions from regions with disturbed contact areas, do not have a significant impact on the total integrated device properties, except for the loss of photocurrent. Therefore, no change in FF and V_{OC} is visible for the integral device performance of the humidity/dark device. However, in the literature, the opinions about the role of humidity or oxygen in organic solar cells are contradictory, or no differentiation is made at all. A report by Hermenau et al.⁵⁴ is one of the few which documented them separately. Thereby, they found that both molecular oxygen and water diffuse through the aluminum electrode. According to their results, oxygen diffused rather through selected pinholes in the aluminum film, forming Al_2O_3 islands near the organic interface as a consequence. For water, they suggested diffusion along the grain boundaries of the evaporated aluminum layer, resulting in rather homogeneous degradation of the device. Although we can definitely confirm their further observation that humid air seems more reactive than dry molecular oxygen, which is well known from metal corrosion, we cannot confirm the homogeneous degradation by water. Therefore, we suggest that in the present case, water diffusion is also rather subject to pin hole-transport. We assume that at the bottom of this pin hole, it might react to form an oxide or hydroxide, but apparently to such an extent (regarding its thickness) that it cannot be overcome by an applied voltage, and rather leads to

completely insulated areas. The presence of LiF underneath the aluminum might also have some effect. Although it is still not entirely clear why a sub monolayer of LiF between the organic acceptor and aluminum electrode improves the devices, it is a known fact that LiF added to aluminum melts acts as an oxidation inhibitor by the formation of AlF at the surface. It is very likely that also in this case, this could have prevented the formation of interfacial oxide in the air/dark and air/light devices in this study. In humid conditions, the LiF layer might get partially dissolved, exposing a fresh aluminum surface, which then would quickly react with water via $\text{Al}_3^+ + \text{H}_2\text{O} \rightarrow \text{Al}(\text{OH})_3 + 3\text{H}^+$. This might not only cause formation of an oxide/hydroxide island but also, due to the production of hydrogen, lead to delamination of the electrode by formation of bubbles.

CONCLUSIONS

We aimed to gain information about the occurring degradation mechanisms in organic solar cells without the involvement of acidic PEDOT:PSS, which in standard solar cells dominates the degradation discussion. Therefore, we investigated the impact of chosen environmental exposure conditions on the performance of devices with the architecture ITO/P3HT:PCBM/LiF/Al, that is, without any hole-transport layer between ITO and the organic active layer. Among the different conditions, argon storage acted as the blind sample and was compared to exposure to dry air in the dark or with illumination, and to humid air in the dark, with different exposure durations of up to 240 min. We found that the photophysics of the active layer stay unchanged for all applied conditions, and it showed no signs of photodegradation. In general, exposure to oxygen (air) did not lead to significant performance loss. The small difference to the argon-stored samples seems to originate from small device defects, which are also visible in traces in the argon-stored devices. Devices exposed to humid air, on the other hand, did show huge performance losses during the same exposure times. EQE spectra identified the aluminum side as the primary suspect and LBIC scans showed time-dependent formation of patches of significantly reduced photocurrent contribution, but instead of the usual interfacial charge extraction barriers, rather, insulating behavior was found. Different from previous reports, it is suggested that not only oxygen, but also water is transported through pinholes in aluminum to the organic/electrode interface, leading to the formation of insulating islands and not homogeneous device degradation. The fact that no island formation is seen for dry air exposure is assigned to the protective properties of the LiF interlayer.

ASSOCIATED CONTENT

Supporting Information

The Supporting Information is available free of charge on the ACS Publications website at DOI: 10.1021/acsami.7b08365.

Table summarizing constants, fitting parameters, and charge mobilities as derived from space-charge-limited current modeling on photovoltaic devices exposed to Ar/dark, air/dark, air/light, or humidity/dark for 60 min or 240 min; LBIC map of a fresh device before exposure (PDF)

AUTHOR INFORMATION

Corresponding Author

*Email: hchien@tugraz.at

ORCID

Huei-Ting Chien: 0000-0003-3703-9411

Bettina Friedel: 0000-0001-5917-6615

Notes

The authors declare no competing financial interest.

ACKNOWLEDGMENTS

H.-T.C. and B.F. are grateful to Sergey M. Borisov for the access to equipment and valuable discussions, and to the Austrian Science Fund (FWF) for financial support (Project No. P 26066).

REFERENCES

- (1) Yu, G.; Gao, J.; Hummelen, J. C.; Wudl, F.; Heeger, A. J. Polymer Photovoltaic Cells: Enhanced Efficiencies via a Network of Internal Donor–Acceptor Heterojunctions. *Science* 1995, 270, 1789–1791.
- (2) Brabec, C. J. Organic Photovoltaics: Technology and Market. *Sol. Energy Mater. Sol. Cells* 2004, 83, 273–292.
- (3) Lungenschmied, C.; Dennler, G.; Neugebauer, H.; Sariciftci, S. N.; Glatthaar, M.; Meyer, T.; Meyer, A. Flexible, Long-Lived, Large-Area, Organic Solar Cells. *Sol. Energy Mater. Sol. Cells* 2007, 91, 379–384.
- (4) Krebs, F. C.; Spanggaard, H.; Kjær, T.; Biancardo, M.; Alstrup, J. Large Area Plastic Solar Cell Modules. *Mater. Sci. Eng., B* 2007, 138, 106–111.
- (5) Kim, Y.; Cook, S.; Tuladhar, S. M.; Choulis, S. A.; Nelson, J.; Durrant, J. R.; Bradley, D. D. C.; Giles, M.; McCulloch, I.; Ha, C.-S.; Ree, M. A Strong Regioregularity Effect in Self-Organizing Conjugated Polymer Films and High-Efficiency Polythiophene: Fullerene Solar Cells. *Nat. Mater.* 2006, 5, 197–203.
- (6) Goh, C.; Kline, R. J.; McGehee, M. D.; Kadnikova, E. N.; Fréchet, J. M. J. Molecular-Weight-Dependent Mobilities in Regioregular Poly(3-hexyl-thiophene) Diodes. *Appl. Phys. Lett.* 2005, 86, No. 122110.
- (7) Ma, W.; Yang, C.; Gong, X.; Lee, K.; Heeger, A. J. Thermally Stable, Efficient Polymer Solar Cells with Nanoscale Control of the Interpenetrating Network Morphology. *Adv. Funct. Mater.* 2005, 15, 1617–1622.
- (8) Li, G.; Shrotriya, V.; Huang, J.; Yao, Y.; Moriarty, T.; Emery, K.; Yang, Y. High-Efficiency Solution Processable Polymer Photovoltaic Cells by Self-Organization of Polymer Blends. *Nat. Mater.* 2005, 4, 864–868.
- (9) Moulé, A. J.; Meerholz, K. Controlling Morphology in Polymer–Fullerene Mixtures. *Adv. Mater.* 2008, 20, 240–245.
- (10) Alem, S.; de Bettignies, R.; Nunzi, J.-M.; Cariou, M. Efficient Polymer-Based Interpenetrated Network Photovoltaic Cells. *Appl. Phys. Lett.* 2004, 84, 2178–2180.
- (11) Irwin, M. D.; Buchholz, D. B.; Hains, A. W.; Chang, R. P. H.; Marks, T. J. P-Type Semiconducting Nickel Oxide as an Efficiency-Enhancing Anode Interfacial Layer in Polymer Bulk-Heterojunction Solar Cells. *Proc. Natl. Acad. Sci. U.S.A.* 2008, 105, 2783–2787.
- (12) Chien, H.-T.; Pözl, M.; Koller, G.; Challenger, S.; Fairbairn, C.; Baikie, I.; Kratzer, M.; Teichert, C.; Friedel, B. Effects of Hole-Transport Layer Homogeneity in Organic Solar Cells – A Multi-Length Scale Study. *Surf. Interfaces* 2017, 6, 72–80.
- (13) Green, M. A.; Emery, K.; Hishikawa, Y.; Warta, W.; Dunlop, E. D. Solar Cell Efficiency Tables (version 46). *Prog. Photovoltaics* 2015, 23, 805–812.
- (14) Greenbank, W.; Hirsch, L.; Wantz, G.; Chambon, S. Interfacial Thermal Degradation in Inverted Organic Solar Cells. *Appl. Phys. Lett.* 2015, 107, No. 263301.

- (15) Jørgensen, M.; Norrman, K.; Gevorgyan, S. A.; Tromholt, T.; Andreasen, B.; Krebs, F. C. Stability of Polymer Solar Cells. *Adv. Mater.* **2012**, *24*, 580–612.
- (16) Jørgensen, M.; Norrman, K.; Krebs, F. C. Stability/Degradation of Polymer Solar Cells. *Sol. Energy Mater. Sol. Cells* **2008**, *92*, 686–714.
- (17) Gevorgyan, S. A.; Madsen, M. V.; Roth, B.; Corazza, M.; Hösel, M.; Søndergaard, R. R.; Jørgensen, M.; Krebs, F. C. Lifetime of Organic Photovoltaics: Status and Predictions. *Adv. Energy Mater.* **2016**, *6*, No. 1501208.
- (18) Cao, Y.; Yu, G.; Zhang, C.; Menon, R.; Heeger, A. J. Polymer Light-Emitting Diodes with Polyethylene Dioxothiophene–Polystyrene Sulfonate as the Transparent Anode. *Synth. Met.* **1997**, *87*, 171–174.
- (19) Heithecker, D.; Kammoun, A.; Dobbertin, T.; Riedl, T.; Becker, E.; Metzendorf, D.; Schneider, D.; Johannes, H.-H.; Kowalsky, W. Low-Voltage Organic Electroluminescence Device with an Ultrathin, Hybrid Structure. *Appl. Phys. Lett.* **2003**, *82*, 4178–4180.
- (20) de Jong, M. P.; van Ijzendoorn, L. J.; de Voigt, M. J. A. Stability of the Interface between Indium-Tin-Oxide and Poly(3,4-ethylenedioxythiophene)/Poly(styrenesulfonate) in Polymer Light-Emitting Diodes. *Appl. Phys. Lett.* **2000**, *77*, 2255–2257.
- (21) So, F.; Kondakov, D. Degradation Mechanisms in Small-Molecule and Polymer Organic Light-Emitting Diodes. *Adv. Mater.* **2010**, *22*, 3762–3777.
- (22) Friedel, B.; Brenner, T. J. K.; McNeill, C. R.; Steiner, U.; Greenham, N. C. Influence of Solution Heating on the Properties of PEDOT:PSS Colloidal Solutions and Impact on the Device Performance of Polymer Solar Cells. *Org. Electron.* **2011**, *12*, 1736–1745.
- (23) Friedel, B.; Keivanidis, P. E.; Brenner, T. J. K.; Abrusci, A.; McNeill, C. R.; Friend, R. H.; Greenham, N. C. Effects of Layer Thickness and Annealing of PEDOT: PSS Layers in Organic Photodetectors. *Macromolecules* **2009**, *42*, 6741–6747.
- (24) Meyer, J.; Khalandovsky, R.; Görrn, P.; Kahn, A. MoO₃ Films Spin-Coated from a Nanoparticle Suspension for Efficient Hole-Injection in Organic Electronics. *Adv. Mater.* **2011**, *23*, 70–73.
- (25) Zilberberg, K.; Trost, S.; Schmidt, H.; Riedl, T. Solution Processed Vanadium Pentoxide as Charge Extraction Layer for Organic Solar Cells. *Adv. Energy Mater.* **2011**, *1*, 377–381.
- (26) Steirer, K. X.; Chesin, J. P.; Widjonarko, N. E.; Berry, J. J.; Miedaner, A.; Ginley, D. S.; Olson, D. C. Solution Deposited NiO Thin-Films as Hole Transport Layers in Organic Photovoltaics. *Org. Electron.* **2010**, *11*, 1414–1418.
- (27) Savva, A.; Burgués-Ceballos, I.; Papazoglou, G.; Choulis, S. A. High-Performance Inverted Organic Photovoltaics Without Hole-Selective Contact. *ACS Appl. Mater. Interfaces* **2015**, *7*, 24608–24615.
- (28) Seeland, M.; Rosch, R.; Hoppe, H. In *Stability and Degradation of Organic and Polymer Solar Cells*; Krebs, F. C., Ed.; Wiley: Chichester, U.K., 2012; Chapter 3, pp 39–70.
- (29) Jeranko, T.; Tributsch, H.; Sariciftci, N. S.; Hummelen, J. C. Patterns of Efficiency and Degradation of Composite Polymer Solar Cells. *Sol. Energy Mater. Sol. Cells* **2004**, *83*, 247–262.
- (30) Rivière, G. A.; Simon, J.-J.; Escoubas, L.; Vervisch, W.; Pasquinielli, M. Photo-Electrical Characterizations of Plastic Solar Modules. *Sol. Energy Mater. Sol. Cells* **2012**, *102*, 19–25.
- (31) Lloyd, M. T.; Peters, C. H.; Garcia, A.; Kauvar, I. V.; Berry, J. J.; Reese, M. O.; McGehee, M. D.; Ginley, D. S.; Olson, D. C. Influence of the Hole-Transport Layer on the Initial Behavior and Lifetime of Inverted Organic Photovoltaics. *Sol. Energy Mater. Sol. Cells* **2011**, *95*, 1382–1388.
- (32) Kroon, J. M.; Wienk, M. M.; Verhees, W.; Hummelen, J. C. Accurate Efficiency Determination and Stability Studies of Conjugated Polymer/Fullerene Solar Cells. *Thin Solid Films* **2002**, *403–404*, 223–228.
- (33) Bull, T. A.; Pingree, L. S. C.; Jenekhe, S. A.; Ginger, D. S.; Luscombe, C. K. The Role of Mesoscopic PCBM Crystallites in Solvent Vapor Annealed Copolymer Solar Cells. *ACS Nano* **2009**, *3*, 627–636.
- (34) Krebs, F. C.; Søndergaard, R.; Jørgensen, M. Printed Metal Back Electrodes for R2R Fabricated Polymer Solar Cells Studied Using the LBIC Technique. *Sol. Energy Mater. Sol. Cells* **2011**, *95*, 1348–1353.
- (35) Vorasayan, P.; Betts, T. R.; Gottschalg, R. Spatially Distributed Model for the Analysis of Laser Beam Induced Current (LBIC) Measurements of Thin Film Silicon Solar Modules. *Sol. Energy Mater. Sol. Cells* **2011**, *95*, 111–114.
- (36) Koishiyev, G. T.; Sites, J. R. Impact of Sheet Resistance on 2-D Modeling of Thin-Film Solar Cells. *Sol. Energy Mater. Sol. Cells* **2009**, *93*, 350–354.
- (37) Karpov, V. G.; Compaa, A. D.; Shvydka, D. Effects of Nonuniformity in Thin-Film Photovoltaics. *Appl. Phys. Lett.* **2002**, *80*, 4256–4258.
- (38) Schaffer, C. J.; Palumbiny, C. M.; Niedermeier, M. A.; Jendrzewski, C.; Santoro, G.; Roth, S. V.; Müller-Buschbaum, P. A Direct Evidence of Morphological Degradation on a Nanometer Scale in Polymer Solar Cells. *Adv. Mater.* **2013**, *25*, 6760–6764.
- (39) Wang, W.; Schaffer, C. J.; Song, L.; Körstgens, V.; Pröller, S.; Indari, E. D.; Wang, T.; Abdelsamie, A.; Bernstorff, S.; Müller-Buschbaum, P. In Operando Morphology Investigation of Inverted Bulk Heterojunction Organic Solar Cells by GISAXS. *J. Mater. Chem. A* **2015**, *3*, 8324–8331.
- (40) Grossiord, N.; Kroon, J. M.; Andriessen, R.; Blom, P. W. M. Degradation Mechanisms in Organic Photovoltaic Devices. *Org. Electron.* **2012**, *13*, 432–456.
- (41) Rösch, R.; Tanenbaum, D. M.; Jørgensen, M.; Seeland, M.; Bärenklau, M.; Hermenau, M.; Voroshazi, E.; Lloyd, M. T.; Galagan, Y.; Zimmermann, B.; et al. Investigation of the Degradation Mechanisms of a Variety of Organic Photovoltaic Devices by Combination of Imaging Techniques—the ISOS-3 Inter-Laboratory Collaboration. *Energy Environ. Sci.* **2012**, *5*, 6521–6540.
- (42) Tress, W.; Corvers, S.; Leo, K.; Riede, M. Investigation of Driving Forces for Charge Extraction in Organic Solar Cells: Transient Photocurrent Measurements on Solar Cells Showing S-Shaped Current-Voltage Characteristics. *Adv. Energy Mater.* **2013**, *3*, 873–880.
- (43) Madogni, V. I.; Kounouhewa, B.; Akpo, A.; Agbomahena, M.; Houkpatin, S. A.; Awanou, C. N. Comparison of Degradation Mechanisms in Organic Photovoltaic Devices upon Exposure to a Temperate and a Subequatorial Climate. *Chem. Phys. Lett.* **2015**, *640*, 201–214.
- (44) Brenner, T. J. K.; Vaynzof, Y.; Li, Z.; Kabra, D.; Friend, R. H.; McNeill, C. R. White-Light Bias External Quantum Efficiency Measurements of Standard and Inverted P3HT:PCBM Photovoltaic Cells. *J. Phys. D: Appl. Phys.* **2012**, *45*, No. 415101.
- (45) Manceau, M.; Bundgaard, E.; Carlé, J. E.; Hagemann, O.; Helgesen, M.; Søndergaard, R.; Jørgensen, M.; Krebs, F. C. Photochemical Stability of π -Conjugated Polymers for Polymer Solar Cells: A rule of thumb. *J. Mater. Chem.* **2011**, *21*, 4132–4141.
- (46) Manceau, M.; Rivaton, A.; Gardette, J.-L.; Guillerez, S.; Lemaître, N. The mechanism of Photo- and Thermo-oxidation of Poly(3-hexylthiophene) (P3HT) Reconsidered. *Polym. Degrad. Stab.* **2009**, *94*, 898–907.
- (47) Hintz, H.; Egelhaaf, H.-J.; Peisert, H.; Chassé, T. Photo-Oxidation and Ozonization of Poly(3-hexylthiophene) Thin Films as Studied by UV/VIS and Photoelectron Spectroscopy. *Polym. Degrad. Stab.* **2010**, *95*, 818–825.
- (48) Hintz, H.; Egelhaaf, H.-J.; Lüer, L.; Hauch, J.; Peisert, H.; Chassé, T. Photodegradation of P3HT—A Systematic Study of Environmental Factors. *Chem. Mater.* **2011**, *23*, 145–154.
- (49) Deschler, F.; De Sio, A.; von Hauff, E.; Kutka, P.; Sauermann, T.; Egelhaaf, H.-J.; Hauch, J.; Da Como, E. The Effect of Ageing on Exciton Dynamics, Charge Separation, and Recombination in P3HT/PCBM Photovoltaic Blends. *Adv. Funct. Mater.* **2012**, *22*, 1461–1469.
- (50) Lombardo, C. J.; Glaz, M. S.; Ooi, Z.-E.; Bout, D. A. V.; Dodabalapur, A. Scanning Photocurrent Microscopy of Lateral Organic Bulk Heterojunctions. *Phys. Chem. Chem. Phys.* **2012**, *14*, 13199–13203.
- (51) Murgatroyd, P. N. Theory of Space-Charge-Limited Current Enhanced by Frenkel Effect. *J. Phys. D: Appl. Phys.* **1970**, *3*, 151–156.

(52) Wetzelaer, G.-J. A. H.; Van der Kaap, N. J.; Koster, L. J. A.; Blom, P. W. M. Quantifying Bimolecular Recombination in Organic Solar Cells in Steady State. *Adv. Energy Mater.* 2013, 3, 1130–1134.

(53) Schafferhans, J.; Baumann, A.; Wagenpfahl, A.; Deibel, C.; Dyakonov, V. Oxygen Doping of P3HT:PCBM Blends: Influence on Trap States, Charge Carrier Mobility and Solar Cell Performance. *Org. Electron.* 2010, 11, 1693–1700.

(54) Hermenau, M.; Riede, M.; Leo, K.; Gevorgyan, S. A.; Krebs, F. C.; Norrman, K. Water and Oxygen Induced Degradation of Small Molecule Organic Solar Cells. *Sol. Energy Mater. Sol. Cells* 2011, 95, 1268–1277.

Short-Term Environmental Effects and their Influence on Spatial Homogeneity of Organic Solar Cell Functionality

Huei -Ting Chien^{1}, Peter W. Zach², Bettina Friedel^{1,3}*

¹Institute of Solid State Physics, Graz University of Technology, Austria

²Institute of Analytical Chemistry and Food Chemistry, Graz University of Technology, Austria

³Energy Research Center, Vorarlberg University of Applied Sciences, Austria

*Email: hchien@tugraz.at

| Atmosphere | t (min) | μ_0 ($\times 10^{-7} \text{ m}^2/\text{Vs}$) | γ ($\times 10^{-4} (\text{m/V})^{0.5}$) | R | V_{bi} (V) |
|---------------------------------------|---------|--|--|------|--------------|
| Ar | 60 | 1.29 | -3.6 | 0.91 | 0.42 |
| Air | 60 | 1.24 | -3.6 | 0.88 | 0.42 |
| Air&light | 60 | 1.31 | -3.7 | 0.89 | 0.42 |
| H ₂ O full device area | 60 | 0.95 | -3.1 | 0.88 | 0.44 |
| H ₂ O area corrected (80%) | 60 | 1.20 | -3.1 | 0.89 | 0.44 |
| Ar | 240 | 1.46 | -3.7 | 0.87 | 0.42 |
| Air | 240 | 1.24 | -3.5 | 0.90 | 0.42 |
| Air&light | 240 | 1.31 | -3.9 | 0.92 | 0.42 |
| H ₂ O full device area | 240 | 0.60 | -2.9 | 0.91 | 0.44 |
| H ₂ O area corrected (40%) | 240 | 1.19 | -2.9 | 0.91 | 0.44 |

Table S1. Summary of the fitting parameters and derived charge mobilities of space-charge limited current characteristics of devices at exposure of 60 minutes and 240 minutes.

Table S1 summarizes the constants and fitting parameters for each type of samples processed in this study, i.e. after 60 min or 240 min exposure in Ar/dark, air/dark, air/light and humidity dark. Constants during the fit were the devices' thickness L with 100 nm and the organic materials' dielectric constant ϵ , which was chosen with the value 3. The build-in voltage V_{bi} with values between 0.42 and 0.44 V and the fitting parameter γ with values between -2.9 and $-3.9 \times 10^{-4} (\text{m/V})^{0.5}$, were quite comparable between different devices. The quality of the fits, represented by R , is with values around 0.9, generally quite high. The obtained zero-field mobilities of Ar, Air, Air&light present comparable values for 60 min exposure and 240 exposure, respectively. The

humidity-exposed sample show a by 20% reduced charge mobility for 60 min exposure and a 60% reduced for 240 min exposure, compared to other environmental conditions. The reduced charge mobility is related to the lack of contribution of failing areas as identified in photocurrent maps (Figure 5). After an according area correction for the humidity exposed devices (80% effective area for 60 min and 40% for 240 min), the charge mobilities show again comparable values to other exposure conditions.

In addition to the LBIC maps of 60 min and 240 min exposed devices in the main paper (Figure 5), here the map of a fresh (0 min) device is presented for reference in Figure S1. The high photocurrent output appears very homogeneous, without any patterns or discrete features.



Figure S1. LBIC map of the area (1.5 mm x 4.0 mm) of a fresh device before any exposure (0 min).

Conclusions

OPV offers the ability of low-cost manufacturing and large-scale roll-to-roll-processing in the photovoltaic industry due to the properties of materials and solution processability. However, the efficiency and stability of these types of devices are still far lower than the Si-based SC. A significant number of studies have been dedicated to improving OPV's efficiency and lengthening its lifetime. One of the biggest developments has been achieved by applying the BHJ structure and the introduction of HTL. PEDOT:PSS, which significantly improves the efficiency of SC, is one of the most used HTL materials. However, it has also been proved that PEDOT:PSS causes short lifetime, inhomogeneity and irreproducibility of the device. These correspond to the high sensitivity of the material to environmental conditions such as oxygen, illumination, and moisture or its inhomogeneous colloidal feature. Further research regarding the major causes and degradation mechanisms that limit the device efficiency and lifetime is one way toward developing high performance and stable OPV. In recent years, spatially resolved techniques have been widely applied as tools to characterize surface and device performance and localize fabrication and degradation defects.

Throughout this work, surface and device inhomogeneity of P3HT:PCBM BHJ OPV with and/or without the influence of HTL were investigated. Three different HTL materials were compared, one commercial ink PEDOT:PSS, one quasi-continuous MoO_3 and one colloidal MoO_3 from two different precursor solutions. The degradation mechanisms of the device caused by different environmental conditions, dry air with <20% relative humidity in the dark, dry air with illumination (10% of AM 1.5G) and humid air with >80% relative humidity in the dark were studied. The whole work was investigated mainly based on spatially-resolved characterization techniques, including LBIC, surface morphology, chemical property, and contact potential difference accompanied by the device physics and photophysics to clarify the causes of device failure and environmental degradation mechanisms of OPV with and/or without the influence of HTLs.

Initial work was presented with a comparison of the morphology and contact potential difference distribution of HTL layers and ITO electrodes and spatial photocurrent distribution of the OPVs at different scales of resolution to understand the influence of HTL on the device homogeneity and performance. The results indicated that the homogeneity of the anode film and device performance was significantly increased with incorporation of any HTL. Regardless of continuous or nanoparticle layers, MoO_3 HTLs gave a considerably identical performance with higher efficiency and homogeneity. Different from the MoO_3 HTLs, PEDOT:PSS HTL presented spatial inhomogeneities and charge transfer barriers in the device, which were proved independent of its colloidal feature.

Next, prepared HTLs were exposed to different environmental conditions and compared their surface and device inhomogeneity with freshly prepared samples, to gain information on the

potential degradation mechanisms influenced directly by HTLs with different environmental effects. The surface and bulk chemistry of the HTLs, along with the devices' charge transport dynamics, spatial photocurrent distribution and local device physics were compared. The results showed that fresh PEDOT:PSS layers presented interfacial resistance due to the rigid non-equilibrium state, the longer relaxation time of layers leading to the improvement. The two MoO₃ films show highly stable electrical behavior and homogeneity for any condition, except for humidity exposure of the nanoparticle layer. The device with humid exposed MoO₃ nanoparticle HTL presented some device failure due to the partial interfacial contact loss upon water-uptake of the HTL. The device with humid exposed PEDOT:PSS, showed seriously decreased photocurrent and series resistance corresponding to the hygroscopic nature of PEDOT:PSS. This was caused by the consecutive swelling and shrinking of the layer on top of the ITO substrate and after incorporation within the device. When comparing the device's performance with humid exposed nanoparticle MoO₃ and PEDOT:PSS, the photocurrent losses were mainly related to the amount of absorbed water in the HTL, inducing loss of active area in terms of the partial delamination of the interfacial contact.

Finally, the study aimed at obtaining the information on the degradation mechanisms in OPVs without the impact of acidic PEDOT:PSS or other HTLs. The non-encapsulated devices were exposed to different environments. Here, an Ar-stored sample acted as the blind sample for the comparison of different exposure conditions. The result showed that the photophysics of the active layer stayed undamaged without a sign of photodegradation for all different environmental treatments. In general, devices exposed to dry air did not induce serious performance loss. No island formation was observed for dry air exposure assigned to the protective behavior of the LiF interlayer. However, devices exposed to humid air presented significantly reduced SC performance during the same exposure times. EQE spectra specified the cathode Al side as the main suspect and LBIC maps showed great photocurrent losses with increasing exposure time due to the formation of insulating islands as water penetrated into the organic/electrode interface of the device through the pinholes of Al.

In conclusion, independent of colloidal or continuous form, MoO₃ has been shown to be a better candidate for the HTL material, leading to higher performance and homogeneity of the device, even with the treatment of different environmental conditions. The major environmental source leading to strong and fast reduced device performance is humid air. The partial contact loss of SC was observed owing to the delamination at the anode/HTL or HTL/active interface after nanoparticle HTLs absorbed moisture. The formation of the insulating barrier at the interface between LiF/Al and the active layer was seen when the device without HTL was directly exposed to the humid air environment, facilitating the penetration of water into the device from the Al cathode.

Acknowledgements

I would like to thank all the people who have helped me in the last few years and apology to all those people who I do not mention here.

First, I would like to thank the financial support of the Austrian Science Fund (FWF), Project No. P 26066.

Specially thanks go to Prof. Bettina Friedel for providing me the opportunity to work on this interesting topic, and for all the patience guidance and helpful mentoring of my work. I would like to thank Prof. Robert Schennach for his great advices and supports to obtain my degree. I acknowledge all the members in the OPV group for their friendly help and discussion. Thanks to all the staff and colleagues at the Institute of Solid State Physics for the technical and administrative support.

I also want to thank Prof. Martijn Kemerink and Prof. Gregor Trimmel for their kindness to be the second reviewer and examiner on my thesis and research.

Last but not least, I would like to sincerely thank my family and friends for their encouragement, company and support.

Publications and Conference contributions

Publications:

Chien, H.-T.; Pilat F.; Griesser T.; Fitzek H.; Poelt P.; Friedel B.; Influence of Environmentally Affected Hole Transport Layers on Spatial Homogeneity and Charge Transport Dynamics of Organic Solar Cells. (accepted in *ACS applied materials & interfaces*)

Chien, H.-T.; Zach, P. W.; Friedel, B. Short-Term Environmental Effects and Their Influence on Spatial Homogeneity of Organic Solar Cell Functionality. *ACS applied materials & interfaces* **2017**, *9*, 27754–27764.

Chien, H.-T.; Pölzl, M.; Koller, G.; Challinger, S.; Fairbairn, C.; Baikie, I.; Kratzer, M.; Teichert, C.; Friedel, B. Effects of hole-transport layer homogeneity in organic solar cells – A multi-length scale study. *Surfaces and Interfaces* **2017**, *6*, 72–80.

Ebner, M.; Schennach, R.; **Chien, H.-T.**; Mayrhofer, C.; Zankel, A.; Friedel, B. Regenerated cellulose fiber solar cell. *Flex. Print. Electron.* **2017**, *2*, 14002.

Dunst, S.; Rath, T.; Reichmann, A.; **Chien, H.-T.**; Friedel, B.; Trimmel, G. A comparison of copper indium sulfide-polymer nanocomposite solar cells in inverted and regular device architecture. *Synthetic Metals* **2016**, *222*, 115–123.

Conference contributions:

Chien, H.-T.; Zach, P. W., Borisov S. M., Friedel, B. Short Term Environmental Effects and their Influence on Spatial Homogeneity of Organic Solar Cell Functionality. 4th World Congress and Expo on Nanotechnology and Materials Science, **2017** April, Barcelona, Spain (Poster)

Chien, H.-T.; Pölzl, M.; Koller, G.; Challinger, S.; Fairbairn, C.; Baikie, I.; Kratzer, M.; Teichert, C.; Brenner T.; Böhm M.; Friedel, B. Effects of Hole-Transport Layer Homogeneity in Organic Solar Cells – A Multi-Length Scale Study. Material Research Society (MRS) Spring Meeting, **2016** March, Phoenix, USA (Poster)

Chien, H.-T.; Pölzl, M.; Koller, G.; Baikie, I.; Brenner T.; Böhm M.; Friedel, B., Hole-Transport Layers Beyond PEDOT:PSS – Low-Temperature Solution-Processed MoO_x Derivatives in Organic Solar Cells. 13th European Conference on Molecular Electronics, **2015** Sep., Strasbourg, France (Poster)

Chien, H.-T.; Brenner T.; Böhm M.; Friedel, B., Hole-Transport Layers Beyond PEDOT:PSS – Low-Temperature Solution-Processed MoO_x Derivatives in Organic Solar Cells. European Materials Research Society Spring Meeting, **2015** May, Lille, France (Poster)